SOILS and ROCKS

An International Journal of Geotechnical and Geoenvironmental Engineering

Soils and Rocks publishes papers in English in the broad fields of Geotechnical Engineering, Engineering Geology, and Geoenvironmental Engineering. The Journal is published quarterly in March, June, September and December. The first issue was released in 1978, under the name *Solos e Rochas*, being originally published by the Graduate School of Engineering of the Federal University of Rio de Janeiro. In 1980, the Brazilian Association for Soil Mechanics and Geotechnical Engineering took over the editorial and publishing responsibilities of *Solos e Rochas*, increasing its reach. In 2007, the journal was renamed Soils and Rocks and acquired the status of an international journal, being published jointly by the Brazilian Association for Soil Mechanics and Geotechnical Engineering, by the Portuguese Geotechnical Society, and until 2010 by the Brazilian Association for Engineering Geology and the Environment.

Soils and Rocks

1978,	1 (1, 2)
1979,	1 (3), 2 (1,2)
1980-1983,	3-6 (1, 2, 3)
1984,	7 (single number)
1985-1987,	8-10 (1, 2, 3)
1988-1990,	11-13 (single number)
1991-1992,	14-15 (1, 2)
1993,	16 (1, 2, 3, 4)
1994-2010,	17-33 (1, 2, 3)
2011,	34 (1, 2, 3, 4)
2012-2019,	35-42 (1, 2, 3)
2020,	43 (1, 2, 3, 4)
2021,	44 (1,2

ISSN 1980-9743
ISSN-e 2675-5475 CDU 624.131.1

Soils and Rocks
An International Journal of Geotechnical and Geoenvironmental Engineering
ISSN 1980-9743 ISSN-e 2675-5475

Publication of
ABMS - Brazilian Association for Soil Mechanics and Geotechnical Engineering
SPG - Portuguese Geotechnical Society
Volume 44, N. 2, April-June 2021

Table of Contents

EDITORIAL

Soils and Rocks reviewers in 2020
R.P. Cunha, A. Vieira

LECTURE

Judgement in geotechnical engineering practice
José António Mateus de Brito

ARTICLES

Centrifuge modeling of normal faulting and underground tunnel in sandy soil deposit
Ali Nabizadeh, Alireza Seghateh Mojtahedi

Soil-structure interaction analysis in reinforced concrete structures on footing foundation
Yago Ryan Pinheiro dos Santos, Maria Isabela Marques da Cunha Vieira Bello, Alexandre Duarte Gusmão, Jonny Dantas Patricio

Dynamic driving formulas and static loadings in the light of wave equation solutions
Faiçal Massad

Reinforcing effect of recycled polypropylene fibers on a clayey lateritic soil in different compaction degrees
Natalia de Souza Correia, Sabrina Andrade Rocha

An experimental study on improvement of cohesive soil with eco-friendly guar gum
Baki Bagriacik, Bahadir Ok, Mustafa Tahseen Mohamed Ali Kahiyah

Proposal for considering the group effect in the prediction of settlements in pile groups through load transfer methods
Francisco Vladson Cardins Gomes Filho, Alfran Sampaio Moura

Geogrid mechanical damage caused by recycled construction and demolition waste (RCDW) under in-field cyclic loading
Kátia Regina Monteiro Barbosa, Eder Carlos Guedes dos Santos, Alexandre Duarte Gusmão

Hydraulic conductivity and undrained shear strength of clay- construction and demolition solid waste materials mixtures
Mohammed Abdulnafaa, Muwafaq Awad, Ali Cabalar, Nurullah Akbulut, Burak Ozufacik

Comparative analysis of Piled Raft Foundation System (PRFS) settlements placed on soft soils via geotechnical centrifuge
Edgar Rodríguez Rincon, Bernardo Caicedo Hormaza, Juan Felix Rodríguez Rebolledo

TECHNICAL NOTES

Limitations of the Danish driving formula for short piles
Silvio Heleno de Abreu Vieira, Francisco R. Lopes

Physical, chemical and microstructural characterization of two problematic soils from the Paraguayan Chaco
Hugo Carlos Scheuermann Filho, Gustavo Dias Miguel, Lucas Festugato, Rubén Alejandro Quiñonez Samaniego, Eduardo José Bittar Marín

A simple approach to predict settlement due to constant rate loading in clays
Raphael F. Carneiro, Denise M. S. Gerscovich, Bernadete R. Danziger

Interpretation of bi-directional tests on piles with the evaluation of stress relief at the pile toe
Thais Lucouvicz Dada, Faiçal Massad

CASE STUDY

Assessment of seismic vulnerability index of RAJUK area in Bangladesh using microtremor observations
Abdul L. Helaly, Mehedi A. Ansary

Combined analysis of landslide susceptibility and soil water dynamics in a metropolitan area, northeast Brazil
Cristiane Ribeiro de Melo, Paulo Abadie Guedes, Samuel França Amorim, Fellipe Henrique Borba Alves, José Almir Cirilo

DISCUSSION

Discussion of "Determination of liquid limit by the fall cone method"
Kátia Vanessa Bicalho, Janaina Silva Hastenreiter Küster, Lucas Broseghini Totola, Letícia Garcia Crevelin Cristello

LECTURE

Soils and Rocks
An International Journal of Geotechnical and Geoenvironmental Engineering
www.soilsandrocks.com
ISSN 1980-9743
ISSN-e 2675-5475

Judgement in geotechnical engineering practice

José António Mateus de Brito[1#]

Lecture

Keywords
Judgment in geotechnical engineering
Expert judgment
Codification
Incidents and accidents
Cut and cover excavations
Pile support systems

Abstract

Professional judgement is the basis for many of the decisions taken by geotechnical engineers to make progress in the design, execution and works supervision. Judgment is a mandatory component of any engineering achievement, essential to assess the various uncertainties that inevitably affect engineering practice. Confidence in such judgements can result in small to big consequences, not only for the engineer itself, but also for others, sometimes with the risk of human loss and significant damage. The definition and the development of judgment in geotechnical engineering is discussed. The bases of the judgement are analysed in detail and the heuristics and bias, responsible for failures in the judgment, are identified. The importance of experts' judgement and codification are highlighted and ways to improve judgment are also described. The lessons learned in a case study of one accident and two incidents that have occurred during the execution of the Lisbon Terreiro do Paço metro station construction works are presented to highlight the importance of an informed decision making informed through the engineering judgement.

1. Judgment in geotechnical engineering

1.1 Introduction

Judgment is paramount in engineering practice as it results from the use of intuition and reasoning, as well as from a fragment of codes, practical rules, applied science and evaluation and management processes. In various decisions concerning, for example, the option to stabilize a slope with a nailed shotcrete lining instead of an anchored structure, or the option for a rockfill dam solution on a rocky foundation, as an alternative to a concrete dam, the geotechnical engineer needs judgment to take his decisions and guide his actions. As pointed out by Parkin (2000), these judgments are informed by experience, expertise, reasoning or analysis. They are carried out during the development of the process, or after silent deliberation, and may be the result of solitary work on the computer or the result of extensive consultation, conflict and persuasion. From immediate to strategic, judgments define the structure of engineering.

To better understand what judgment is, it is relevant to look at its etymology. It is found in latin as *iudicium*, resulting from the verb *iudicare*, which means to judge. This verb, in turn, is composed of *ius*, which is fair, and *dicere*, which means to say. It is also possible to go to the Indo-European root of this verb and find **deik-*, which has the meaning of showing and pronouncing with solemnity. Thus, it is clear that judgment is the competence to pronounce what is correct, which is why it is also defined as the use of discernment, which in turn implies the separation between right and wrong.

The art of geotechnical engineering has been described as the ability to make sound decisions face up to imperfect knowledge. The resulting decisions and forecasts always incorporate uncertainty to a lesser or greater degree, so the engineer has to apply judgment, that is, the very real interpretive process that results from the sum of experience, discernment and intuition. Sometimes judgements under uncertainty are quantified as numerical probabilities (subjective probabilities), using the same laws of statistic probabilities (Vick, 2002).

The uncertainty of knowledge in geotechnical applications is subdivided into three subcategories: uncertainty in the geological-geotechnical characterisation, uncertainty of models and uncertainty of parameters.

Judgement, as it is used in geotechnical engineering, is also used in other engineering specialities and in other professions which have to face uncertainties, like medicine.

1.2 Soil engineering problem solving

Five decades ago, right in the introduction to the Soil Mechanics and Foundations class of Instituto Superior

#Corresponding author. E-mail: jmateusdebrito@gmail.com
[1]TPF - Consultores de Engenharia e Arquitetura, S. A., Lisboa, Portugal

Submitted on March 1, 2021; Final Acceptance on March 3, 2021; Discussion open until: Invited Lecture. No discussions.

https://doi.org/10.28927/SR.2021.063821

Técnico, in Lisbon (Mineiro, 1971), when geotechnicians of a new generation were taking their first steps in geotechnics, it was taught that the resolution of a soil engineering problem was a combination of various factors and knowledge, almost always differently from case to case, and that the ability to judge became indispensable to achieve the best solution, and also that the satisfactory solution of soil engineering problems always involved the combination of soil mechanics and one or more components, including geology, experience and economics as shown in Figure 1 (Lambe & Whitman, 1969). This was one of the quotes that immediately alerted and sensitized to the importance of the practice of engineering judgement and that now accompanies the professional life of so many geotechnicians. It is also the inspirational quote of the theme of this paper. The motivation for this reflection resulted from practising the professional activity of geotechnical engineering and from the raised questions of whether the judgements that were being made in the projects, taken as engineering decisions and actions, would be the most appropriate ones.

These combined factors turn any problem involving soils unique and, for all practical purposes, impossible to obtain an exact solution. Hence the importance of robust engineering judgement. Lambe & Whitman (1969) appropriately state that while a sound knowledge of soil mechanics is essential to a successful soil engineer, engineering judgement is usually the distinguishing feature of the exceptional soil engineer. This was, however, a seldom explored aspect of the judgement as before it was restricted to the final decision-making phase of the geotechnical process, after gathering all the knowledge about the process in question. However, it was neither defined nor known what the engineering judgement really was, and what kind of knowledge and preparation was required to make judgments, what were the heuristics and bias and associated uncertainties, as well as which risks were involved. Nevertheless, it had the advantage of combining judgement together with other components of geotechnics, which, to a certain extent, was a precursor of the progressive relevance that the judgement has acquired over the last 50 years.

The main question that arises when talking about judgement are as follows (adapted from Marr, 2019):

- All engineers use judgement, but how do they use it?
- How do you develop the ability to make engineering judgements?
- How do you know if the judgment made is robust and how can it be improved?
- What is the importance of judgement in geotechnical engineering? In which areas it is most relevant?
- What are the heuristics and bias from the judgment?
- Are most of judgements risks related? Do our judgments have risks? Does our risk assessment depend on judgment?
- To what extent can structured judgments contribute to the development of geotechnical engineering?

1.3 What is the engineering judgement?

Judgment is a cognitive ability of our brain leading us or not to make decisions and develop actions. In institutional settings, where major objectives shape our behaviour, we use reasoning and, maybe, analysis to help judgment (Parkin, 2000). Marr (2006) seeks to be more objective, defining judgment as the exercise of thinking clearly, logically and calmly about a problem, weighing the known facts, suppositions, missing information and consequences and then taking a decision. It is the ability to arrive at sensible decisions about a problem in the presence of incomplete and contradicting information. To demonstrate the importance of the judgement, Table 1 is presented, highlighting the central role that the judgement plays in the four phases where the geotechnical engineering process is developed: defining, investigating and characterizing, analysing, designing (prediction), and observing and evaluating (Marr, 2006, 2020). In each one of these phases, critical thinking skills are required, and therefore judgment plays a central role in all phases of the geotechnical engineering process.

The geotechnical process is largely a matter of decision-making in an environment that is inherently uncertain and requires much judgment. At each stage of the process, judgments are often made throughout the day. It is the most important ability beyond the mental and physical skills and the five senses.

An important concept linked to judgment is the subjective probability, which is defined as the probability of an uncertain event that corresponds to the quantitative

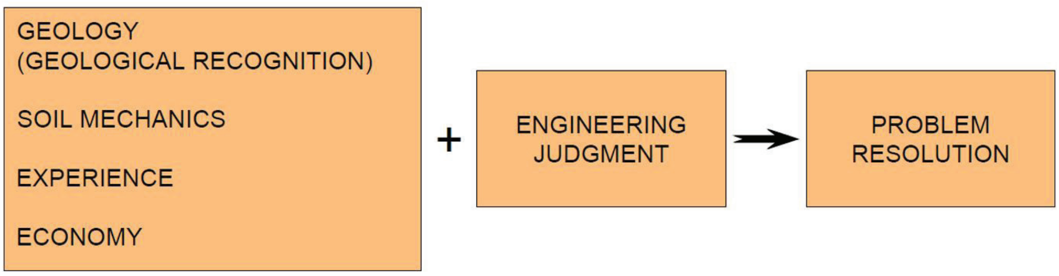

Figure 1. The solution of problems of soil engineering (Lambe & Whitman, 1969).

Table 1. Judgement in the stages of the geotechnical engineering process (Marr, 2006).

STEP	DESCRIPTION
Define, Investigate and Characterize	Define project needs, then gather relevant information and data. Use interpolation, extrapolation, deduction and inference, along with judgement, to develop a generalized mental and analytical model of the subsurface conditions
Analyze	Use evaluated information, empirical correlations, engineering knowledge and judgement to determine input parameters for the mental and analytical model to analyse and predict possible performance. Use judgement to fill data gaps and simplify complex projects conditions to render a manageable model
Design	Apply the mental and analytical model to determine specific requirements for the design to meet project requirements. Develop trial designs. Use judgement to assess viability, safety and constructability of design options and select the optimal combination for project conditions. Use model and judgement to predict the performance of the final design
Observe and Evaluate	Monitor actual performance during construction and operation. Question models and judgement where unexpected outcomes occur. Use models and judgement to modify remaining construction or operating conditions where needed. Learn and document what to do differently next time

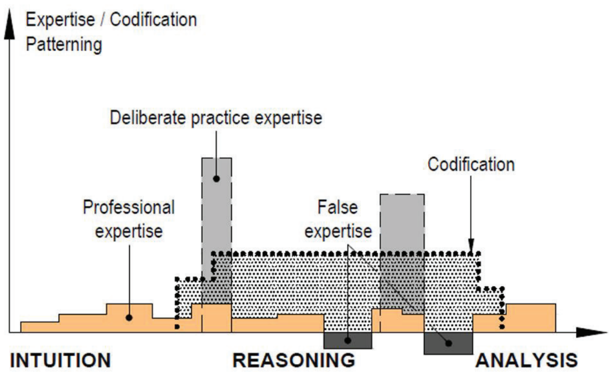

Figure 2. Specialization, codification and cognitive continuum (adapted from Parkin, 2000).

measure of the subjective evaluation (or belief) in the result, according to the state of knowledge at the time it is evaluated. Subjective probability can be considered, in a simpler way, as the quantified expression of a judgment or opinion about the likelihood of an uncertain event. Naturally, the judgment is inseparable from the individual and, therefore, it is inherently subjective, making the subjective probability go hand in hand with the judgment.

1.4 The development of the judgement

Bandura (1986), considered the father of social cognitive theory, showed that human functioning is determined by the interaction of personal characteristics, behaviour and environmental factors. Each influences the others in time and all influence all stages of the judgment function for action. People do not perceive the same attributes (or clues) or do not reach the same conclusions. How do this ability to make sound judgments develop? Margolis (1987) in his treatise on cognition and judgement indicates that it is a natural step in contemporary brain evolution. The steps of cognitive development appear to be seven: simple feedback, pattern recognition, learning, choice, intuitive judgment, reasoning, and calculation.

Intuitive judgment is an innate skill that is shared by humans with other mammals, which developed during the prehistory of our species. Reasoning, on the other hand, has probably developed together with language over the last 100,000 years. Finally, our ability to develop mathematical analysis is very recent and has to be formally learned (Parkin, 2000).

In recent times intuitive judgement has been supplemented and helped by reasoning and calculation. The relationship between these three functions in modern judgement can be explained by the extension of Brunswick's (Brunswik, 1952) perception research, which provided the basis for the study of intuitive judgement called cognitive continuum theory (Hammond, 1996). How do people use their reasoning skills and intuitive judgment to track modern technical and social problems? According to Hammond (1996) the answer lies in the ability to go back and forth between the intuitive mode and the more analytical mode, during the period of time necessary to reflect on the problem and arrive at a judgment, as outlined in Figure 2, adapted from Parkin (2000). This figure shows the fluctuation of the intensity of professional specialisation along the cognitive continuum from intuition to analysis with the nature of the task. In some situations, errors related to rules or knowledge resulting from false specialisation may manifest. It turns out that no matter how analytical the engineers may be, in the end the intuitive judgement is always present. It is evident that what we can calculate, allows us to make better judgements and result in better engineering solutions.

1.5 Biases and heuristics of the judgement

Over the past 70 years, research into the psychology of judgement and decision-making has shown that human judgement fails due to many cognitive biases. In practice, people use simple mental strategies or practical rules to simplify the task of quantifying subjective probabilities. In cognitive psychology, this is called heuristics. Heuristics lead to systematic errors called cognitive biases. The conclusion is that people use practical rules to simplify judgments that do not follow the standards. In any area of human knowledge, it appears that judgment is affected by a series of heuristics to simplify the processing of cognitive data. These are useful in making the job simpler, but also divert personal judgements to a number of directions, particularly to the reasoning region of the cognitive continuum. These biases are important, but in real dynamic situations, the ability to correct these judgments have been developed over time with the disclosure of new data. Faulty judgments are essentially the result of reasoning that deals incorrectly with lack of data, irrelevant data, erroneous assumptions, ambiguities, poor verification, mood effects, irrational thoughts and incorrect probabilistic thoughts. These failed judgments result in consequences that can be more significant and bigger than generally imagined. Wikipedia (en.wikipedia.org/wiki/List of cognitive biases) give 124 examples of cognitive bias. From the 30 cognitive biases on this list, which Marr (2020) considered to affect the judgment of geotechnical engineering, the most common ones are given in Table 2.

When making judgments to fill data gaps in information and knowledge, engineers intrinsically make subjective assessments of the importance of the various uncertainties, that is, they make a subconscious risk assessment weighing the uncertainties and assessing the potential consequences of possible outcomes of decisions and recommendations.

Table 2. List of some cognitive biases that affect judgment in geotechnical engineering (Adapted from Marr, 2020).

COGNITIVE BIAS	DESCRIPTION
Availability	Over-relying on information that's readily available or easily recalled
Authority bias	Attributing greater accuracy and more influence by opinion of an authority figure
Concrete information	Putting higher value to information from our own experience or that of trusted colleagues rather than abstract information in a document
Conservation bias (belief revision)	Favouring prior evidence over new evidence
Information bias	Biased conclusions resulting from inaccurately measured or classified data or information
Neglect of probability	Disregarding probability when making a decision involving uncertainty
Not invented here	Aversion to ideas, products or methods developed by others
Overconfidence	Having more confidence in the accuracy of individual's knowledge, judgements and actions than is justified
Self-serving bias	Claiming more responsibility for successes than failures
Shared information bias	Spending more time and energy discussing already familiar things and less time on unfamiliar things

But they take shortcuts with consequent biases that might lead to faulty results. Most engineers deal with uncertainty using heuristics that ignore many of the most basic rules of probability. A surprising number of engineers take subjective probabilities for granted, considering them coherent and calibrated while in fact they are not (Baecher & Christian, 2003). This is why probabilistic thinking needs to be taught and practiced.

1.6 Expert judgement

An expert is a person trained in a particular domain and the specialization can be found throughout the cognitive continuum. Being an expert involves knowledge and practice. Expert judgment can be developed using judgments from any region of the cognitive continuum and can vary in the degree of specialization. Short-term memory (working memory) can only absorb, store and process between 5 and 9 cues of information at any given time (Simon, 1981). Specialization in a domain of knowledge can represent between 50,000 and 100,000 cues of information stored in long-term memory. Achieving a state of specialization requires about 10 years of continuous deliberate practice and this practice must be maintained if the level of specialization is to be kept high. Considerable deliberate practice, consisting of trial and error and feedback during this period, is necessary to fully develop specialization in a domain of knowledge or practice (Parkin, 2000).

One of the aspects that distinguishes a professional from a beginner is the degree to which he is able to accumulate experience and implement this to new situations. In fact, what is important is not to accumulate any experience, but to accumulate assessed experience. When applied appropriately, engineering judgement reflects accumulated and assessed experience (Baecher & Christian, 2003).

As Marr (2019) states, experts are characterised by:

- Being excellent in their own domain;
- Realizing high standards in their own domain;
- Solving problems quickly with few errors;
- Having superior short-term and long-term memories;
- Seeing and representing a problem in their domain at a deeper level than beginners;
- Spending considerable time analysing a problem qualitatively;
- Having strong self-regulatory skills.

The deliberate practice of specialisation, unavailable to most professionals, is represented as a narrow but intense block, which can be located in any area of the cognitive continuum (Figure 2). Naturally, the further one goes to the analytical side of the cognitive continuum, the more defensive the judgments will be, but the intuitive element will always be present.

It should be noted that no matter of excellent the experts may be, it is not possible to eliminate the subjective nature of judgements, consequently neither the uncertainty and probability of their failure. One might make judgments in an environment of imperfect mental models using uncertainty and incomplete information processed by a biased mind, which leads to potentially failed judgments.

1.7 Codification

A high degree of specialisation among professionals is rare due to the fact that few professionals deliberately use the practice in their learning strategies, taking little advantage of reliable feedback during professional practice. Professional work does not go wrong more often due to the collective capacity to externalise specialisation in the form of practical rules, codes, standards and specifications. Codification makes a large degree of specialisation unnecessary for good professional practice (Parkin, 2000). Figure 2 shows that the codification increases in the reasoning-analysis zone of the continuum, but neglects the intuitive zone and the extreme of the continuum that depends on the creative use of mathematics, using computational models, each time more complex, that help to strengthen knowledge and reduce uncertainties.

1.8 Judgement and risk

Risk is the effect of uncertainty on objectives, whether positive or negative, as defined in NP ISO 31000 (2012). It is the combination of the probability of an uncertain event times the consequences. Risks are associated with the possibility that judgments will lead to wrong decisions or assessments. There are important uncertainties in risk analysis that are not susceptible to a quantitative assessment based on data and have been addressed using professional judgment and expert opinion based on intuition, past experience and other qualitative beliefs.

Risk assessment creates a way to quantify the uncertainty in judgements and decisions and to communicate that degree of uncertainty. Risk management is a systematic process of identifying, analysing, planning, observing, communicating and responding to risk, in order to reduce uncertainty. So, judgment and risk are closely linked. It is necessary to recognise this fact and its consequences and to develop a better understanding of the links and better use of tools to identify, quantify and manage risk.

1.9 How to obtain and improve the judgment of geotechnical engineering

Where to get the ability to make engineering judgments and how to develop and improve this ability? These themes are not explicitly included in the geotechnical disciplines in university programmes or in engineering textbooks. Apart from applied analysis science, not much is taught in modern engineering courses and universities and is not easy to find experienced design staff. The practice of project and project management has been learned for many years through immersion in a specialised project environment. Young engineers will become progressively more useful as they work backwards in analysing and detailing the demanding art of project design. Analytical techniques are now aided by software sets, often linked to graphical outputs. This analysis and modelling are often mistakenly referred to as a project and an undue emphasis is placed on its performance in universities.

Some of the relevant information on judgement in geotechnical engineering is thanks to Ralph Peck. During his long career as a professor and engineer, with talent, hard work, perseverance and good judgement, he made several contributions that drew attention to the importance of engineering judgement (Peck, 1969, 1980, 1981, Dunnicliff & Deere, 1984, NGI, 2000, Dunnicliff & Nancy, 2006). In a video (Peck, 1991) interesting topics are presented stating that successful engineering practice requires a high degree of engineering judgment, with a sense of proportion being one of the main facets of engineering judgment, and without which an engineer cannot test the results of a calculation in relation to its reasonableness (ability to establish criteria for reasonable behaviour for the design).

There is a clear message from some eminent geotechnicians like Terzaghi, Peck and Lambe, that good judgement results from evaluated experience that is learned not only from one's own experience but also from that of the others. Thus, in order to improve judgement, it is necessary to disseminate the experiences more, good or bad, as well as the respective results. The complexity of the project and innovation will continue to challenge the limits of human cognition, and it is important to ensure that safety is maximized at each stage of the engineering process. To do this properly, geotechnicians should be free to add to their domain of knowledge the causes of bad behaviour and rupture by learning from incidents and disasters as soon as they occur.

From the literature of judgment and personal practical experience, the following suggestions can be added to obtain and improve the judgment of geotechnical engineering:

- Get a good education and follow the literature; young engineers should have experts as mentors, in order guide them on how errors can be avoided or quickly corrected and should be encouraged to develop skills in drafting, drawing and make rough calculations as a safety precaution against inadequate computer analysis;
- Make a career plan and obtain a variety of training and experience in the first years of their profession even if it is necessary to change to new employers to find the right job and mentoring; civil engineers who wish to practice on design should be encouraged to have one or two years of experience on site, as early as possible in their careers; as these field experiences will remain in the memory for a lifetime and will fundamentally enrich the clues available in the short-term memory during the project process;

- Increase the power of observation and develop the ability to register what is seen;
- Expand the evaluation of the experience by obtaining feedback from own judgments to learn what went well and wrong, to improve future decision-making; get field experience and feedback during construction; visit other works and study their results;
- Be well grounded in the theoretical bases of the models and their limitations and have simple methods of checking and gaining a sense of proportion;
- Identify and understand the gaps in knowledge and data and the implications of these gaps in the judgments;
- Avoid impulsive or stressful decisions; instincts can cause the loss of the main facts and the benefits of deliberate thinking; sleep on the main decisions, because their subjective results can change with more reflection;
- Maintain the connection with experts in the knowledge domain so that errors can be avoided or corrected;
- Consider the effects of our own decisions made with stakeholders - customers, owners, users, public and the company itself;
- Be confident that judgements and decisions can be justified to third parties;
- Have the main calculations and drawings reviewed by an experienced engineer using different tools; for innovative or large-scale projects or when the safety of the population and the possible damage caused by the deficient behaviour of the works are factors to be considered in the project; all key calculations and drawings should be verified by an experienced independent consulting firm;
- Maintain humility in knowledge and openness to learn from one's own mistakes;
- Remain open to questioning, revision, reflection, learning and failure;
- Document and reflect on successful and failed judgements.

2. Lessons learned from incidents occurred during the construction of a major geotechnical works: Terreiro do Paço metro station in Lisbon

2.1 Introduction

Terreiro do Paço metro station is part of the Blue Line of the Lisbon Metro, located in the zone that connects Baixa-Chiado Metro Station to Santa Apolónia Metro Station. It started operating at the end of 2007. The station is located between the east building of Terreiro do Paço Square, occupied by the Finance Ministry, and the south and southeast maritime station, a ground floor building already built in the 20th Century (Figures 3 and 4). A large part of the station's implantation area was reclaimed from the river with fills, placed before and after the 1755 earthquake.

The metro tunnel was previously executed with a tunnel boring machine (TBM) between 1997 and 1999. At the site, the tunnel axis is located at an average depth of 19 m (-16.00 m elevation), all its section excavated in the smooth alluvial deposits of the Tagus River, where thickness reaches about 26 m in the station area (Figure 4).

After the construction of the tunnel, during the early phase of the station construction according to the initial

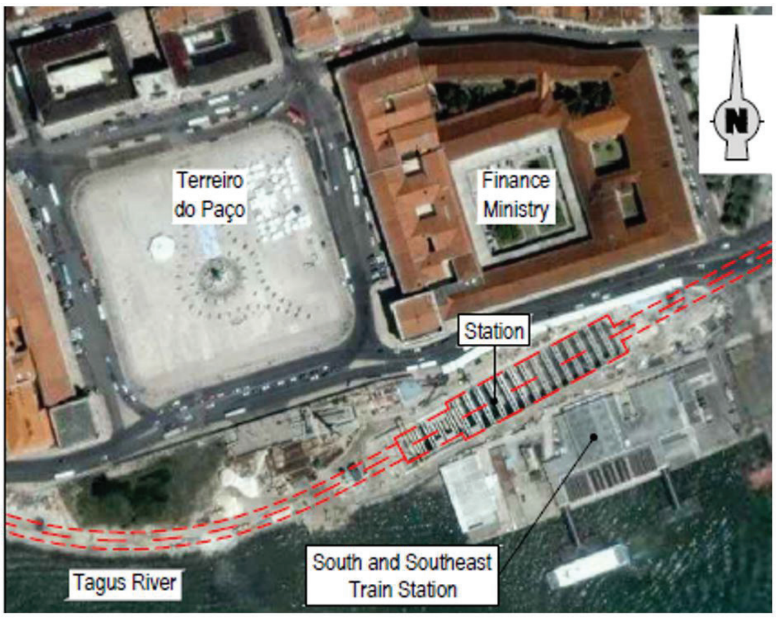

Figure 3. General plan of the site and of the station (Brito & Fernandes, 2006a).

Figure 4. View of the eastern area of Terreiro do Paço square and the Finance Ministry building, with the location of the tunnel and the station (Brito & Fernandes, 2006a).

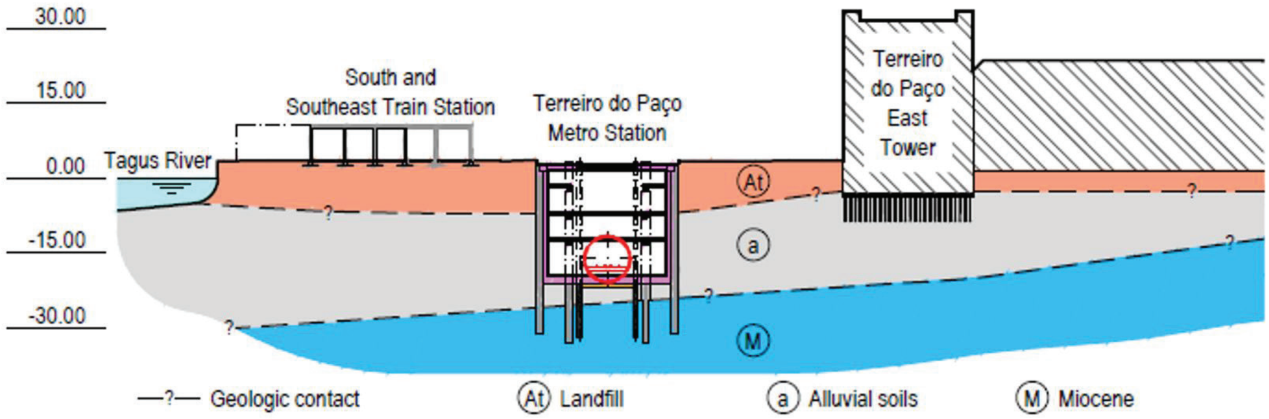

Figure 5. Schematic section across the Tagus River, the station and the east tower of Finance Ministry (Brito & Fernandes, 2006a).

project, in mid-2000, an accident of a certain severity occurred. This accident began during the first phase of the station's west portal treatment by drilling holes in the lower prefabricated lining segments of the tunnel for the execution of jet grouting. Strong run-off of water and sandy soils began flowing through these holes into the tunnel, with the consequent subsidence of the terrain surface located above the tunnel.

The works on the station were restarted in 2001, following a new project, and completed in 2006. In the final phase of excavation inside the station, in 2003, two incidents of some gravity occurred, with the entry of water and sandy clay alluvial deposits through openings between the retaining wall piles, when the fifth and final phase of excavation was to be carried out. Given the risk of another incident of a similar nature (considering the uncertainty of the position of the piles), the excavation and retaining works were interrupted for a period of 8 months for a better study of the situation and also for the analysis of possible mitigation solutions to be implemented prior to the restart of the works.

2.2 Geological conditions

Figure 5 includes a simplified geological transversal section to the station axis. The substratum is composed of Miocene formations, covered by soft alluvial deposits and fills. The surface of the substrate descends progressively towards the river with a slight inclination towards S-SW.

Figure 6 shows a longitudinal geological profile of the northern wall of the station. As reported by Brito & Fernandes (2006a), landfill soils with variable thickness occur in depth, sometimes mixed with alluvial deposits, containing stones and obstacles, sometimes of large dimensions. This is followed by the predominantly clay-muddy alluvial deposits, ranging from soft clays to sands (some very clean). However, there is a very significant predominance of clean sands at the base of the alluvial deposits. Underlying the alluvial deposits are the Miocene formations, consisting of clays from "Forno do Tijolo", with a hard consistency, interspersed with layers of dense sands with artesianism.

It can be seen in Figure 6 that around the zone of the tunnel accident and in incident areas of the station, there are soft clays and small layers of clean sands of medium to fine grain size.

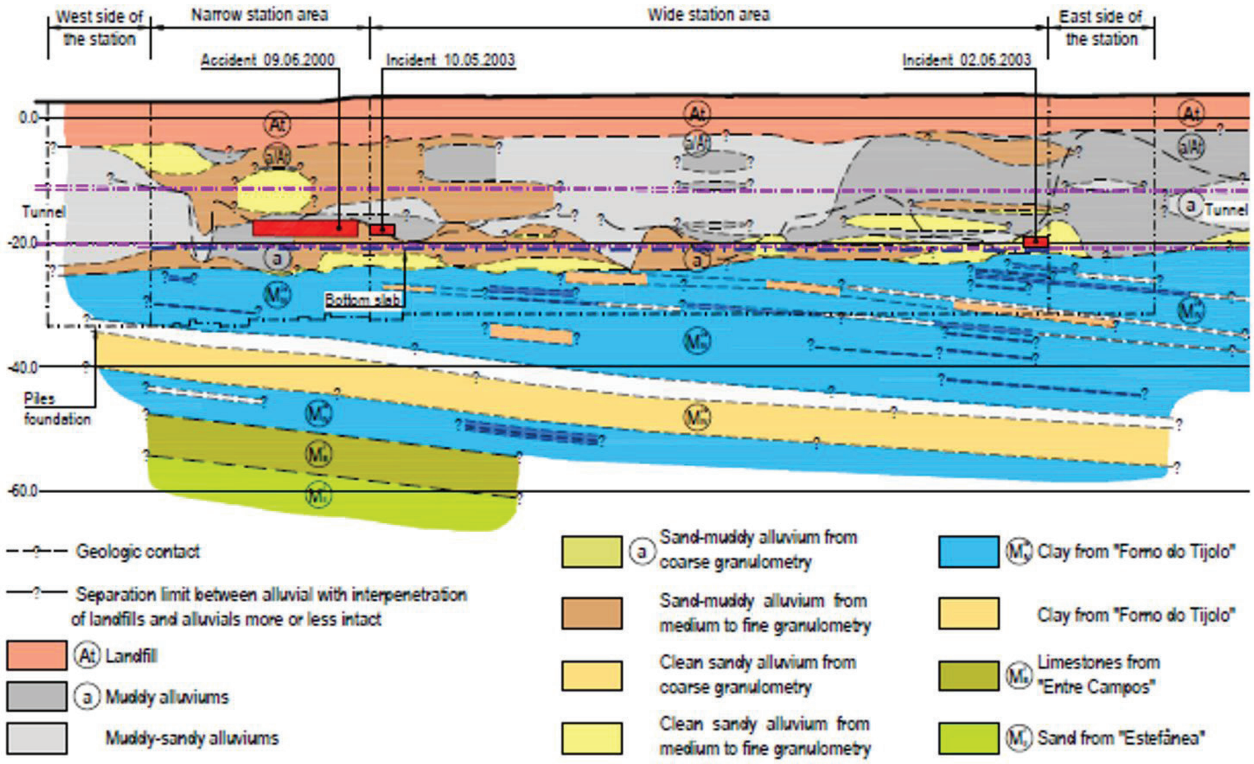

Figure 6. Longitudinal geological profile corresponding to the north side of the tunnel and the station with the location of the tunnel accident and the station incidents (Brito & Fernandes, 2006a).

2.3 Tunnel accident occurred on 9 June 2000

2.3.1 Treatment solution for the west portal

Due to the accident occurred during the initial works of the station first project, the tunnel structure was seriously damaged along about 25 m. After this accident, the tunnel was initially filled with water and, in a second phase, with light plastic concrete, along a length corresponding to that of the future station, plus about 20 m next to each portal (Salgado, 2014). This information was relevant for the design of the new station structure and its connection to the tunnel structure at the two portals.

Figure 7 a show a cross-section with the two phases, foreseen in the initial project of the station, for the execution of consolidation and waterproofing jet grouting columns of the surrounding area of the west portal. In this initial project the jet grouting columns would be executed from inside the tunnel, in a first phase, and from the top of the landfill soils in a second phase. Figure 7 b show a section of the initial project with the location plan of the jet grouting columns to be executed from inside of the tunnel, with a total of 243 columns with 0.8 m diameter and length of 4 to 6 m in triangular pattern of 0.6 m (Ferconsult, 2001). It was specified that the length of the carotted holes should not exceed what was strictly necessary to cross the concrete lining of the tunnel, in order to avoid puncturing the cement of the exterior injections made during the tunnel construction. However, this condition would have been difficult to meet given that the inclination of the holes was vertical or close to vertical.

Initially 13 holes with 152 mm diameter were drilled to allow the subsequent execution of jet grouting, but water and soil entered the last hole drilled. Meanwhile, water and soil began to appear in another two holes, and the site was abandoned by the staff. In four hours, there were signs of structural damage and water entering through the lining joints of the tunnel. Simultaneously with the entry of water and soil, settlements and cracking occurred in front of the tower of the Finance Ministry building (Salgado, 2014).

2.3.2 Immediate stabilising measures

It was observed that the greatest impact on the surface was located in a restricted area of the landfill in front of the tower of the Ministry of Finance building, with a record maximum settlement of 230 mm.

The stabilising measure was filling the tunnel with water to counteract the ingress of water and soil into the tunnel, in order to minimise damage and reduce settlements on the surface. To do this, concrete plugs had to be made in the shafts situated in the tunnel in mid distances to the adjacent

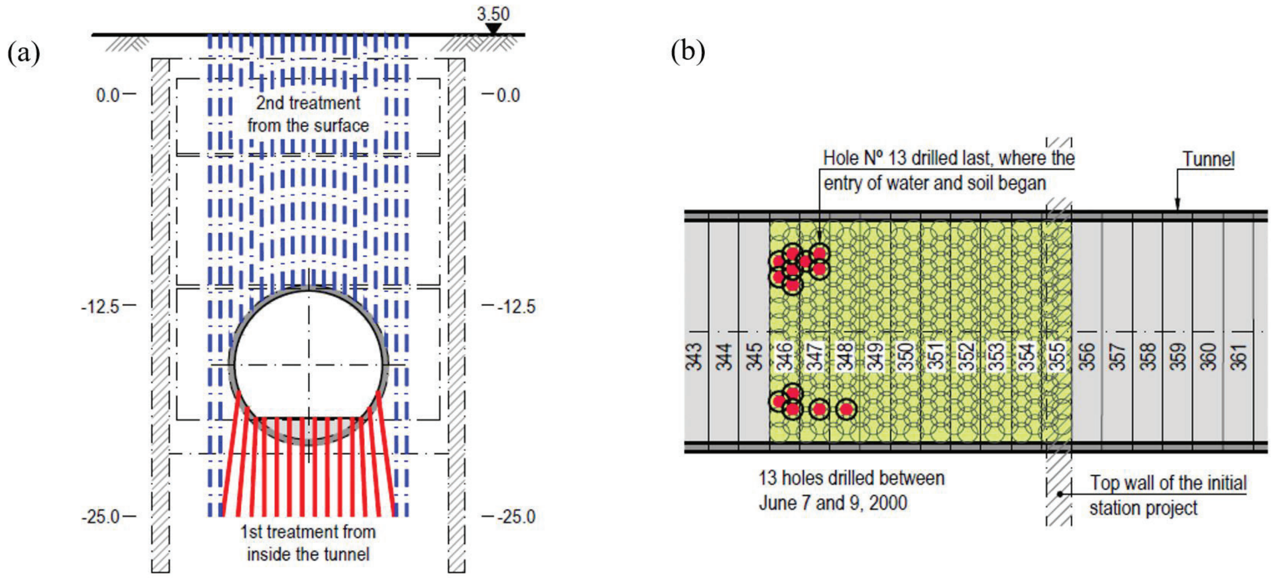

Figure 7. (a) Execution phases of the jet grouting columns of the west portal; (b) Location plan of the columns to be executed from inside the tunnel and the holes executed before the incident occurred (adapted from Ferconsult, 2001).

stations. The filling with water, done in four phases, as the concreting in the plugs continued, took place for about a month.

Given the favourable evolution of the tunnel settlements, measured after filling with water, inspections were carried out inside the tunnel with an underwater robot coupled with a video camera and also by divers, which confirmed that the most affected area coincided with the 345 to 349 concrete lining segments. Subsequently, in the excavations made to build the station, it was possible to visualize the tunnel's extrados in the most affected area, as illustrated in Figure 8.

The horizontal deformations recorded in this area reached a maximum of about 60 cm, resulting from the temporary imbalance of the tunnel confinement due to the phenomenon of liquefaction that occurred following the drilling carried out. On the south side, no pathologies were detected in the tunnel lining nor any deformations were observed.

2.3.3 Reinforcement and stabilisation actions in the medium term

For the reinforcement of the tunnel in the incident area, taking into account that after the reinforcement it would be necessary to carry out the excavation in the incident area for the construction of the future station, it was decided to fill the tunnel with lightweight concrete placed in several phases, through holes in the upper part of the tunnel, after the previous execution of three gravel plugs at west, east and in the central area of the new station.

The reinforcement works were successfully completed about 6 months after the incident, when the total stability was restored and the displacement rates observed were already low.

2.3.4 Instability mechanism

The cause of this accident was the inability of the sandy soils to resist the high hydraulic gradients occurred in some of the holes drilled in the tunnel, thus initiating a process of static liquefaction with the consequent entry of water and soil into the tunnel, as schematically represented in Figure 9 a.

The mechanism of the flow of soil particles into the tunnel resulted from:

- High hydraulic gradient, due to a large difference in water pressure over a very short distance (outside and inside the tunnel);
- Unconfined surface, allowing the particles to flow freely through the holes in the concrete lining;
- Incoherent soils with relatively high permeability, made up of sands and silty sands, very susceptible to liquefaction.

The nature and thickness of the sandy alluvial deposits surrounding the tunnel in the west portal (presence of thin or thicker sand layers) was critical to the occurrence of this incident. The deposition environment in estuary, where sediments are frequently rearranged due to tidal currents, causing a rapid change in the type of soil deposited, was conducive to the formation of these randomly oriented thin sandy layers, interspersed in the finest deposits and even of alluvial sand layers with greater expression.

2.3.5 Lessons learned

In the initial design phase of the station, the accident was predictable based on existing information. However, there was only the concern that the holes would not be in

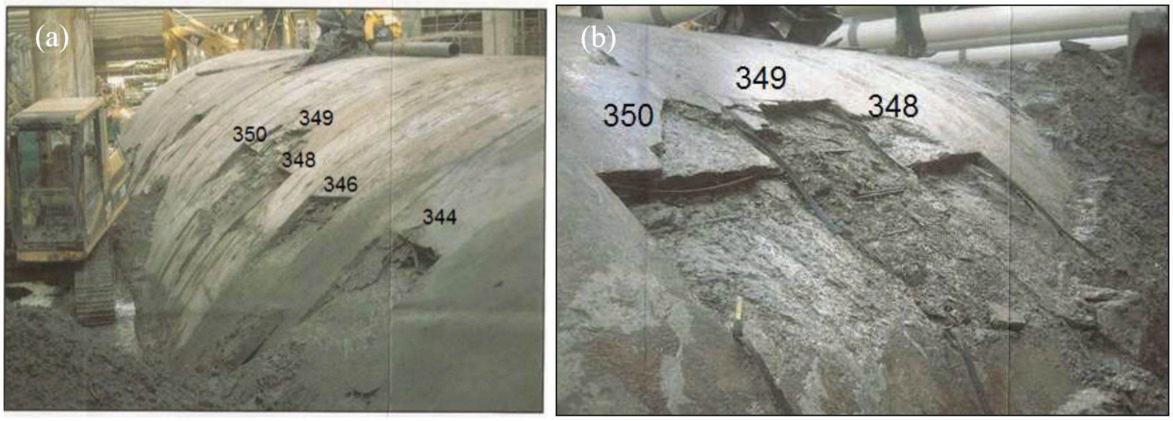

Figure 8. Views from the east and west sides of the lining segments 344 to 350 of the extrados of the north side of the tunnel (Salgado, 2014).

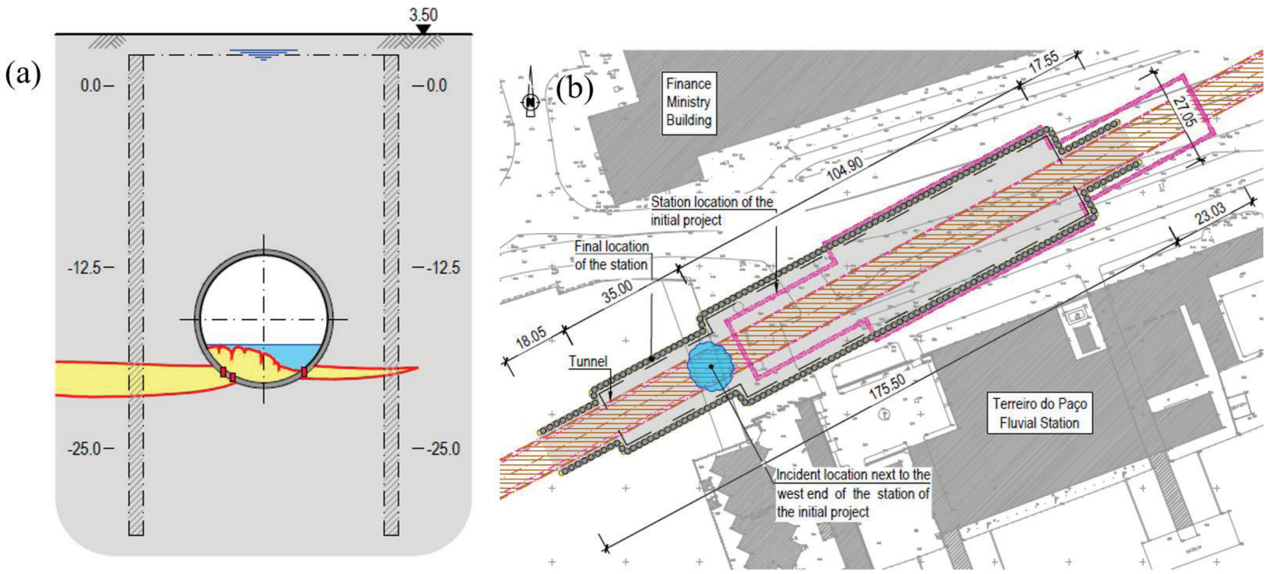

Figure 9. (a) Schematic section of the water and soil entrance into the tunnel (Ferconsult, 2012); (b) Location of the stations of the initial and final project and the accident area (Ferconsult & Metropolitano de Lisboa, 2011).

contact with the ground, since it was specified that these holes should have the length strictly necessary to cross the concrete lining and not perforate the cement grout injected during the construction of the tunnel. But it was impossible to prevent water from entering, as the thickness of the injection grout not enough to resist the pressure of the outside water. The design of the tunnel portals treatment was probably based on the assumption of the presence of low permeability soft clays and sandy-clays alluvial deposits with hydraulic behaviour controlled by the fine fraction. This assumption was not supported by the available geotechnical information and resulted in an unacceptable risk.

Clearly, very biased judgements were made by the entities involved in the design and execution, due to a lack of perception of the risks associated with the opening of the holes. On the other hand, if the holes had been obturated immediately after drilling, there will be no or much fewer negative consequences. The information available at the time indicated the probability of the presence of clean and very permeable sands, but the contract documents did not include any specific references to this risk and to special precautions to avoid it, and no contingency means were mobilised to control the problem immediately.

2.3.6 Transfer of the station

During the tunnel reinforcement and stabilisation works, a new project was developed for the station, implemented in such a way that the incident area was inside it (Ferconsult & Metropolitano de Lisboa, 2001), as shown in Figure 9 b.

2.4 Presentation of the second project of the station

2.4.1 Design constraints

The design of the station was conditioned by the following aspects (Brito & Fernandes, 2006a, b):

- The excavation to be carried out was very deep, of around 25 m;
- The soils involved, to greater depths than the excavation, had very weak mechanical characteristics; they consisted of fills and soft alluvial deposits of the Tagus River, consisting of organic silty clays and soft sands, to a depth of 26 m, underlying very hard Miocene clay soils; the pressures to be balanced by the curtain were therefore very high;
- The groundwater level was very close to the surface of the terrain, being influenced by the tides;
- The soils interested in the excavation exhibited an extremely high complexity and variability;
- In the surroundings of the excavation there were old public buildings of exceptional patrimonial value, endowed with direct or semi-direct foundations in the embankments and alluvial deposits;
- As a result of the tunnel accident, very significant movements had taken place in the west area of the works, although practically stabilised in the start-up phase of the station construction, which had naturally reduced the tolerance of the surrounding buildings to any further movements.

2.4.2 Final structure

In simplified terms, the structure of the station corresponds to a large reinforced concrete box, built from the surface, connected to the tunnel in the two portals, at a distance of about 140 m and with a width of 16 m in the narrow area and 24 m in the wide part. Figure 10 illustrates the cross-sections of the final internal structure of the station in both areas, the position of the tunnel and the surrounding soils. The top of the substratum occurs slightly below the base of the station bottom slab.

2.4.3 Peripheral curtain

Reinforced concrete and bentonite-cement secant piles with 1.50 m diameter were chosen for the peripheral curtain. Bentonite-cement piles 1.75 m axis spacing were previously executed. The reinforced concrete piles were then built, alternately with the first ones and partially sectioning them, also with a 1.75 m spacing. All piles penetrated at least 8 m into the Miocene substrate. Figure 11 presents the plan and the elevation of the peripheral curtain and Figure 12 shows the theoretical position of the piles and the lining wall.

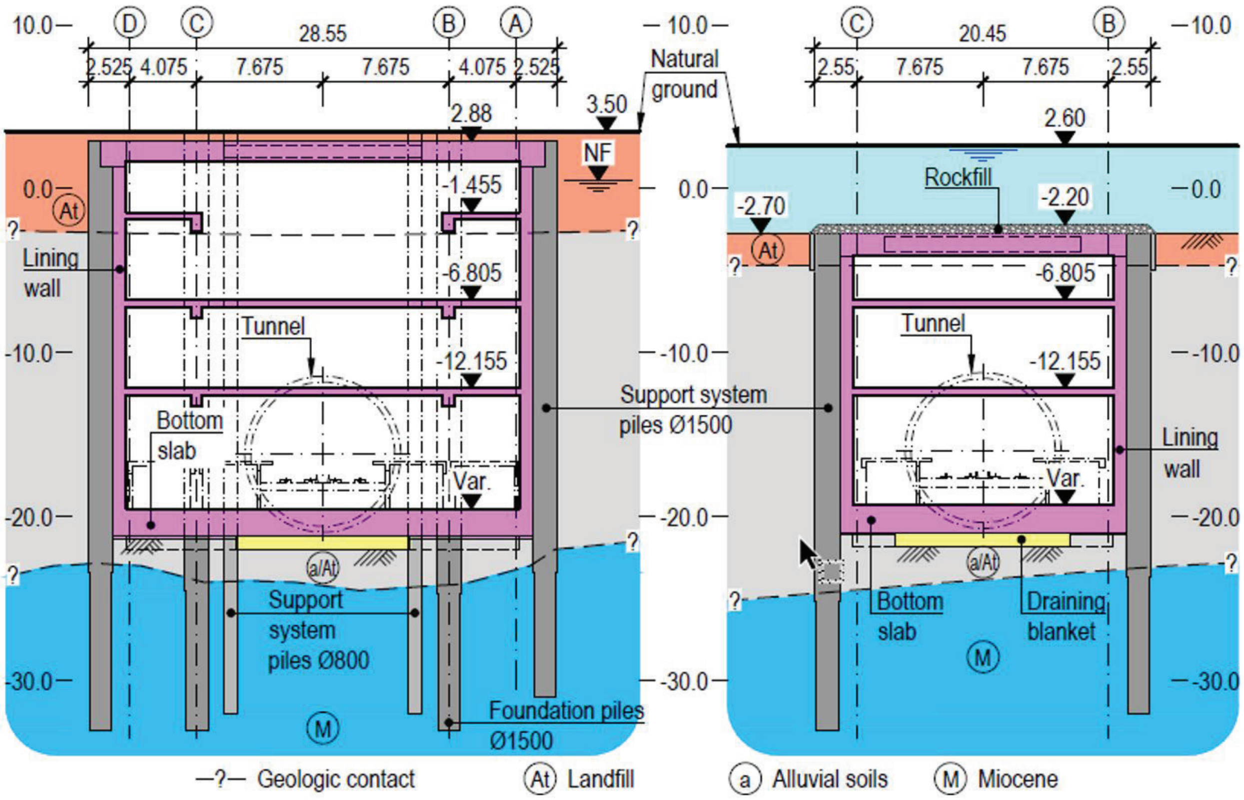

Figure 10. Cross-sections of the wide and narrow areas of the station (Brito & Fernandes, 2006a).

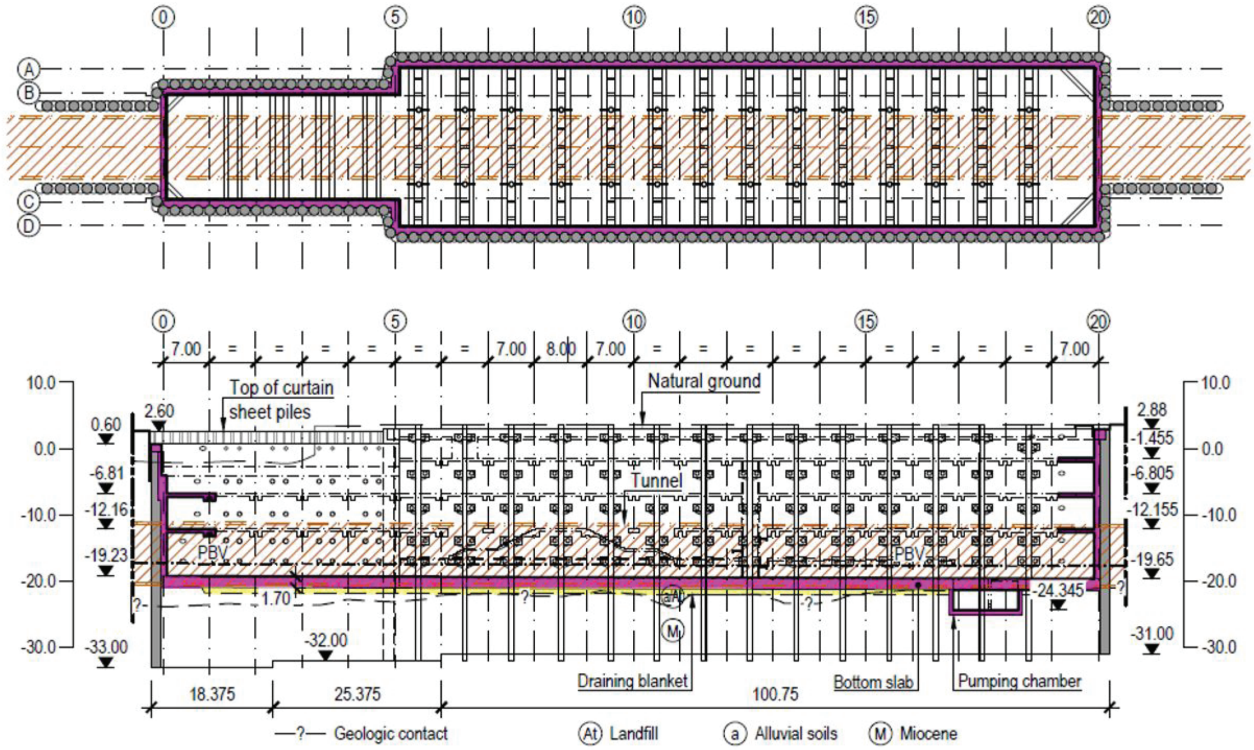

Figure 11. Plan and northern elevation of the peripheral curtain of secant piles and the shoring system (Brito & Fernandes, 2006a).

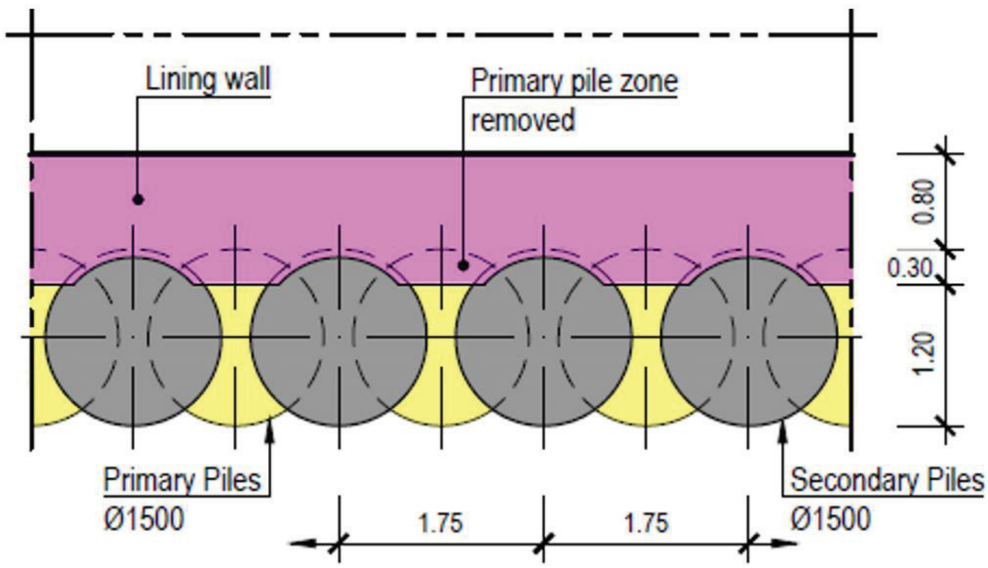

Figure 12. Plan of the theoretical position of the piles and the lining wall (Brito & Fernandes, 2006a).

The piles were connected by a reinforced concrete top beam. from which top-down method is used for constructing a reinforced concrete interior lining wall with a thickness of 0.80 m and structurally connected to the reinforced concrete piles (Figure 12). This wall was extended to the base of the excavation and connected there to the bottom slab (Figure 10). The base of the curtain was between the elevations -31.00 m (north and east) and -33.00 m (south and west) and the maximum depth of the excavation was of 25 m (Figure 11).

For the temporary shoring system five levels of horizontal steel strut pairs were used, between the longitudinal faces (north and south) of the curtain, consisting of tubular profiles of large diameter (ϕ711 mm) and thickness from 16 to 25 mm with an average horizontal spacing of 3.50 m. In the wide area of the station, the struts were provided with bracing elements in the vertical plane at two points supported on steel piles ϕ800 filled with concrete, embedded in the subsoil and installed prior to excavation. Figure 11 shows the position of the shoring in the northern wall elevation. Figure 13 shows the cross-sections of the shoring system in the wide and narrow areas of the station. The struts were strongly prestressed during the installation, with a uniform prestress load of 3500 kN per strut, introduced by 4 hydraulic jacks (Figure 14).

Figure 15 shows a view of the curtain and shoring system of the wide (left), and narrow areas (right), obtained from the Terreiro do Paço east tower.

Figure 16 shows the south and north walls of the station in the excavation phase below the 3rd strut level.

In the wide area of the station this temporary shoring system has been accompanied by a 3 m thick jet grouting slab, placed between the tunnel and the longitudinal curtains, with its median plane coinciding with the tunnel "equator" (Figures 13 and 17). This slab, combined with the tunnel itself and the corresponding filling material, provided a particularly suitable support to the curtain at a depth of about 18-21 m. This has significantly reduced the displacement of the curtain compared to a solution method by using only conventional struts.

2.5 Execution phasing

Figure 18 shows the construction phases of the station wide area. Prior to the excavation, in addition to the peripheral curtain, piles similar to the curtain were built in the wide area of the station, for the foundation of the internal structure columns and the bottom slab. These piles were executed from the surface and concreted to the level foreseen for the bottom slab to which they were structurally connected. Steel piles filled with concrete were also installed for bracing the struts, which were later used, together with the former, as the foundation of the internal structure. Then, in the same wide area, the jet grouting slab was constructed between the tunnel and the longitudinal curtains.

The successive excavation phases (including the dismantling of everything involved in the system, such as the jet grouting slab, the lining and the filling of the tunnel) were articulated with the construction of the reinforced concrete lining, the installation and prestress of the shoring and the lowering of the groundwater level inside by means of deep shafts installed up to the substrate. Once the excavation bottom was reached and the drainage system was built, the

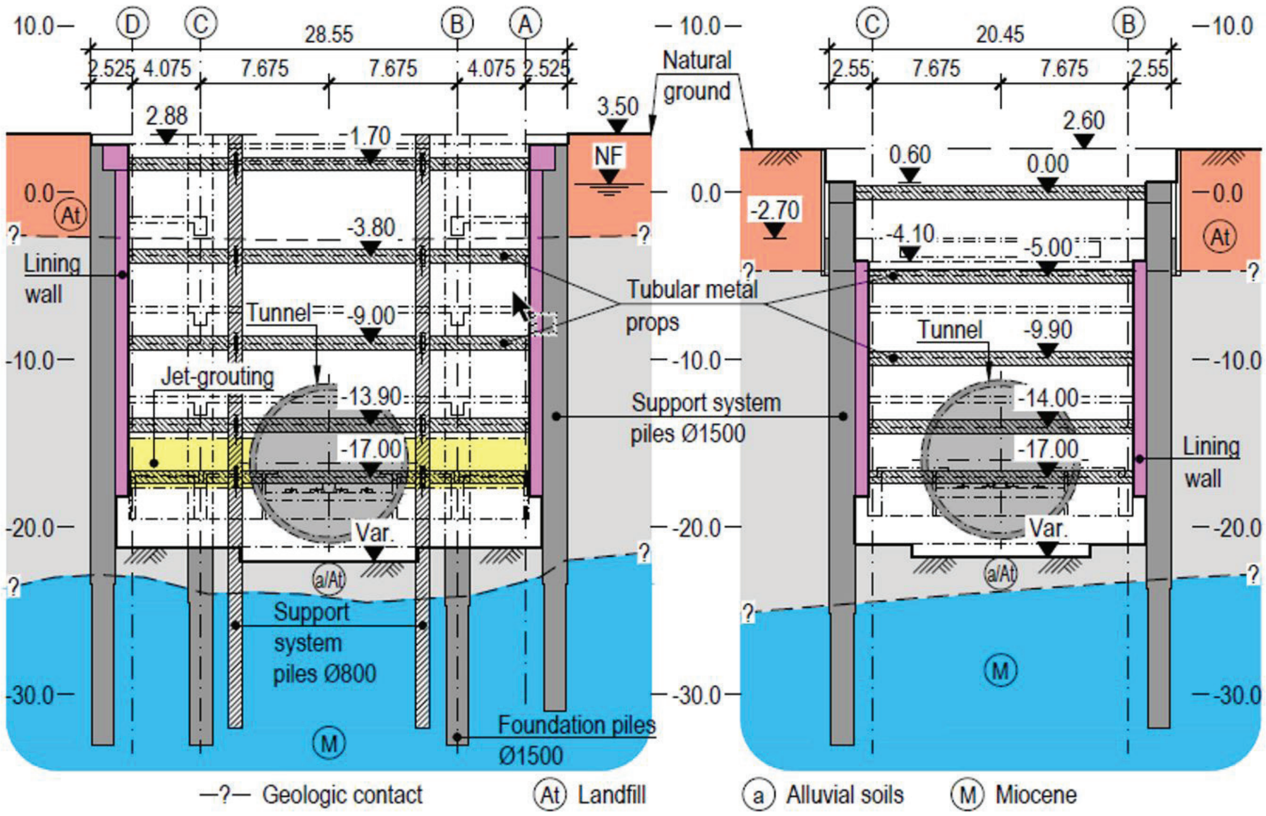

Figure 13. Cross sections of the wide and narrow areas of the station after completion of the last excavation phase (Brito & Fernandes, 2006a).

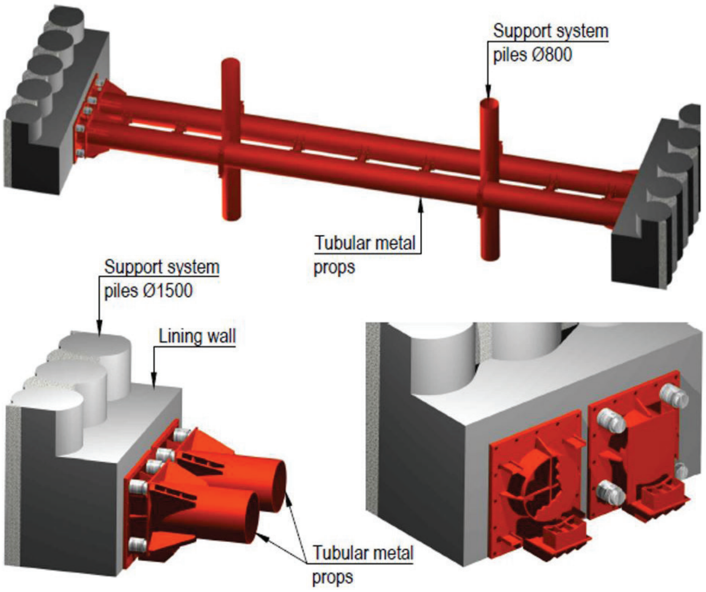

Figure 14. Struts system of the station wide area and the device for the application of prestress (Brito & Fernandes, 2006a).

Figure 15. View of the curtain and shoring system from the Terreiro do Paço east tower (Brito et al., 2016).

Figure 16. Excavation phase below the 3rd struts level on the south and north walls (Brito & Fernandes, 2006a).

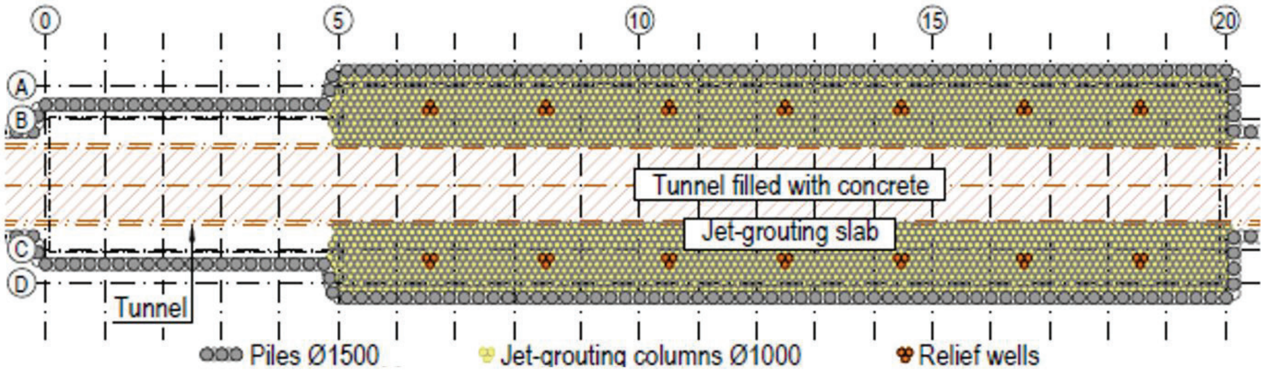

Figure 17. Plan of the jet grouting slab (Brito & Fernandes, 2006a).

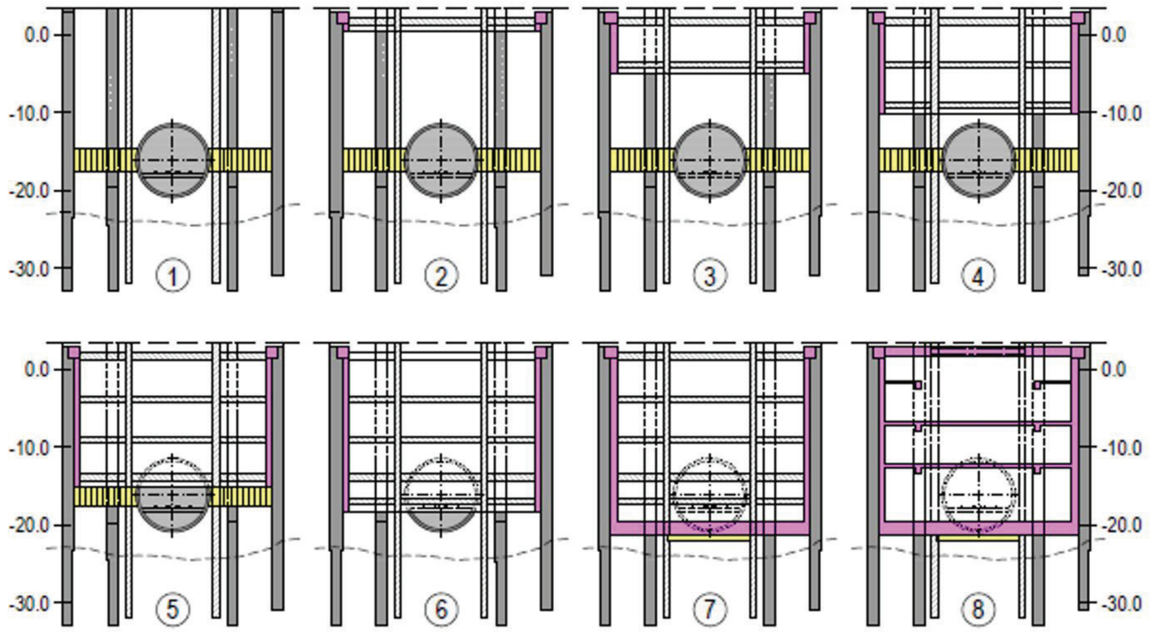

Figure 18. Representative phases of the construction phase of the wide area (eastern) of the station (Brito & Fernandes, 2006a).

bottom slab, the columns (existing only in the east area) and the successive slabs and beams of the final structure were executed from the bottom up, in articulation with the removal of the temporary shoring.

2.6 Portals

On the two extreme transversal walls of the station adjacent to the portals, the piles could not pass through the tunnel. It was then necessary to complement the pile curtain on these sites with a system which would allow the excavation to be carried out safely, as well as the construction of the final internal structure of the station, adequately connected to the tunnel lining. The extreme importance of the performance of such a system can be evaluated taking into account that the soft alluvial soils in contact with the clay substrate, located near the base of the tunnel, 25 m below the groundwater level, were at certain points made of clean sand.

As shown in Figures 19a and b, the solution consisted of surrounding the tunnel sections adjacent to the station with a mass of soil treated with jet grouting which would have to fulfil two essential conditions: be practically impermeable and also be resistant to water and soil pressures on its outer face. In order to meet these conditions, it was essential, on one hand, to ensure good penetration of the jet grouting mass into the Miocene substrate and, on the other hand, to make a good connection between itself, the tunnel lining and the station structure. To achieve this last requirement, the peripheral pile wall of the station was extended about 16 m beyond the plane of the portals, in order to confine the tunnel and the jet grouting, as can be seen in Figure 11.

Only vertical jet grouting columns were decided to be used, which meant, for the columns under the tunnel, that the lining of the tunnel would be crossed by drilling at two points, as shown in Figure 19b). This option was taken on

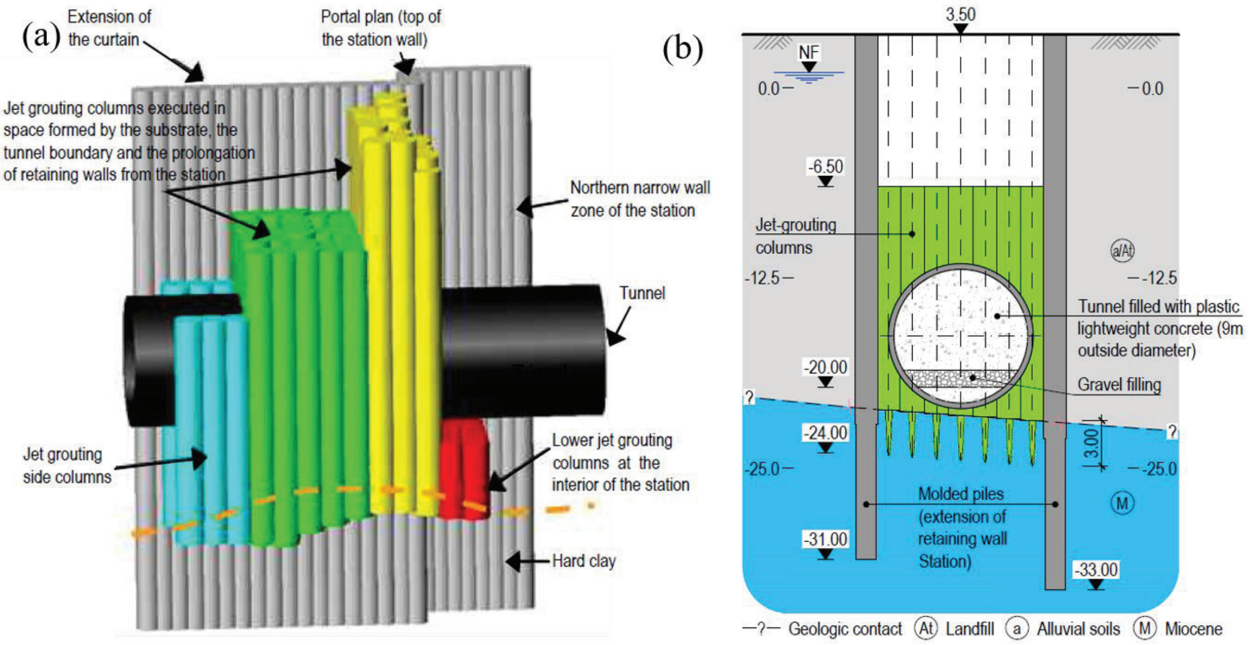

Figure 19. (a) 3D view of the jet grouting treatment on the west portal; (b) Cross section of the west portal plane, showing the area treated with jet grouting (Brito & Fernandes, 2006a).

the basis that the tunnel at these locations was filled with concrete and that there was no immediate adverse effect of these holes on the internal stability of the tunnel. In any case, an attempt has been made to minimise the number of holes so as not to weaken the concrete lining, in order to ensure the stability conditions of the tunnel in the phase of the concrete filling removal. For this purpose, large diameter jet grouting columns (Ø > 2.0 m) were used, executed with triple jet method (Candeias et al., 2005, Matos Fernandes et al., 2007).

2.7 Monitoring plan

The construction was monitored throughout the construction period by a very complete system of observation devices, whose transversal profile is shown in Figure 20. This system proved to be extremely useful in the critical phases of the station execution and in the sequence of incidents that occurred and in the subsequent outside treatment of the curtain.

2.8 Incidents during the final excavation phase

2.8.1 Location of the incidents and state of progress of the works at the time they occurred

In the final phase of the excavation two important incidents occurred, water and solid material entering through the curtain, at levels close to those at the base of the excavation. The first occurred on May 10, 2003, at the re-entrant corner of the north side coinciding with the axis 5, and the second on June 2, at the re-entrant corner of the south side coinciding with the axis 20 (Figure 11).

At the time of the first incident, in the wide area of the station, the excavation base was at approximately at the level -18.50 m (about 22.00 m deep) and the installation of the 5th level of struts was almost complete; the last excavation phase was therefore to be carried out in order to reach the level of -22.00 m corresponding to the maximum depth (25.50 m). In the narrow area, the 4th level of struts had already been installed and the excavation below it had been taken to about the level -20.00 m (to the base of the, tunnel), about 2 m below the level foreseen in the designed construction phasing (level -18.20 m). This over-excavation of about 2 m was motivated by the need to better examine the tunnel concrete lining that was being removed, since it was in this area that the tunnel structure had suffered the most significant damages in the accident of June 2000.

On the other hand, at the time of the second incident, the excavation at corner zone where it occurred was completed, with ongoing preparatory work for the construction of the bottom slab, which was already concreted in the symmetrical corner on the north side.

2.8.2 Incident of May 10, 2003

2.8.2.1 Description of the incident and measures taken to control water and alluvial deposits inlet

The incident was manifested by the entry of water and the dragging of solid, silty-clayey and sandy material

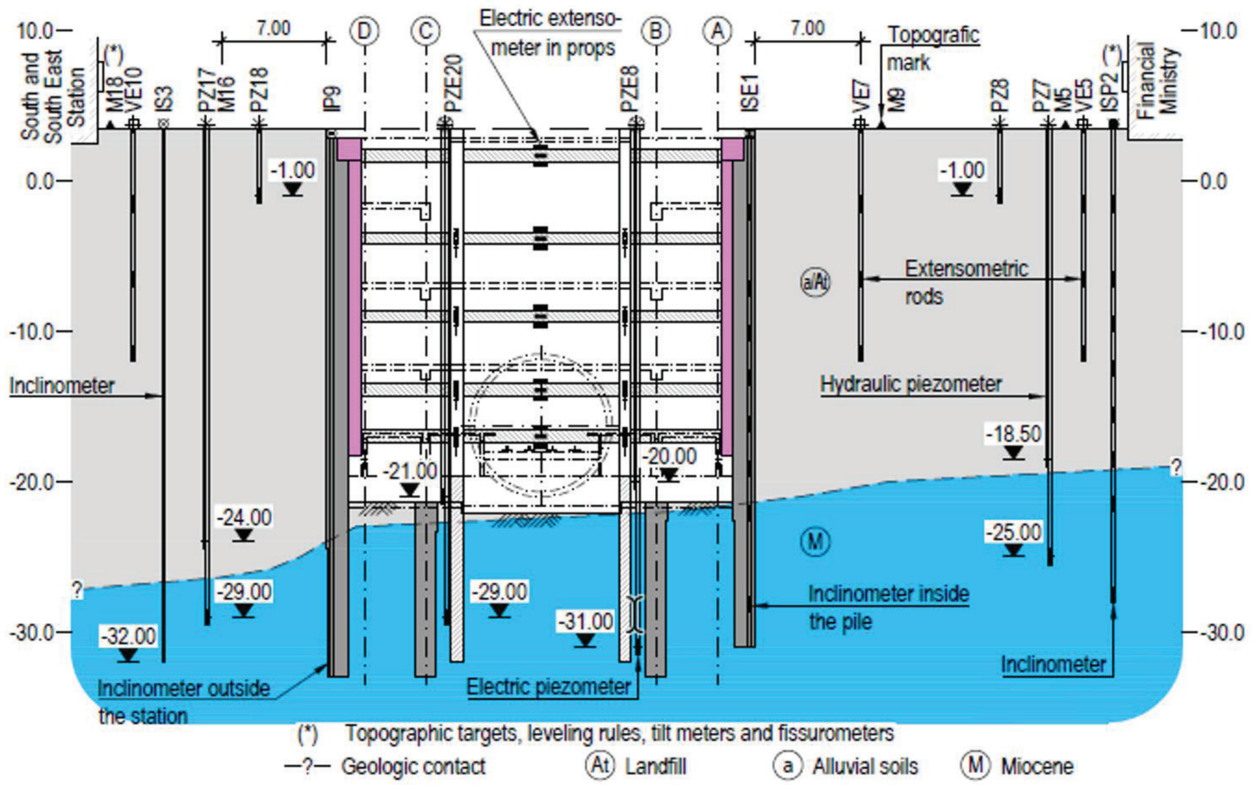

Figure 20. Typical cross-section of observation devices (Brito & Fernandes, 2006a).

in the re-entrant corner on the north side coinciding with the axis 5. At that time, the base of the excavation was at the level of the working platform foreseen for the installation of the 5th level of struts (between about the levels -18.00 m and -19.00 m) and the water inlet and drag of material occurred at approximately the level -19.00 m. At that level, outside the area adjacent to the curtain, the soils were constituted by sandy-clay alluvial deposits with a slightly thick passage of clean sandy alluvial deposits over the Miocene substrate. As can be seen in Figure 21a and b, the entry of water and alluvial soil into the excavation occurred more significantly when the soil between the EP63 and EP65 primary piles was excavated. This terrain, during the excavation with the backhoe bucket and the progressive inflow of water from outside, collapsed by "blocks" of sandy-clay alluvial deposits, clearly showing the distance between those primary piles. Figure 21 a show the opening filled with alluvial deposits, and it is not possible to see the secondary corner pile (ES65), which, if it were in its correct position, would be visible. Figure 21b highlights this fact, since it was possible to insert a wooden beam to a certain depth (at least 0.50 m) beyond the visible soils face between piles.

In the emergency operations carried out immediately in order to control the entry of water and alluvial soils, sand bags were first placed, already available on site for the case of an eventual emergency during the execution of the waterproofing plugs of the tunnel portals. It was progressively necessary to place cement bags, concrete and geotextile blanket until it formed a plug in a conical shape against the corner of the curtain and with the top at the level of the base of the lining wall (level of -15.10 m) as shown in Figure 22. In the opening between the piles a tube was introduced to capture part of the tributary flow to the corner.

2.8.2.2 Immediate consequences outside the curtain

After the incident, the following events were immediately registered outside the curtain:

- Settlements and cracks in the surface in the vicinity of north corner 5 in front of the tower of the Finance Ministry building; these settlements evolved rapidly and covered an area of about 500 m^2 with visible subsidence and radiating from the point of entry of water and material into the excavation; the settlements tended to stabilise quickly after the entry of water and alluvial soils was eliminated;
- The maximum settlement registered on the surface was 28 mm on a mark located 25 m from corner 5; a settlement of 5 mm was registered in the tower;
- Two piezometers, with the chambers in the alluvial sand layer at levels -18.50 m and -18.00 m, (at distances from the corner concerned of 8 m and 40 m, respectively) showed a drastic reduction in pressure of 12 m and 7 m respectively; the water pressures returned to normal values, when the entry of water started to be controlled;

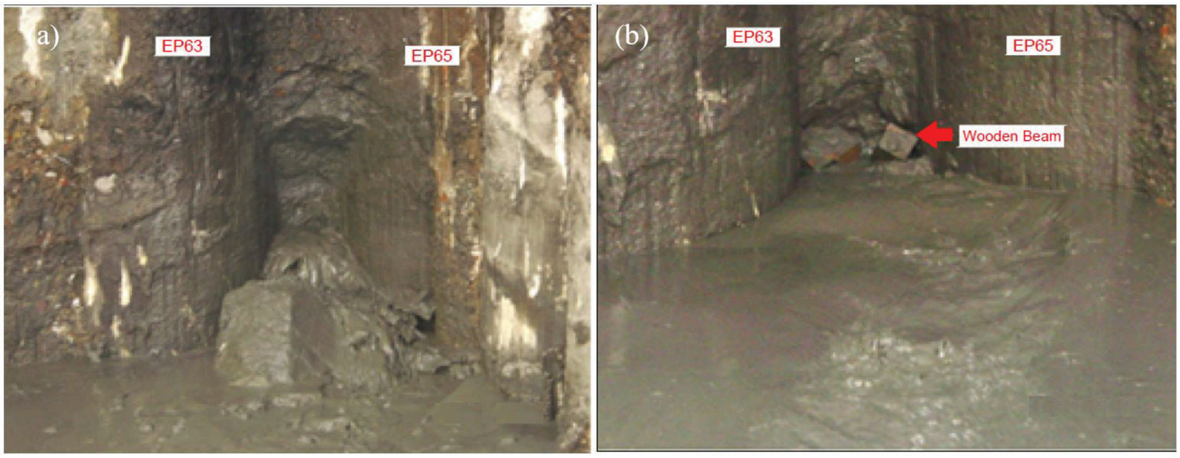

Figure 21. (a) Initial phase of water inflow and dragging of sandy-muddy alluvial deposits in the north corner 5; (b) Most significant water inflow and alluvial deposits shortly after the start of the incident.

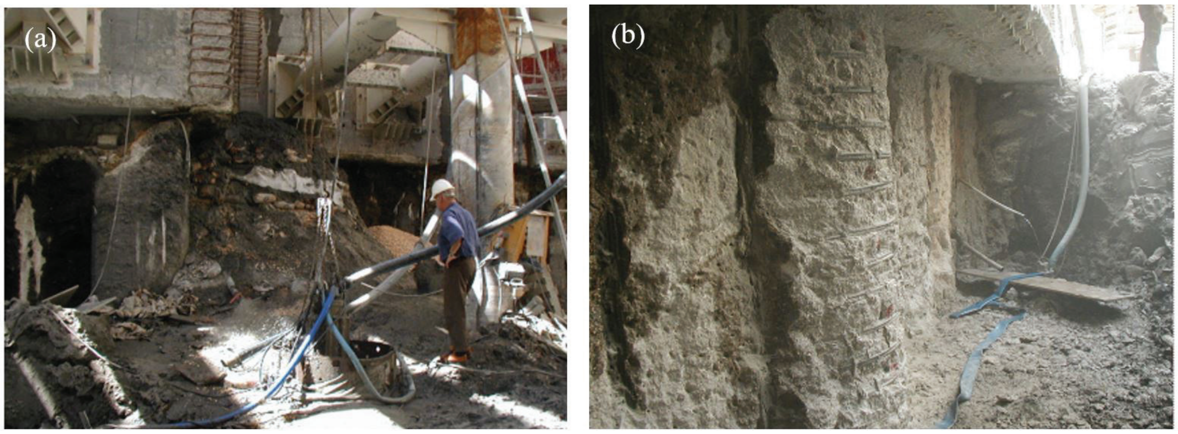

Figure 22. (a) Plug of sand bags, cement and concrete bags, about 3 m high; (b) Retaining piles from the narrow area on the north side between axes 3 and 5 after excavation up to the level -20.00 m, plug of sand bags and the underside of the lining wall at the level -18.20 m.

- An inclinometer, located about 5 m from north corner 5, has recorded significant displacements to the base of the alluvial deposits (at about 25 m deep) with a maximum displacement of the order of 30 mm at 16 m deep;
- The effect of the incident was felt only on the north side of the curtain and up to more than 100 m away from corner 5 in the piezometers, surface marks and extensometric rods installed in the alluvial deposits.

The piezometers installed on the Miocene substrate inside and outside the curtain, did not register any variation in the water level and in the piles, no cracks or anomalies in the lining wall and in the top beam indicating settlements of the retaining curtain, proving that the Miocene formations were not affected.

2.8.2.3 Action that stopped solid material to enter to the curtain inside

The action that succeeded in preventing solid material from entering the excavation the day after the incident was the placing of the plug and the injection of cement grout into holes adjacent to the entry point, executed outside the curtain. The flow of clean water has dropped to a relatively low amount (about 24 m^3/day). The flow rate was later reduced when the curtain was treated at the back. It was about 3 m^3/day when the concreting of the bottom slab was completed. Then it was diverted to the blanket drain with connection to the definitive pumping well of the station.

2.8.2.4 Survey of the piles position at north corner 5

Following the completion of the waterproofing treatment in north corner 5 (as described in chapter 2.9.6), an inspection shaft was opened manually between approximately the levels 15.30 m and -18.00 m. The survey of the positioning of the piles was not entirely conclusive in relation to the position of the ES65 secondary corner pile as, for safety reasons, it was not possible to dig the shaft much deeper and to remove, between piles, part of the constituent materials of the plug. However, with the information available, namely the position inferred from Figure 21, it was possible to define the most likely position of the ES65 pile. Figure 23 shows the survey of the position of the retaining piles at corner 5, here the deviation of the ES65 pile from the theoretical position was of about 0.75 m at level -18.00 m, which corresponds to an inclination of 1/28.

At the bottom of the shaft, one could see the inflow of water that was rising and being directed to the intake pipe. This water inflow was concentrated in the corner between the EP65 and ES65 piles. As Figure 23 shows, the area where the water inflow was observed corresponded exactly to the area of lack of overlap between the EP65 and ES65 piles.

2.8.2.5 Complementary aspects

In the corner concerned, as well as in the symmetrical corner 5 (south), small water transfers (without solid material) have been taking place since the first excavation phases. This was manifested in particular by the appearance of water in contact between the base of the back of the lining wall and the piles curtain. These transfers were reduced or disappeared by means of cement injections between the two walls (the lining wall and the pile wall), carried out before the incident.

The sandy soils dragged inside the station had a similarity, due to their aspect and granulometry, with the alluvial sands overlying the Miocene substrate that were excavated inside the excavation. The dragged sands had also small fragments of wood, bricks and coal, indicating that they came from alluvial deposits.

2.8.2.6 Conclusion on the cause of the incident

The incident was caused by an opening in the piles curtain, in particular in the contact of the EP65 primary pile with the ES65 secondary pile, where the influx of water and alluvial soils was triggered when the excavation reached approximately the level -18.00 m. This opening was caused by a deviation of the axis of the ES65 pile, located at the corner of the curtain, resulting from an inclination proven to be greater than 1/30 with respect to its theoretical axis, much higher than the maximum allowable inclination of 1/100, thus not guaranteeing water tightness.

2.8.3 Incident of June 2, 2003

The second incident was very similar but less serious than the first, with dragging water and soil into the excavation. The consequences on the outside were similar but the maximum settlement did not exceed 5 mm.

Following the second incident, it was decided to stop the work, due to the uncertain position of the piles, until the survey of its position and the analysis of the possible mitigating solutions be implemented to guarantee the tightness of the curtain.

2.9 Measures adopted to continue the work in safe conditions

2.9.1 Assessment of risk scenarios

Some entities involved in the work, namely the contractor consortium and the supervision team, developed some biased judgments attributing the origin of the incidents to the existence of the permeable layer of sand with artesianism, interspersed in the Miocene clays (Figure 6).

Thus, following the second incident, it was decided that, in addition to stop the excavation, curtain works and the execution of the bottom slab, a review of risk scenarios and the precautionary and reinforcement measures to be adopted should also be made.

The following scenarios were analysed:

- Hydraulic lifting (“heaving”) from the bottom of the excavation;

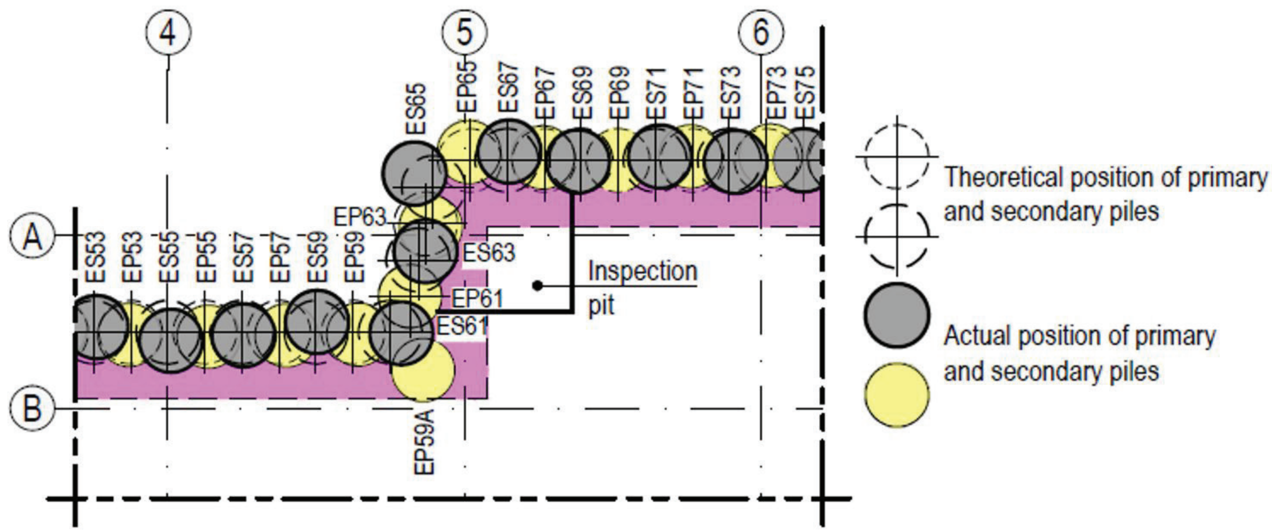

Figure 23. Plan at level -18:00 from survey of the piles position at north corner 5.

- Erosion in the contact between curtain / ground (“roofing”);
- Internal erosion of the soils (“piping”);
- Water inflows due to poor overlap between primary and secondary piles;
- Water inflows due to lack of integrity of the primary piles;
- Water inflows due to the lack of integrity of the secondary piles;
- Water inflows through openings in the contact between piles, in the last stages of excavation;
- Hydraulic uplift of Miocene clays in the west part of the station due to the artesianism of the Miocene of compact sandy silt levels closest to the bottom of the excavation (around -33.00 m);
- Water inflows, in the west portal, resulting from eventual deficiencies in the surrounding treatment by jet-grouting.

The survey of the position of the piles allowed to identify as a cause of the important inflows of water to excavation with transport of solid material, the deviations of the piles in relation to their theoretical verticality, deviations that reduced or even cancelled the overlaps between primary and secondary piles, in the body of the curtain, at the top of the Miocene or just below, especially at deeper levels of excavation. In fact, the analysis of these deviations showed that, in many cases, the specified vertical tolerance of 1/100 was substantially exceeded. These piles deviations were naturally more significant at lower levels, not guaranteeing a minimal overlap between primary and secondary piles. However, no inflow of water from the tip of the piles were detected inside the excavation perimeter, confirming very low permeability of the Miocene and its great resistance to “roofing” phenomena.

It should also be noted that, although the flow rates affluent to the bottom of the excavation could be of varied origins, namely of the Miocene compact sandy silt levels closer to the bottom of the excavation, this situation was investigated with tests that revealed low coefficients of permeability and inexistence of artesianism that would be critical to the local stability of the bottom of the excavation. In addition, all fine levels of silts and silty clays, more permeable than Miocene clays, were intercepted by the relief holes inside the excavated enclosure, and it should be noted that the flow rate in the relief wells was always modest.

As additional emergency precautionary measures, to be used only in the event of a new incident, it was foreseen:

- The maintenance on site of a stock of sand and cement bags, geotextile and gravel for the formation of a plug, similar to those carried out in the corners of the two incidents that occurred;
- The realization of a network of pumping holes outside to relieve water pressure in the alluvial sands layer.

2.9.2 Holes for lowering the water table in holes outside the containment

Pumping holes were made on the periphery of the curtain down to the top of the substratum, with the location shown in Fig. 24. These holes, equipped at the base with a pump ready to operate, were intended to reduce outside water pressures at the level of the alluvial base, in case a new incident, similar to the previous ones, would occur in the last excavation phase, necessary for the concreting of the bottom slab. This system proved to be quite effective in the water lowering tests carried out. This emergency measure was not necessary.

2.9.3 Interruption of work and survey of the position of the piles

Following the first incident, the design team requested a survey of the position of the primary and secondary piles. However, given the practical difficulty of accessing the primary piles without the excavation of the surrounding soils, this survey was not carried out. Following the occurrence of the second incident, the designer proceeded to a thorough inspection of some primary piles on the south wall on the

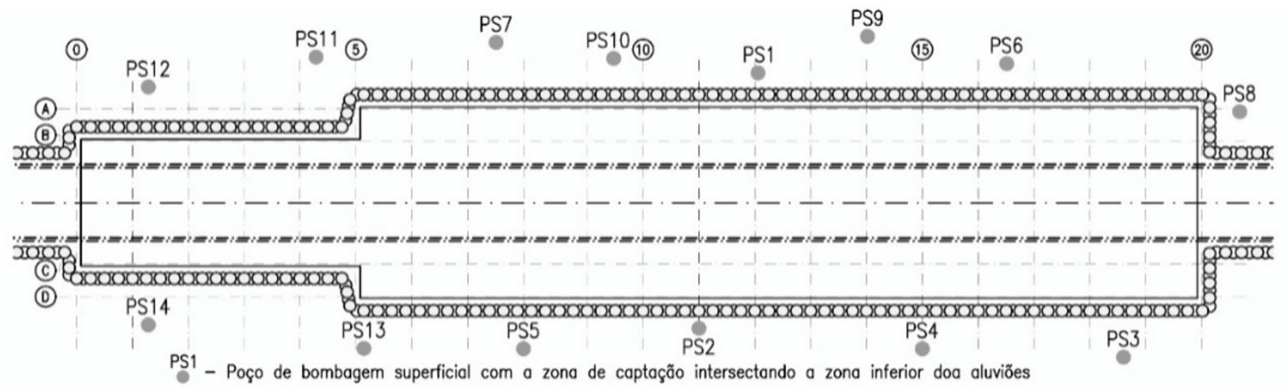

Figure 24. Location of pumping holes in the alluvium outside the station (Brito & Fernandes, 2006a).

east side between EP158 and EP174, located between axes 16 and 18, and on the north east side piles. After this inspection, the design team considered essential to carry out the survey of the position of all the piles at the elevation at which the excavation was located (elevation -18.70 m in a large part of the wide area at the date of the second incident), in order to identify the eventual existence of critical areas of the pile curtain.

With the occurrence of the two incidents, it was found that the lack of verticality of the piles could result, with the works development, in similar or even more serious incidents than the ones that occurred and with unforeseeable consequences. The most serious situation of a rupture that would be difficult to control could result in significant damage to the tower and to the other buildings.

On the other hand, in the narrow area it was decided to fill the zone to the level -16.00 m (about 4 m), where the lining wall was not yet been built to install the 5th level of struts, and where, as mentioned, there was executed an over-excavation of about 2 m.

2.9.4 Analysis of the results of the survey of the position of piles

The analysis of the pile survey, allowed to verify the existence of:

- Zones, more or less located, where some of the piles had slopes of about 1/50, resulting in a very reduced thickness of the primary piles (as they were removed with the execution of the secondary piles), so localized ruptures of primary piles could not be excluded; this situation resulted from the fact that the piles were inclined in the transversal direction of the station with the primary ones inclined inwards and the secondary ones towards the outside;
- Zones where the resistant thickness of the primary piles was insufficient due to a significant overlap with the secondary piles, where the inclinations of the piles were also about 1/50;
- Zones where the distance from the adjoining primary piles was high, therefore it was not possible to exclude the existence of openings between piles as the excavation proceeds; in these zones the situation mentioned resulted from the fact that the secondary piles incline in opposite directions, predominantly in the longitudinal direction of the station, with an inclination between 1/40 and 1/70.

As an example of the lack of verticality of the piles Figure 25 a is presented. This figure was obtained at the time of opening the inspection ditch for observation of the piles, before the general excavation for the execution of the bottom slab. It is observed the great deviation of the secondary piles in relation to the primary piles, well evidenced by the distance to the posterior line of reinforcement steel of the lining wall, conducting to a great concrete thickness of the lining wall. It should be noted that, if the execution of the piles had respected the specified tolerances, at the elevation at which the lining wall was located (-18.20 m), the maximum deviation from the vertical should be about 0.25 m in relation to the face back of the lining wall. As an example of the distance between primary and secondary piles, Figure 25 b is shown.

2.9.5 Curtain design considerations

Regarding the openings between piles, resulting from the deviation of piles from their theoretical axis of implantation

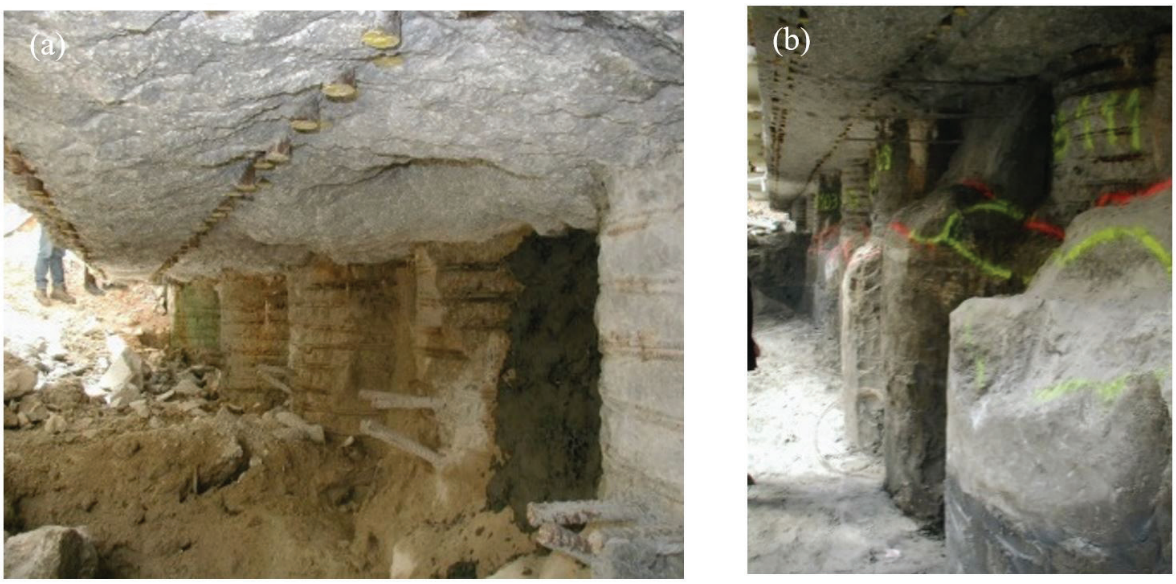

Figure 25. (a) Curtain piles at the level of the bottom slab; (b) Very significant spacing between primary bentonite-cement piles, in the foreground, and secondary reinforced concrete piles, in the background.

beyond the limit defined in the technical specifications, the design team considered it opportune to make the following considerations in the report delivered to the owner, following the first incident:

- During the design phase, several work meetings were held involving the project team, the contractor and the owner's team and consultants;
- The type of containment curtain adopted in the design phase - reinforced concrete and bentonite cement piles 1.5 m in diameter curtain - resulted from the suggestion of the contracting consortium, welcomed by the remaining stakeholders in the process, as an alternative to a conventional curtain of reinforced concrete slurry walls;
- The curtain of secant piles appeared as more appropriate for a ground that, on the one hand, could present large buried obstacles (wooden piles, masonry of old quay walls, etc.), offering, on the other hand, better guarantees of stability when crossing low-resistance soft clay layers; in addition, it is essential to underline that the joints between piles offered better watertight conditions than those of a slurry wall;
- It is also worth noting that in the design phase the modulation initially proposed by the contractor consortium, piles with a diameter of 1.50 m with 2.00 m axis spacing, was reduced for piles of the same diameter with 1.75 m axis spacing; with this reduction, implying that in the middle plane of the wall the primary bentonite-cement piles were only 0.25 m between the reinforced concrete piles, an attempt was made to increase the tightness conditions of the curtain (this change resulted from the fact that the execution equipment of the piles allow to ensure only a tolerance of 1/100 instead of the tolerance of 1/200 in relation to the verticality of the piles specified by the design team); the tolerance adopted of 1/100 corresponded to a maximum theoretical spacing of the position of each pile of only 0.25 m, at the -22.00 m level of the excavation bottom;
- Thus, the designed curtain corresponded to a more conservative option than a conventional curtain, allowing the construction experience to ensure, despite the verified incidents, that the option taken was appropriate.

2.9.6 Treatment with multiple injections of the ground in critical areas outside the curtain

Taking in account the survey results concerning the piles position, the solution that came to be adopted to guarantee the necessary safety conditions for the advance of the excavation and the execution of the bottom slab, was the treatment of the ground at the back of the curtain with multiple injections of grout in manchette tubes with 0.50 m spaced holes. The injections were repeated in all the manchette tubes the number of times necessary to reach pre-established limit values for injection pressure and cement grout absorption.

As shown in Figure 26 injection treatment involved:

- All corners (re-entrant or protruding) of the station, with the exception of the north corner coinciding with axis 20, on which the bottom slab was already built;
- The areas outside the corners where the most significant deviations were detected;
- All the narrow area of the station, due to the difficulty in carrying out a rigorous survey and in safe conditions of the position of the piles.

Depending on the situation assessed, two types of injection hole patterns were defined, with two and three rows of holes, in the locations shown in Figure 26 and 27. The injection length was defined in the upper zone with 2 m overlap with respect to the lining wall already made and in the lower zone with a penetration of 4 m or 6 m in the Miocene substrate due to the smaller or greater spacing of the piles (Figure 27 c).

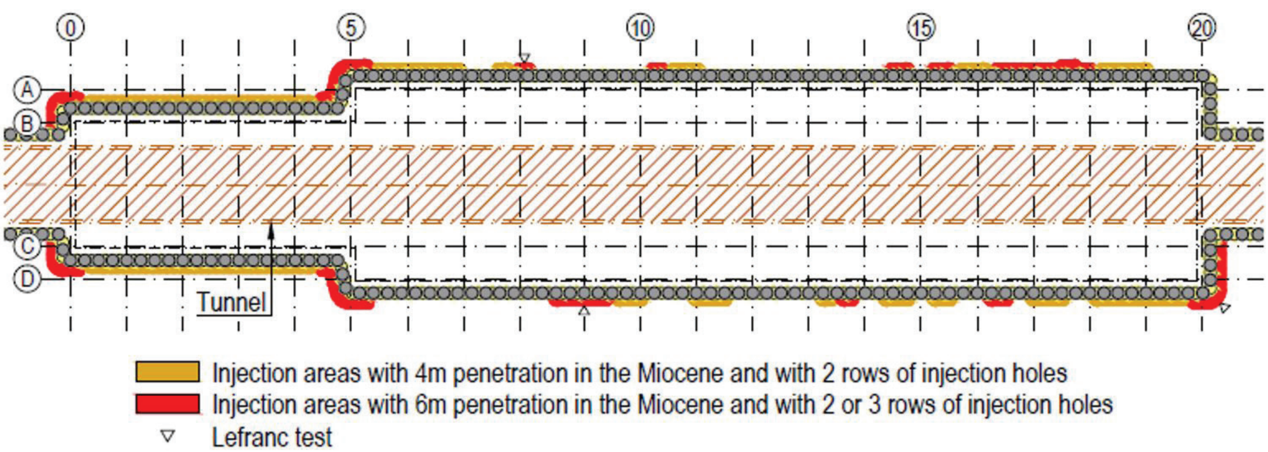

Figure 26. Location of the injected areas outside curtain (Brito & Fernandes, 2006a).

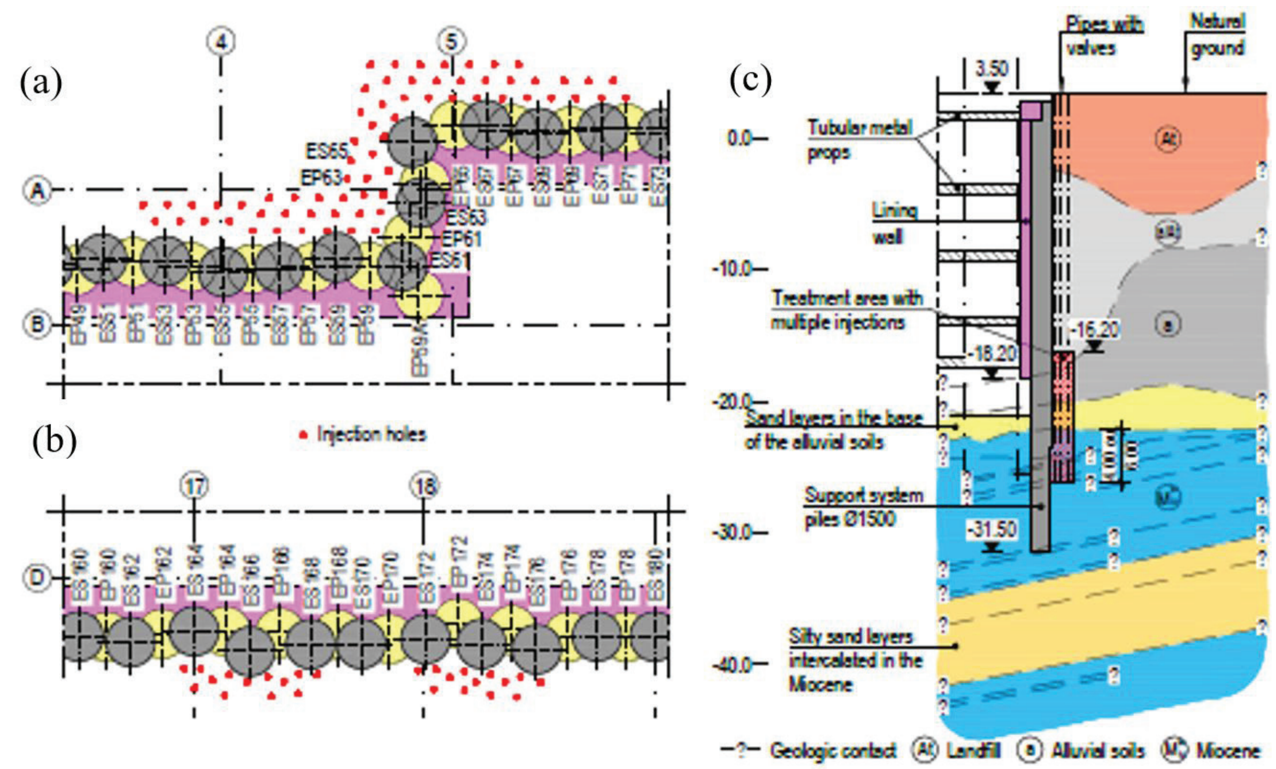

Figure 27. (a) Plan of injection holes in continuous meshes with two and three rows in the north wall in the vicinity of axis 5; (b) Plan of injection holes in meshes located with two rows in the south wall in the vicinity of axes 17 and 18; (c) Vertical cross section in the north corner 5 with indication of the injection holes with manchette tubes and the area treated with multiple injections (Brito & Fernandes, 2006a).

In Figure 28 a one of the 3-row mesh of injection holes can be seen. As shown in Figure 28 b, during the execution of the injections, some grouting entrances were registered inside the station through openings in the curtain.

The efficiency of the treatment was evaluated by means of Lefranc tests, performed before and after the treatment by injections, as well as by examining the samples collected in the boreholes necessary to carry out these same tests. Although it was not completely effective, as it did not eliminate the flow affluent to the interior of the station, the treatment by multiple injections proved to be very efficient. This efficiency was attested by the fact that, during the period in which the waterproofing injections took place in the narrow area of the station, there was a progressive decrease in the influx of water to the alluvium overlying the Miocene substrate inside the station, with the progressive reduction of the flow rate pumped into the relief wells installed there.

2.9.7 Impact of the injection treatment at the back of the curtain

The impact of treatment by injections on the back of the curtain was significant, and was basically reflected in the following:

- Increased forces in the support system, in particular at two lower levels (4^{th} and 5^{th} levels) closest to the injected areas;
- Modification of the type of movement of the curtain, which in the upper zone moved against the supported soils;
- Lifting of a few millimetres from the curtain, registered in most superficial marks.

It should be noted that, in the narrow zone, the forces on some struts, particularly those on the 4th level, reached very high values, close to alarming levels. Those struts, before the injections, already had considerable forces installed, as a result of the over-excavation mentioned above. As the injections further increased those forces, it was necessary to introduce another adjustment to the constructive phasing initially envisaged in that area. This adjustment essentially consisted of reinforcing the 4th level with two more provisional struts and the advancing with the construction of some beams of the final structure.

2.10 Lessons learned

Flaws that lead to the occurrence of the incidents have resulted from the deficiencies in the execution of the piles, as the verticality tolerance of 1/100 was not obeyed. These

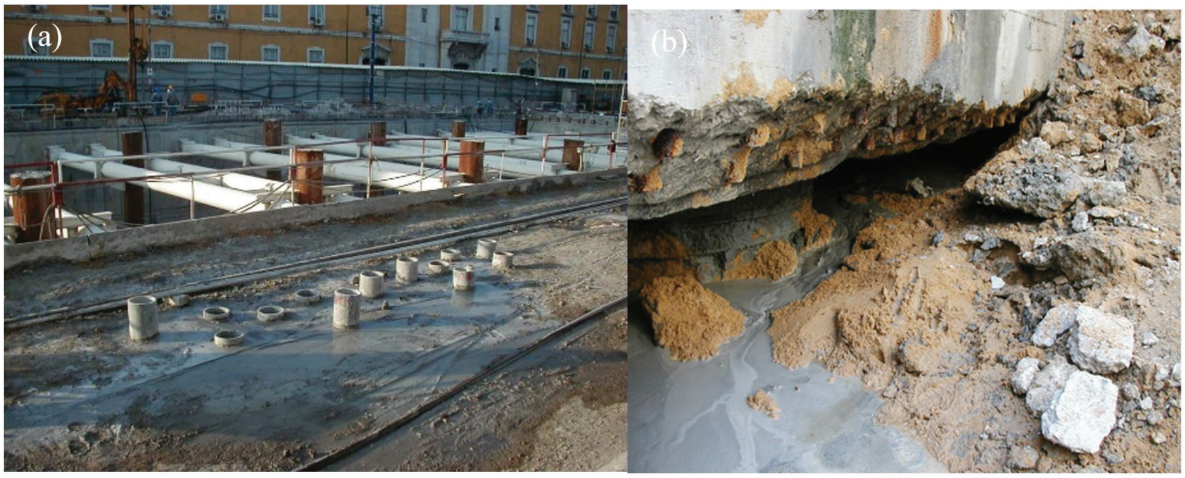

Figure 28. (a) Implantation of three rows of injection holes in the south wall in the vicinity of axis 9; (b) Injection cement grout from the outside of the curtain affluent to the interior near the corner 5 south.

flaws would have been avoided if an effective control of the verticality of the piles have taken place, either during the execution of the piles, or during the subsequent excavation phases with the observation of the respective position, which would have been allowed to take the mandatory provisions in time to avoid the incidents. This situation can be attributed to a judgmental bias that may have resulted from the excessive trust that was placed in the contractor consortium.

The failure was worsened in the re-entrant corners, since here there was a tendency for corner piles to move away from adjacent piles located in the two perpendicular alignments. In the four re-entrant corners, this tendency could have been avoided if four additional piles had been executed. It should be noted that the contractor consortium carried out additional piles at the two protruding corners of the transition zone between the wide and narrow areas of the station, in order to avoid deviation of the corner piles to the interior side of the station, as can be seen in Figure 23. For reflection, we may ask if the contractor consortium should not have proposed the execution of these additional piles, or if this should have been anticipated in the design phase.

In view of the occurrence of incidents, it is also legitimate to ask, if the use of concrete slurry walls would not have been more convenient, since, with the execution of L-corner panels, the problem of the corners would not have existed and the verticality control during the execution would have been more effective due to the characteristics of the slurry wall equipment more scaled up to that control. If these were the only conditioning factors for the choice of the solution, the slurry wall solution would probably have been adopted. However, the expected presence of old foundations of large dimensions in the fill and soft clay layers with low-resistance, made the pile solution more appropriate, as mentioned in chapter 2.9.5.

During design and execution there was intervention of expert judgement in several areas. It should be noted that the project was not revised by an independent entity.

3. Final considerations

Engineering judgment has always played an important role in geotechnical engineering. Before the advent of modern computers, projects were developed essentially based on the experience acquired in previous similar works. Currently, where design and analysis are assisted by computer, engineering judgment remains, or is increasingly indispensable for successful engineering, since geotechnical problems cannot yet be solved even by advanced numerical analysis without the introduction of geological conditions and geotechnical parameters that seek to bring the complex reality closer. On the other hand, the results of the computational analyses also have to be judged to be accepted or rejected, based on their plausibility. No doubt that what can be calculated improves judgment, allows to make better judgments and achieve better engineering solutions.

The development of geotechnical engineering and the increased complexity of geotechnical works requires increasingly the need to deepen the judgments. Aspects of geotechnical engineering which are not yet, and possibly never will be, subject to theoretical analysis, will require much more judgment. It must therefore be cultivated, recognized and used, which will surely render a progressive improvement in the safety of geotechnical works.

Acknowledgements

The author would like to express his gratitude to the Geotechnicians Association of Former Students from Universidade Nova de Lisboa (AGAA-UNL) and to the Portuguese Geotechnical Society (SPG) for the honourable distinction to present this Manuel Rocha Lecture. The author is especially grateful to Prof. António Mineiro, an inspiring figure at the beginning of his geotechnical career and with whom he learned to make good judgments and to develop critical thinking in geotechnical engineering and also to thank to all colleagues with whom he worked at Hidrotécnica Portuguesa, Cenor and TPF companies, the spirit of team that has always chaired in all moments of fruitful debate and difficult decisions taken in the design and execution phases of many geotechnical works.

The author also thanks the great involvement of Metropolitano de Lisboa, Ferconsult and Metropaço (Teixeira Duarte, OPCA and Mota-Engil), in the most difficult moments of the station's execution and other entities and consultants, especially LNEC and Prof.[s] António Mineiro and Maranha das Neves, also stressing the great dedication and commitment of the vast team of Cenor (now TPF) employees in participating in the project and monitoring the work execution, with emphasis on Eng.ºs Fortes Monteiro, Miguel Albergaria and Alfredo Nunes and Dr. Sérgio Rosa and the essential participation of Prof.[s] Manuel Matos Fernandes, António Silva Cardoso and Jorge Almeida e Sousa, in the conception and design of the station witch was decisive for the success of this work.

Declaration of interest

The author declare that he has no competing financial interests or personal relationships that could have appeared to influence the work reported in this paper.

References

Baecher, G.B., & Christian, J.T. (2003). *Reliability and statistics in geotechnical engineering* (618 p.). Wiley.

Bandura, A. (1986). *Social foundations of thought & action, a social cognitive theory*. Prentice Hall.

Brito, J. A. M., Fernandes, M. M., Monteiro, R. F. & Cardoso, A. S. (2016). Rehabilitation of soils and foundations. Terreiro do Paço Lisbon metro station. *Revista Construção Magazine*, 73, 10-17. (in Portuguese).

Brito, J.M., & Fernandes, M.M. (2006a). Terreiro do Paço Lisbon metro station. Design, construction and observation (PPT presentation). In *X Congresso Nacional de Geotecnia*. Lisboa: SPG (in Portuguese).

Brito, J.M., & Fernandes, M.M. (2006b). Terreiro do Paço Lisbon metro station. Conception, design forecast and performance. In *III Congresso Luso-Brasileiro* (Vol. 1, pp. 21-42). Curitiba. (in Portuguese).

Brunswik, E. (1952). *The conceptual framework of psychology. International encyclopedia of unified science* (Vol. 1, No. 10). Chicago: The University of Chicago Press.

Candeias, M.A.S., Brito, J.A.M., Fernandes, M.M., & Lopes, P.G. (2005). Terreiro do Paço Metro Station – A jet grouting solution to link the pre-existing tunnel to the cut-and-cover excavation. In *Proceedings of the 6th International Conference Ground Improvement Techniques* (14 p.). Singapore: CI-Premier.

Dunnicliff, J., & Deere, D.U. (Eds.). (1984). *Judgment in geotechnical engineering, The professional legacy of Ralph B. Peck* (332 p.). John Wiley.

Dunnicliff, J., & Nancy, P.Y. (Eds.). (2006). *Ralph B. Peck. Educator and engineer. The essence of the man*. BTech Publishers Ltd.

Ferconsult, & Metropolitano de Lisboa. (2001). *Description of 2000 incident and details of the initial project of the new Terreiro do Paço Lisbon metro station*. Ferconsult & Metropolitano de Lisboa. Internal document. (in Portuguese).

Ferconsult. (2002). *Terreiro do Paço Lisbon metro station – general project*. Ferconsult. Internal document. (in Portuguese).

Hammond, K.R. (1996). *Human judgment and social policy: irreducible uncertainty, inevitable error, unavoidable injustice* (448 p.). Oxford University Press.

Lambe, T.W., & Whitman, R.V. (1969). *Soil mechanics* (576 p.). John Wiley & Sons, Inc.

Margolis, H. (1987). *Patterns, thinking, and cognition: a theory of judgment* (332 p.). University of Chicago Press.

Marr, W.A. (2006). Geotechnical Engineering and Judgment in the Information Age. In *Proc. Geo-Congress 2006* (Vol. 1, pp. 52-68). Reston: ASCE.

Marr, W.A. (2019). Geotechnical judgment and risk. H. Bolton Seed Medal Lecture. In *Proceedings of the Geo-Congress 2019.* Reston: ASCE.

Marr, W.L. (2020). *Geotechnical judgment. Risk in geotechnical practice*. ASCE Geo-institute. Geostrata.

Matos Fernandes, M., Maranha das Neves, E., Salgado, F., Caldeira, L., Pina, R., Flor, A., Brito, J.M., & Tavares, A. (2007). Jet grouting solutions for cut-and-cover subway metro stations in Lisbon downtown. In *Proceedings of the XIV ECSMGE* (Vol. 2, pp. 895-900). Madrid.

Mineiro, A.J.C. (1971). *Soil mechanics and foundations course*. Instituto Superior Técnico (in Portuguese).

Norwegian Geotechnical Institute – NGI. (2000). *Ralph B. Peck. Engineer. Educator. A man of judgement* (Publication 207, 75 p.). Norwegian Geotechnical Institute.

NP ISO 31000. (2012). *Risk management. Main guidelines*. Instituto Português da Qualidade, Caparica, Portugal (in Portuguese).

Parkin, J. (2000). *Engineering judgment and risk* (224 p.). Thomas Telford.

Peck, R.B. (1969). *A man of judgment*. The 2nd R.P. Davies Lecture on the practice of engineering. W. VA. Univ. bull. series 70, No. 5-2, Nov. 10 p.

Peck, R.B. (1980). Where has all the judgment gone? The 5th Laurits Bjerrum Memorial Lecture. *Canadian Geotechnical Journal*, 17(4), 584-590.

Peck, R.B. (1981). Geotechnical judgment and risk. H. Bolton Seed Medal Lecture. In *Proceedings of the Geo-Congress 2019.* Reston: ASCE.

Peck, R.B. (1991). *Engineering judgement.* Retrieved in March 1, 2021, from https://peck.geoengineer.org/resources/videos/singleVideo/41

Salgado, F. (2014). Incident at the Terreiro do Paço Lisbon metro in July, 2000. In *Proceedings of the XIV Congresso Nacional de Geotecnia* (28 p.). Coimbra. (in Portuguese).

Simon, H.A. (1981). *The sciences of the artificial* (3rd ed., 231 p.). MIT Press.

Vick, S.G. (2002). *Degrees of belief: subjective probability and engineering judgment* (455 p.). ASCE.

Manuel Rocha (1913-1981) was honoured by the Portuguese Geotechnical Society with the establishment of the Lecture Series bearing his name in 1984.

Having completed the Civil Engineering Degree at the Technical University of Lisbon (1938) he did post-graduate training at MIT. He was the driving force behind the creation of the research team in Civil Engineering that would lead to the foundation of the National Laboratory for Civil Engineering (LNEC), in Lisbon. He was Head of LNEC from 1954 to 1974 and led it to the cutting edge of research in Civil Engineering.

His research work had great impact in the area of concrete dams and rock mechanics. He was the 1st President of the International Society for Rock Mechanics and organized its 1st Congress in Lisbon (1966). He did consultancy work in numerous countries. He was Honorary President of the Portuguese Geotechnical Society, having promoted with great commitment the cooperation between Portugal and Brazil in the area of Civil Engineering, and member of the National Academy of Sciences of the USA. Recognized as a brilliant researcher, scientist and professor, with a sharp, discerning intellect allied to a prodigious capacity for work and management, he was truly a man of many talents.

The 2020 Manuel Rocha Lecture was presented by **José Mateus de Brito**, 71 years old, Geotechnical Consultant, former Head of Geotechnical Department, Partner and Member of the Board Directors of TPF and Cenor Engineering Consulting Companies in Lisbon, Portugal. He got his degree in Civil Engineering in 1972 at Instituto Superior Técnico. He was Assistant Professor of Soil Mechanics, Foundation Design and Seismic Engineering at Instituto Superior Técnico, between 1972 and 1989. He is Geotechnical Expert and Counsellor Member of the Portuguese Engineers Association. He has been involved in consulting and design, including large dams, reservoirs and tailing dams, canals, highways, metros, railways and tunnel systems, bridge and building foundations, cut and cover urban excavations, pile support systems, foundations and soil improvement. He has also experience in supervision, control and management of hydraulic schemes and metro and rail systems. He was Project Manager of recent relevant projects like Sivas Sarkisla Bozkurt Dam, Turkey; Algiers Metro Line 1 – Emir Abdelkader Square-Martyrs Square, Algeria; Foundation Treatment of Road Accesses to Northern Lisbon Logistics Platform, Portugal; Cerro da Mina Reservoir at Somincor Mine, Portugal; Lisbon Metro Terreiro do Paço Underground Station, Portugal. José Mateus de Brito is author and co-author of more than one hundred communications at national and international congresses and delivered several lectures. He has integrated several committees, namely the Dam Safety Commission in Portugal. He was awarded with the Tectonika Engineering Prize 2018 for the work of recognized value developed in geotechnical engineering at the International Construction and Public Works Fair, Lisbon.

ARTICLES

Soils and Rocks
v. 44, n. 2

Soils and Rocks

An International Journal of Geotechnical and Geoenvironmental Engineering

www.soilsandrocks.com

ISSN 1980-9743
ISSN-e 2675-5475

Centrifuge modeling of normal faulting and underground tunnel in sandy soil deposit

Ali Nabizadeh[1#], Alireza Seghateh Mojtahedi[2]

Article

Keywords
Centrifuge modelling
Tunnels
Sands
Normal fault rupture
Fault/tunnel interaction

Abstract

Earthquakes of large magnitudes cause fault ruptures propagation in soil layers and lead to interactions with subsurface and surface structures. The emergence of fault ruptures on or adjacent to the position of existing tunnels cause significant damage to the tunnels. The objective of this paper is to study the interaction of an embedded tunnel within a soil layer and the soil deformations imposed upon by normal faulting. A centrifuge modeling under 80-g acceleration was conducted to investigate the rupture propagation pattern for different relative tunnel positions. Compared with the free field condition, due to tunnel and normal fault rupture interactions, focused on soil relative density and tunnel rigidity in this research, found that they can dramatically modify the rupture path depending on the tunnel position relative to the fault tip. The tunnel diverts the rupture path to its sides. This study presents the normal fault-tunnel interaction with the tunnel axis parallel to the normal fault line, to examine the changes that take place in fault rupture plane locations, the vertical displacement of the ground surface with tunnel presence and the effect of tunnel rigidity and soil density on fault tunnel interaction.

1. Introduction

Earthquakes are potentially devastating natural events, which threaten lives, destroy properties, and disrupt life-sustaining services. The primary cause of earthquakes is the rupture of faults in the earth's crust and the associated rapid slip on these faults. In most cases, the existence of fault ruptures as well as local soil failures cause permanent ground deformations during a strong earthquake. Surface faulting is arguably the most severe seismic hazard for long lifeline facilities. For example, the fault movements of the 1999 Kocaeli and Duzce Earthquakes in Turkey were the main cause of extensive damage to the tunnel lines (Ulusay et al., 2001; Russo et al., 2002). Landslides caused by the 1930 North Izu and the 1978 Izu Oshima Island Japan earthquakes, were responsible for severe damages to the Tanna and Inatori Tunnels, respectively (Konagai et al., 2007). The 1999 Chi-Chi Earthquake in Taiwan resulted in a surface faulting of 4.0m vertical movement and severely damaged different types of tunnels (Wang et al., 2001; Konagai et al., 2007). The Wrights tunnel, a railroad tunnel crossing the San Andreas Fault, was damaged and deformed during the 1906 San Francisco earthquake (Prentice & Ponti, 1997).

The interaction of long underground structures, such as transportation tunnels, utility tunnels, oil and gas tunnels, which often cross such geological faults, with the fault rupture is still somewhat unclear for designers. Researchers found the presence of an underground structure in a soil deposit may further modify the rupture path as it propagates from the bed rock to the ground surface. Researchers have also studied on the interaction between faults and tunnels and they found that depending on the relative position of the fault tip, the tunnel longitudinal axis and the depth of the tunnel, additional axial forces and bending moments occur in the tunnel lining, which must be considered in the tunnel design (Baziar et al. 2020).

Physical modeling tests were conducted to investigate the propagation of dip-slip earthquake faults through soil layers in free field and with the presence of foundations and pipelines (e.g. Johansson & Konagai, 2004, 2006, 2007; Bransby et al., 2008a, b; Ahmed & Bransby, 2009; Loli et al., 2012; Rasouli & Fatahi, 2019; Agalianos et al. 2020; Tsatsis et al., 2019) along with numerical modeling tests (e.g. Yilmaz & Paolucci, 2007; Lin et al., 2007; Anastasopoulos et al., 2007; Loukidis et al., 2009; Baziar et al., 2012; Anastasopoulos et al., 2013; Oettle & Bray, 2013; Lee et al., 2012; Baziar et al., 2015; Tsai et al., 2015; Mortazavi Zanjani & Soroush, 2019; Thebian et al., 2018; Ghadimi Chermahini & Tahghighi, 2019). General findings include the realization that both normal and reverse fault propagations through soil is a progressive event, and

[#]Corresponding author. E-mail address: ali.nabizadeh@sru.ac.ir
[1]Shahid Rajaee Teacher Training University, Department of Civil Engineering, Tehran, Iran.
[2]Amirkabir University of Technology (Tehran Polytechnic), MSc Graduate of Civil Engineering-Geotechnical Engineering, Tehran, Iran.

Submitted on November 9, 2020; Final Acceptance on March 3, 2021; Discussion open until August 31, 2021.
https://doi.org/10.28927/SR.2021.059520

the final surface emergence of the fault rupture is dependent on soil layer depth, soil properties, dip angle and fault mode. These findings have been supported by field evidences (e.g. Kelson et al., 2004; Anastasopoulos, 2005; Bray & Kelson, 2006; Wang, 2008; Faccioli et al., 2008).

While only a few studies have reported on the interaction between tunnels and faulting events (Lin et al., 2007; Baziar et al., 2016; Naeij et al., 2019), most findings are based on field events (e.g. Wang et al., 2001 & Konagai et al., 2007). A comprehensive study of field observations from the Chi-Chi earthquake (Wang et al., 2001) showed an interaction between the faulting phenomena and tunnel. Centrifuge testing was used in other investigations to analyze the propagation of reverse faulting in single layered and multilayered soils (Tali et al., 2019), as well as the interaction of reverse faulting and tunnel lining (Baziar et al., 2014). Baziar et al. (2020) found out a shallow tunnel with less burial depth of tunnel has less internal forces than a deep tunnel due to reverse faulting displacement. Kiani et al. (2016) investigated on segmental tunnels and normal faulting by using centrifuge tests in sand layer. They found out the failure in the segmental tunnel was not sudden and tunnel lining could deviate the faulting path. Cai et al. (2019) studied on tunnel damages due to normal faulting in sand layers. They reported with the presence of a tunnel, the tunnel could act as a shielding to reduce surface settlements after normal faulting. To date, no centrifuge modeling has been conducted to investigate normal fault–tunnel interaction with the tunnel axis parallel to the normal fault line in drained sandy soil deposit.

This paper investigates tunnel performance, as embedded in soil deposit, subjected to normal dip-slip faulting using centrifuge modeling under 80-g centrifugal acceleration. The centrifuge modeling was used to allow detailed examination of the factors affecting the tunnel–fault interaction in a controlled environment and with real dimensions. The effects of burial depth, tunnel location, soil relative density and tunnel rigidity on the fault tunnel interaction have been examined within the range of tests performed in this study.

2. Experimental method

2.1 Model geometry and container

The tunnel and soil layer geometries are shown in Figure 1 schematically. A dip-slip normal fault rupture is propagated by downward displacement of the bedrock at 60 ° to the horizontal axis (α). The tunnel with the diameter of *D* and thickness of t, embedded in the soil layer, had a distance of (*X*, *Y*) from the fault tip, such that the tunnel was in the faulting zone obtained from the free field tests. A 60° fault dip angle was selected based on the common reported field conditions (Kelson et al., 2004; Anastasopoulos & Gazetas, 2007a, b; Faccioli et al., 2008).

2.2 Model preparation and material type

Special traveling pluviation apparatus was constructed to prepare a uniform relative density of the tested soil in the soil sample box. The sand was pluviated from specific heights, aiming to give uniform relative densities of 50-70% and soil unit weights of 15-16 kN/m^3. The obtained soil is classified as poorly graded sand (SP) according to the Unified Soil Classification System. A series of direct-shear tests were conducted to investigate the soil frictional angle and cohesion, and the results of the peak frictional angles were $\varnothing = 38°$ for $D_r = 70\%$, $\varnothing = 36°$ for $D_r = 50\%$ and a secant shear modulus *G* of 0.5 MPa for a relative density of 55% (Lin et al., 2007; Baziar et al., 2014). The selected tested quartz sand had a specific gravity (G_s) of 2.65, maximum and minimum dry unit weights of 16.6 kN/m^3 and 13.8 kN/m^3, respectively, and an almost linear failure envelope and cohesion of near zero for the tested stress levels. The dilation angle of sand was ψ = 10°-11°. Table 1 reports the physical properties of

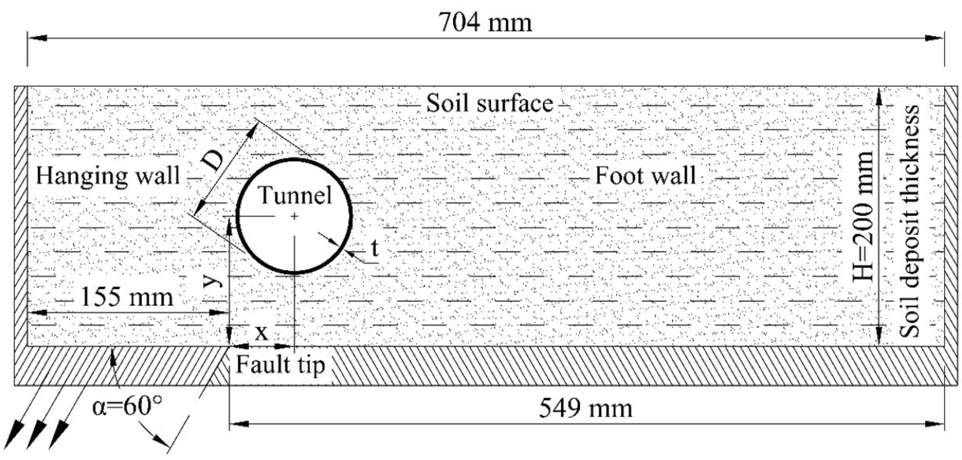

Figure 1. Schematic sketch of studied problem, indicating dimension at the model scale, interaction of normal fault rupture and tunnel.

quartz sand used in the presented study. Lee et al. (2012) reported all properties of the tested crushed quartz sand.

The tunnels were constructed from aluminum alloy (6061-T6) tubes. The external diameters of the tunnels were D = 49.4 and 49.8 mm and had thicknesses of t = 1.2 and 1.4 mm, respectively. Table 2 reports the mechanical properties of the aluminum alloy (6061-T6) used in the current tests. The external part of the aluminum tube was coated with a 0.5 mm thick LOCTITE Hysol Product epoxy to simulate the friction between the soil and tunnel. The friction between the soil and the epoxy coating, as measured from the direct shear test for the specimen with half epoxy and half sand, was about 22°. Since the resistance of the epoxy coating was very small, it did not affect the rigidity of the aluminum tube.

The well-known basic scaling law for centrifuge modeling derives from the need to ensure the similarity between the tested model and the prototype with following relationship: $(EI)_{model} * N^4 = (EI)_{prototype}$. Where N is the gravity level in the centrifuge test (in this study N = 80).

In these experiments, layers of 15 mm thick sand were initially poured and followed by 5 mm thick sand dyed with blue ink to highlight the rupture path and shear localization, observed from the front face of the soil container. Once the desired soil thickness was achieved, the aluminum tube was embedded parallel to the fault tip in the soil layer. Sand shedding was continued in the same manner until the soil deposit reached to the thickness of 200 mm.

2.3 Model instrumentation

Measurement of the surface displacement was achieved using a surface profile scanner integrated with two laser displacement transducers (LDT) and positioned on the center line of the tested sand bed during the normal faulting tests, see Figure 2b. Driving the scanner on the centerline of the fault box enables it to scan continuously the soil surface elevation. A CCD camera was installed at the front face of the acrylic plate window of the strong-box to record the soil deformation, faulting outcrop and its deviation after finishing each test. Besides, at the end of each test, soil layers were removed carefully and the tunnel movement was measured by instrumentation.

2.4 Centrifuge modeling and testing program

Figure 2b illustrates the key sketch for observing the surface rupture and distorted surface. In this figure, W indicates the distance from the bedrock fault to the location of the right side surface outcropping, α is the dip angle of the fault plane, H is the thickness of the soil deposit and h indicates the vertical offset of the fault. According to Figure 2b for studying the critical conditions, the tunnel

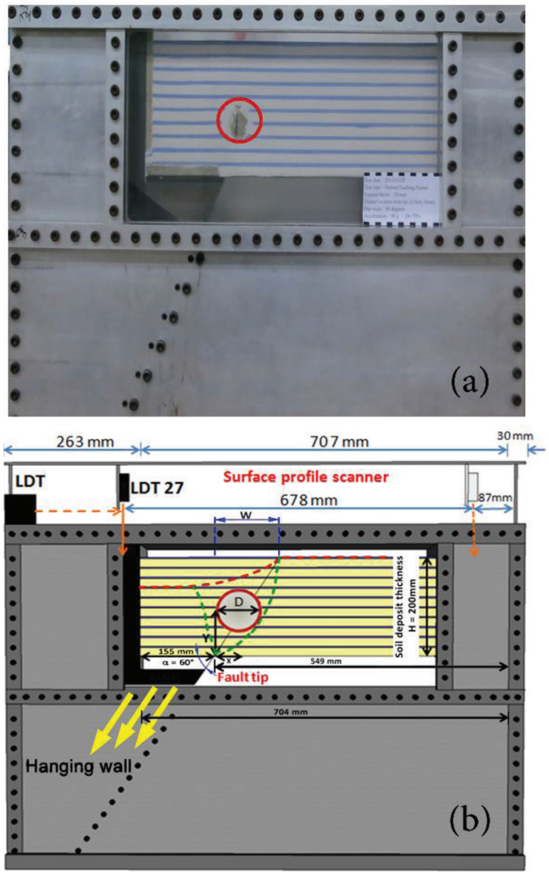

Figure 2. The centrifuge apparatus: (a) Cross section of the experimental apparatus installed in the plane strain container; (b) photograph of the apparatus and schematic diagram of the studied problem (normal fault rupture).

Table 1. Physical properties of quartz sand.

Soil Type	G_s	$\rho_{max}\left(\mathrm{kN/m^3}\right)$	$\rho_{\min}\left(\mathrm{kN/m^3}\right)$	$d_{50}\,(\mathrm{mm})$	$d_{10}\,(\mathrm{mm})$	$\phi\ (D_r = 70\%)$
SP	2.65	16.6	13.8	0.193	0.147	38°

Table 2. Mechanical properties of the aluminum alloy used in this study (6061-T6).

Unit weight	Young's modulus	Poisson's ratio	Tensile yield stress	Tensile strength
$(\mathrm{kN/m^3})$	$E\,(\mathrm{GPa})$	ν	$f_{yk}\,(\mathrm{MPa})$	$f_{bk}\,(\mathrm{MPa})$
27	70	0.33	500	600

was embedded part in, part outside of the fault zone in the free field test. In all tests the height of soil deposit (H) was 200 mm. In order to observe the shear zone of faulting and the tested models, an acrylic plate window was installed on the front face of the fault box. A translating base and a wall on the left side of the container simulated the normal fault with downward movement of the base and were supported by a jack serving as an actuator. The maximum stroke height using this apparatus in the normal faulting mode was 50 mm, representing a 4 m fault-displacement at the prototype scale. The downward movement (h) was increased and the vertical displacement of the surface was recorded at each increment of 2.5 mm of fault throw (equivalent of 0.2 m at the prototype scale).

The centrifuge tests were conducted at the National Central University of Taiwan. The equivalent prototype dimensions were 80 times greater than the tested model. The dimensions of the centrifuge platform were 1000 mm × 550 mm × 720 mm (length × width ×height), and the maximum payload of the platform was 400 kg at an acceleration of 100g. Lee et al. (2006, 2012) previously reported the equipment details and NCU centrifuge specifications.

A list of the tested models is shown in Table 3. Following the two free-field tests, four further tunnel tests were conducted to investigate the effects of tunnel position, tunnel depth (with dimensionless ratio of H_c/D, which H_c is the burial depth of the tunnel (Overburden pressure) and D is the diameter of the tunnel), tunnel rigidity and soil relative density.

3. Results of the centrifuge tests

3.1 Free field test with D_r =50%

Before studying the fault–tunnel interaction, it was important to investigate the behavior of normal fault propagation in dry sandy soil layer without an underground tunnel. Consequently, test 1 was conducted as a free field test for a dry sand layer of 200 mm (16 m at equivalent prototype scale) in depth and 50% in relative density.

A selection of the digital images captured after test 1 is shown in Figure 3. Figure 3a shows the image of the final fault throw at h = 50 mm (h/H = 0.25, h = 4 m at equivalent prototype scale). Figure 3b shows the digitization on the image of the subsurface deformation profile at h = 50 mm. As seen in Figure 3b the maximum width between two fault rupture planes, visible on the soil surface, was 100 mm at the end of the test, and the final failure mechanism (right side rupture) has a displacement discontinuity with a dip angle (70◦), slightly steeper than what was applied at the base of the soil layer.

Figure 4 shows the surface deformation according to different fault throws. The fault outcropping position on the soil surface, at the end of the test (h/H = 0.25), is at X = 150 mm from fault tip shown as W parameter in the figure (W/H = 0.75). As seen in Figure 4, the surface fault outcropping starts to appear at X = 125 mm (at h/H = 0.05, or

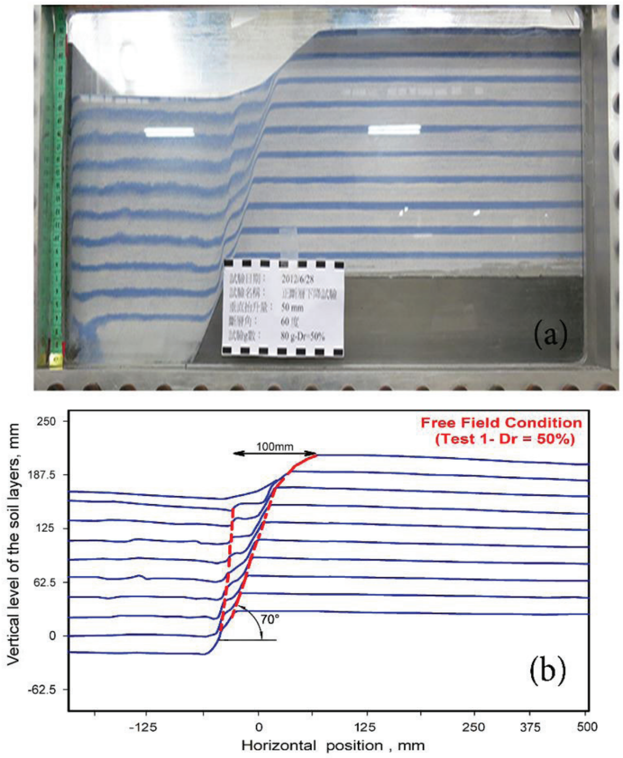

Figure 3. Free-field normal fault rupture (test 1- $D_r = 50\%$): (a) Images of deformed soil specimen for the final fault throw; h/H = 0.25 (b) Digitization on image of subsurface deformation profile at h/H = 0.25.

Table 3. Specifications of the performed centrifuge tests for normal fault rupture.

Normal Fault rupture						
Test Number	X (mm)	Y (mm)	H_c/D	D_r (%)	Tunnel Thickness (mm)	Tunnel Diameter (mm)
1	-	-	-	50	-	-
2	-	-	-	70	-	-
3	55	130	0.92	70	1.2	49.4
4	40	100	1.52	50	1.2	49.4
5	25	75	2.03	70	1.2	49.4
6	25	75	2.01	70	1.4	49.8

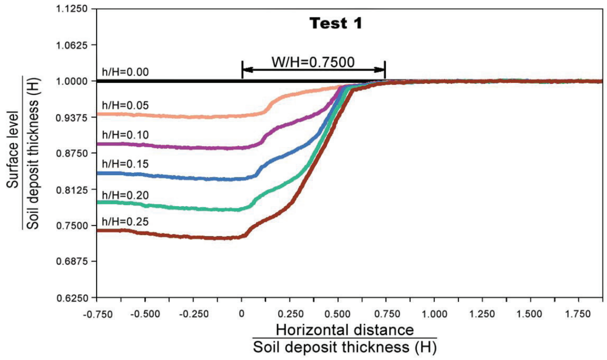

Figure 4. The ground surface level for the free-field condition for different fault throws (test 1- $D_r = 50\%$).

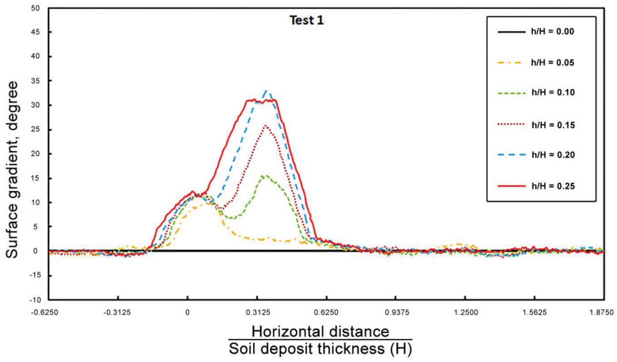

Figure 5. Surface gradient (ground surface inclination) against position for different fault throws (test 1).

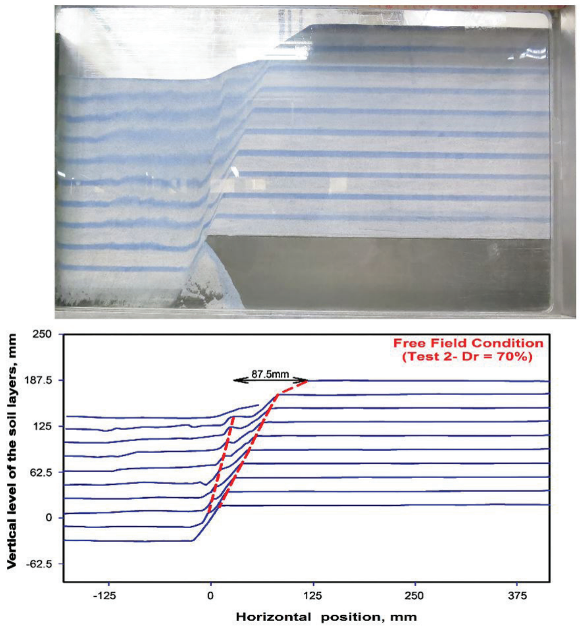

Figure 6. Free-field normal fault rupture (test 2- $D_r = 70\%$): Image of deformed soil specimen for the final fault throw; $h/H = 0.25$.

$h = 10$ mm at the model scale). A short vertical localization on the left side of the hanging wall and a longer localization (not very steep) on the right side of the soil surface observed. The same trend is observed with increasing the fault throw.

At the final vertical level of $h/H = 0.25$ (Figure 3), two rupture planes propagated in the soil layer. Figure 4 shows that propagating the fault to the ground surface at $h/H \approx 0.05$ deforms the soil surface. Finally, a fault outcropping h/H of larger than 0.10 strongly prevents further surface settlement and soil deformation, as the right and left side rupture planes are propagated up to the soil surface.

The results demonstrate that the fault propagation is a progressive phenomenon due to the ductility of the soil, as pointed out by prior researchers (e.g. Bransby et al., 2008a; Baziar et al., 2014, 2016, 2020). The initial localizations are likely to be due to high dilation behavior at small shear strains on the initial deformation of the soil layer.

Figure 5 shows that the surface gradient (ground surface inclination) width changes -75 mm $< x <$ 156 mm as the fault displacement increases. In addition, the position of the maximum surface gradient is almost constant from the base discontinuity as the fault throw increases.

3.2 Free field test with D_r = 70%

The typical pattern of the fault rupture propagation through a dry sandy soil deposit with $D_r = 70\%$ is illustrated in Figure 6. Compared with test 1, the left rupture in test 2 is observed to be closer to the right rupture when reaching to the ground surface. A low relative density soil enables the fault movement to spread out over a wider zone than a high relative density soil similar to the reverse fault tests conducted by Baziar et al. (2014, 2016).

On the other hand, a normal fault produced rupture planes within the model ground and was propagated up to the ground surface for both tests 1 and 2. As the relative density of ground model became greater, due to the reduction of void ratio and increasing of soil mass strength, the rupture planes appeared to be closer to each other.

The vertical components of the surface displacements, as observed by analyzing the LDT results, were shown in Figure 7. As seen in Figure 7, the surface displacement discontinuity is positioned at $W/H = 0.687$, giving an angle of 40° on the soil surface.

3.3 Interaction of the normal fault rupture with tunnel

In order to examine the interaction of the tunnel and normal fault rupture, four factors were considered including the possible tunnel presence, tunnel depth, soil relative density and tunnel rigidity. The results from the four tests are presented and discussed in the following sections.

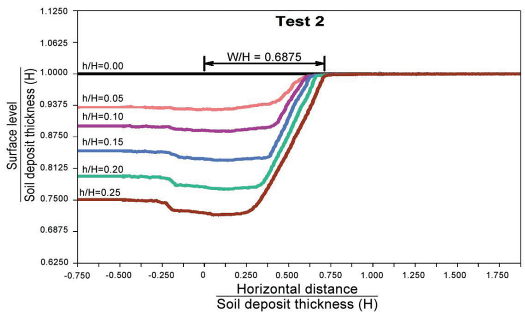

Figure 7. The ground surface level for the free-field condition for different fault throws (test 2- $D_r = 70\%$).

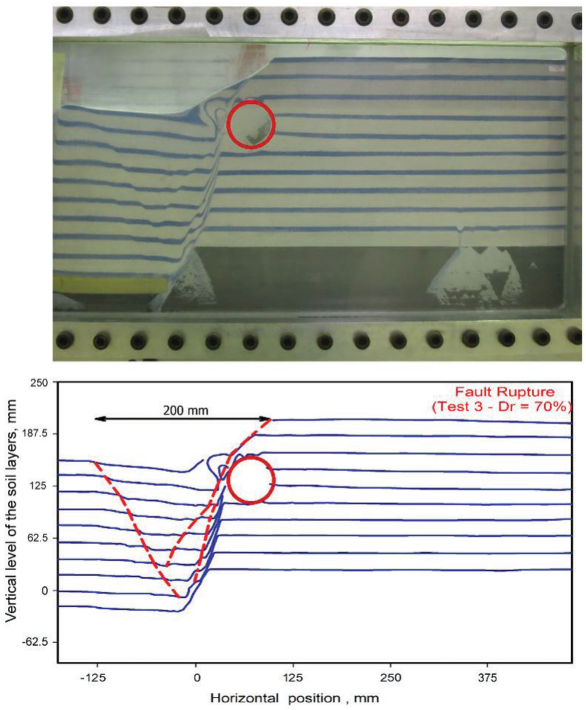

Figure 8. Tunnel test (test 3; $H_c/D = 0.92$; $X = 55$ mm; $Y = 130$ mm; $t = 1.2$ mm; $D = 49.4$ mm): Image of the deformed soil specimen for the final fault throw; $h/H = 0.25$ ($D_r = 70\%$).

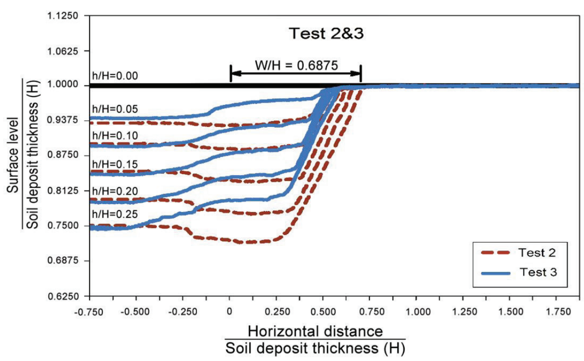

Figure 9. The ground surface level with the presence of tunnel for different fault throws (test 3- $D_r = 70\%$).

3.3.1 Effect of tunnel on fault rupture path and surface displacement: base case *X*=55 mm, *Y*=130 mm

A tunnel measuring D = 49.4 mm in diameter and t = 1.2 mm in thickness (D = 4.24 m in diameter and t = 0.24 m in thickness at equivalent prototype scale) was selected as the base condition (test 3 of Table 3). These parameters were selected as typical of those expected for a medium flexible tunnel considering centrifuge scaling law. The digital image, captured at the final stage of this test (h/H = 0.25), is shown in Figure 8. As seen in the figure, the tunnel was embedded near the soil surface. Figure 9 shows that there are two specified localizations for small fault displacements h/H = 0.05. The localization for larger fault displacements (h/H = 0.25) was found to be very steep, similar to that observed in the free-field test. However, an observable slip plane was formed far away from the footwall side. Due to the h/H = 0.25 fault displacement, the right side shear plane in Figure 8 did not reach to the soil surface, and the left side shear plane propagated from the left hand edge of the tunnel before reaching the soil surface. Contrary to the free field test, the main rupture at this fault displacement does not emerge at the ground surface. A third localization for the final fault throw of $h/H \approx 0.25$ appears to propagate upwards from the displacement singularity of the tunnel's left hand edge and reaches to the surface. As seen in Figure 8, the final fault rupture emerged from the left side of the tunnel, deviating the fault rupture from the free-field case. Due to the h/H = 0.25 fault movement in this test, the tunnel experienced significant rotation ($\Delta\theta$ = 26°) and horizontal ΔX = 3.8 mm (ΔX = 0.3 m at equivalent prototype scale) and vertical ΔY = 6.2 mm (ΔY = 0.5 m at equivalent prototype scale) movements. The final rotation and the final tunnel dimensions of X, Y have been measured by instrumentation after removing the sand layers very carefully at the end of each test for the final fault throw of 50 mm. The final tunnel movements also verified with the digital image analysis in the centrifuge laboratory.

Figure 8 also shows that the tunnel presence increased the distance between the shear planes to about 200 mm towards the hanging wall.

It can be observed from the Figure 9 that the position of the large deformation is very different from the deformations in the free field test. However, no further upward localization is observed on the hanging wall at h/H > 0.05, which is consistent with the mechanism shown in Figure 9. This suggests that once the final mechanism is mobilized, fault deviation prevents any further localization. According to Figure 9 obviously deviation of the rupture plane to the left or right side of the tunnel will depend crucially on the location of the tunnel relative to the imposed rupture plane.

3.3.2 Effect of burial depth on fault–tunnel interaction

To examine the effect of burial depth on fault–tunnel interaction, a centrifuge model test with test parameters similar to test 3, minus the tunnel location changed to $X = 25$ mm and $Y = 75$ mm ($X = 2$ m and $Y = 6$ m at equivalent prototype scale), was conducted in test 5. The ratio of H_c/D was increased from 0.92 to 2.03. As shown in Figure 10 (test 5), the burial depth of the tunnel strongly impacts the surface fault rupture and rupture path. In test 5, the tunnel location is close to the fault tip, and the right rupture reaches the soil surface. In test 3, the right rupture was placed 112.5 mm farther from the fault tip, whilst in test 5, the right rupture distance was increased to 126.5 mm farther from the fault tip.

However, for the final fault throw of $h/H = 0.25$ ($h = 50$ mm at model scale), three rupture planes were formed. Unlike test 3, the right side rupture plane reached the ground surface with the angle of about 40°, while the left side rupture plane didn't reach to the ground surface.

Ground surface measurements in Figure 10 indicate that the W/H is approximately 0.633 for the deep tunnel (H_c/D = 2.03), while the W/H for the shallow tunnel ($H_c/D = 0.92$) on the ground surface is 0.587. Furthermore, three distinct scarps appear on the ground surface at the final fault throw ($h/H = 0.25$).

The block within two main rupture planes is rotating clockwise and may also be subjected to some amount of shearing. This mechanism is facilitated by tunnel presence and could be considered as a force on the lining due to normal fault rupture. In other words, in normal faulting, increasing the height of the soil above the tunnel (H_c/D) is one of the factors that affect the propagation of the ruptures in the smaller zones towards the hanging wall, which is due to the tunnel presence.

The measurements also show that in test 3 with the ratio of H_c/D equal to 0.92 at $X = 55$ mm, $Y = 130$ mm, tunnel shifting after the ground rupture is smaller than that obtained for the tunnel with the ratio of H_c/D equal to 2.03 located at $X = 25$ mm, $Y = 100$ mm in test 5. The tunnel in test 5 is distinctly shifted downward with an almost 38.75 mm vertical displacement.

The differences in the tunnels and soil responses between tests 3 and 5 have revealed that tunnel location significantly influences the interaction between the fault and the tunnel. Further investigation is needed to study tunnel response in greater depth.

3.3.3 Effect of soil relative density (D_r) on fault–tunnel interaction

The soil parameters in test 4 were almost similar to those in test 3, with the exception that the soil relative density was reduced from 70% to 50% to examine the effect of soil relative density on fault–tunnel interaction (Figure 11). This density could be considered for loose to medium sand. Since the soil test with a relative density of 70% after two times repetition with a similar location of the tunnel to the test 4 has been failed, therefore test 4 has been compared to the test 3.

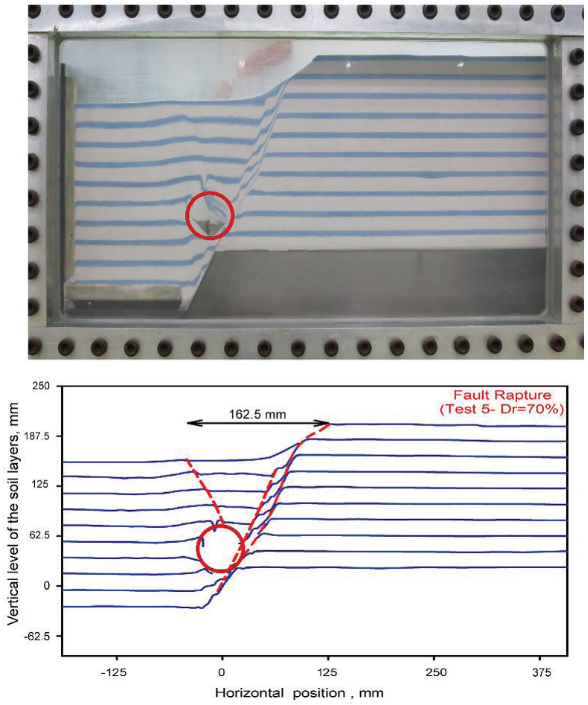

Figure 10. Effect of burial depth on fault tunnel interaction (test 5; H_c/D = 2.03; X = 25 mm; Y = 75 mm; t = 1.2 mm; D = 49.4 mm): Image of deformed soil specimen for the final fault throw; h/H = 0.25 ($D_r = 70\%$).

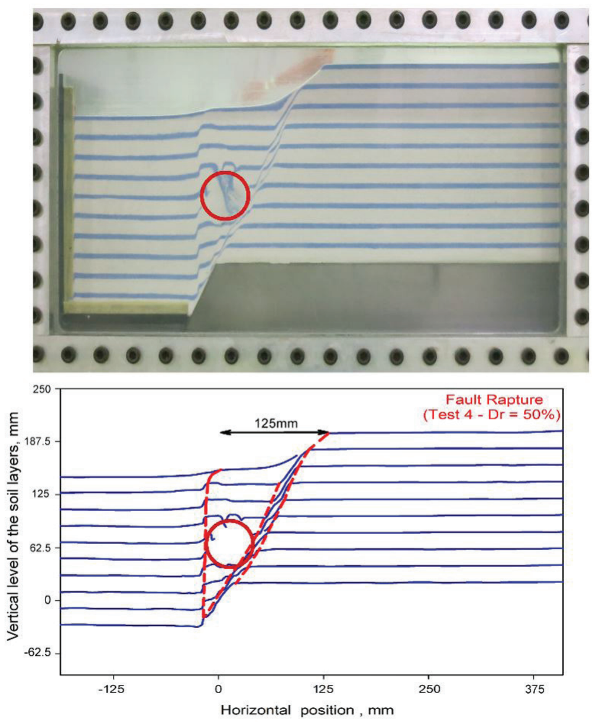

Figure 11. Effect of soil relative density on fault tunnel interaction (test 4; H_c/D = 1.52; X = 40 mm; Y = 100 mm; t = 1.2 mm; D = 49.4 mm): Image of deformed soil specimen for the final fault throw; h/H = 0.25 ($D_r = 50\%$).

As seen in Figure 11, the different relative density of the ground model with tunnel presence does not affect the number of rupture planes. The distance between the two rupture planes on the ground surface in test 4 with the ratio of H_c/D = 1.52 is about 125 mm. In addition, the tunnel in normal fault condition causes the fault movement to propagate to the ground surface and spread over a wider shear zone rather than a similar test with low relative density of dry sandy soil.

On the other hand, Figure 11 shows that the change in the model relative density as long as the tunnel straddled the line of the rupture plane gained from the free field tests (test 1 and test 2), has a different pattern of rupture plane developments. As seen, the model with 50% relative density generates three continuous rupture planes. While the left and right ruptures reach to the ground surface, the middle rupture does not reach to the soil surface. The underground tunnel causes the left rupture to bend and pass near the tunnel until it finally reaches the ground surface. Near the surface, the left rupture is inclined towards the footwall. Ground surface measurement also indicates that the ratio of W/H on the ground surface is approximately 0.75.

Although the final failure mechanisms of the lower relative density model were similar to those of the higher relative density model and a single strong discontinuity was deviated to the left edge of the tunnel, the high relative density model experienced a larger distance between the rupture planes. Once the final mechanism was formed ($h/H \approx 0.25$), the higher relative density model ($D_r = 70\%$) experienced a distance of 200 mm between the rupture planes, whereas the lower relative density model ($D_r = 50\%$) showed a distance of 125 mm. This distance between the rupture planes may cause considerable damage or even the collapse of the surface structures.

The vertical components of the surface deformations, measured by LDT analyses, are shown in Figure 12. This figure shows that the surface localization in the right side of the faulting zone for the $D_r = 50\%$ model is positioned 150 mm (W/H = 0.75) away from the fault tip and has a 47° angle on the soil surface, which is the same angle for the model with 70% soil relative density. Three distinct scarps were observed on the surface at the final fault throw of h/H = 0.20 (h = 40 mm at model scale) in test 3, while the number of scarps in test 4 at h/H = 0.20 were six. In addition, surface deformation of the lower relative density soil was more complex and less smooth than that of the higher relative density models. Due to the high number of localized deformations on the soil surface, is dangerous for surface structures.

3.3.4 Effect of tunnel rigidity (*EI*) on fault-tunnel interaction

To examine the effect of tunnel rigidity on fault–tunnel interaction, test 6 was conducted with similar conditions as test 5, except that the tunnel had slightly higher rigidity as a result of increased diameter and thickness. The reason for choosing a slight increase in the diameter and thickness of the tunnel was to examine more accurately the process of changes in how the fault planes deviate.

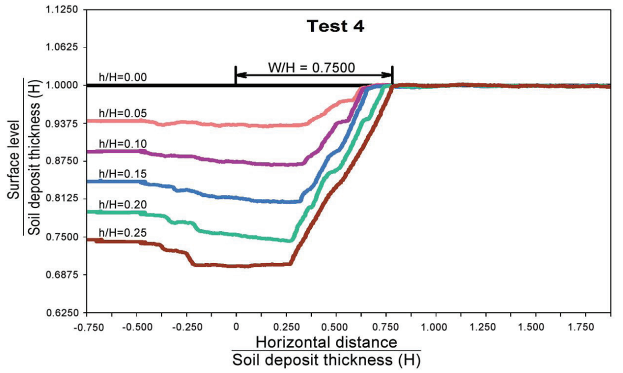

Figure 12. Effect of soil relative density on fault tunnel interaction: The ground surface level for different fault throws (test 4; H_c/D = 1.52; X = 40 mm; Y = 100 mm; t = 1.2 mm; D = 49.4 mm; $D_r = 50\%$).

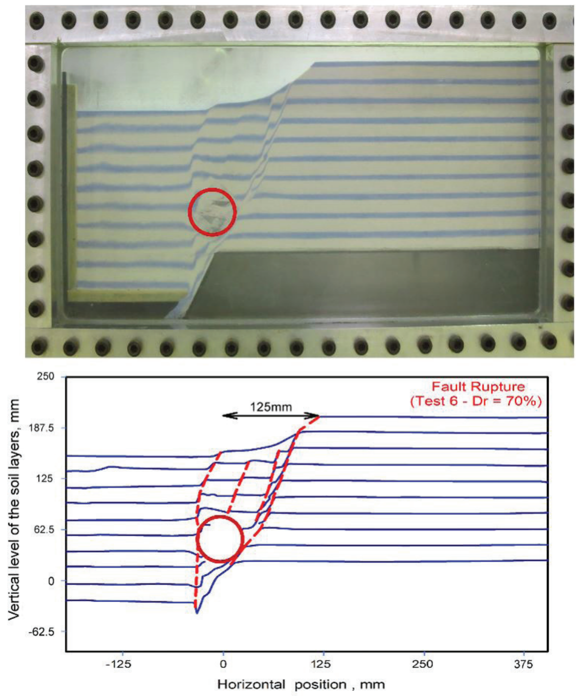

Figure 13. Effect of tunnel rigidity on fault tunnel interaction (test 6; H_c/D = 2.01; X = 25 mm; Y = 75 mm; t = 1.4 mm; D = 49.8 mm): Image of deformed soil specimen for the final fault throw; h/H = 0.25.

Images, captured at the final stage of test 6 and shown in Figure 13, indicate clear localization at the soil surface for h/H = 0.21 (h = 42.5 mm at the model scale) on the right side of the tunnel. The rupture path on the left side of the tunnel towards the hanging wall also showed to have clear localization, but this rupture was more inclined to the footwall near the soil surface. Two shear localizations were observed for the ruptures on the right side, near the ground surface. Therefore, it can be said that within the conditions of the tests performed, increasing the rigidity of a medium flexible tunnel changes the shear plane patterns and leaves the surface uneven. In fact, four shear planes were developed in the soil layer of the tunnel with higher rigidity. The distance between the two main rupture planes on the right side of the tunnel decreased as the tunnel rigidity was increased. The rigid tunnel increased the stresses placed on the soil beneath as a result of increasing both the shear strength and stiffness. It is obvious that parametric studies and repetition of different conditions will be needed to obtain general results. Test 6 showed that the left side of the rupture plane was also inclined towards the footwall, and the faulting zone was smaller than that of test 5. Figure 13 illustrate that an increase in the number of scarps on the soil surface, proving that fault localization, near the soil surface, increases in the presence of a tunnel with higher rigidity.

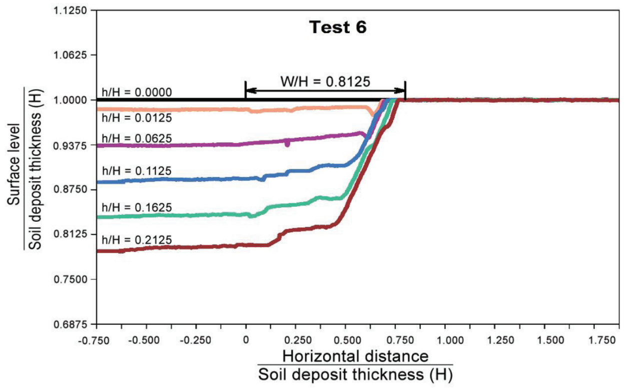

Figure 14. Effect of tunnel rigidity on fault tunnel interaction: The ground surface level for different fault throws (test 6; $H_c/D = 2.01$; $X = 25$ mm; $Y = 75$ mm; $t = 1.4$ mm; $D = 49.8$ mm).

Figure 14 also presents that an initial localization was formed at the base towards the footwall in test 6. The second localization (also see Figure 13) propagated upwards from the right side of the tunnel until it formed a continuous shear plane. The third rupture plane was created from the top of the tunnel to the soil surface, and the forth shear plane was deviated near the fault tip, before reaching the ground surface.

Tunnel rotation and movement for test 5 was qualitatively similar to the same values of test 6 at the final fault throw of $h/H = 0.25$. However, the final rotation of the medium flexible tunnel was 42°, as compared with the 38° of the tunnel with more rigidity. The difference in values could be explained by the slight differences in tunnel diameter or tunnel thickness.

The results of the rigid and medium flexible tunnels suggest that the kinematic restraint of the rigid tunnel alone is governed by the fault outcropping location and additional rupture plane developments.

4. Discussion and implications for design

Previous researchers have reported experimental studies, which helped to identify the most relevant aspects pertaining the normal faulting problem (Lee & Hamada, 2005; Bransby et al., 2008a; Loli et al., 2012). The results of the centrifuge model tests reported in the present study have confirmed the following findings:

Tunnels can deviate earthquake fault ruptures away from the fault tip and create additional rupture planes. Such phenomena should be considered for the design of surface structures.

In the case where the tunnel was located close to the surface, two fault rupture paths developed on the right side of the tunnel. Coming in contact with the tunnel, the rupture paths were bent by the underground tunnel; the two paths collided and a new rupture path was created in upward direction towards the hanging wall. This phenomenon led to the existence of three fault ruptures in the soil layer. The faulting zone at the soil surface affected a large area of the soil surface, which might be very dangerous for surface structures and should be considered in the design of such structures. The positions of the maximum surface gradient and surface displacement were changed as a result of the tunnel presence.

In the case where the tunnel was embedded in a deep soil layer, close to the fault tip and inside the faulting zone, the deep tunnel affected the displacement and deformation of the ground as well as the reduction of the faulting zone width within the overburden soil layer. Therefore, while increasing the tunnel depth minimized the faulting zone, the number of ruptures on the ground surface remained similar.

When the tunnel was embedded in loose sandy soil inside the faulting zone, the right and left side ruptures reached to the ground surface and the faulting zone width decreased. The number of scarps increased due to the presence of loose sandy soils. Further investigation is required to sufficiently understand the phenomena and develop general design methods.

Fault deviation in the case of the normal faulting was found to be more the result of tunnel rigidity than the kinematic restraint of the tunnel; a medium flexible tunnel behaved differently, compared with a higher rigidity tunnel. The rigid tunnel showed a different fault propagation pattern and the development of four shear planes. Movement and rotation of the tunnel cross section were similar to those of the medium flexible tunnels. The rigid tunnel increased the stresses placed on the soil beneath as a result of increasing both the shear strength and stiffness. The number of scarps on the ground surface also increased in the presence of the tunnel with higher rigidity. This suggests that the fault localization near the soil surface increases in the presence of a tunnel with high rigidity.

The results presented here indicate subtle interaction between the fault and the tunnel, which is sensitive to the burial depth of the tunnel, soil relative density and tunnel rigidity. All the tunnels, investigated in the present test series, caused the fault rupture path to deviate and create additional rupture planes, but each tunnel underwent different amounts of rotation. Such rotations are enough to damage or destroy the tunnels.

Figure 15 plots three components of tunnel displacement against fault throw. The vertical and horizontal displacements of the tunnel suggest that the occurrence of the fault throw causes the tunnel to move downward. This was confirmed by the measurements of the tunnel displacements and rotations obtained in the first and final steps of the tests.

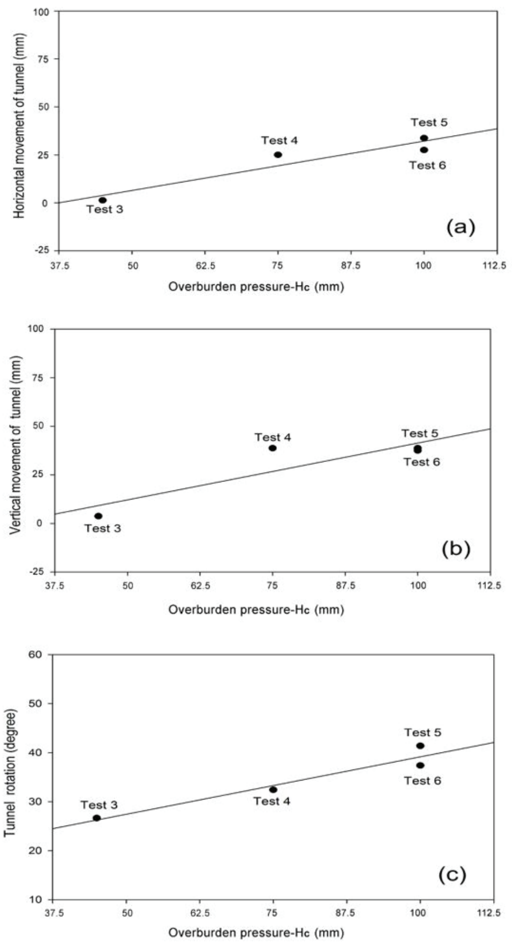

Figure 15. Tunnel movement against overburden pressure for the final fault throw; $h/H = 0.25$ (a) Horizontal movement of the tunnel (b) Vertical movement of the tunnel (c) Tunnel rotation.

Tunnel movement increases with increasing an overburden pressure (H_c) on the tunnel, which is embedded near the faulting zone. The tunnel rotation and movement for a low rigidity tunnel was qualitatively similar to the rigid one for the final fault throw ($h/H = 0.25$).

Table 4 compares the characteristics of the ruptures, both with and without the tunnel presence after the final fault throw by referring to the test 1 and test 2. As evident, while tunnel presence decreased the maximum surface gradient, it increased the number of scarps on the ground surface and the number of ruptures in the soil layer. Also it can be observed with the presence of tunnel when the tunnel overburden pressure (H_c) increased, the width of the distorted outcrop (W) and the number of scarps increased. As well at the same overburden depth, with increasing the tunnel rigidity, the width of distorted surface (W), the number of scarps and the number of ruptures increased.

5. Conclusions

This research aimed to analyze the interaction between normal faulting and tunnel in dry sandy soils for the first time using NCU geotechnical centrifuge equipment. After understanding this phenomenon, using present centrifuge tests, and then numerical and parametric studies some design recommendations can be documented. In this study the propagation of a normal fault in the free-field conditions was similar to that observed by previous researchers. A progressive localization of shear deformation running from the base of the soil layer up to the ground surface was observed. Once this localization reached to the soil surface, no further deformation of the soil occurred outside the faulting zone. The following results were obtained from the conditions of the centrifuge tests performed:

1. Tunnels caused the earthquake fault ruptures to deviate away from the paths observed in the free field tests and also created additional rupture planes (similar to the reverse fault tests conducted by the researchers of the present paper (Baziar et al., 2014, 2016, 2020)). Although this test and the aforementioned reverse fault tests confirm that fault deviation is possible due to the presence of a shallow tunnel, a single test

Table 4. Characteristics of ruptures with and without the presence of tunnel after the final fault throw (h = 50mm).

Test Condition	Test Number	H_c/D	W/H	Number of ruptures	Number of scraps	Maximum surface gradient (degree)	Affected width on the soil surface /H
Free field (D_r = 50%)	1	-	0.75	2	2	33	1.156
Free field (D_r = 70%)	2	-	0.687	2	2	37	1.218
Effect of shallow tunnel	3	0.92	0.587	3	3	35	1.250
Effect of deep tunnel	5	2.03	0.633	3	4	30	1.062
Effect of soil density	4	1.52	0.75	3	6	30	1.250
Effect of tunnel rigidity	6	2.01	0.812	4	5	29	1.062

is not enough to validate such claim. Consequently, further tests were carried out to investigate whether the deviation was caused by tunnel presence. Because of centrifuge tests are too expensive, more parametric studies are needed by numerical analysis, which could be verified with the test results of normal faulting;

2. Embedding the tunnel in a soil layer increased the number of scarps and differential displacements (slope) of the ground surface. This increase of differential displacement was highlighted with a larger increase in the fault displacement;
3. The position of the fault relative to the tunnel appeared to be considered in the interaction response. Hence, a range of possible fault positions should be considered in the design and in the parametric studies if the fault position is uncertain;
4. Surface deformation of the lower relative density soil was more complex and less smooth than that of the higher relative density models. Due to the high number of localized deformations on the soil surface, is dangerous for surface structures. The number of scarps increased due to the presence of loose sandy soils. Further parametric studies are required to sufficiently understand the phenomena and develop general design methods;
5. All the tested tunnels underwent significant rotation and displacement. This rotation appeared to increase with increasing the burial depth;
6. A rigid tunnel was also able to deviate the earthquake fault ruptures from the paths observed in the medium flexible tunnel test. The rotation and displacement of both rigid and flexible tunnels were almost similar;
7. For all of the tunnels investigated here, the additional fault rupture plane compared with the free field condition was developed on the left side of the tunnel.

Declaration of interest

The authors declare that they have no known competing financial interests or personal relationships that could have appeared to influence the work reported in this paper.

Authors' contributions

Ali Nabizadeh: supervision, writing - review & editing. Alireza Seghateh Mojtahedi: writing - original draft, writing - review & editing, data curation.

List of symbols

α	Dip angle of the fault plane
H_c	Burial depth of tunnel (overburden pressure)
D	Diameter of the tunnel
t	Thickness of the tunnel
D_r	Relative density
E	Young's modulus
G	Shear modulus
G_s	Specific gravity
ϕ	Friction angle
H	Height of soil deposit
h	Vertical offset of the fault
γ	Unit weight
W	Distance from the fault tip to the location of the right side surface outcropping

References

Agalianos, A., Coquereaumont, O.D.C.D., & Anastasopoulos, I. (2020). Rigid slab foundation subjected to strike-slip faulting: mechanisms and insights. *Geotechnique*, 70(4), 354-373. http://dx.doi.org/10.1680/jgeot.18.P.280.

Ahmed, W., & Bransby, M.F. (2009). Interaction of shallow foundations with reverse faults. *Journal of Geotechnical and Geoenvironmental Engineering*, 135(7), 914-924. http://dx.doi.org/10.1061/(ASCE)GT.1943-5606.0000072.

Anastasopoulos, I. (2005). *Fault rupture-soil-foundation-structure interaction* [Ph.D. dissertation]. School of Civil Engineering, National Technical University.

Anastasopoulos, I., & Gazetas, G. (2007a). Foundation-structure systems over a rupturing normal fault: Part I. Observations after the Kocaeli 1999 earthquake. *Bulletin of Earthquake Engineering*, 5(3), 253-275. http://dx.doi.org/10.1007/s10518-007-9029-2.

Anastasopoulos, I., & Gazetas, G. (2007b). Foundation-structure systems over a rupturing normal fault: part II. Analysis of the Kocaeli case histories. *Bulletin of Earthquake Engineering*, 5(3), 277-301. http://dx.doi.org/10.1007/s10518-007-9030-9.

Anastasopoulos, I., Gazetas, G., Bransby, M.F., Davies, M.C.R., & Elnahas, A. (2007). Fault rupture propagation through sand: finite-element analysis and validation through centrifuge experiments. *Journal of Geotechnical and Geoenvironmental Engineering*, 133(8), 943-958. http://dx.doi.org/10.1061/(ASCE)1090-0241(2007)133:8(943).

Anastasopoulos, I., Kourkoulis, R., Gazetas, G., & Tsatsis, A. (2013). Interaction of piled foundation with a rupturing normal fault. *Geotechnique*, 63(12), 1042-1059. http://dx.doi.org/10.1680/geot.12.P.114.

Baziar, M.H., Nabizadeh, A., & Jabbary, M. (2012). Evaluation of Fault-foundation interaction using numerical studies. In *Proceedings of the 15th World Conference on Earthquake Engineering*, Lisbon, Portugal.

Baziar, M.H., Nabizadeh, A., & Jabbary, M. (2015). Numerical modeling of interaction between dip slip fault and shallow foundation. *Bulletin of Earthquake Engineering*, 13(6), 1613-1632. http://dx.doi.org/10.1007/s10518-014-9690-1.

Baziar, M.H., Nabizadeh, A., Khalafian, N., Lee, C.J., & Hung, W.Y. (2020). Evaluation of reverse faulting effects on the mechanical response of tunnel lining using centrifuge tests and numerical analysis. *Geotechnique*, 70(6), 490-502. http://dx.doi.org/10.1680/jgeot.18.P.019.

Baziar, M.H., Nabizadeh, A., Jung Lee, C., & Yi Hung, W. (2014). Centrifuge modeling of interaction between reverse faulting and tunnel. *Soil Dynamics and Earthquake Engineering*, 65, 151-164. http://dx.doi.org/10.1016/j.soildyn.2014.04.008.

Baziar, M.H., Nabizadeh, A., Mehrabi, R., Lee, C.J., & Hung, W.Y. (2016). Evaluation of underground tunnel response to reverse fault rupture using numerical approach. *Soil Dynamics and Earthquake Engineering*, 83, 1-17. http://dx.doi.org/10.1016/j.soildyn.2015.11.005.

Bransby, M.F., Davies, M.C.R., Elnahas, A., & Nagaoka, S. (2008a). Centrifuge modeling of normal fault-foundation interaction. *Bulletin of Earthquake Engineering*, 6(4), 585-605. http://dx.doi.org/10.1007/s10518-008-9079-0.

Bransby, M.F., Davies, M.C.R., Elnahas, A., & Nagaoka, S. (2008b). Centrifuge modeling of reverse fault-foundation interaction. *Bulletin of Earthquake Engineering*, 6(4), 607-628. http://dx.doi.org/10.1007/s10518-008-9080-7.

Bray, J.D., & Kelson, K.I. (2006). Observations of surface fault rupture from the 1906 earthquake in the context of current practice. *Earthquake Spectra*, 22(52), 569-589. http://dx.doi.org/10.1193/1.2181487.

Cai, Q.P., Peng, J.M., Ng, C.W.W., Shi, J.W., & Chen, X.X. (2019). Centrifuge and numerical modelling of tunnel intersected by normal fault rupture in sand. *Computers and Geotechnics*, 111, 137-146. http://dx.doi.org/10.1016/j.compgeo.2019.03.010.

Faccioli, E., Anastasopoulos, I., Gazetas, G., Callerio, A., & Paolucci, R. (2008). Fault rupture–foundation interaction: selected case histories. *Bulletin of Earthquake Engineering*, 6(4), 557-583. http://dx.doi.org/10.1007/s10518-008-9089-y.

Ghadimi Chermahini, A., & Tahghighi, H. (2019). Numerical finite element analysis of underground tunnel crossing an active reverse fault: a case study on the Sabzkouh segmental tunnel. *Geomechanics and Geoengineering*, 14(3), 155-166. http://dx.doi.org/10.1080/17486025.2019.1573323.

Johansson, J., & Konagai, K. (2004). Fault induced permanent ground deformations-Simulations and experimental verification. In *Proceedings of the 13th World Conference on Earthquake Engineering* (Paper No. 479), Vanvouver, B.C., Canada.

Johansson, J., & Konagai, K. (2006). Fault induced permanent ground deformations an experimental comparison of wet and dry soil and implications for buried structures. *Soil Dynamics and Earthquake Engineering*, 26(1), 45-53. http://dx.doi.org/10.1016/j.soildyn.2005.08.003.

Johansson, J., & Konagai, K. (2007). Fault induced permanent ground deformations: experimental verification of wet and dry soil, numerical findings' relation to field observations of tunnel damage and implications for design. *Soil Dynamics and Earthquake Engineering*, 27(10), 938-956. http://dx.doi.org/10.1016/j.soildyn.2007.01.007.

Kelson, K.I., Kang, K.H., Page, W.D., Lee, C.T., & Cluff, L.S. (2004). Representative styles of deformation along the Chelungpu fault from the 1999 Chi-Chi (Taiwan) earthquake: geomorphic characteristics and responses of man- made structures. *Bulletin of the Seismological Society of America*, 91(5), 930-952. http://dx.doi.org/10.1785/0120000741.

Kiani, M., Akhlaghi, T., & Ghalandarzadeh, A. (2016). Experimental modeling of segmental shallow tunnels in alluvial affected by normal faults. *Tunnelling and Underground Space Technology*, 51, 108-119. http://dx.doi.org/10.1016/j.tust.2015.10.005.

Konagai, K., et al. (2007). *Annual report of the research and development program for resolving Critical Issues, Earthquake damage in active-faulting areas: creation of a comprehensive data archive and suggestions for its application to remedial measures for civil infrastructure systems*. Special Coordination Funds for Promoting Science and Technology, Ministry of Education, Culture, Sports, Science and Technology.

Lee, C.J., Wang, C.R., Wei, Y.C., & Hung, W.Y. (2012). Evolution of the shear wave velocity during shaking modeled in centrifuge shaking table tests. *Bulletin of Earthquake Engineering*, 10(2), 401-420. http://dx.doi.org/10.1007/s10518-011-9314-y.

Lee, C.J., Wu, B.R., Chen, H.T., & Chiang, K.H. (2006). Tunnel stability and arching effects during tunneling in soft clayey soil. *Tunnelling and Underground Space Technology*, 21(2), 119-132. http://dx.doi.org/10.1016/j.tust.2005.06.003.

Lee, W.J., & Hamada, M. (2005). An experimental study on earthquake fault rupture propagation through a sandy soil deposit. *Journal of Structure Engineering and Earthquake Engineering*, 22, 1-13. http://dx.doi.org/10.2208/jsceseee.22.1s.

Lin, M.L., Chung, C.F., Jeng, F.S., & Yao, T.C. (2007). The deformation of overburden soil induced by thrust faulting and its impact on underground tunnels. *Engineering Geology*, 92(3-4), 110-132. http://dx.doi.org/10.1016/j.enggeo.2007.03.008.

Loli, M., Bransby, M.F., Anastasopoulos, I., & Gazetas, G. (2012). Interaction of caisson foundations with a seismically rupturing normal fault: centrifuge testing versus numerical simulation. *Geotechnique*, 62(1), 29-43. http://dx.doi.org/10.1680/geot.9.P.153.

Loukidis, D., Bouckovalas, G., & Papadimitriou, A. (2009). Analysis of fault rupture propagation through uniform soil cover. *Soil Dynamics and Earthquake Engineering*, 29(11-12), 1389-1404. http://dx.doi.org/10.1016/j.soildyn.2009.04.003.

Mortazavi Zanjani, M., & Soroush, A. (2019). Numerical modelling of fault rupture propagation through layered sands. *European Journal of Environmental and Civil*

Engineering, 23(9), 1139-1155. http://dx.doi.org/10.1080/19648189.2017.1344148.

Naeij, M., Soroush, A., & Javanmardi, Y. (2019). Numerical investigation of the effects of embedment on the reverse fault-foundation interaction. *Computers and Geotechnics*, 113, 103098. http://dx.doi.org/10.1016/j.compgeo.2019.103098.

Oettle, N.K., & Bray, J.D. (2013). Fault rupture propagation through previously ruptured soil. *Journal of Geotechnical and Geoenvironmental Engineering*, 139(10), 1637-1647. http://dx.doi.org/10.1061/(ASCE)GT.1943-5606.0000919.

Prentice, C., & Ponti, D. (1997). Coseismic deformation of the Wrights tunnel during the 1906 San Francisco earthquake: A key to understanding 1906 fault slip and 1989 surface ruptures in the southern Santa Cruz Mountains, California. *Journal of Geophysical Research*, 102(B1), 635-648. http://dx.doi.org/10.1029/96JB02934.

Rasouli, H., & Fatahi, B. (2019). A novel cushioned piled raft foundation to protect buildings subjected to normal fault rupture. *Computers and Geotechnics*, 106, 228-248. http://dx.doi.org/10.1016/j.compgeo.2018.11.002.

Russo, M., Germani, G., & Amberg, W. (2002). Design and construction of large tunnel through active faults: a recent application. In *Proceedings of the International Conference of Tunnelling and Underground Space Use* (pp. 16-18), Istanbul, Turkey.

Tali, N., Lashkaripour, G.R., Hafezi Moghadas, N., & Ghalandarzadeh, A. (2019). Centrifuge modeling of reverse fault rupture propagation through single-layered and stratified soil. *Engineering Geology*, 249, 273-289. http://dx.doi.org/10.1016/j.enggeo.2018.12.021.

Thebian, L., Najjar, S., Sadek, S., & Mabsout, M. (2018). Numerical investigation of dip-slip fault propagation effects on offshore seabed sediments. *Engineering Geology*, 237, 149-167. http://dx.doi.org/10.1016/j.enggeo.2018.02.008.

Tsai, C.-C., Meymand, P., Dawson, E., & Wong, S.A. (2015). Behaviour of segmental pipeline protective vaults subjected to fault offset. *Structure and Infrastructure Engineering*, 11(10), 1369-1389. http://dx.doi.org/10.1080/15732479.2014.964733.

Tsatsis, A., Loli, M., & Gazetas, G. (2019). Pipeline in dense sand subjected to tectonic deformation from normal or reverse faulting. *Soil Dynamics and Earthquake Engineering*, 127, 105780. http://dx.doi.org/10.1016/j.soildyn.2019.105780.

Ulusay, R., Aydan, O., & Hamada, M. (2001). The behavior of structures built on active fault zones: examples from the recent earthquakes in Turkey. In *Workshop on Seismic Fault-Induced Failures: Possible Remedies for Damage to Urban Facilities* (pp. 1-26), Japan.

Wang, L. (2008). The characteristics of disasters induced by the Wenchuan Mw 8.0 Earthquake. In S. Prakash (Ed.), *International Conference on Case Histories in Geotechnical Engineering*, Washington, DC.

Wang, W.L., Wang, T.T., Su, J.J., Lin, C.H., Seng, C.R., & Huang, T.H. (2001). Assessment of damages in mountain tunnels due to the Taiwan Chi-Chi Earthquake. *Tunnelling and Underground Space Technology*, 16(3), 133-150. http://dx.doi.org/10.1016/S0886-7798(01)00047-5.

Yilmaz, M.T., & Paolucci, R. (2007). Earthquake fault rupture-shallow foundation interaction in undrained soils: a simplified analytical approach. *Earthquake Engineering & Structural Dynamics*, 36(1), 101-118. http://dx.doi.org/10.1002/eqe.625.

Soils and Rocks

An International Journal of Geotechnical and Geoenvironmental Engineering

www.soilsandrocks.com

ISSN 1980-9743
ISSN-e 2675-5475

Soil-structure interaction analysis in reinforced concrete structures on footing foundation

Yago Ryan Pinheiro dos Santos[1#], Maria Isabela Marques da Cunha Vieira Bello[1], Alexandre Duarte Gusmão[2], Jonny Dantas Patricio[3]

Article

Keywords
Soil-structure interaction
Foundations
Rock mass
Settlements
Field instrumentation

Abstract

Soil-structure interaction (SSI) evaluates how soil or rock deformability imposes on the structure a different load path in a hypothesis of fixed supports, altering the loads acting on the structural elements and the ground. This paper discusses the results of the SSI effects in two buildings with a reinforced concrete structure and shallow foundations in a rock mass. The settlements were monitored by field instrumentation in five stages of their construction, making it possible to estimate through interpolation curves the settlements values of some points. The numerical modeling and structural analysis of the buildings were obtained for two different cases of soil-structure interaction. The structure was considered having fixed supports (non-displaceable) and displaceable supports (with stiffness spring coefficients K). The results reveals the occurrence of SSI effects, with a load redistribution between the columns that occurred differently for the different construction stages. Structural modeling proved to be quite representative, pointing to higher vertical load values than the average values present in building edge zones, which contradicts the conventional idea that central columns are more loaded than the edge columns. The soil-structure interaction analyses resulted in different behaviors regarding both towers; pointing out that low settlements and building symmetry in plan minimize the effects of interaction, with no tendency of load redistribution between columns as the structure rigidity increases, as construction development.

1. Introduction

Reinforced concrete structure projects are elaborated usually considering three distinct parts: the superstructure, composed of slabs, beams, and columns; the infrastructure, consisting of the foundation elements (shallow or deep), and finally, soil or rock mass, which support the requests coming from superstructure. The interaction between these parts is the soil-structure interaction (SSI), whose mechanism describes the structural system performance.

The principal consideration of SSI studies in buildings is the adoption of flexible supports. The conventional approaches to determine settlement has been estimated based on elastic theory.

Shallow spread footings are generally designed as foundations at rock sites (Chaudhary, 2016). Individual footing foundation settlement analysis usually assumed the soil/rock to consist of independent linear springs (Winkler's hypothesis) or uses Elastic Continuum Method (Winkler, 1867).

Meyerhof (1953), Morris (1966), Lee & Brown (1972), and Poulos (1975) proposed SSI analysis. Factors such as floor numbers, construction processes and sequence, building shape and other effects related to soil/rock and structure behavior, contribute to the mechanisms of this mutual influence (Gusmão, 1994).

Danziger et al. (2005), Mota (2009), Savaris et al. (2011), Santos (2016) analyzed real cases of buildings through monitored settlements. The settlements measurement along different construction stages enables to observe loads redistribution between central and the edge reinforced concrete columns. In general, there was a tendency of load relief in the central column and overload the edge column, after considerations of SSI; Rosa et al. (2018) also point out that the greater load and settlement redistribution are usually observed more effectively at the beginning of construction, when the building structure stiffness tends to increase until the first floors.

[#]Corresponding author. E-mail address: yago_ryan@hotmail.com
[1]Universidade Federal de Pernambuco, Departamento de Engenharia Civil, Caruaru, PE, Brasil.
[2]Universidade de Pernambuco, Departamento de Engenharia, Recife, PE, Brasil.
[3]Universidade Federal de Campina Grande, Departamento de Engenharia Civil, Campina Grande, PB, Brasil.

Submitted on September 29, 2020; Final Acceptance on May 5, 2021; Discussion open until August 31, 2021.

https://doi.org/10.28927/SR.2021.058020

Santos & Corrêa (2018) also assessed load redistribution caused by SSI among foundations elements in a building with concrete walls by means of iterative numerical analyses, and observed a tendency of load transfer to supports under greater settlements to supports with lower settlements, and finally a uniformity of settlements among columns.

Other analyses, such as the dynamic effects of vibrations and seismicity combined with soil-structure interaction in buildings (Papadopoulos et al., 2017; Amini et al., 2018; Gómez-Martínez et al., 2020) point to the idea that the SSI mechanisms play a considerable role on behavior of buildings, directly influencing the propagation of vibrations throughout the structural elements; therefore, the consideration of SSI is extremely important for controlling the performance of structures when subjected to these events.

Considering the importance of the subject concerning economic, safety, performance and durability factors, the present paper has the objective to contribute to the study of soil-structure interaction by the analysis of the SSI effects to represent the behavior of a reinforced concrete structure with spread footings foundation.

2. Characterization of the study area

The study considered two residential buildings with reinforced concrete frame structures, called “tower A” and “tower B”, located in Caruaru, Pernambuco, Brazil. Tower A is 32-floor and tower B is 35-floor. The geological-geotechnical investigation comprised 14 boreholes performed by rotary-percussion drilling. The ground boreholes at tower A location reached depths between 5.27 m and 11.30 m, with a light-colored shallow soil layer composed of sand and gravel, followed by a light-colored altered rock layer. The tower B boreholes have depths between 3.80 m and 10.80 m, with a superficial layer of a sandy embankment and light sandy soil with gravels, followed by altered light-colored rock.

Cataclastic metamorphic rock was observed on depths between 0.40 m and 11.30 m the Tower A location, and between 0.50 m and 10.80 m on the Tower B location. The Rock Quality Designation (RQD) values were higher than 75%, being classified as a good to excellent recovery RQD, and absence of water table. Figures 1a and 1b show the representative geotechnical profile of towers A and B, respectively. Unconfined compressive strength test was performed on eight cylindrical rock samples with dimensions of 5.4 cm × 10.8 cm (diameter × height), extracted from different depths of drilling. The samples presented unconfined compression strength (UCS) between 83.0 MPa and 175.0 MPa, with an average value of 110.90 MPa, a standard deviation of 33.13 MPa, and a coefficient of variation (COV) of 30%.

Figure 2 shows the foundation plan of towers A and B, and the location of their respective boreholes. Due to the ground characteristics, shallow spread and combined footings foundation. All footings were designed for allowable pressure of 1040 kPa for the case where it considers the combination of permanent loads and wind action.

3. Field instrumentation for building settlements monitoring

The settlements were monitored during buildings construction by field instrumentation. Ten topographic monitoring bolts were installed on all 22 and 18 columns located on the ground floor of towers A and B, respectively. Readings were taken at five different construction stages. The first reading was taken when bolts were installed (reading 0), and the last reading was performed at a stage near to the construction end. Table 1 shows the construction stages of towers A and B at the time of the readings.

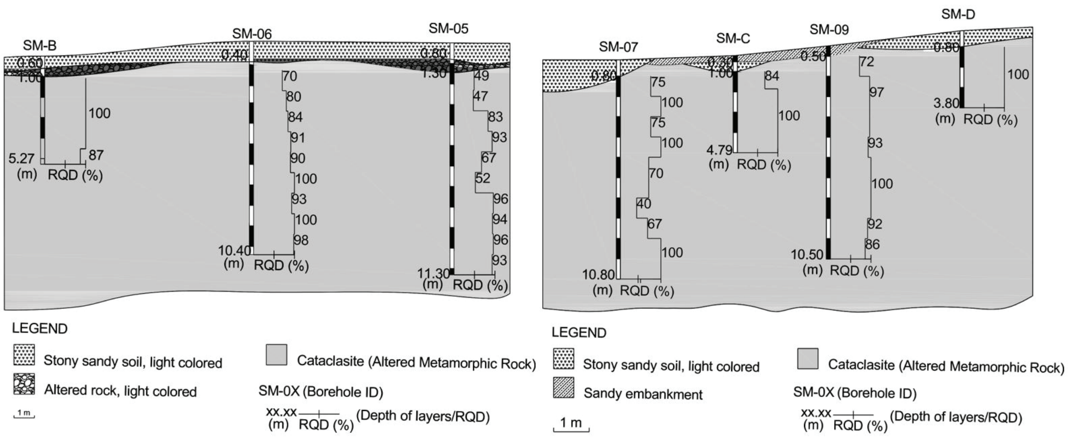

(a) (b)

Figure 1. Representative geotechnical underground profiles: towers (a) A and (b) B.

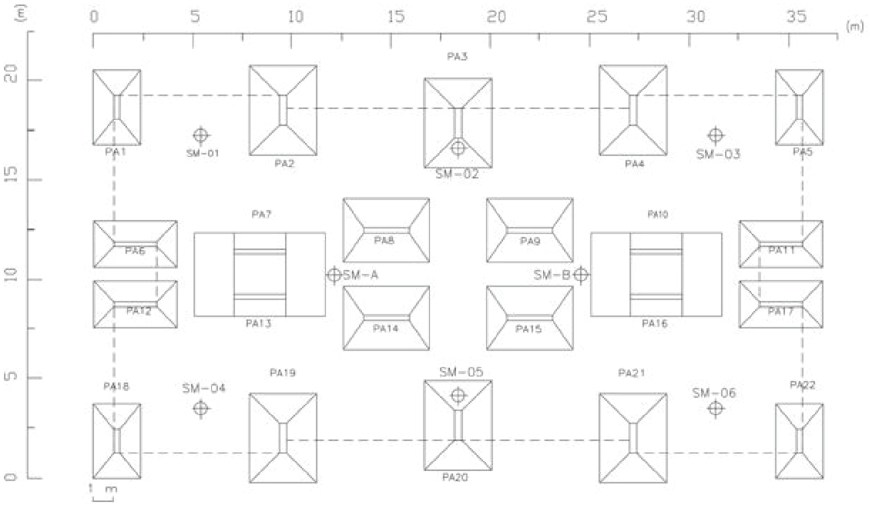

(a)

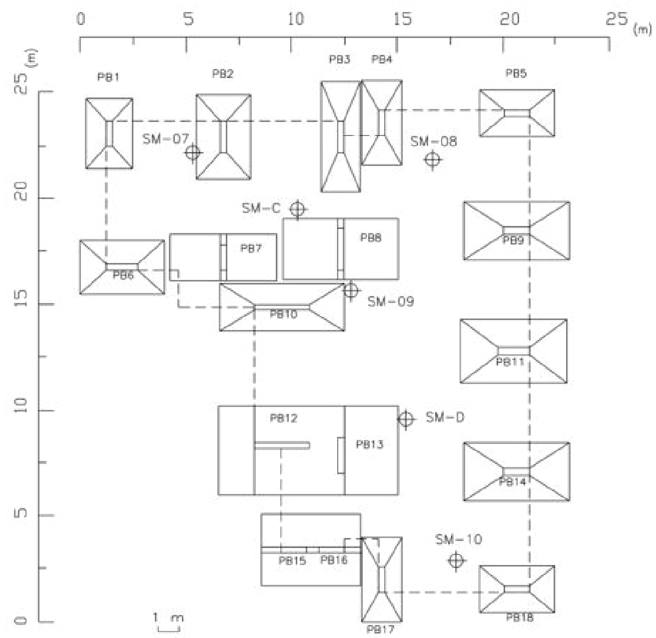

(b)

Figure 2. Location of the rotary-percussion drilling and plan of the shallow foundation: (a) tower A and (b) tower B.

Table 1. Construction stages of towers A and B.

Reading n.		0	1	2	3	4
Time passed (days)		0	265	355	530	708
Stage	TOWER A	ground floor slab	7th floor type subfloor	5th floor-type inner wall cladding	5th floor-type external wall cladding	32th floor-type ceiling
	TOWER B	ground floor slab	1st floor-type inner wall cladding	9th floor-type inner wall cladding	5th floor-type ceiling	34th floor-type ceiling

4. Structural modeling of buildings

The structural model of both buildings was constructed using TQS software® (TQS, 2021) considering initially fixed supports (non-displaceable) to determine the support reactions in each stage of the construction of tower A and B (Table 2 and 3, respectively). After, the support reactions were related to monitored settlement to determine spring coefficients K. Two analyses of the support springs was done of soil-structure interaction, called SSI 1 and SSI 2.

In SSI 1 analysis, spring coefficients at the different construction stages (K_i) were obtained by the ratio of the vertical support reaction (Fz_i) to the monitored settlement by each support (δ_i) (Equation 1). The average spring coefficient of the structural supports for each construction stage (K_m) was determined in SSI 2 analysis. This coefficient was obtained by the ratio of the vertical support reaction average of the structure for each construction stage (Fz_m) to the average monitored settlement δ_m (Equation 2).

$$K_i = \frac{Fz_i}{\delta_i}\left(kN / m\right) \tag{1}$$

$$K_m = \frac{Fz_m}{\delta_m}\left(kN / m\right) \tag{2}$$

For each monitored settlement reading, the elastic supports of the structure had an associated K value that was fed into the TQS software® for both analyses, corresponding to each foundation element. Then, the superstructure will respond according to the SSI mechanisms, with its flexible supports, obtaining values of resulting loads after interaction.

5. Results and discussion

Results of settlement estimation, analysis of soil-structure interaction considering foundation on rock are presented and discussed.

5.1 Buildings settlement analysis

Figure 3a and 3b show the settlements evolution with time of tower A and B, respectively.

Settlement readings no. 1, 2, and 3 of tower A shows the greatest deformations are observed around the PA20 column, where the highest settlements of these readings were recorded (9.84 mm, 14.48 mm and 18.37 mm). The settlement reading no. 4 showed the greatest deformation in lower right portion of the ground, which was observed surrounding PA21 column (17.38 mm). Settlement reduction for PA20 in stage 4 may be related to some reading error during monitoring; however, it was decided to proceed the analysis with this value.

Analyzing the tower B, readings no. 1, 2 and 3 show a more significant deformation surrounding PB03 and PB04 (upper edge) and PB11 (right edge), where settlement

Table 2. Support reactions (loads) of tower A.

Column	Support reactions - loads (kN)			
	Stage 1	Stage 2	Stage 3	Stage 4
PA01	3072.49	4462.57	5922.30	6897.41
PA02	5229.71	7731.26	10285.79	11755.32
PA03	5283.67	7935.31	10783.15	12461.64
PA04	5202.24	7649.84	10168.07	11623.87
PA05	3049.93	4266.37	5634.86	6564.85
PA06	3035.21	4543.99	6147.93	7036.71
PA07	4112.35	6679.63	9151.75	10129.81
PA08	4842.22	7809.74	10889.10	12076.11
PA09	4574.4	7125.00	10083.70	11196.15
PA10	3941.66	6184.22	8525.87	9422.51
PA11	3239.26	4905.98	6759.09	7711.64
PA12	3202.97	4746.08	6389.25	7293.74
PA13	4431.18	7091.65	9675.60	10695.84
PA14	4937.37	7929.42	10741.95	11870.10
PA15	4725.48	7369.27	10059.17	11077.45
PA16	3693.47	5707.46	7825.44	8619.07
PA17	3705.24	5521.07	7515.44	8549.42
PA18	3332.46	4853.01	6279.38	7268.23
PA19	5937.99	8721.09	11351.15	12894.26
PA20	5727.08	8491.54	11245.20	12856.99
PA21	5822.24	8580.81	11205.96	12743.19
PA22	3482.55	4952.09	6325.49	7288.83
TOTAL	94581.20	143257.40	192965.60	218033.10

Table 3. Support reactions (loads) of tower B.

Column	Support reactions - loads (kN)			
	Stage 1	Stage 2	Stage 3	Stage 4
PB01	2923.38	3804.32	4662.69	5307.21
PB02	4331.12	6031.19	7449.71	8408.15
PB03	3808.24	5365.09	6154.79	6839.53
PB04	3152.93	4483.17	5468.09	6262.70
PB05	2849.81	3883.78	4531.24	5155.16
PB06	3184.33	4370.36	5289.55	6024.32
PB07	4131.97	6148.91	7646.90	8505.27
PB08	6144.98	8799.57	11448.27	12435.16
PB09	4993.29	7182.88	8968.30	10159.24
PB10	3901.44	5420.03	6277.42	7014.15
PB11	7087.73	10429.01	12049.62	13207.20
PB12	3985.80	5954.67	7119.12	8086.38
PB13	8035.37	14353.01	13143.44	13894.88
PB14	5640.75	8458.18	9716.81	10981.31
PB15	1552.92	2279.84	1672.61	1753.05
PB16	6427.51	9999.33	8629.86	8932.01
PB17	2725.22	6367.67	4679.37	5321.93
PB18	2735.03	3878.87	4269.31	4897.15
TOTAL	77611.82	117209.88	129177.10	143184.80

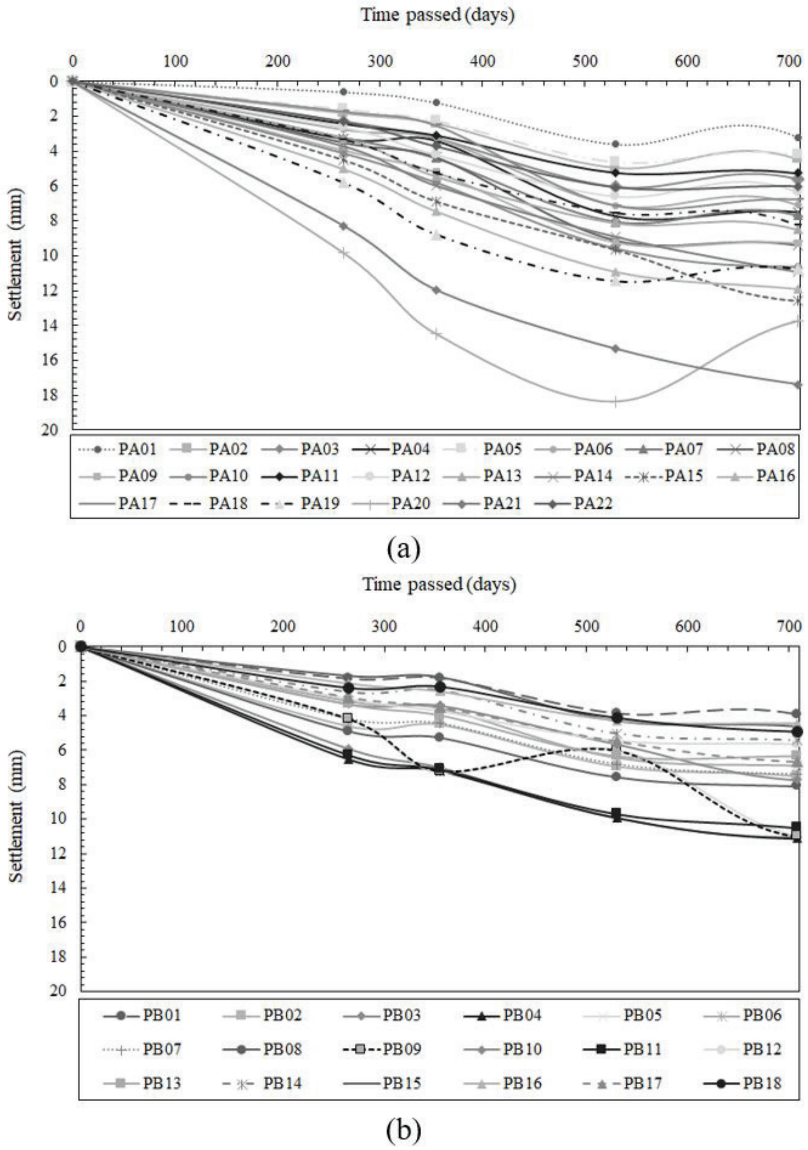

Figure 3. Settlement evolution with the observed time: (a) tower A; (b) tower B.

values were 5.90 mm, 6.51 mm and 6.27 mm in reading no. 1, 6.98 mm, 7.18 mm and 7.10 mm in reading no. 2 and 9.90 mm, 9.91 mm and 9.69 mm in reading no. 3 in this order, respectively. The settlement of reading no. 4 has the highest settlement surrounding PB03, PB04 and PB05 (11.02 mm, 11.11 mm and 11.00 mm, respectively), and surrounding PB09 (11.00 mm) and PB11 (10.50 mm). Note that the most significant settlements were maintained at all stages in PB04 column and similarly in PB11 column. PA21 and PA01 of tower A presented the highest and lowest final absolute settlements (17.38 mm and 3.20 mm, respectively); PB04 and PB01 of tower B presented the highest and lowest final absolute settlements (11.11 mm and 3.92 mm, respectively).

Figures 4 and 5 shows settlement isolines and 3D representation of settlement for the ground of tower A and B, respectively, in stage 3.

A tendency of the highest measured settlement was observed to occur in the lower edge of the foundation of both towers A and B, differing from what commonly happens, which is higher settlement in the central region of building, reported by Gusmão (1994). This fact can be attributed to the geomechanical conditions of the subsoil and to fact that the loads resulting from the columns are larger in this area, which causes larger ground deformations.

5.2 Analysis of the soil-structure interaction

Figure 6 and Figure 7 show examples of force redistribution on the foundation between the columns of tower A and B, respectively, in which the painted areas refer to force increase and the blank areas refer to force reduction in the columns.

The redistribution of forces observed is distinct for SSI 1 analysis. While for SSI 2, this redistribution is more

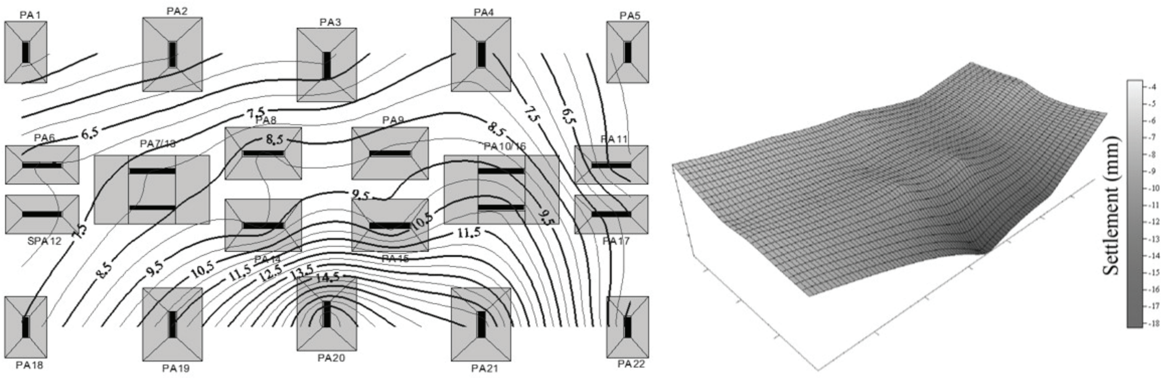

(a) (b)

Figure 4. (a) Settlement isolines curves and (b) shape of ground surface settlement of tower A – Stage 3.

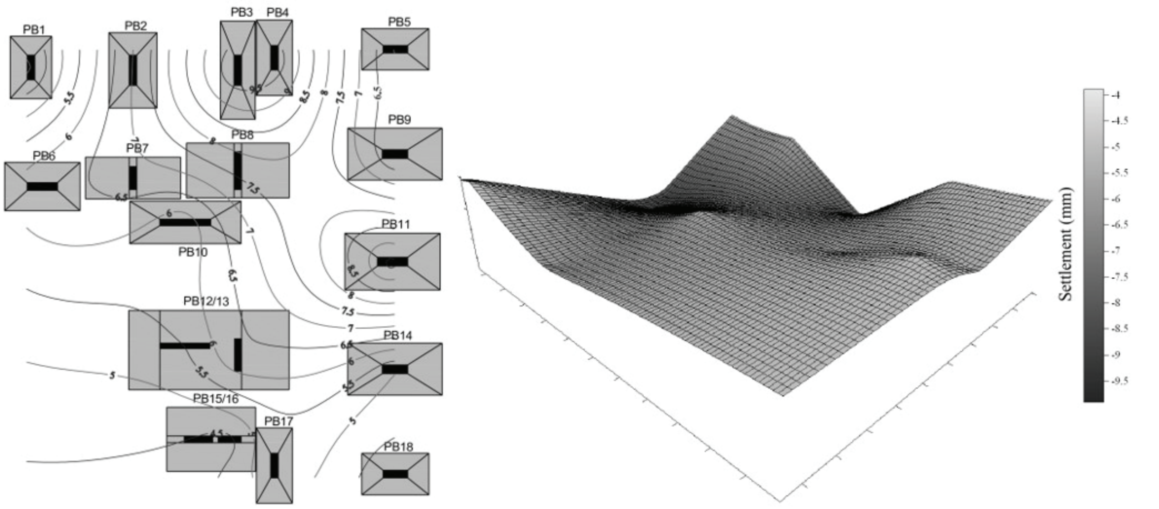

(a) (b)

Figure 5. (a) Settlement isolines curves and (b) shape of ground surface settlement of tower B – Stage 3.

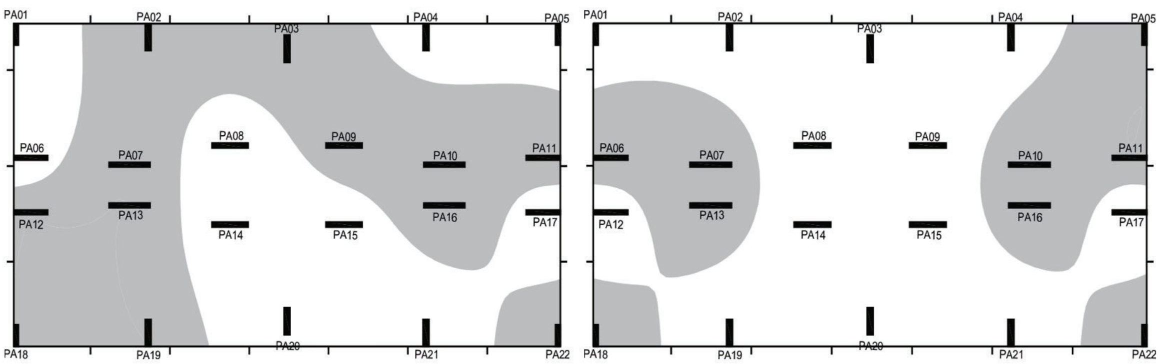

(a) (b)

Figure 6. Efforts redistribution in plant between the columns of tower A in (a) SSI case 1 and (b) SSI case 2 - stage 4.

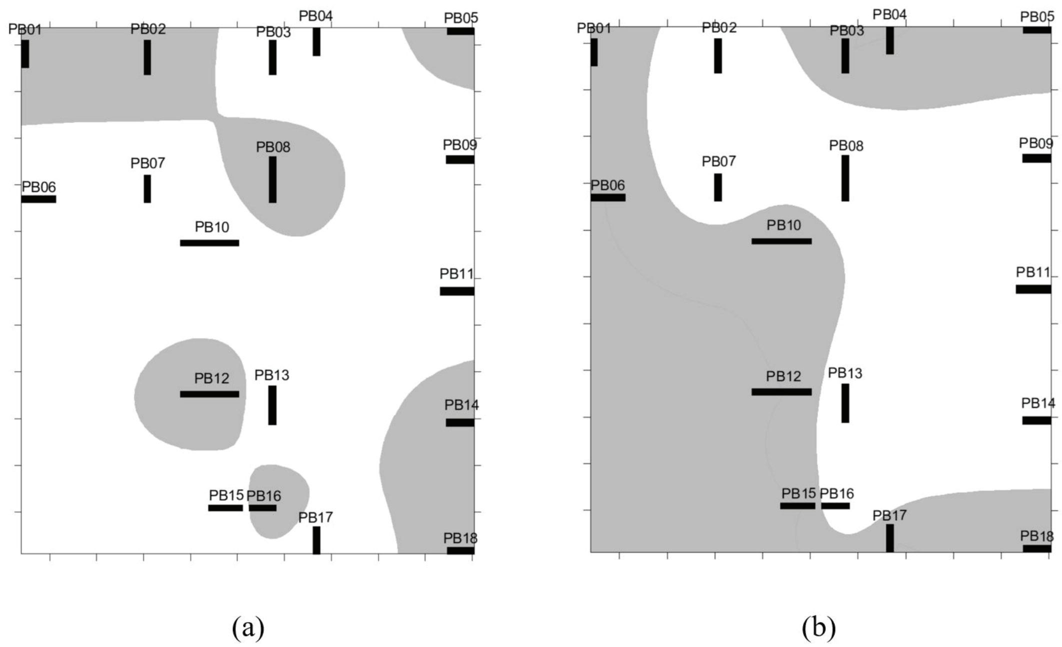

Figure 7. Efforts redistribution in plant between the columns of tower B in (a) SSI 1 and (b) SSI 2 - stage 4.

Table 4. Redistribution of total efforts in percentage (%) - towers A and B.

Stage	Redistribution (%)							
	Central columns				Edge columns			
	Tower A		Tower B		Tower A		Tower B	
	SSI 1	SSI 2	SSI 1	SSI 2	SSI 1	SSI 2	SSI 1	SSI 2
1	-0.67	-0.66	-1.32	-10.07	1.10	0.88	0.37	3.07
2	-0.72	-0.55	-0.68	-12.01	1.08	0.67	0.17	3.97
3	-0.51	-0.51	-1.55	-11.81	0.63	0.55	0.47	3.89
4	0.09	-0.57	0.11	-11.93	-0.25	0.68	-0.10	3.79

subtle, presenting the same behavior in stages 2, 3 and 4, in which the same columns are relieved and overloaded. This phenomenon can be explained by the fact that the adoption of the K_m spring coefficient is determined by the average loading and the average settlement of the building columns, where each support has a dislocation with the same rigidity. This makes the SSI behavior more uniform, reducing even more the rock mass variability, thus generating very similar results.

Table 4 shows loads redistribution, through the rate of load gain or loss of towers columns. Considering tower A, in SSI 1 and SSI 2 analysis, there was variation in load redistribution behavior between its columns. In terms of total efforts, stages 1, 2, and 3 showed the expected behavior for the column's redistribution considering the SSI, in which the central columns are relieved, and the edge columns show a load increase.

In SS1 and SSI 2 analyses considering the tower B, the most significant load relief in the central columns and the highest load gain in the edge columns in terms of total forces was observed at the construction stage 3 (-1.55% and 0.47%, respectively). For SSI 2, all construction stages behaved as expected. The greatest relief of total forces in the central columns occurred at stage 2 (-12.01%), as well as the greatest total force gain in the edge columns, with a value of 3.97%. Comparing the towers, the redistribution of total forces between central and edge columns is slightly more expressive in SSI 2. Stage 4 behaved contrary to the previous stages considering the SS1 analysis in both towers, which may be associated with the amount of total forces that was redistributed at a given stage.

Figure 8 and Figure 9 relate, respectively for towers A and B, the percentage of central columns that undergo stress-relief and the number of edge columns that experienced an increase of forces in function of the construction stage. In SSI 1 analysis, a total of 4 central columns of tower A experienced force relief (50%), in stages 1 and 3.

Regarding the increase of forces in the edge columns, the redistribution was more significant in construction stages 2 and 3, where 7 columns (50%) were overloaded after the analysis. For the SSI 2 analysis, 35.70% of the edge columns exhibited gain of forces during all construction stages. This behavior was similar to the central columns, where, until stage 4, 50% of the columns showed load relief. For tower B, in SSI 1 analysis, a total of 2 central columns underwent

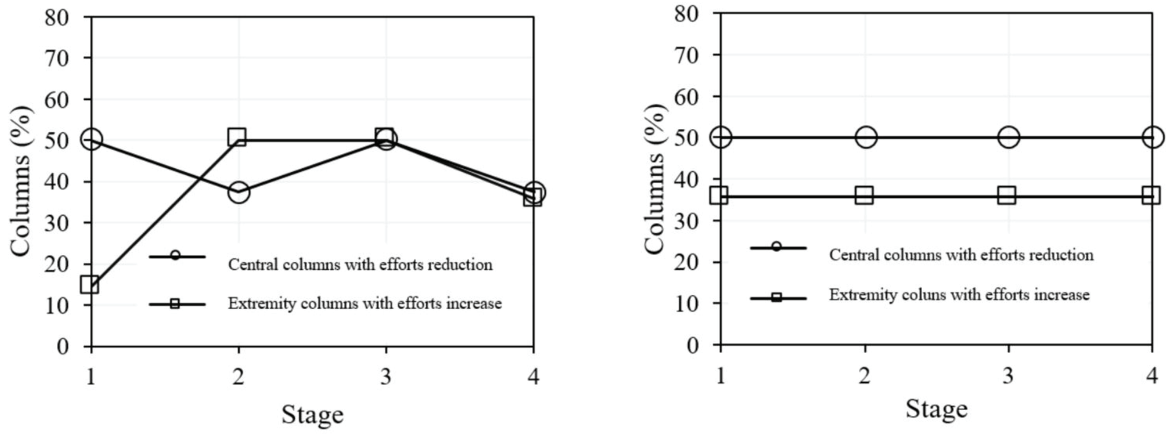

(a) (b)

Figure 8. Central columns with reduction and edge columns with efforts increase of tower A: (a) SSI case 1; (b) SSI case 2.

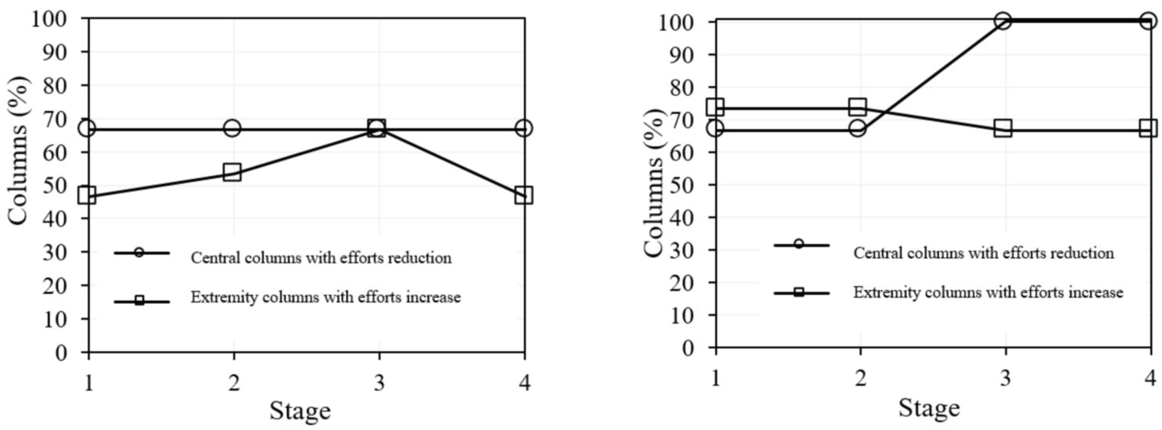

(a) (b)

Figure 9. Central columns with reduction and end edge columns with efforts increase of tower B: (a) SSI case 1; (b) SSI case 2.

to effort relief (66.67%). Regarding the edge columns, the force gain was more significant in stage 3, in which 66.67% (10 edge columns) experienced this type of redistribution. In SSI 2 analysis, 66.67% of the total central columns presented load relief for the other stages. The edge columns showed an increase in forces of 73.33% (11 columns) in stages 1 and 2, reducing this ratio to 66.67% in other stages (10 columns).

This behavior shows the phenomenon of load redistribution in the columns related to the SSI, with a load relief of the central columns and overload of the edge columns. It should also be noted that not all central and edge columns, in most observed construction stages, were relieved and overloaded, respectively. Danziger et al. (2005) and Santos (2016) also noted this fact.

The following analysis consists of evaluating the redistribution of forces between the columns considering the settlement experienced by them. Therefore, considering the average settlement observed for each of the construction stages, it was possible to determine the columns that experienced settlement superior and inferior to the average value. This happened because the tendency is that the columns that present settlement above the average are the most loaded ones, and those with settlement lower than the average are the least loaded. Then, after the SSI, it is expected stress relief on columns with the above average settlement and stress gain on columns that have below-average settlement, considering that the most loaded ones are not in center but at the edge. Figure 10 and Figure 11 show the number of columns that have been relieved and those that experienced force increase after the soil-structure interaction (cases 1 and 2) for the buildings, considering this analysis.

Considering tower A for the SSI 1 analysis (Figure 10a), the largest reduction in efforts of them occurred in stage no. 1, in 91.70% of the columns. Concerning the number of columns that had load increase, this gain was more significant in stage 4 (61.50%).

Analyzing the results obtained through SSI 2 (Figure 10b), the force reduction between the columns that presented higher settlement than the average was more significant in stages 3 and 4, with 77.80% of these columns that suffered such redistribution and being less expressively in stage 2.

In tower B, during SSI 1 (Figure 11a), the reduction of efforts between the columns that presented settlement higher than the average is more expressive in stage 3, where 75% of these columns were relieved. Concerning the increase of efforts between the columns that presented settlement lower than the observed average, the stage 3 is also the one with the most significant amount, where 90% of these columns gain some load with the SSI. Considering SSI 2 (Figure 11b), the tower presented the largest number of columns with settlement larger than the observed average, and that suffered a reduction of its efforts in stage 3, which relief occurred in 50% of these elements. The force gain in the columns with lower settlements than the average was more expressive in stages 1, 2, and 3, which 70% of these columns were more overload than the analysis without the interaction. Figure 12 and Figure 13 represent the force redistribution in terms of reduction and increase of maximum forces, for the construction stages of towers A and B, respectively.

In both analyses, force relief and gain are observed as the construction nears completion. In tower A, concerning the SSI 1 analysis, the greatest force gain was noted in PA22 in stages 3 and 4, and the greatest force relief in PA20, in stage 2. As for SSI 2 analysis, the PA16 was the one that obtained the greatest efforts gain in stages 3 and 4. The greatest effort relief was observed in PA08 in stage 3.

In tower B, for SSI 1 analysis, the greatest force gain was observed in PB15 (24.83%) at stage 2, and the greatest stress relief in PB17 at construction stage 4. According to the SSI 2 analysis, the largest increase was observed in PB15 at stage 4 (Figure 13b), while the most significant reduction was observed in stage 1, in PB16 (Figure 13b). Such variation may be attributed to the asymmetry of the building plan, making the redistribution not to be observed in a more uniform and less accentuated way as observed between the columns of tower A.

Figures 14a and 14b represent the redistribution, in average terms, of the column forces in towers A and B, respectively, in SSI 1 and SSI 2 analyses. This figure shows that the average force redistribution occurred between the columns that were relieved and that gained load after the soil-structure interaction, for the analyzed construction stages.

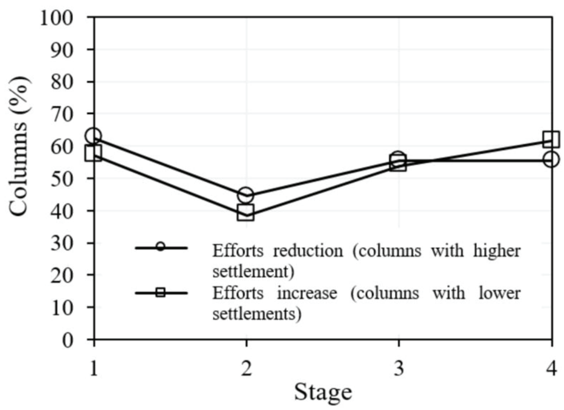

(a)

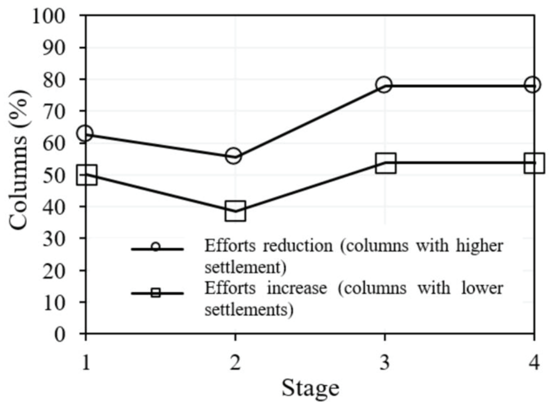

(b)

Figure 10. Columns with force reduction (higher settlement) and increase (lower settlements) in tower A: (a) SSI 1; (b) SSI 2.

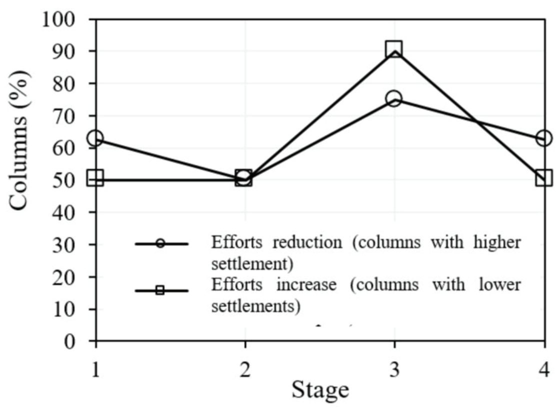

(a)

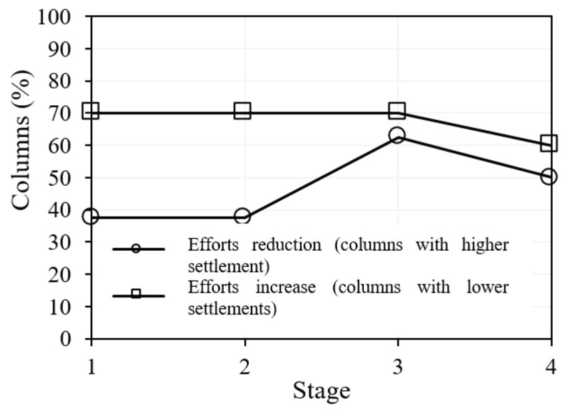

(b)

Figure 11. Columns with force reduction (higher settlement) and increase (lower settlements) in tower B: (a) SSI 1; (b) SSI 2.

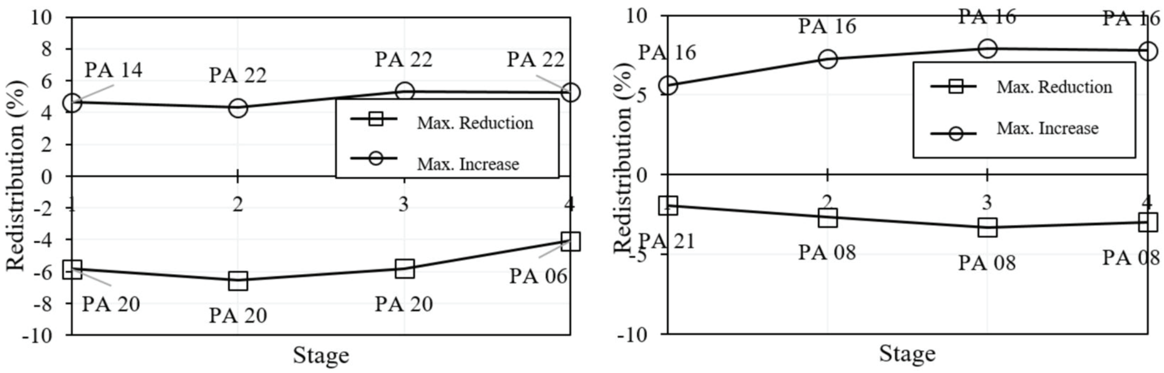

(a) (b)

Figure 12. Force redistribution in terms of reduction and a maximum increase of tower A: (a) SSI case 1; (b) SSI case 2.

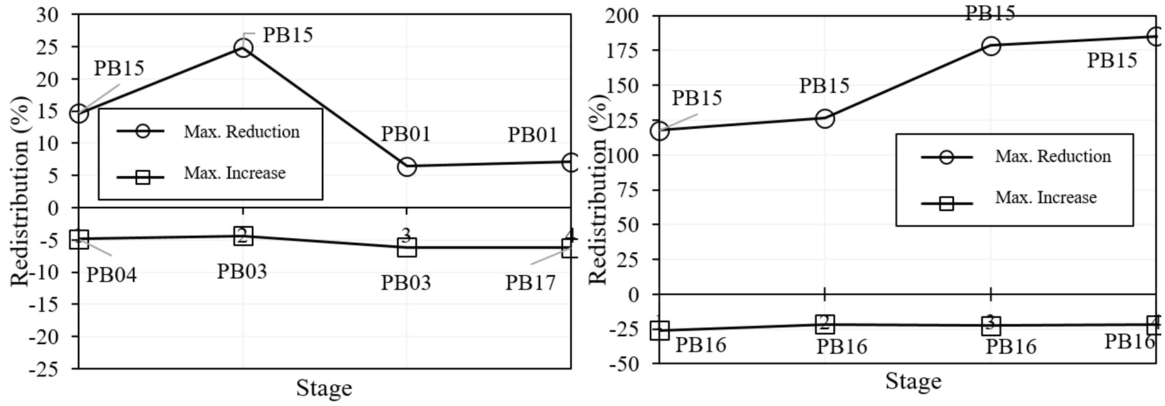

(a) (b)

Figure 13. Force redistribution in terms of reduction and a maximum increase of tower B: (a) SSI case 1; (b) SSI case 2.

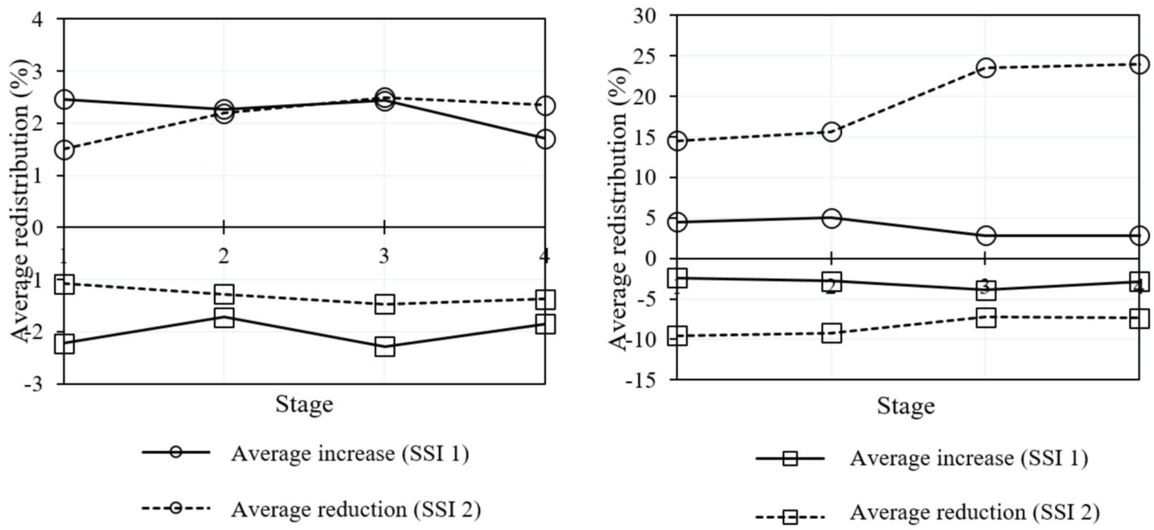

(a) (b)

Figure 14. Force redistribution between the columns in average terms: (a) tower A; (b) tower B.

It was not possible to notice a tendency to reduce the force redistribution between the columns as the construction comes to its conclusion (the increase of the structure rigidity) as stated by Gusmão (1994) and Santos (2016). This can be attributed to low settlement values and symmetry in plan observed in tower A, and low settlement values of tower B, thus minimizing the SSI effects.

6. Conclusions

The structural modeling proved to be quite representative, pointing to vertical load values higher than the average values present in building edge zones, contradicting the conventional idea that the central columns are more loaded than the edge columns.

The soil-structure interaction analyses resulted in different behaviors regarding both towers, construction stages, and SSI 1 and SSI 2 analyses. Redistribution values were lower in tower A compared to tower B. This fact can be explained by the asymmetry in plan of tower B projection, differing from the plan projection of tower A, which is symmetrical, and thereby, has a smaller redistribution, varying slightly from its efforts when non-displaceable structure is considered. There was no decreasing trend in force redistribution between the columns of both towers as the construction was near to the conclusion (the increase of the structure rigidity). The phenomenon behaved quite distinctly between the stages.

Analyses that include maximum values of force reduction and gain, as well as those that demonstrate redistribution by relating the settlement magnitude, give a more complete and comprehensive view of the phenomena attributed to the SSI.

Acknowledgements

The authors acknowledge the support from Gusmão Associated Engineer, TQS Computing, for the license granted to use CAD/TQS software®, to the engineers Eurico Júnior, Marília Santos and Danilo Guerra, in research concerning Santos (2018).

Declaration of interest

There is no conflicting interests.

Author's contributions

Yago Ryan Pinheiro dos Santos: data curation, conceptualization, methodology, validation, writing - original draft preparation. Maria Isabela Marques da Cunha Vieira Bello: validation, supervision, writing - reviewing and editing. Alexandre Duarte Gusmão: data curation, validation, supervision. Jonny Dantas Patricio: supervision, writing - reviewing and editing.

List of symbols

Fz_i	Vertical Support Reaction
Fz_m	Vertical Support Reaction Average
K	Spring Coefficient
K_i	Spring Coefficient at the Different Construction Stages
K_m	Average Spring Coefficient
RQD	Rock Quality Designation
SSI	Soil-Structure Interaction
UCS	Unconfined Compressive Strength
δ_i	Monitored Settlement
δ_m	Average Monitored Settlement

References

Amini, F., Bitaraf, M., Nasab, M.S.E., & Javidan, M.M. (2018). Impacts of soil-structure interaction on the structural control of nonlinear systems using adaptive control approach. *Engineering Structures*, 157, 1-13. http://dx.doi.org/10.1016/j.engstruct.2017.11.071.

Chaudhary, M.T.A. (2016). Effect of soil-foundation-structure interaction and pier column non-linearity on seismic response of bridges supported on shallow foundations. *Australian Journal of Structural Engineering*, 17(1), 67-86. http://dx.doi.org/10.1080/13287982.2015.1116178.

Danziger, B.R., Carvalho, E.M.L., Costa, R.V., & Danziger, F.A.B. (2005). Case study with soil-structure interaction analysis. *Civil Engineering Magazine*, 23, 43-54.

Gómez-Martínez, F., Millen, M.D.L., Costa, P.A., & Romão, X. (2020). Estimation of the potential relevance of differential settlements in earthquake-induced liquefaction damage assessment. *Engineering Structures*, 211, 110232. http://dx.doi.org/10.1016/j.engstruct.2020.110232.

Gusmão, A.D. (1994). Relevant aspects of soil-structure interaction in buildings. *Soils and Rocks*, 17(1), 47-55.

Lee, I.K., & Brown, P.T. (1972). Structure-foundation interaction analysis. *Journal of the Structural Division*, 98(11), 2413-2431.

Meyerhof, G.G. (1953). Some recent foundation research and its application to design. *Structural Engineering*, 31, 151-167.

Morris, D. (1966). Interaction of continuous frames and soil media. *Journal of the Structural Division*, 92(5), 13-44. http://dx.doi.org/10.1061/JSDEAG.0001505.

Mota, M.M.C. (2009). *Soil-structure interaction in deep foundation buildings: numerical method and observed field results* [Doctoral thesis]. University of São Paulo (in Portuguese). https://doi.org/10.11606/T.18.2009.tde-15122009-111356

Papadopoulos, M., Van Beeumen, R., François, S., Degrande, G., & Lombaert, G. (2017). Computing the modal characteristics of structures considering soil-structure interaction effects. *Procedia Engineering*, 199, 2414-2419. http://dx.doi.org/10.1016/j.proeng.2017.09.296.

Poulos, H.G. (1975). Settlement analysis of structural foundation systems. In *Proc. 4th Southeast Asian Conference on Soil Engineering* (pp. 52-62), Kuala Lumpur, April 1975. Kuala Lumpur: The Institution.

Rosa, L.M.P., Danziger, B.R., & Carvalho, E.M.L. (2018). Soil-structure interaction analysis considering concrete creep and shrinkage. *Ibracon Structures and Materials Journal*, 11(3), 564-585. http://dx.doi.org/10.1590/S1983-41952018000300008.

Santos, M.G.C., & Corrêa, M.R.S. (2018). Analysis of the effects of soil-structure interaction in reinforced concrete wall buildings on shallow foundation. *Ibracon Structures and Materials Journal*, 11(5), 1076-1109. http://dx.doi.org/10.1590/S1983-41952018000500010.

Santos, M.J.A.P. (2016). *Soil x structure interaction: analysis of a work case with repression monitoring since the beginning of construction* [Master's dissertation]. Rio de Janeiro State University (in Portuguese). Retrieved in April 20, 2021, from http://www.bdtd.uerj.br/handle/1/11641

Santos, Y.R.P. (2018). *Study of the soil-structure interaction of a construction case of rocky mass foundations* [Master's dissertation]. Federal University of Pernambuco (in Portuguese). Retrieved in April 20, 2021, from https://repositorio.ufpe.br/handle/123456789/31862

Savaris, G., Hallak, P.H., & Maia, P.C.A. (2011). Understanding the mechanism of static soil-structure interaction: a case study. *Soils and Rocks*, 34(3), 195-206.

TQS. (2021). *About TQS.* Retrieved in April 20, 2021, from https://www.tqs.com.br/

Winkler, E. (1867). *Die lehre von elasticitaet und festigkeit*. Verlag H. Dominicus (in German).

Soils and Rocks

An International Journal of Geotechnical and Geoenvironmental Engineering

www.soilsandrocks.com

ISSN 1980-9743
ISSN-e 2675-5475

Dynamic driving formulas and static loadings in the light of wave equation solutions

Faiçal Massad[1#]

Article

Keywords
Dynamic formulas
Driven piles
Bearing capacity
Static and dynamic displacements
Elastic rebounds

Abstract

The advances in pile monitoring have motivated attempts to support dynamic formulas to estimate pile bearing capacity. Based on numerical analysis of the wave equation and the results of dynamic loading tests in three piles the paper deals with the investigation of the soundness of some of the most used in Brazil, namely, the so called Chellis-Velloso Formula, the Energy Approach Equation and Uto's Formula. The former gained strength through a misinterpretation of Casagrande (1942) statement that the elastic compression of a pile during driving is a measure of the dynamic force with which the soil is tested, and not of its static resistance. Therefore, the elastic compression and rebound, measured during driving, are generally smaller than the corresponding static values. The second is based on an elasto-plastic load-displacement relationship without physical meaning, besides the fact that the effective energy in driving a pile is related to the work of dynamic forces and has nothing to do with the static resistances. The third was derived from a simplified solution of the wave equation, assuming among other hypothesis that there is no friction along pile shaft. The paper shows the ineffectiveness of attempts to universally validate these formulas with dynamic pile monitoring and the implications in the simulation of static loadings.

1. Introduction

Dynamic formulas have the appeal of their simplicity, especially those that depend on the set (s), the elastic rebound (K) and the efficiency (η) of the driving system. The trend today is to take advantage of the dynamic monitoring of a certain number of piles and obtain parameters such as η to be used in other piles of the work along with direct measurements of s and K, say, with pencil and paper.

However, some of the most used dynamic formulas in Brazil, namely the Chellis-Velloso Formula, the Energy Approach Equation, and the Uto's Formula have required adjustments considering the geometry and kind of piles, the types of soils, among other factors. The question that arises refers to the general validity of these formulas.

Furthermore, in this context the simulation of static loadings through dynamic tests with increasing energy is discussed.

2. The Chellis-Velloso formula

The well-known formula of Chellis (1951) modified by Velloso (1987) is based on Hooke's law and uses measurements of elastic rebound to estimate static resistance, as shown in Equations 1 and 2.

$$R = \frac{C_2 \cdot E \cdot S}{\alpha \cdot L} = \frac{(K - C_3) \cdot K_r}{\alpha} \tag{1}$$

$$K_r = \frac{E \cdot S}{L} \tag{2}$$

In these equations $R=RMX$ is the static mobilized resistance; K_r, the pile stiffness; C_2, the pile elastic shortening or pile compression; E, the dynamic Young's modulus; S, the area of the pile cross section; L, its length; K, the elastic rebound; C_3, the toe "quake", usually taken equal to 2.5mm; and α, a factor dependent on the distribution of lateral friction and tip load, given by:

$$\alpha \cong \beta + \lambda \cdot (1 - \beta) \tag{3}$$

where λ is the coefficient of Leonards & Lovell (1979) and β is the relationship between tip load and total load. Velloso (1987) suggested using α =0.7, an average value.

[#]Corresponding author. E-mail address: faical.massad@usp.br
[1]Universidade de São Paulo, Escola Politécnica, São Paulo, SP, Brasil.

Submitted on January 4, 2021; Final Acceptance on April 21, 2021; Discussion open until August 31, 2021.

https://doi.org/10.28927/SR.2021.061921

3. The energy approach equation

The Energy Approach Equation, as presented by Paikowsky & Chernauskas (1992), takes the form of Equation 4.

$$R_u = RMX = \frac{2.\kappa.EMX}{s + DMX} \tag{4}$$

These authors assumed an elasto-plastic relation between resistance and displacement, as shown in Figure 1. The maximum energy delivered to the pile (*EMX*) was equated to the work done by the resistance (R_u *or RMX*) offered by the soil to the penetration of the pile [*RMX.(s+DMX)/2*], where *DMX=s+K*. Based on a case study, Paikowsky & Chernauskas (1992) proposed a reduction parameter κ=0.8, arguing that part of the applied energy *EMX* is dissipated in the mobilization of viscous or dynamic resistances.

Aoki (1997) interpreted the driving process in the light of the Hamilton's Principle of energy conservation and came up with a similar expression, using the ζ symbol instead of *2κ*. The parameter ζ would depend on the magnitude and nature of the reaction forces (conservative or non-conservative) and could vary between 1 (permanent displacement predominates) and 2 (elastic displacement predominates).

4. The Utos's formula

Uto et al. (1985) presented a simple formula based on the solution of one-dimensional wave equation, admitting as the boundary condition the displacement-time curves for the top and the tip of the pile. Several simplifying hypotheses were assumed, among which the following stand out: a) lateral friction and viscous resistance (damping) at the tip of the pile were neglected during driving; and b) the set (*s*) was taken equal to the toe quake (C_3). They came to the following equations:

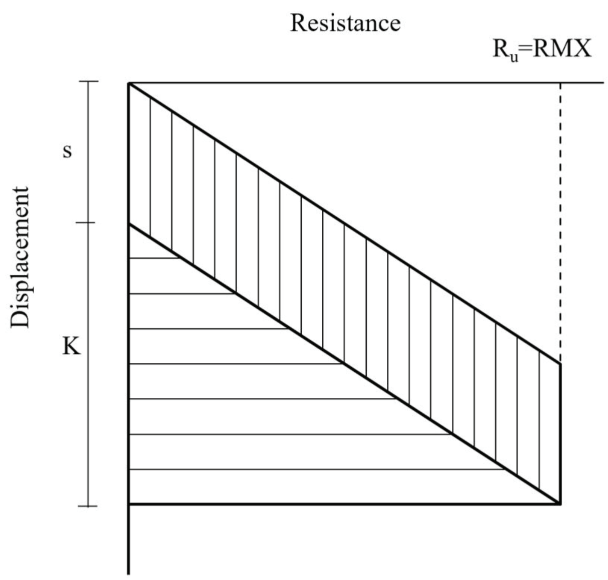

Figure 1. Resistance vs displacement.

$$R_d^{tip} = \frac{K_D \cdot E \cdot S}{e_o.L} = \frac{K_D.K_r}{e_o} \tag{5}$$

$$e_o = \left(\xi.\frac{W_H}{W_P}\right)^{\frac{1}{3}} \tag{6}$$

where R_d^{tip} is the dynamic resistance mobilized at the pile tip; e_o, a wavelength correction factor, is a function of both, (a) the relationship between the weights of the hammer (W_H) and the pile (W_P), and (b) the pile type, through the parameter ξ, that assumes a figure of 1.5 for steel piles and 2.0 for concrete piles.

5. Differences in C_2 and *K* static and dynamic

5.1 Theoretical background

For the pile element in Figure 2a, the equation of the balance of the acting forces during driving can be written as follows (see attached list of symbols):

$$F = \pi.D.f.dx + \left(F + dF\right) + \rho.S.dx.\frac{d^2u}{dt^2} \tag{7}$$

According to Smith (1960), the shaft friction (*f*) is given by:

$$f = k.u.\left(1 + J.\frac{du}{dt}\right) = f^{est}.\left(1 + J.\frac{du}{dt}\right) \tag{8}$$

valid for *u* smaller than the quake. If not, *k.u* is equal to the maximum shaft friction (f_{max}^{est}).

Equation 7 may be rewritten as:

$$\frac{dF}{dx} = -\pi.D.f - \rho.S.\frac{d^2u}{dt^2} \;\; with \;\; \rho.S = \frac{E,S}{c^2} \tag{9}$$

Note that:

$$\pi.D.f.dx = R_m = R_d + R_e \tag{10}$$

where R_e, R_d and R_m are respectively the static, dynamic, and total resistances in the element. By Hooke's Law it follows:

$$\varepsilon = -\frac{du}{dx} = \frac{F}{E \cdot S} \tag{11}$$

This equation shows that it is the dynamic force *F* that generates the elastic shortenings (*du*) in the element and not the static force R_e, confirming the above-mentioned statement of Casagrande (1942).

By deriving both members from Equation 11 the term *dF/dx* is obtained, which, replaced in Equation 9, results in the Wave Equation:

$$\frac{d^2u}{dx^2} = \frac{\pi \cdot D \cdot f}{E \cdot S} + \frac{\rho}{E} \cdot \frac{d^2u}{dt^2} \tag{12}$$

At time *t*, *F* varies as follows along depth (*x*):

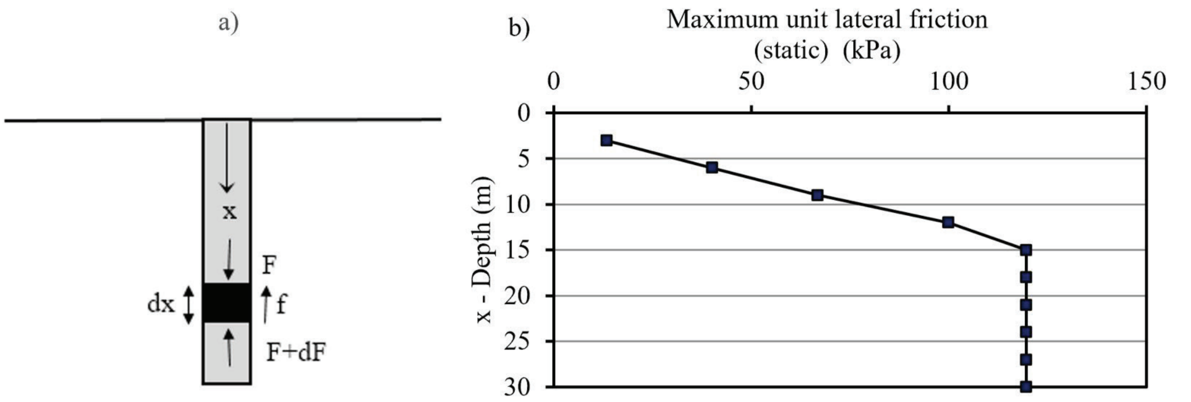

Figure 2. (a) Forces and stresses in pile element of height dx; (b) Maximum unit lateral friction (static) vs depth.

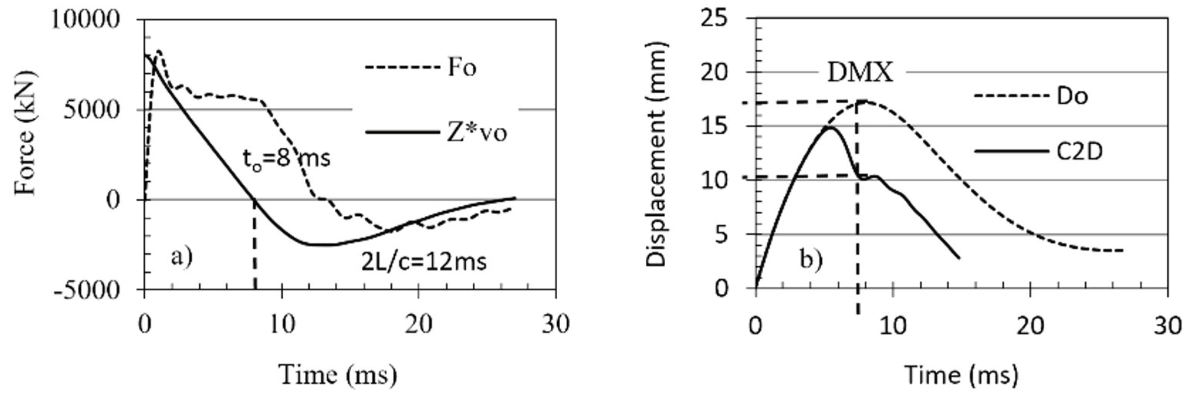

Figure 3. Forces (a) and displacements (b) vs time, with v_o=4.33 m/s at t=0.

$$F(x) = F_o - \sum_0^x R_m - \frac{E.S}{c^2} \cdot \int_0^x \frac{d^2u}{dt^2} \cdot dx \qquad (13)$$

where F_o stands for $F(x)$ at pile top (x=0).

5.2 Numerical wave equation solutions for simple cases

Consider the solution of the wave equation presented in Figure 3a obtained through the methodology of Smith (1960) applied to a steel pipe pile (see Table 1), excited at the top by a speed v_o=4.33 m/s at time $t=0$, due to the blow of a hammer. It was assumed that static maximum unit lateral frictions (Figure 2b) are known a priori just like the toe static resistance (R_p), the shaft (q_s) and tip (q_t) quakes, and "Smith dampings" of friction (J_s) and tip (J_t), indicated in Table 2. Under these conditions, the maximum static lateral (A_{lr}) and tip ($Q_{pr}= R_p.\ S_p$) loads are 8081 kN and 1225 kN, respectively, adding up 9306 kN.

From Figure 3a one may conclude that for $t=t_o$=8 ms the speed at the top (v_o) is zero and therefore the displacement at the top reaches its maximum value, *DMX* in Figure 3b. This figure also displays the calculated C_{2D} by the difference of the top and tip pile displacements at each time. For the same time t=8 ms, Figure 4 shows the distribution along the shaft of the maximum static resistance and of the dynamic (F) axial force. From its analysis, it can be concluded that (see the list of symbols attached):

a) the forces F for t=8 ms were lower than the maximum static resistances (Figure 4), with C_{2D}=10.1 mm (Figure 3b) which is smaller than the corresponding static value, given by:

$$C_{2E} = \frac{\lambda * A_{lr} + Q_{pr}}{K_r} = \frac{0.6 * 8081 + 1225}{316} \cong 19.2\,mm \qquad (14)$$

and K_D=C_{2D}+q_t≈11.8 mm against K_E= C_{2E}+C_3 ≈20.9 mm. As *DMX*=17.1 mm (Figure 3b), it follows that s=*DMX*-K_D=5.3mm; the values of λ and K_r are given in Tables 1 and 2; and

b) these differences between static and dynamic values (Figure 4) result from Equation 13: the total resistances (R_m) interact with the inertial forces, due to acceleration, which acts either up or down, as illustrated in Figure 5.

The same Pile E-1 was also submitted to a simulation of the dynamic loading test with increasing energy, as proposed by Aoki (1989). The speed at the top due to the impact of the hammer was varied between 1.08 and 6.49 m/s, which implied in *EMX* increasing from 6 to 228 kN.m, as shown in Table 3

Table 1. Characteristic of pile excited with v_o=4.33 m/s at time t=0.

Pile	D_e (cm)	D_i (cm)	S (cm^2)	S_p (cm^2)	L (m)	E (GPa)	K_r (kN/mm)	c (m/s)
E-1	91.4	88.2	451.4	6561	30	210	316	5125

Legend: see attached list of symbols.

Table 2. Assumed parameters for Pile E-01.

Pile	λ	R_p (kPa)	q_s (mm)	q_t=C_3 (mm)	J_s (s/m)	J_t (s/m)
E-1	0.6	1867	5.73	1.76	0.12	0.18

Legend: see attached list of symbols.

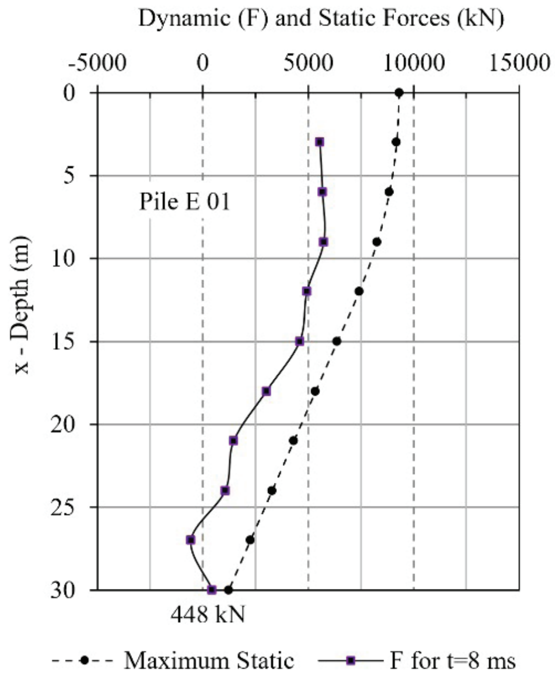

Figure 4. Axial Forces vs depth (v_o=4.33 m/s at t=0).

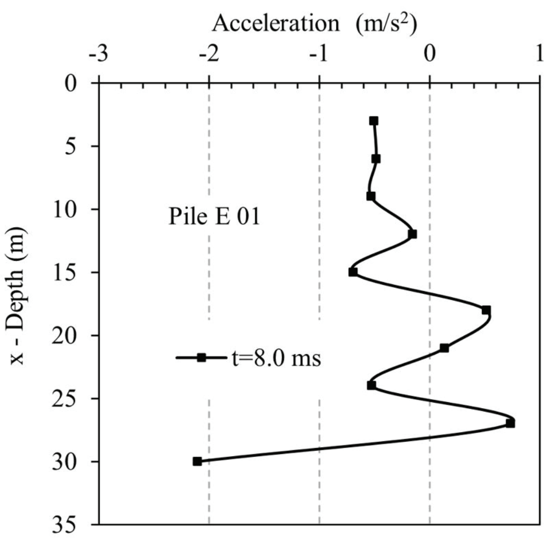

Figure 5. Acceleration vs depth (v_o=4.33 m/s at t=0).

with other data of this simulation; note that the set varies with time (s_{to}< s_{tf}). The results in Table 4 confirms that the dynamic values of elastic compression (C_{2D}) and rebound (K_D) are lower than the corresponding static values (C_{2E} and K_E).

5.3 Evaluation of Chellis-Velloso formula

The differences between static and dynamic values of C2 lead to the first conclusion about the Chellis-Velloso Formula, Equations 1 to 3. With the values of K_r=316 kN/mm (Table 1), λ=0.60 (Table 2) and β=1225/9306=13.2% it follows for blow 5 of Tables 3 and 4:

$$\alpha \cong 0.132 + 0.6 \cdot (1 - 0.132) = 0.652 \tag{15}$$

$$R = \frac{10.1 * 316}{0.652} = 4895\,kN \tag{16}$$

much smaller than:

$$R = \frac{19,2 * 316}{0.652} = 9306\,kN \tag{17}$$

confirming the note of Velloso & Lopes (2002) that Equation 1 refers to static calculation. And these authors added that this formula may be valid for short piles, with lengths of the order of the wavelength and so the whole pile is compressed, which does not occur on long piles.

6. Force or resistance vs displacement. Evaluation of the energy approach equation

Figure 6 shows the progress of the mobilized static resistance (R_e) along the depth (x) and the time (t). For t=8 ms the static resistances in the elements (R_e) already reach the maximum available values.

Figure 7 reveals that the total static (R_{eT}) and the total dynamic+static resistances (R_{mT}=R_{eT}+R_{dT}) reach maximum values at a time t≈7 ms, therefore close to 8 ms, at which time the maximum displacement (DMX) occurs, as seen above (Figure 3b). It is also interesting to note that as time proceeds, the portions of the dynamic resistances vanish, as the pile is no more in movement.

The dynamic displacement (D_m) progresses along the depth (x) and time t (from 2 to 8 ms) as shown in Figure 8.

Table 3. Data on simulated dynamic loading tests with increasing energy - Pile E-1.

Blow #	v_o (t=0) (m/s)	EMX (kN.m)	t_o (ms)	RMX (kN)	DMX (mm)	s_{to} (mm)	s_f (mm)
1	1.08	6	7.6	4168	4.1	0.0	0.0
2	1.50	12	7.6	5451	5.8	0.4	0.4
3	2.16	25	7.6	7015	8.4	1.5	1.6
4	3.05	50	7.6	8643	12.0	3.1	3.1
5	4.33	101	8.0	9306	17.1	5.3	5.9
6	6.49	228	8.4	9306	26.4	10.6	14.8

Legend: see attached list of symbols.

Table 4. Other results of increasing energy loading tests - Pile E-1.

Blow #	v_o (t=0) (m/s)	C_{2D} (mm)	C_{2E} (mm)	K_D (mm)	K_E (mm)
1	1.08	2.6	8.7	4.1	10.4
2	1.50	3.6	11.0	5.4	12.8
3	2.16	5.1	13.9	6.9	15.6
4	3.05	7.1	17.2	8.9	19.0
5	4.33	10.1	19.2	11.8	20.9
6	6.49	14.0	19.2	15.8	20.9

Legend: see attached list of symbols.

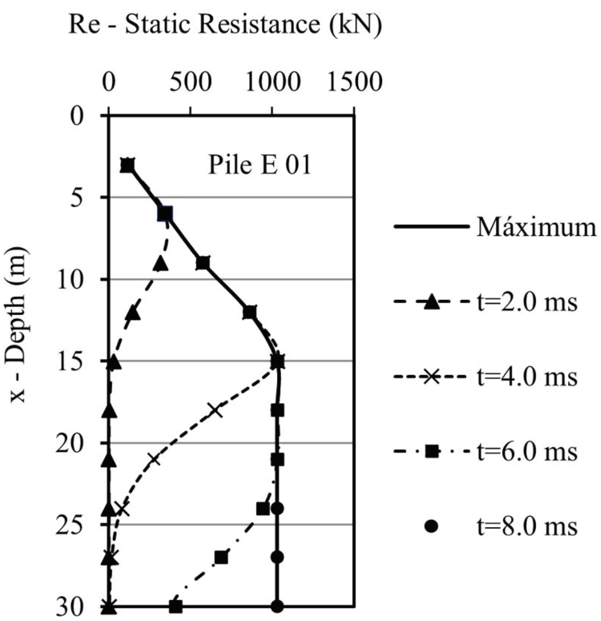

Figure 6. Static Resistances vs depth and time (v_o=4.33 m/s at t=0).

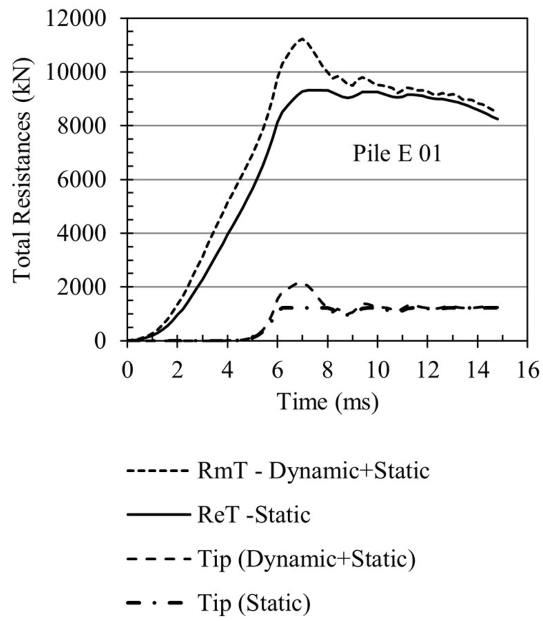

Figure 7. Total Resistances vs time (v_o=4.33 m/s at t=0).

Figure 9 shows that there is a mismatch between the mobilization of the R_{eT} and the development of displacements at the top (D_o): D_o grows faster than R_{eT}.

Moreover, the relationship between the total static resistance (R_{eT}) and the dynamic displacement at the top (D_o) (Figure 10) is not elasto-plastic, as is supposed by the Energy Approach Equation (Equation 4 and Figure 1). It is concluded, therefore, that this equation does not represent reality: it is a fiction.

Figure 11 is an extension of Figure 10, as it includes all blows of Tables 3 and 4, in addition to blow 5 (v_o=4.33 m/s at t=0). It also includes the envelop representing the curve *RMX* as a function of *DMX*. This same curve is reproduced in Figure 12, along with two others: a) the *RMX* curve as a function of *DMX* plus the sets of the previous blows, as proposed by Aoki (1989) and Niyama & Aoki (1991);

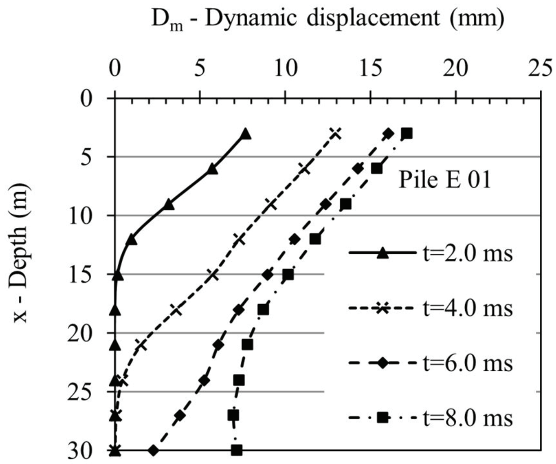

Figure 8. Dynamic Displacements vs depth and time (v_o=4.33 m/s at t=0).

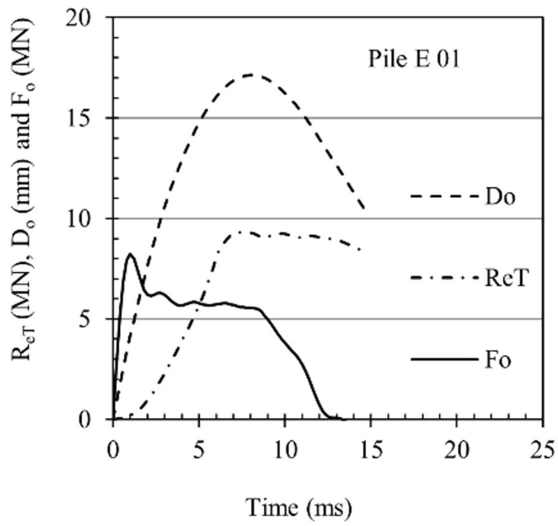

Figure 9. Force, Resistance and Displacement along time (v_o=4.33 m/s at t=0).

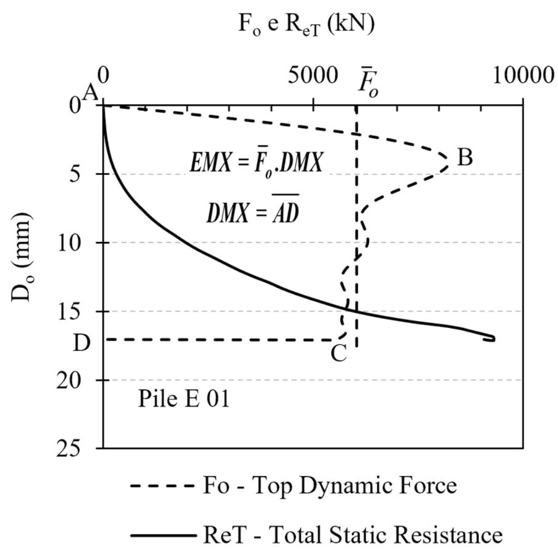

Figure 10. Force or Resistance vs. Displacement (D_o) (v_o=4.33 m/s at t=0).

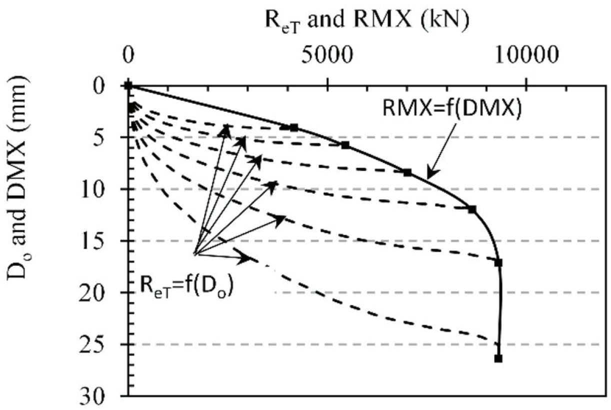

Figure 11. Resistances vs. D_o and R_{eT} (Blows of Tables 3 and 4).

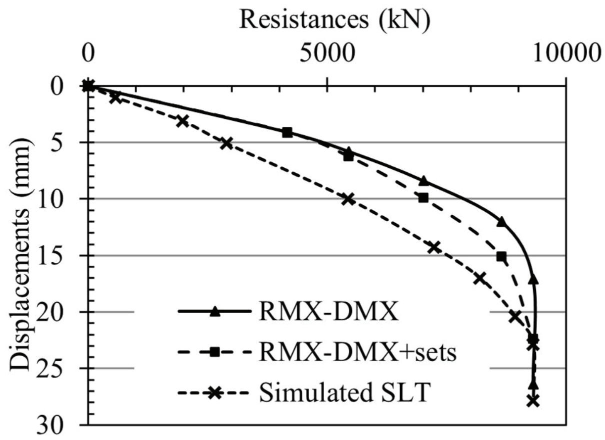

Figure 12. Resistances-Displacements curves (Blows of Tables 3 and 4).

and b) the load-displacement curve for blow 6 of Table 3 simulating the static loading test (SLT) obtained through the Method of Coyle & Reese (1966), considering the maximum resistances, quakes, and pile stiffness. It is concluded that for the analyzed pile E-1 the Aoki-Niyama curve falls short of the simulated curve.

At time $t \approx 8$ ms $v_o=0$ (Figure 3a), $D(t)$ and $E(t)$ reach the maximum values, DMX and EMX, respectively. The $F_o.v_o$ product assumes negative values between 8 and 13 ms (Figure 13a), hence the inflection in the $E(t)$ curve as displayed in Figure 13-b. The value of EMX can be obtained as shown in Equation 18, where $\bar{F}_o$ is an average value between t=0 and t=8 ms. In fact, the third term in this equation is a result of the application of the Mean Value Theorem (Pastor et al., 1958), because in the interval 0 to 8 ms the following inequation holds: $F_o.v_o \geq 0$.

$$EMX = \int_0^{t_o} F_o v_o dt = \bar{F}_o \cdot \int_0^8 v_o dt = \bar{F}_o\left[D(8) - D(0)\right] = \bar{F}_o DMX \quad (18)$$

Another conclusion arises from the $ABCD$ curve of Figure 10, which represents the variation of F_o with D_o between 0 and t=8 ms. The area bounded by this curve corresponds

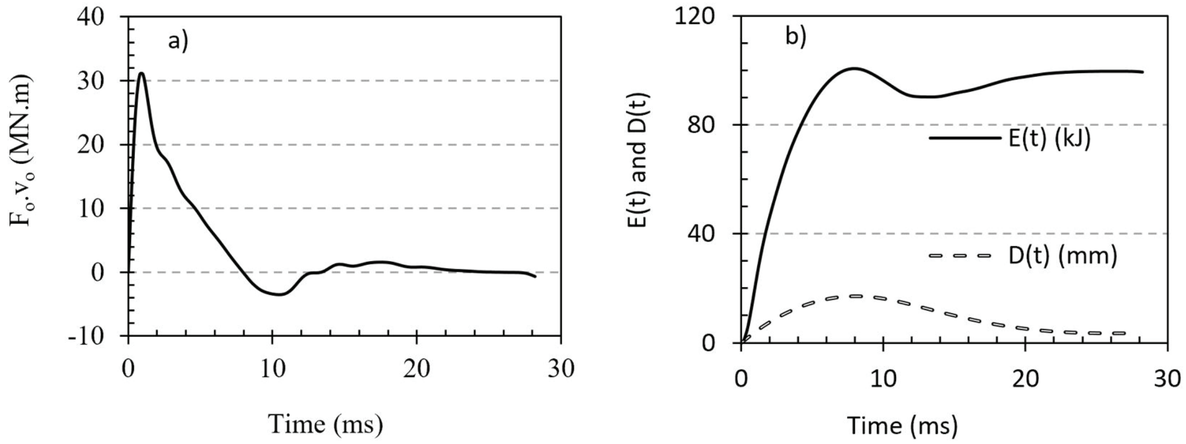

Figure 13. a) The product $F_o.v_o$ vs time and b) Energy (E) and Displacement (D) vs time.

to the *EMX* value, which has nothing to do with the work of total static resistance R_{eT}, putting again the Energy Approach Equation in question.

7. Evaluation of Uto's formula

Another conclusion refers to the application of the Uto's Formula, Equations 5 and 6. For the type of pile (E-1) the correction factor e_o (Equation 6) assumes a value of the order of 1.10, so that for blow 5 of Table 4:

$$R_d^{tip} = \frac{11.8*316}{1.10} \cong 3390\,kN \gg 448\,kN\;(see\;Figure4) \tag{19}$$

It is interesting to mention the results indicated in Figure 14, related to pile E-1, blow 5 (v_o=4.33 m/s at t=0), but assuming that the maximum static lateral and tip loads are 5000 kN and 4306 kN, respectively, adding up the same total static load 9306 kN. The distribution of the shaft friction (f) along depth was supposed to be the same (λ=0.6).

Figure 14 shows that for t=8.8 ms the dynamic force F is resisted only by the tip, with R_d^{tip} =4078 kN. As K_D=15.3, the Uto's Formula gives:

$$R_d^{tip} = \frac{15.3*316}{1.10} \cong 4400\,kN \tag{20}$$

about 8% more. This case fulfills one of the conditions of Uto´s Formula, i.e, practically no dynamic shaft friction.

8. Evidence from three case histories

Next, results of dynamic loading tests with increasing energy on three case histories comprising pipe piles will be presented. The piles were quite different as shown in Table 5.

The subsoil in the case of Osasco (SP) consisted of 3.5 m of a landfill (SPT=4 to 5), followed by layers of soft fluvial clays up to 9.1 m (SPT=1 to 3) and residual soil (SPT=25 to 55). The water level was 3 m deep.

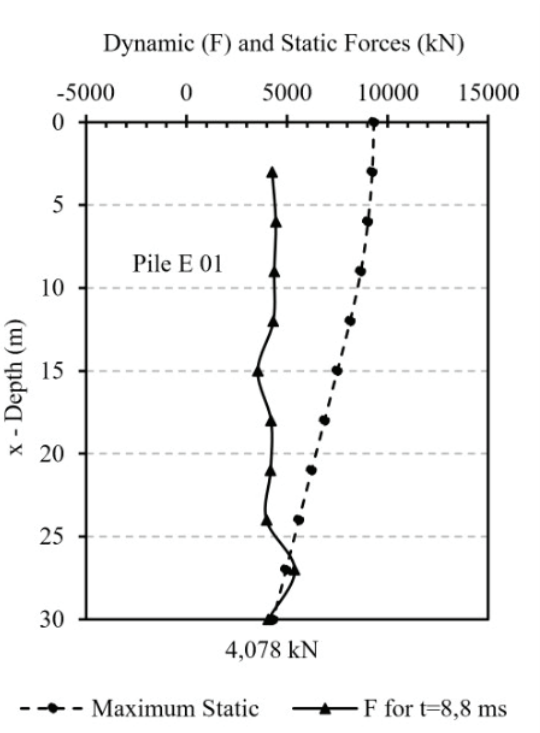

Figure 14. Axial Forces vs depth (v_o=4.33 m/s at t=0 and max. static tip load =4306 kN).

In the case of a pier of Santos (SP), below 6 m of water there was a layer of 20 m of a soft Holocene clay (SPT=1 to 5), followed by 10 m of fine clayey sand (SPT=7 to 33) and 8 m of a Pleistocene clay (SPT~7) over thick sand layer (SPT~40).

Finally, the subsoil in Cubatão (SP) consisted of sandy fill 6 m thick (SPT=1 to 10), followed by a layer of a Holocene marine clay (SPT=1 to 5) up to 24 m deep. Below there were two layers of sand (SPT=15 to 30 and 30 to 15, respectively) up to roughly 40 meters deep, followed by residual soil of gneiss. The water level was 1 m deep.

Details of the hammers and of the instruments that were used and the sequence of blows in each pile are presented in the references shown in Table 5. The collected data were analyzed through the CAPWAP software by specialized technicians, with match quality control. Static loading simulations were made for the blows of maximum energy. Some results of dynamic loading tests on these piles are presented in Table 6 and in Figures 15 to 17.

Table 5. Characteristic of the piles submitted to dynamic loading tests.

Case	*Type*	*D_e (cm)*	*D_i (cm)*	*L (m)*	*L_c (m)*	Reference
1. Osasco	Concrete	38.0	20.3	14.1	13.8	Murakami & Massad (2016)
2. Santos	Concrete	80.0	50.0	52.0	43.4	Valverde & Massad (2018)
3. Cubatão	Steel pipe	91.4	88.2	40.1	33.3	Valverde & Massad (2018)

Legend: see attached list of symbols.

Table 6. Dynamic loading tests results for the blows of maximum energy.

Case	*Kr (kN/mm)*	*EMX (kN.m)*	*RMX (kN)*	*DMX (mm)*	*A_l (kN)*	*Q_p (kN)*
Osasco	253	20.8	2001	12.5	1001	1000
Santos	201	133.2	8041	26.4	6225	1816
Cubatão	280	84.4	559	16.4	4647	4912

Legend: see attached list of symbols.

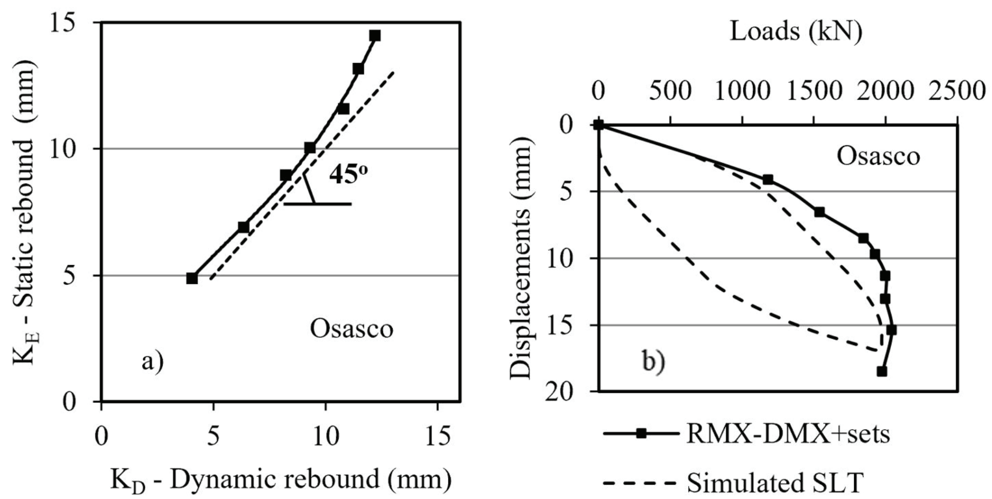

Figure 15. First case history - a) K_E vs K_D and b) Loads vs displacements.

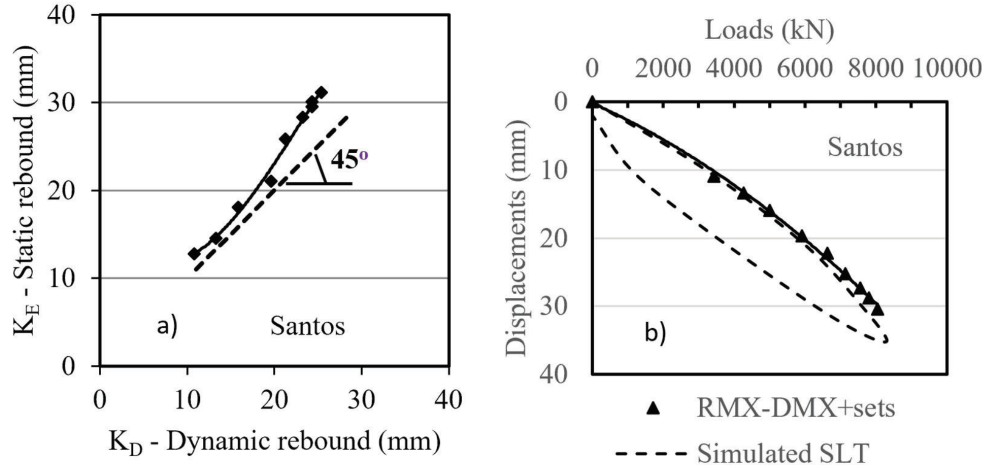

Figure 16. Second case history - a) K_E vs K_D and b) Loads vs displacements.

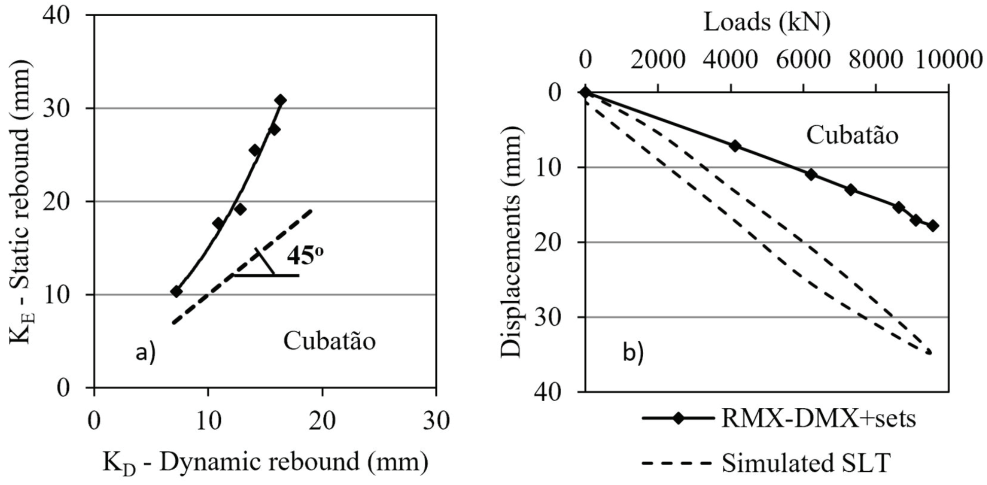

Figure 17. Third case history - a) K_E vs K_D and b) Loads vs displacements.

As can be seen, there are different behaviors in terms of: a) the rebounds K_E and K_D, on the one hand; and b) of the load-displacement curves, on the other hand. In fact:

a) the elastic rebounds (K_D), measured during pile driving, are lower than the corresponding static values (K_E), again because they are related to the dynamic forces and not to the resistance of the soil, as Casagrande intuited; and
b) the curves *RMX-DMX* plus the sets of the previous blows fall short of the simulated static curves with only 1 stroke. The pile in Santos (Figure 16) was an exception, due to higher values of the set (*s*), accumulating about 5mm up to the last stroke.

These differences depend on several factors, such as the distribution of the load in depth (friction and tip), the set values, among others. The phenomenon of pile driving is quite complex.

9. Conclusions

Elastic compression and rebound measured during pile driving may be lower than the corresponding static values because they are related to the dynamic forces and not to the static resistance of the soil, as Casagrande intuited.

This fact explains why the curve *RMX-DMX* plus the sets of the previous blows can fall short of the simulated static curve with one single stroke. Moreover, it conceptually invalidates the use of the Chellis-Velloso Formula to estimate the bearing capacity of a pile.

This last conclusion extends to the Energy Approach Equation based on an elasto-plastic relationship without physical meaning; furthermore, it wrongly relates the transferred energy (*EMX*) to the work of the soil resistances instead of the involved dynamic forces.

The Uto's Formula has restricted use in view of the adopted hypotheses, allowing its application to determine the dynamic force at the tip in cases where lateral friction is exceedingly small.

This makes conceptually unsuccessful attempts to universally validate these formulas. But nothing prevents their use in engineering practice as empirical correlations with correction factors, supported by the dynamic monitoring of some piles of a given work and place.

Acknowledgements

The author thanks the support received from the Polytechnic School of São Paulo University.

Declaration of interest

The author declares absence of conflicting interests.

Author's contributions

Faiçal Massad: conceptualization, methodology, validation, writing, and editing.

References

Aoki, N. (1997). *Determinação da capacidade de carga última de estaca cravada em ensaio de carregamento dinâmico de energia crescente* [Unpublished doctoral dissertation]. Engineering School of São Carlos, University of Sao Paulo. In Portuguese.

Aoki, N. (1989). A new dynamic load test concept. In *Proceedings of the XII International Conference on Soil Mechanics and Foundation Engineering* (pp. 1-4, Discussion section 14), Rio de Janeiro. ISSMGE.

Casagrande, A. (1942). Discussions on the progress report of the Committee on the Bearing Value of Pile Foundations. *Proceedings of the ASCE*, 68(2), 324-331.

Chellis, R.D. (1951). *Pile foundations.* New York: McGraw-Hill Company.

Coyle, H.M., & Reese, L.C. (1966). Load transfer for axially loaded piles in clay. *Journal of the Soil Mechanics and Foundations Division*, 92(2), 1-26. http://dx.doi.org/10.1061/JSFEAQ.0000850.

Leonards, G.A., & Lovell, D. (1979). Interpretation of load tests on high-capacity driven piles. In R. Lundgren (Ed.), *Behavior of deep foundations* (pp. 388-415). Philadelphia: ASTM International.

Murakami, D.K., & Massad, F. (2016). Determinação do quake de estacas pré-moldadas de concreto através de provas de carga estática e ensaios de carregamento dinâmico. *Geotecnia*, 137, 79-98. http://dx.doi.org/10.24849/j.geot.2016.137.05.

Niyama, S., & Aoki, N. (1991). Correlations between static and dynamic load tests in the experimental field of EPUSP. In *Proceedings of the 2nd Seminar on Special Foundations and Geotechnical Engineering* (Vol. 1, pp. 285-293). São Paulo: ABEF.

Paikowsky, S.G., & Chernauskas, L.R. (1992). Energy Approach for capacity evaluation of driven piles. In *Proceedings of the 4th International Conference on the Application of Stress-Wave Theory to Piles* (pp. 21-24). Philadelphia: ASTM International.

Pastor, J.R., Calleja, P., & Trejo, C.A. (1958). *Análisis matemático* (Vol. 1). Buenos Aires Editorial Kapelusz. In Spanish.

Smith, E.A.L. (1960). Pile driving analysis by the wave equation. *Journal of the Soil Mechanics and Foundations Division*, 86(4), 35-61. http://dx.doi.org/10.1061/JSFEAQ.0000281.

Uto, K., Fuyuki, M., & Sakurai, M. (1985). An equation for the dynamic bearing capacity of a pile based on wave theory. In *Proceedings of the International Symposium on Penetrability and Drivability of Piles* (pp. 201-204). Tokyo: Japanese Geotechnical Society.

Valverde, R., & Massad, F. (2018). Maximum envelope of lateral resistance through dynamic increasing energy test in piles. *Soils and Rocks*, 41(1), 75-88. http://dx.doi.org/10.28927/SR.411075.

Velloso, D.A., & Lopes, F.R. (2002). *Fundações profundas* (Vol. 2). Rio de Janeiro: COPPE-UFRJ.

Velloso, P.P.C. (1987). *Fundações: aspectos geotécnicos* (5. ed., Vol. 2-3). Rio de Janeiro: Departamento de Engenharia Civil, PUC.

List of symbols

A_l	Static lateral load
A_{lr}	Maximum static lateral load
c	Wave velocity
C_2	Pile elastic shortening
C_{2D}	Dynamic Pile elastic shortening
C_{2E}	Static Pile elastic shortening
C_3	Toe quake
$D_i;D_e$	Inside and outside pile diameters
D_m	Dynamic displacement
D_o	Value of D_m at pile top (x=0)
DMX	Maximum value of D_m
E Pile	Young's Modulus
EMX	Maximum transferred energy
e_o	Uto's wavelength correction factor (see Equation 6)
F	Axial dynamic force
FMX	Maximum value of $F_{o.}$
F_o	Value of F at pile top (x=0)
$\bar{F}_o$	Average value of F_o between t=0 and $t=t_o$
f	Unit lateral friction (dynamic + static)
f^{est}	Unit lateral friction (static)
f^{est}_{max}	Maximum unit lateral friction (static)
J	Damping factor
J_s	Smith damping (shaft)
J_t	Smith damping (toe)
k	Spring constant
K	Elastic rebound
K_D	Elastic rebound (dynamic)
K_E	Elastic rebound (static)
K_r	Pile Stiffness (Equation 2)
$L;L_c$	Total and embedded pile length
q_s	Shaft quake
q_t	Toe quake
Q_p	Static tip load
Q_{pr}	Maximum static tip load
R,	*RMX* Maximum mobilized loads
R_e	Static resistance in element
R_{eT}	Total static resistance (shaft and toe)
R_d	Dynamic resistance in element
R_{dT}	Total dynamic resistance (shaft and toe)
R_d^{tip}	Mobilized dynamic resistance at the pile tip
R_m	Total resistance in element (R_m=R_e+R_d)
R_{mT}	Total resistance (R_{mT}=R_{eT}+R_{dT})
R_p	Toe resistance
$s;s_f$	Set; final set
SLT	Static Load Test
s_{to}	Set for $t=to$
$S;S_p$	Cross sections of pile (shaft and tip)
t;t$_o$	Time; Time for v=0
u	Axial displacement in element
$v;v_o$	Velocity of element; v at pile top (x=0)
x	Depth
Z	Impedance equals to $E.S/c$
W_H; W_P	Hammer and Pile Weights
α	Parameter of Velloso (Equation 3)
β	Relationship between tip and total loads
κ	Reduction parameter of Paikowsky and Chernauskas (Equation 4)
λ	Leonard and Lovell's coefficient (Equation 3)
ξ	Parameter of Uto's Formula (Equation 6)
ζ	Aoki's parameter
ρ	Specific mass of pile

Soils and Rocks
An International Journal of Geotechnical and Geoenvironmental Engineering
www.soilsandrocks.com
ISSN 1980-9743
ISSN-e 2675-5475

Reinforcing effect of recycled polypropylene fibers on a clayey lateritic soil in different compaction degrees

Natalia de Souza Correia[1#], Sabrina Andrade Rocha[2]

Article

Keywords
Soil improvement
Soil-fiber properties
Lateritic soil
Direct shear test
Compaction degree

Abstract

The present research investigates the reinforcing effect of recycled polypropylene (R-PP) fibers on a compacted clayey lateritic soil in different compaction degrees. R-PP fibers of 12 mm length were mixed with the soil in the contents of 0.1 and 0.25% of soil dry weight. Unconfined compression strength tests (UCS), direct shear tests and indirect tensile strength (ITS) tests were conducted. Fibers addition showed no significate alterations in the optimum compaction parameters. The study evidenced increases in UCS, changing the soil behavior from a brittle failure to a ductile failure, while fiber contribution was most effective for 0.25% R-PP fibers content and 95% compaction degree. The use of fibers improved the shear stress-strain behavior of the composites and soils compacted at different degrees of compaction showed similar shear behavior, which is coherent to the soil water retention curves (SWRC) results. Significant increases in the tensile behavior of soil-mixtures for both fiber contents used were observed, and fibers increase was more significate than increase in soil degree of compaction. The stretching of the fibers and fibers orientation at the sheared interface in direct shear tests and the fiber "bridge" effect in ITS tests could be observed.

1. Introduction

Fiber reinforcement remains a viable soil improvement technique that has been the focus of a growing number of investigations due to a wide range of applications and combinations for use in geotechnical works. The technique of soil mechanical stabilization with fibers can be used in retaining structures, subgrade and subbases pavement layers, slope stability, soft soil embankments, soil hydraulic conductivity control, erosion improvement, piping prevention (Shukla, 2017; Tang et al., 2007; Ziegler et al., 1998) and shrinkage cracks mitigation (Ehrlich et al., 2019). According to Hou et al. (2020), as the global community is turning to a more sustainable way of development, engineers are encouraged to use stabilization technologies that can replace or minimize the use of traditional cement and other curing agents.

In general, research has shown that the fibers randomly distributed in the soil matrix have the advantage of intercepting the potential zone of rupture, and by fibers tensile strength mobilization, improve the soil stress-strain behavior, making the mixture more ductile (Consoli et al., 2012; Li & Zornberg, 2013; Shukla, 2017; Yetimoglu & Salbas, 2003; Zornberg, 2002). However, the investigation of the effect of short fibers on the tensile strength of soils has not been taken extensively (Chebbi et al., 2020).

As regards soil-fiber applications, studies using fine or clayey soils have been less explored than sand-fiber studies in the literature, although widely available in many places and with equal potential for application in geotechnical practice. According to Freilich et al. (2010), there is a need for advancing studies in clayey soil-fibers due to the greater complexity related to fiber interaction mechanism in cohesive soils. The behavior of soils reinforced with polypropylene fibers has also been widely studied (Anagnostopoulos et al., 2013; Cai et al., 2006; Mirzababaei et al., 2017; Plé & Lê, 2012; Tang et al., 2007).

A study presented by Zaimoglu & Yetimoglu (2012) showed the UCS effects of a fine-grained soil reinforced with randomly distributed polypropylene fibers (12 mm length). Results demonstrated a trend of UCS values increasing due to fiber content increase in the soil mix and revealed increases up to 85% in the UCS results when 0.75% fiber content was used. Tang et al. (2007) evaluated the behavior of a clayey soil reinforced with different contents of polypropylene fibers (12 mm length) through direct shear tests. Results revealed

[#]Corresponding author. E-mail address: ncorreia@ufscar.br
[1]Universidade Federal de São Carlos, Departamento de Engenharia Civil, São Carlos, SP, Brasil.
[2]Universidade Federal de São Carlos, Programa de Pós graduação em Engenharia Civil, São Carlos, SP, Brasil.

Submitted on December 16, 2020; Final Acceptance on February 24, 2021; Discussion open until August 31, 2021.
https://doi.org/10.28927/SR.2021.061520

that soil shear strength parameters increased with increasing fiber contents. Wang et al. (2017) investigated the strength behaviors of expansive soil-fibers by direct shear test and triaxial compression tests and found that the fibers enhanced shear strength and deviator stress-strain behavior, reducing the post peak strength loss.

The tensile strength of cohesive soil is an important mechanical parameter that controls tensile cracks initiation and propagation characteristics (Tang et al., 2016). Several types of tests are available to investigate soil tensile behavior and although direct tensile tests of soil are more reliable and more precise than indirect tensile tests, they are difficult to perform (Chebbi et al., 2020; Li et al., 2014; Nahlawi et al., 2004). Divya et al. (2014) studied the fiber content and fiber length effect on tensile-strain characteristics and crack formation, in a silty soil mixed with polyester fibers showing that soil-fiber mixtures were able to withstand more deformation and subsequently higher stresses at failure. Ehrlich et al. (2019) observed that the addition of fibers to the soil increases soil tensile strength and delays the crack opening process. Tang et al. (2016) states that few studies have been conducted to investigate the effect of fiber reinforcements on soil tensile properties and the effects of compaction conditions were rarely examined.

This study aims at investigating the effect of recycled polypropylene (R-PP) fibers on a compacted clayey lateritic soil in different degrees of compaction. R-PP fibers (12 mm length) were mixed with natural soil in the contents of 0.1 and 0.25%, aiming soil improvement. Mechanical tests, such as UCS, direct shear and tensile strength tests were conducted to quantify the fibers contribution to soil properties.

2. Experimental programme

2.1 Materials and samples preparation

A lateritic soil was investigated in this research since it represents typical soils that cover a large area in the Brazilian territory and are found in many places in the world. In this research, the soil used was taken from the city of Santa Gertrudes, Sao Paulo, Brazil, and consists of a clay of high plasticity (CH) according to Unified Soil Classification System (SUCS) in (ASTM, 2017a). Although SUCS classifies this soil as a high plasticity clay, it presents a significate percentage of fine sand. In terms of predominant clay minerals, the clay fraction has Kaolinite, Illite, Gibbsite and Hematite (ASTM, 2014a). According to MCT method of soil classification, this lateritic fine-grained soil is classified as LG' (Nogami & Villibor, 1991). The soil sample was characterized according to: specific gravity test (ASTM, 2014b), particle size analysis (ASTM, 2017b), Proctor test (ASTM, 2012) and Atterberg limits tests (ASTM, 2017c). The properties of the soil are presented in Table 1 and particle size distribution curve of the soil is shown in Figure 1.

The technique of filter paper was used to determine the soil water retention curves (SWRC), standardized by (ASTM, 2016a). Soil samples were compacted at optimum water content and in two conditions of compaction degree: 95% and 98%. The SWRC were constructed by the drying process. The SWRC of the lateritic clay soils are presented in Figure 2. The curves were adjusted by the equation of Fredlund & Xing (1994), depicted in Equation 1. The curve adjustment parameters are shown in Table 2.

The clayey soil presents SWRC with unimodal behaviors in both degrees of compaction, which is coherent with the granulometric distribution of this soil. Results showed a great variation of suction pressures over a small range of soil water contents, due to the greater retention capacity of the soil. SWRC with similar behavior to the soil used in this research were obtained by Feuerharmel et al. (2006) and Portelinha & Zornberg (2017) for compacted fine lateritic soils.

$$w(\Psi) = w_r \cdot (w_s - w_r) \cdot \left(w_1 \cdot \left[\frac{1}{1 + (\alpha_1 \cdot \Psi)^{n_1}} \right]^{m_1} + (1 - w_1) \cdot \left[\frac{1}{1 + (\alpha_2 \cdot \Psi)^{n_2}} \right]^{m_2} \right) \tag{1}$$

where: Ψ is the suction (kPa); w is the moisture content (g/g or m^3/m^3), w_s is the saturated moisture content of the soil; w_r is the residual moisture content of the soil; α, n, m (kPa) are curve fitting parameters.

Regarding different degrees of compaction, the SWRC behavior is coherent with expected results since the more pores in the compacted soil, the further the curve rises and the more it flattens (Figure 2). For the same level of moisture content, the soil compacted at 98% degree of compaction showed a lower level of suction in comparison to 95%.

Polypropylene (PP) fibers were used as the reinforcements in this study. The R-PP fibers have 18 micrometers in diameter, 0.9 g/cm³ of specific mass and 12 mm length, zero water absorption. The fibers are made of recycled polypropylene (R-PP). The characterization of the fibers by fiber filament was not done in this research. According to fiber's manufacturer, the breaking tensile strength of the PP fibers is 610 MPa.

Table 1. Physical properties of the CH soil.

Property Value	Symbol	Value
Soil classification (USCS)	CH	-
Percent sand (%)	-	36
Percent fines (<0.074 mm) (%)	-	64
Specific gravity	G_s	2.9
Maximum dry unit weight (kN/m³)	$\rho_{d(max)}$	16.7
Optimum water content (%)	w_{opt}	24.5
Liquid limit	LL	51
Plasticity limit	PL	29
Plasticity index	PI	22

Table 2. Fitting parameters of SWRC.

Fredlund & Xing (1994) parameters - CH soil (drying)					
	θ_r	a_f		m_f	R^2
(m^3/m^3)	(m^3/m^3)	(kPa)	-	-	-
0.452	0.000001648	8192.8	0.98629	2.8702	0.985
0.432	0.000006693	4147.9	0.97284	2.8707	0.987

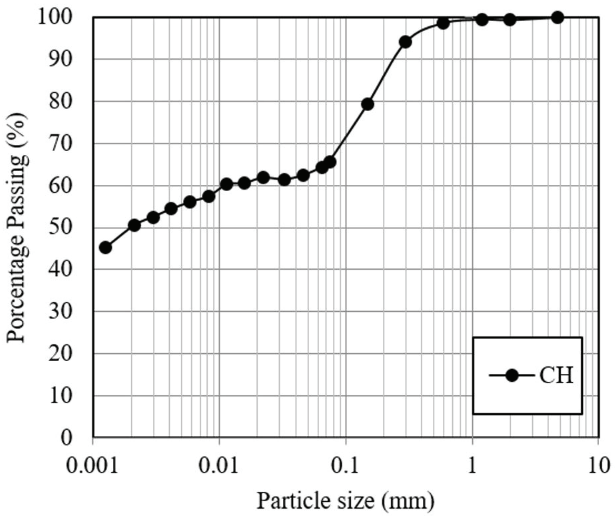

Figure 1. Particle size distribution of the CH soil.

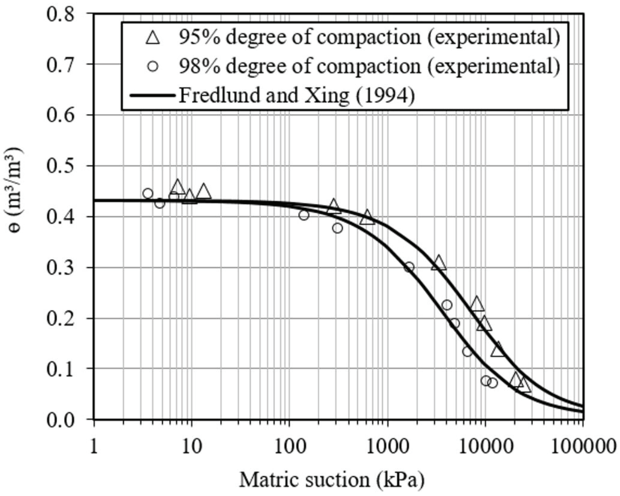

Figure 2. Soil water retention curves of the CH soil in different compaction degrees.

R-PP Fibers were randomly inserted into the soil mass in 0.1% and 0.25% of soil dry weight and were distributed (homogenously) and mixed with the soil. A manual mixer was used to facilitate mixing process. Figure 3 presents soil-fibers mixing process for 0.1% fiber content. Similar fiber contents were found in several studies (Diambra & Ibraim, 2014; Feuerharmel, 2000; Freilich et al., 2010; Li & Zornberg, 2005; Mirzababaei et al., 2017; Özkul & Baykal, 2007; Rowland Otoko, 2014). Soil-fiber mixtures were preserved in air-proof bags for a minimum of 24 hours for moisture homogenization.

2.2 Methods

In order to investigate soil improvement due to fibers inclusion, UCS tests were conducted with following ASTM 2166 (ASTM, 2016b) with samples compacted at the optimum compaction parameters for each soil condition. Natural and fiber-reinforced samples were compacted 95% and 98% compaction degrees. Tests were conducted in triplicates with maximum coefficient of variation of 15%.

For the same conditions of optimum compaction parameters and degrees of compaction, direct shear tests (drained condition) were conducted following ASTM D3080 (ASTM, 2011) on compacted natural soil and R-PP soil mixtures. The test was conducted on shear box of 100 x 100 x 25 mm. Samples were consolidated under vertical stresses of 50, 100 and 200 kPa prior to shearing, and testing loading rate was 0.5 mm/min. Loads and displacements at axial and horizontal directions were recorded automatically by a computer-controlled data collection system. Data of shear stresses as a function of horizontal displacement were recorded up to a total displacement of 15 mm to observe post-failure behaviors.

Brazilian tensile strength method for measuring tensile strength of compacted soils was conducted according to ASTM D3967 (ASTM, 2016c) to quantify the effect of fiber contents on the indirect tensile behavior of the clayey soil.

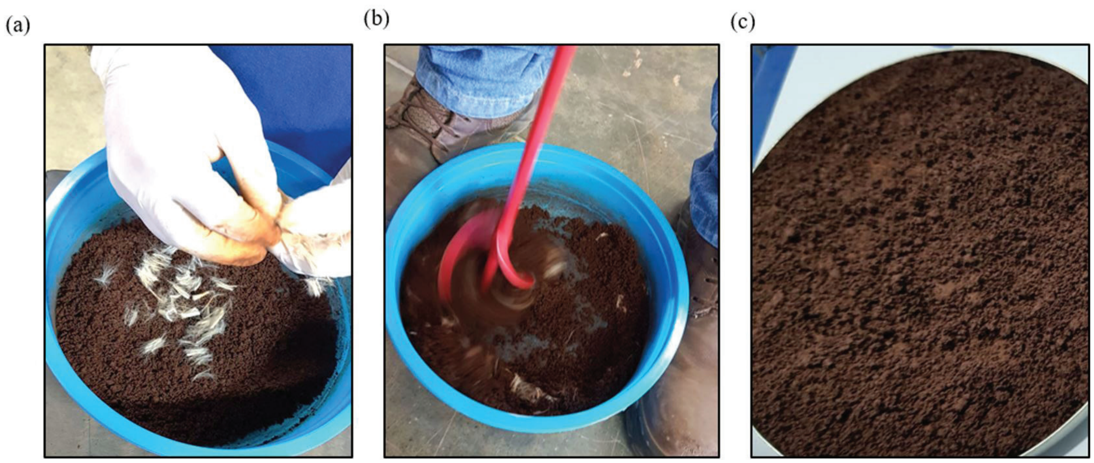

Figure 3. Soil-fiber mixing process: (a) fibers addition; (b) soil mixing process; (c) homogenized soil-fiber mix.

Tests were conducted using samples compacted at 95% and 98% degrees of compaction, in triplicate, and with maximum coefficient of variation of 15%.

3. Results and discussion

3.1 Behavior of R-PP fibers on soil compaction properties

Figure 4 presents the compaction curves of CH soil mixtures with 0.1% and 0.25% fiber content, compared to respective natural soils. Maximum dry unit weight values did not change with fiber inclusion in the clayey soil, while the optimum water content values slightly increased. Results of no significate alterations in the compaction curves of soil-fiber mixtures were evidenced by others studies (Gelder & Fowmes, 2016; Kumar & Singh, 2008; Marçal et al., 2020; Mirzababaei et al., 2013).

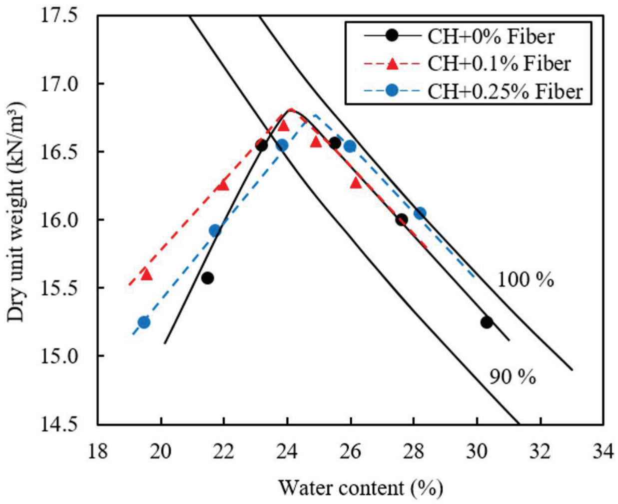

Figure 4. Proctor compaction curves natural soil and R-PP fiber mixtures.

3.2 Influence of R-PP fibers on soil unconfined compression strength

The axial stress-strain curves from UCS tests of natural soil and R-PP fibers reinforced mixtures are shown in Figure 5 for the different soil compaction degrees. Analyzing the stress-strain curves of the natural soil and soil-fiber mixtures, it is observed that for the natural soil there was a significant reduction in resistance after the rupture of the specimen. On the other hand, mixtures of 0.10% soil-fiber and 0.25% soil-fiber showed increases in strength with increase in strains, changing the soil behavior from a brittle failure to a ductile failure. This result is consistent with that presented in previous studies, carried out in clayey soil, using different types of fibers (Marçal et al., 2020; Tang et al., 2007; Tran et al., 2018). Figure 6 shows typical photographs after tests for samples compacted at 95% compaction degree of compaction.

Figure 7 compares UCS results for the different degrees of compaction as function of R-PP fiber content in the clayey soil. For both cases, UCS increased with increasing degree of compaction. However, for 95% degree of compaction, the contribution of 0.1% and 0.25% of R-PP fibers to increase UCS of soil was more significant than the results presented at 98% degree of compaction. This analysis evidenced that the fiber contribution was most effective for 95% degree of compaction, showing that fiber content increase was most significate than compaction degree increase.

The increases obtained in UCS due to the inclusion of fibers are consistent with previous results from the literature that evaluated PP fibers, e.g., (Kumar & Singh, 2008; Santoni et al., 2002; C. Tang et al., 2007; Zaimoglu & Yetimoglu, 2012). Tang et al. (2007) states that this increase in UCS results might be related to the fibers bridging effect,

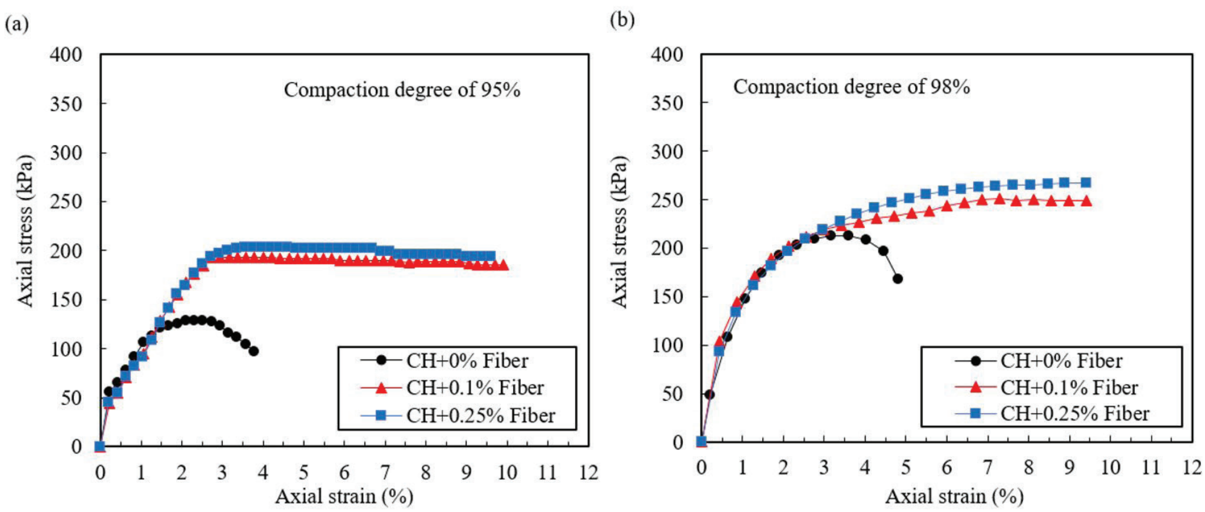

Figure 5. Axial stress-strain results of natural soil and R-PP fiber mixtures: (a) 95% degree of compaction; (b) 98% degree of compaction.

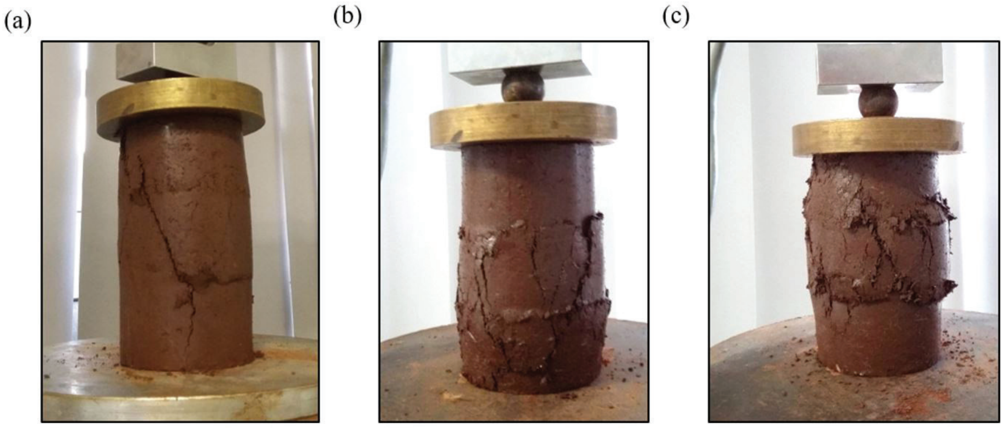

Figure 6. Samples compacted at 95% degree after failure for: (a) natural soil; (b) 0.1% fiber content; (c) 0.25% fiber content.

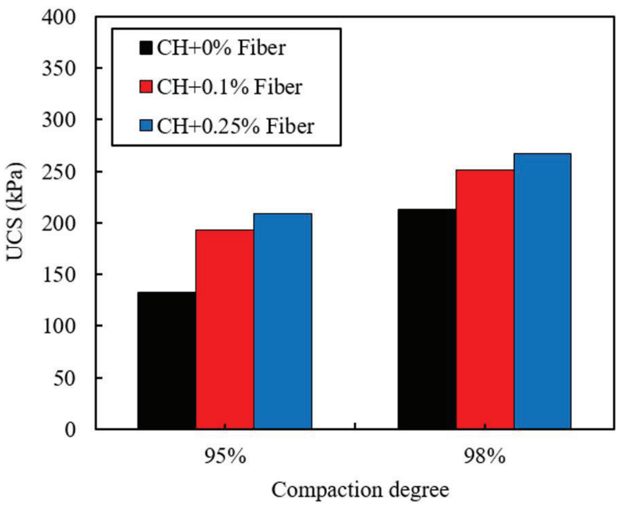

Figure 7. UCS results for both degrees of compaction as function of R-PP fiber content in the clayey soil.

which can efficiently prevent the further development of failure planes and deformations of the soil.

3.3 Influence of R-PP fibers on soil shear strength

Direct shear tests were conducted considering each combination of soil and R-PP fibers and degree of compaction. Results of shear stress-displacement curves are presented in Figure 8. For both degrees of compaction, the inclusion of fibers improved the shear stress-strain behavior of the composite for all the normal stresses analyzed. Results of shear stress for 0.25% fiber content was superior to 0.1% fiber content addition, showing the improvement of soil shear properties due to fiber reinforcement in both degrees of compaction. For 95% degree of compaction (Figure 8a), initial stiffness of the soil increased with R-PP fibers addition, for all normal stresses analyzed, indicating superior fibers mobilization. Still in Figure 8, it is important to highlight that, regarding substantially more ductile behavior for soil-fibers compacted 98% compaction degree in comparison to untreated soil, this may be a prejudice rather than a benefit depending on the desired behavior for the soil.

Figure 9 presents typical photographs after direct shear tests for samples with 0.25% fiber content and 95% degree of compaction. The stretching of the fibers and fibers orientation at the sheared interface can be visualized. Darvishi & Erken (2018) and Kumar & Singh (2008) highlights the mechanism of fibers stretching in the soil matrix during the shearing process. According to Kong et al. (2019), the extension of fibers is due to the rearrangement and microstructure disturbance during shearing provides an important contribution to the strength increase.

Figure 10 shows the shear strength envelopes of CH soil and R-PP fiber-reinforced soils for 95% and 98% degrees of compaction. Results are presented considering values of peak shear strength. Higher shear strength was evidenced in 0.1% and 0.25% soil-fiber mixes for 95% degrees of compaction, where the contribution was more attributed to apparent cohesion than friction. Regarding SWRC data (Figure 2), the soil compacted at 95% degree of compaction presented superior suction than the soil compacted at 98% degree of compaction, which approximates soil shear behaviors. On the other hand, for 98% degrees of compaction, the contribution was more attributed to friction angle. For Shao et al. (2014) and Yetimoglu & Salbas (2003), the increase in the friction angle is most probably associated with mobilization of friction between fibers and the soil particles. It is important to highlight that lateritic soils present good shear strength behavior when unsaturated, as observed by the high soil friction angle.

Figure 11 presents the improvement in soil shear strength properties for all analyzed cases. As observed in UCS tests, results of shear stress for 0.25% fiber content addition was superior to 0.1% fiber content, showing improvement in soil properties due to fiber reinforcement in both degrees of compaction. That means that the number of fibers in the shear plane is a very important parameter (Marçal et al., 2020). In

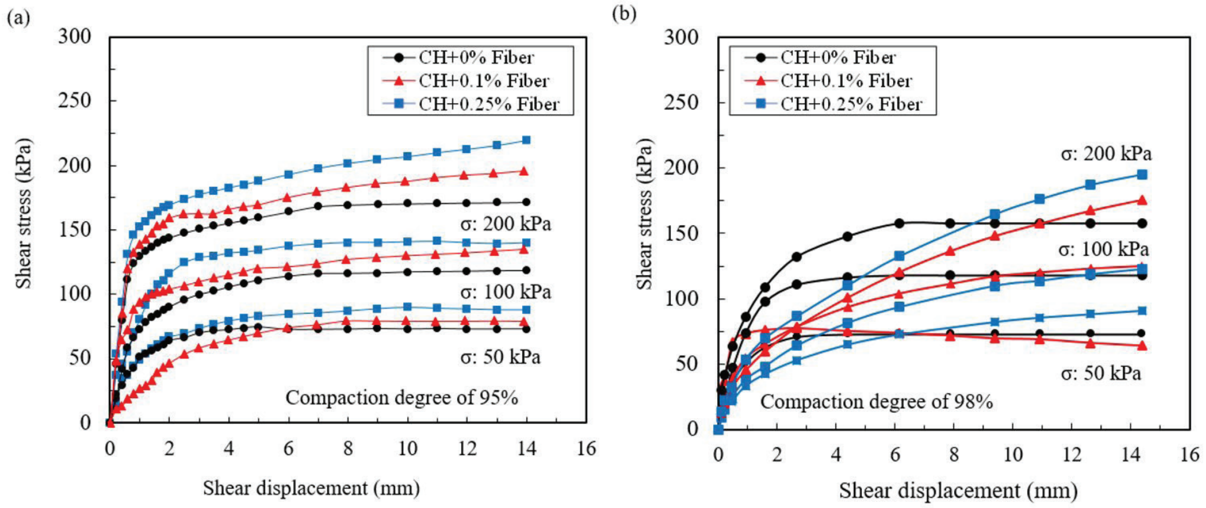

Figure 8. Shear stress-displacement curves of natural soil and R-PP fiber mixtures: (a) 95% degree of compaction; (b) 98% degree of compaction.

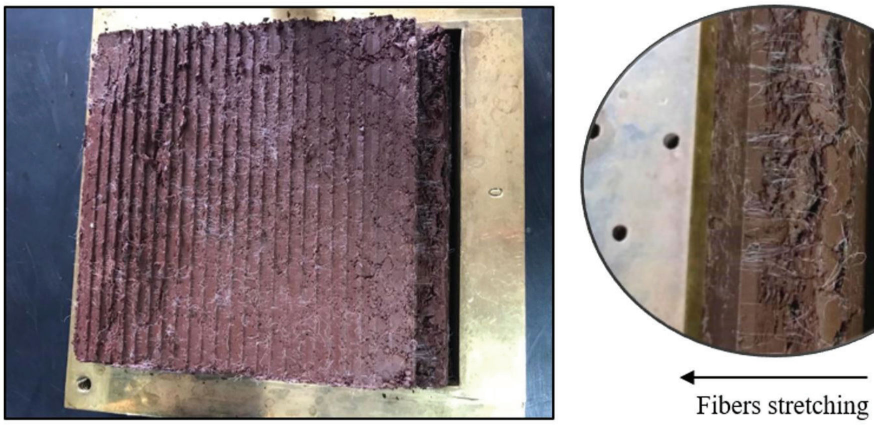

Figure 9. Stretching of the fibers during shearing.

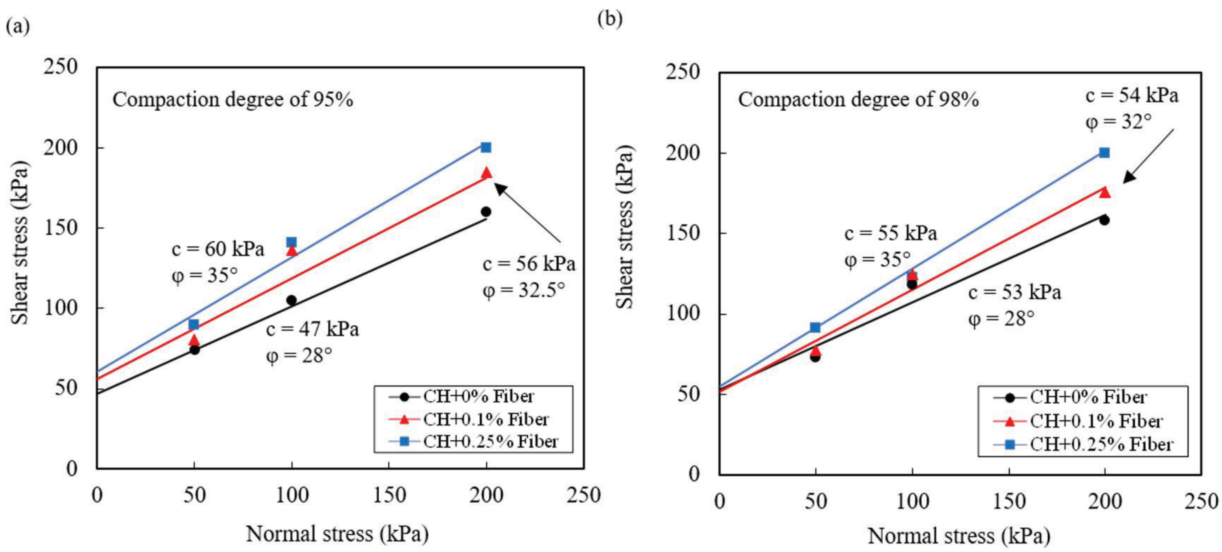

Figure 10. Shear strength envelopes of natural soil and R-PP fiber mixtures: (a) 95% degree of compaction; (b) 98% degree of compaction.

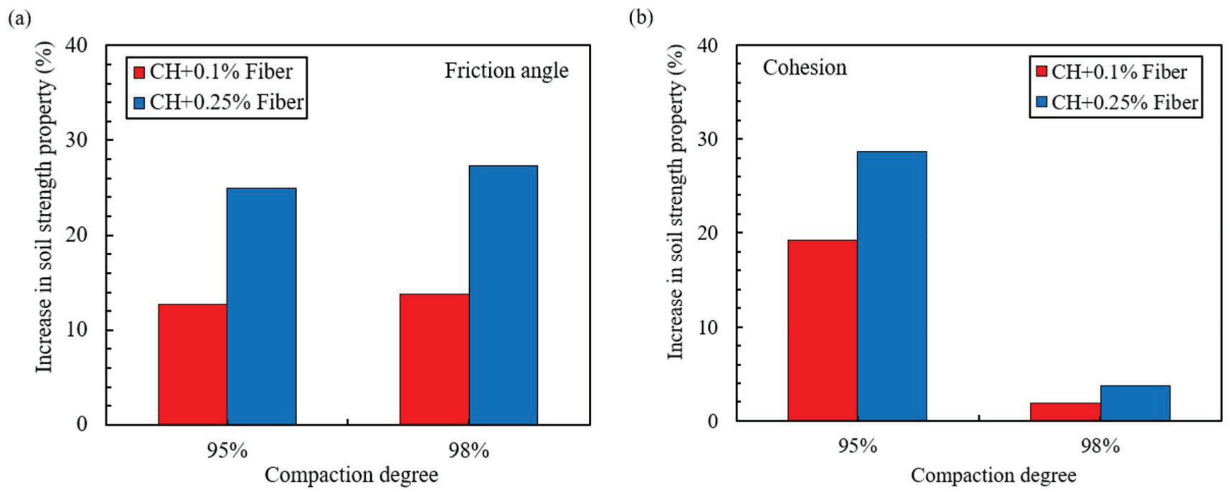

Figure 11. Results of improvement in soil shear strength properties for all analyzed cases: (a) friction angle; (b) cohesion.

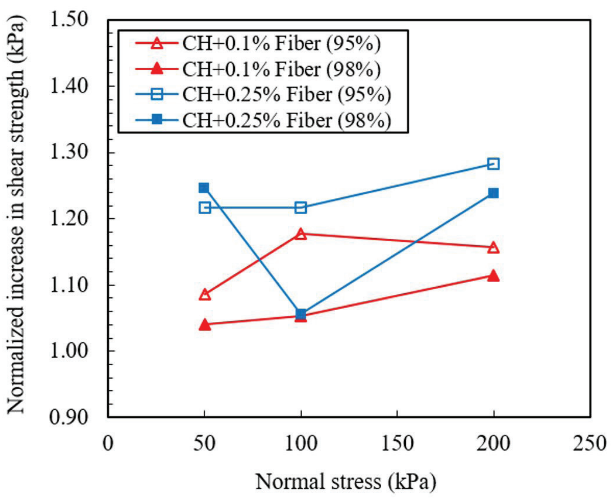

Figure 12. Normalized improvement in soil shear strength after R-PP fibers addition.

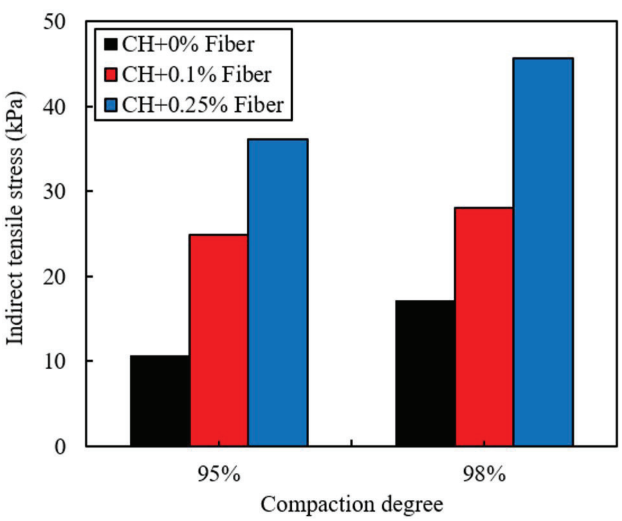

Figure 13. Indirect tensile stress results of natural soil and fiber-soil mixtures.

general, improvement in soil friction angle (Figure 11a) was most significate than improvement in soil apparent cohesion (Figure 11b). Figure 12 presents normalized improvement in shear strength of CH soil and R-PP fiber-reinforced soils for 95% and 98% degrees of compaction. Results showed a slight increase in shear stresses with increasing normal stresses for both compaction degrees and evidences improvement in soil strength after R-PP fibers addition.

3.4 Influence of R-PP fibers on indirect tensile behavior

Indirect tensile strength tests were conducted to quantify the effect of fiber content on the indirect tensile behavior of natural soil since it is an important mechanical parameter that controls the initiation and propagation characteristics of tensile cracks. Figure 13 presents the results of indirect tensile stress of natural clay and 0.1% and 0.25% fiber-soil samples compacted at 95% and 98% degrees of compaction. The tensile strength of the clayey soil increased with increase in fibers content and increased with increase in soil compaction degree. In terms of tensile behavior, the effect of fibers increase was more significate than the effect of compaction properties. Li et al. (2014) mentioned that the fibers share some tensile load for the soil matrix, since the movement of the fibers in the soil matrix is prevented by the interactions between the fibers and the soil matrix, causing greater resistance to the composite.

Figure 14 shows the failure mode of soil-fiber mixtures and fibers stretching details for 0.1% and 0.25% fibers addition. The fiber-reinforced specimens formed the fiber "bridges" reported by Tang et al. (2007). The "bridging" effect of fibers prevented the early development of traction cracks and, consequently, corroborated the more ductile behavior of the soil-fiber mixtures. Tang et al. (2016) states the post-failure tensile behavior is mainly conditioned by

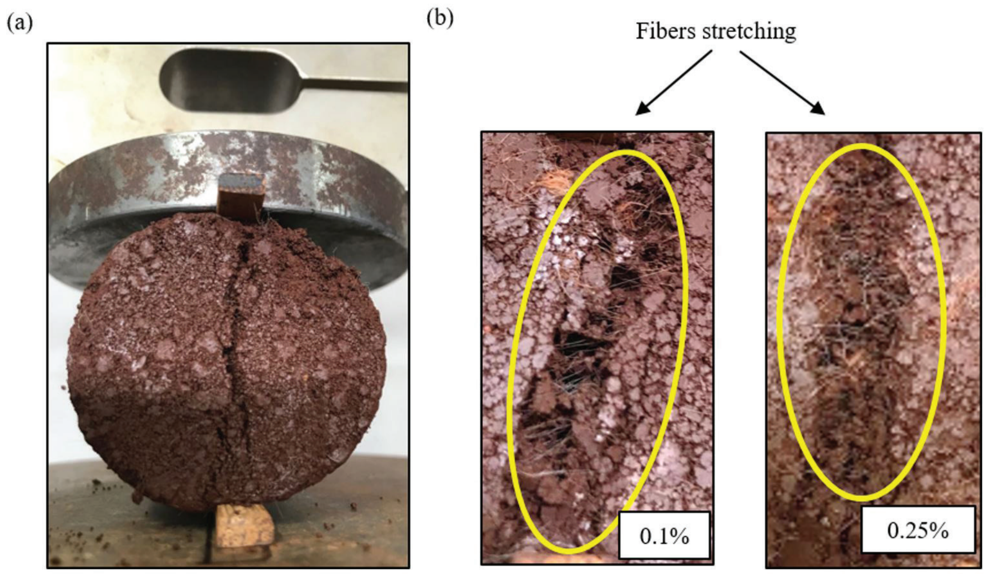

Figure 14. Failure mode of soil-fiber mixtures: (a) detail of rupture; (b) fibers stretching detail at 98% compaction degree.

the interfacial shear strength of the embedded fibers and the tensile strength of the fibers.

4. Conclusions

This study evaluated the reinforcing effect of recycled polypropylene fibers on a clayey lateritic soil compacted in different compaction degrees. The study involved UCS tests, direct shear tests and indirect tensile strength tests. Outcomes of the combinations of fiber contents and degrees of compaction were evaluated. The following conclusions can be drawn:

- The use of R-PP fibers as reinforcements in the clayey lateritic soil revealed an increase in UCS, changing the soil from a brittle behavior to a ductile failure in all evaluated cases. Fibers contribution was most effective for 95% compaction degree. Nevertheless, the increase in fiber content from 0.1 to 0.25% showed a significate effect on the UCS of clayey lateritic soil, being most effective than increasing soil degree of compaction;
- Direct shear tests results indicated that, for both degrees of compaction, the inclusion of R-PP fibers improved the shear stress-strain behavior of the composite with similar results. Higher shear strength was evidenced in 0.1% and 0.25% soil-fiber mixes for 95% degrees of compaction, where the contribution was more attributed to apparent cohesion than friction. Soil compacted at 95% degree of compaction presented superior suction than the soil compacted at 98% degree of compaction, which approximates soil shear behaviors;
- The tensile strength of the clayey soil increased with increase in fibers content and increased with increase in soil compaction degree. In terms of tensile behavior, the effect of fibers increase was more significate than the effect of compaction properties;
- The stretching of the fibers and fibers orientation at the sheared interface could be visualized, while the “bridging” effect of fibers could be overserved in the tensile strength test.

Acknowledgements

Authors acknowledge the Laboratory of Geotechnics and Geosynthetics of the Federal University of Sao Carlos and Laboratory of Geotechnics of Federal University of Viçosa.

Declaration of interest

The authors declare no conflict of interest.

Author’s contributions

Natalia de Souza Correia: supervision, conceptualization, writing - original draft preparation, revision. Sabrina Andrade Rocha: investigation, data curation, validation.

References

Anagnostopoulos, C.A., Papaliangas, T.T., Konstantinidis, D., & Patronis, C. (2013). Shear strength of sands reinforced with polypropylene fibers. *Geotechnical and Geological Engineering*, 31(2), 401-423. http://dx.doi.org/10.1007/s10706-012-9593-3.

ASTM D3080-11. (2011). *Standard test method for direct shear test of soils under consolidated drained conditions.* ASTM International, West Conshohocken, PA. https://doi.org/10.1520/D3080.

ASTM D698-12e12. (2012). *Standard test methods for laboratory compaction characteristics of soil using standard effort (12 400 ft-lbf/ft³ (600 kN-m/m³)).* ASTM International, West Conshohocken, PA. https://doi.org/10.1520/D0698-12E01.1.

ASTM D4452-14. (2014a). *Standard practice for X-ray radiography of soil samples.* ASTM International, West Conshohocken, PA. https://doi.org/10.1520/D4452-14.

ASTM D854-14. (2014b). *Standard test methods for specific gravity of soil solids by water pycnometer.* ASTM International, West Conshohocken, PA. https://doi.org/10.1520/D0854-10.2.

ASTM D5298-16. (2016a). *Standard test method for measurement of soil potential (suction) using filter paper.* ASTM International, West Conshohocken, PA. https://doi.org/10.1520/D5298-16.

ASTM D2166. (2016b). *Standard test method for unconfined compressive strength of cohesive soil.* ASTM International, West Conshohocken, PA. https://doi.org/10.1520/D2166_D2166M-16.

ASTM D3967. (2016c). *Standard test method for splitting tensile strength of intact rock core specimens.* ASTM International, West Conshohocken, PA. https://doi.org/10.1520/D3967-16.

ASTM D2487-17. (2017a). *Standard practice for classification of soils for engineering purposes (unified soil classification system).* ASTM International, West Conshohocken, PA. https://doi.org/10.1520/D2487-17.

ASTM D7928-17. (2017b). *Standard test method for particle-size distribution (gradation) of fine-grained soils using the sedimentation (hydrometer) analysis.* ASTM International, West Conshohocken, PA. https://doi.org/10.1520/D7928-17.

ASTM D4318-17e1. (2017c). *Standard test methods for liquid limit, plastic limit, and plasticity index of soils* (Vol. 4, pp. 1-14). ASTM International, West Conshohocken, PA. https://doi.org/10.1520/D4318-10.

Cai, Y., Shi, B., Ng, C.W.W., & Tang, C.S. (2006). Effect of polypropylene fibre and lime admixture on engineering properties of clayey soil. *Engineering Geology*, 87(3-4), 230-240. http://dx.doi.org/10.1016/j.enggeo.2006.07.007.

Chebbi, M., Guiras, H., & Jamei, M. (2020). Tensile behaviour analysis of compacted clayey soil reinforced with natural and synthetic fibers: effect of initial compaction conditions. *European Journal of Environmental and Civil Engineering*, 24(3), 354-380. http://dx.doi.org/10.1080/19648189.2017.1384762.

Consoli, N.C., Thomé, A., Girardello, V., & Ruver, C.A. (2012). Uplift behavior of plates embedded in fiber-reinforced cement stabilized backfill. *Geotextiles and Geomembranes*, 35, 107-111. http://dx.doi.org/10.1016/j.geotexmem.2012.09.002.

Darvishi, A., & Erken, A. (2018). Effect of polypropylene fiber on shear strength parameters of sand. In *Proceedings of the 3rd World Congress on Civil, Structural, and Environmental Engineering (CSEE'18)*, Budapest, Hungary. https://doi.org/10.11159/icgre18.123.

Diambra, A., & Ibraim, E. (2014). Modelling of fibre-cohesive soil mixtures. *Acta Geotechnica*, 9(6), 1029-1043. http://dx.doi.org/10.1007/s11440-013-0283-y.

Divya, P.V., Viswanadham, B.V.S., & Gourc, J.P. (2014). Evaluation of tensile strength-strain characteristics of fiber-reinforced soil through laboratory tests. *Journal of Materials in Civil Engineering*, 26(1), 14-23. http://dx.doi.org/10.1061/(ASCE)MT.1943-5533.0000772.

Ehrlich, M., Almeida, S., & Curcio, D. (2019). Hydro-mechanical behavior of a lateritic fiber-soil composite as a waste containment liner. *Geotextiles and Geomembranes*, 47(1), 42-47. http://dx.doi.org/10.1016/j.geotexmem.2018.09.005.

Feuerharmel, C., Gehling, W.Y.Y., & Bica, A.V.D. (2006). The use of filter-paper and suction-plate methods for determining the soil-water characteristic curve of undisturbed colluvium soils. *Geotechnical Testing Journal*, 29(5), 419-425. http://dx.doi.org/10.1520/gtj14004.

Feuerharmel, M.R. (2000). *Comportamento de solos reforçados com fibras de polipropileno* [Master's dissertation]. Universidade Federal do Rio Grande do Sul. Retrieved in December 16, 2020, from http://hdl.handle.net/10183/2804

Fredlund, D.G., & Xing, A. (1994). Erratum : equations for the soil-water characteristic curve. *Canadian Geotechnical Journal*, 31(6), 1026. http://dx.doi.org/10.1139/t94-120.

Freilich, B.J.J., Li, C., & Zornberg, J.G.G. (2010). Effective shear strength of fiber-reinforced clays. In *Proceedings of the 9th International Conference on Geosynthetics - Geosynthetics: Advanced Solutions for a Challenging World (ICG 2010)*, Guarujá, Brazil.

Gelder, C., & Fowmes, G.J. (2016). Mixing and compaction of fibre- and lime-modified cohesive soil. *Proc. Institution of Civil Engineers: Ground Improvement*, 169, 98-108. http://dx.doi.org/10.1680/grim.14.00025.

Hou, T., Liu, J., Luo, Y., & Cui, Y. (2020). Triaxial compression test on consolidated undrained shear strength characteristics of fiber reinforced soil. *Soils and Rocks*, 43(1), 43-55. http://dx.doi.org/10.28927/SR.431043.

Kong, Y., Zhou, A., Shen, F., & Yao, Y. (2019). Stress-dilatancy relationship for fiber-reinforced sand and its modeling. *Acta Geotechnica*, 14(6), 1871-1881. http://dx.doi.org/10.1007/s11440-019-00834-6.

Kumar, P., & Singh, S.P. (2008). Fiber-reinforced fly ash subbases in rural roads. *Journal of Transportation Engineering*, 134(4), 171-180. http://dx.doi.org/10.1061/(ASCE)0733-947X(2008)134:4(171).

Li, C., & Zornberg, J.G. (2013). Mobilization of reinforcement forces in fiber-reinforced soil. *Journal of Geotechnical* *and Geoenvironmental Engineering*, 139(1), 107-115. http://dx.doi.org/10.1061/(ASCE)GT.1943-5606.0000745.

Li, C., & Zornberg, J.G. (2005). Interface shear strength in fiber-reinforced soil. In *Proceedings of the 16th International Conference on Soil Mechanics and Geotechnical Engineering: Geotechnology in Harmony with the Global Environment* (Vol. 3, pp. 1373-1376), Osaka, Japan. https://doi.org/10.3233/978-1-61499-656-9-1373.

Li, J., Tang, C., Wang, D., Pei, X., & Shi, B. (2014). Effect of discrete fibre reinforcement on soil tensile strength. *Journal of Rock Mechanics and Geotechnical Engineering*, 6(2), 133-137. http://dx.doi.org/10.1016/j.jrmge.2014.01.003.

Marçal, R., Lodi, P.C., Correia, N. de S., Giacheti, H.L., Rodrigues, R.A., & McCartney, J.S. (2020). Reinforcing effect of polypropylene waste strips on compacted lateritic Soils. *Sustainability*, 12(22), 9572. http://dx.doi.org/10.3390/su12229572.

Mirzababaei, M., Arulrajah, A., Horpibulsuk, S., & Aldava, M. (2017). Shear strength of a fibre-reinforced clay at large shear displacement when subjected to different stress histories. *Geotextiles and Geomembranes*, 45(5), 422-429. http://dx.doi.org/10.1016/j.geotexmem.2017.06.002.

Mirzababaei, M., Miraftab, M., Mohamed, M., & McMahon, P. (2013). Unconfined compression strength of reinforced clays with carpet waste fibers. *Journal of Geotechnical and Geoenvironmental Engineering*, 139(3), 483-493. http://dx.doi.org/10.1061/(ASCE)GT.1943-5606.0000792.

Nahlawi, H., Chakrabarti, S., & Kodikara, J. (2004). A direct tensile strength testing method for unsaturated geomaterials. *Geotechnical Testing Journal*, 27(4), 356-361. http://dx.doi.org/10.1520/gtj11767.

Nogami, J.S., & Villibor, D.F. (1991). Use of lateritic fine-grained soils in road pavement base courses. *Geotechnical and Geological Engineering*, 9(3-4), 167-182. http://dx.doi.org/10.1007/BF00881739.

Özkul, Z.H., & Baykal, G. (2007). Shear behavior of compacted rubber fiber-clay composite in drained and undrained loading. *Journal of Geotechnical and Geoenvironmental Engineering*, 133(7), 767-781. http://dx.doi.org/10.1061/(ASCE)1090-0241(2007)133:7(767).

Plé, O., & Lê, T.N.H.H. (2012). Effect of polypropylene fiber-reinforcement on the mechanical behavior of silty clay. *Geotextiles and Geomembranes*, 32(0), 111-116. http://dx.doi.org/10.1016/j.geotexmem.2011.11.004.

Portelinha, F.H.M., & Zornberg, J.G. (2017). Effect of infiltration on the performance of an unsaturated geotextile-reinforced soil wall. *Geotextiles and Geomembranes*, 45(3), 211-226. http://dx.doi.org/10.1016/j.geotexmem.2017.02.002.

Rowland Otoko, G. (2014). Stress-strain behaviour of an oil palm fibre reinforced lateritic soil. *International Journal of Engineering Trends and Technology*, 14(6), 295-298. http://dx.doi.org/10.14445/22315381/IJETT-V14P257.

Santoni, R.L., Tingle, J.S., & Webster, S.L. (2002). Stabilization of silty sand with nontraditional additives. *Transportation Research Record: Journal of the Transportation Research Board*, 1787(1), 61-70. http://dx.doi.org/10.3141/1787-07.

Shao, W., Cetin, B., Li, Y., Li, J., & Li, L. (2014). Experimental investigation of mechanical properties of sands reinforced with discrete randomly distributed fiber. *Geotechnical and Geological Engineering*, 32(4), 901-910. http://dx.doi.org/10.1007/s10706-014-9766-3.

Shukla, S.K. (2017). *Fundamentals of fibre-reinforced soil engineering* (Developments in Geotechnical Engineering). Switzerland: Springer.

Tang, C.-S., Wang, D.-Y., Cui, Y.-J., Shi, B., & Li, J. (2016). Tensile strength of fiber-reinforced soil. *Journal of Materials in Civil Engineering*, 28(7), 04016031. http://dx.doi.org/10.1061/(ASCE)MT.1943-5533.0001546.

Tang, C., Shi, B., Gao, W., Chen, F., & Cai, Y. (2007). Strength and mechanical behavior of short polypropylene fiber reinforced and cement stabilized clayey soil. *Geotextiles and Geomembranes*, 25(3), 194-202. http://dx.doi.org/10.1016/j.geotexmem.2006.11.002.

Tran, K.Q., Satomi, T., & Takahashi, H. (2018). Improvement of mechanical behavior of cemented soil reinforced with waste cornsilk fibers. *Construction & Building Materials*, 178, 204-210. http://dx.doi.org/10.1016/j.conbuildmat.2018.05.104.

Wang, Y.-X., Guo, P.-P., Ren, W.-X., Yuan, B.-X., Yuan, H.-P., Zhao, Y.-L., Shan, S.-B., & Cao, P. (2017). Laboratory investigation on strength characteristics of expansive soil treated with jute fiber reinforcement. *International Journal of Geomechanics*, 17(11), 04017101. http://dx.doi.org/10.1061/(ASCE)GM.1943-5622.0000998.

Yetimoglu, T., & Salbas, O. (2003). A study on shear strength of sands reinforced with randomly distributed discrete fibers. *Geotextiles and Geomembranes*, 21(2), 103-110. http://dx.doi.org/10.1016/S0266-1144(03)00003-7.

Zaimoglu, A.S., & Yetimoglu, T. (2012). Strength behavior of fine grained soil reinforced with randomly distributed polypropylene fibers. *Geotechnical and Geological Engineering*, 30(1), 197-203. http://dx.doi.org/10.1007/s10706-011-9462-5.

Ziegler, S., Leshchinsky, D., Ling, H.I., & Perry, E.B. (1998). Effect of short polymeric fibers on crack development in clays. *Soil and Foundation*, 38(1), 247-253. http://dx.doi.org/10.3208/sandf.38.247.

Zornberg, J.G. (2002). Discrete framework for limit equilibrium analysis of fibre-reinforced soil. *Geotechnique*, 52(8), 593-604. http://dx.doi.org/10.1680/geot.2002.52.8.593.

List of symbols

CH	High plasticity clay
m_f	curve fitting parameters
n_f	curve fitting parameters
θ_r	volumetric residual moisture content
θ_s	volumetric saturated moisture content
SWRC	Soil water retention curves
w	gravimetric moisture content
w_r	gravimetric residual moisture content
w_s	gravimetric saturated moisture content
α	curve fitting parameters
Ψ	suction
G_s	Specific gravity
$\rho_{d(max)}$	Maximum dry unit weight (kN/m^3)
w_{ot}	Optimum water content (%)
LL	Liquid limit
PL	Plasticity limit
PI	Plasticity index

Soils and Rocks
An International Journal of Geotechnical and Geoenvironmental Engineering
www.soilsandrocks.com
ISSN 1980-9743
ISSN-e 2675-5475

An experimental study on improvement of cohesive soil with eco-friendly guar gum

Baki Bagriacik[1], Bahadir Ok[2#], Mustafa Tahseen Mohamed Ali Kahiyah[1]

Article

Keywords
Weak soil improvement by biopolymer
Environmentally friendly additive
SEM analyses of soils
Curing effect
Organic additive

Abstract

Recently, the demand for environmentally friendly products has been increasing worldwide. In this study, the improvement of cohesive soil with a biopolymer material (Guar Gum), which is a type of additive and organic, environmentally friendly, is investigated. For this purpose, various laboratory tests have been conducted on the biopolymer-added soils, including the compaction test, the Atterberg limits test, and the unconfined compressive strength test. The samples for tests have been prepared that the biopolymer has been mixed with the soil in three different proportions to determine the optimum mixing ratio. Also, in the biopolymer-added soils, some samples have been cured at varying times to determine the effect of curing periods on their strength. For comparison, the tests performed on improved soils have been also carried out on the untreated cohesive soil. For a comprehensive evaluation, scanning electron microscopy analyses (SEM analyses) was carried out on some samples. On the other hand, X-ray fluorescence analysis (XRF analysis) was performed to have an idea about the composition of the cohesive soil. Consequently, the biopolymer additive material has improved the geotechnical properties of the cohesive soil in all mixing ratios and curing times. Moreover, the optimum mixing ratio has been obtained at 1% according to the results of tests.

1. Introduction

The soil is the outer layer that covers the globe and contains crushed rocks, water, mineral materials, and organic matter inside. The soil containing the silt and natural particles is the result of the loss of bonding elements due to the weathering and temperature difference in different seasons with time. Soils can be insufficient for construction requirements due to inadequate of its geotechnical properties such as shear strength and consolidation. Particularly, loose or soft soils can be unable to resist the loads imposed on them. These weak soils need to improve their geotechnical properties to be ready for various engineering projects. Generally, geotechnical properties of weak soils are improved by using compressive mechanisms, or by adding additives to it (Kumar & Kumar, 2020). In previous studies, some additive materials such as cement, lime, fly ash, slag, polymers, glass water, acid, epoxy etc. were used to improve the soil (Marto et al., 2014; Kampala et al., 2014; Arulrajah et al., 2016; Dash & Hussain, 2012; Cristelo et al., 2013; Du et al., 2014; Tingle & Santoni, 2003; Sarici, 2019; Najah et al., 2013; Oliveira Júnior et al., 2019; Menezes et al., 2019). However, these additives can cause serious damage to the environment although they can improve the soil. A few studies have stated some environmental problems and pollutions formed by the use of these additives (Worrell et al., 2001; Afolabi et al., 2012; Chang et al., 2016; Mascarenha et al., 2018). Today in the construction industry as in many fields, environmentally friendly materials are encouraged to be used due to various environmental concerns. Therefore, it is very significant in terms of reducing the damage to the environment of additives and the sustainability of resources to investigate environmentally friendly additives, which do not cause environmental damage, such as biopolymers, in soil improvement. Accordingly, many researchers continue to study these additives (Chang & Cho, 2011; Chang et al., 2015, 2016; Khatami & O'Kelly, 2013; Ayeldeen et al., 2016; Im et al., 2017; Lee et al., 2019; Cabalar et al., 2017; Cole et al., 2012; Ivanov & Chu, 2008; Mitchell & Santamarina, 2005; Fatehi et al., 2018; Soldo et al., 2020).

[#]Corresponding author. E-mail address: bahadirok@atu.edu.tr
[1]Cukurova University, Faculty of Engineering, Civil Engineering Department, Adana, Turkey.
[2]Adana Alparslan Turkes Science and Technology University, Faculty of Engineering, Civil Engineering Department, Adana, Turkey.

Submitted on November 23, 2020; Final Acceptance on May 5, 2021; Discussion open until August 31, 2021.
https://doi.org/10.28927/SR.2021.060020

Biopolymers are polymers produced from biological organisms by biodegradation such as fungi, algae, and bacteria. They consist of polysaccharides, which are mixtures consisting of monosaccharides linked at identified positions. Ultimately, biopolymers are non-toxic and biodegradable due to their structures owned. Hence, they can be accepted as environmentally friendly additives (Cole et al., 2012; Ivanov & Chu, 2008; Mitchell & Santamarina, 2005).

The use of various biopolymers such as natural bitumen, straw, and sticky rice in civil engineering applications goes back to ancient times. For example, sticky rice mortar was used as a binder in the Great Wall of China which still stands nowadays (Chang et al., 2016). In the literature, there are some studies related to the usability of biopolymers to develop the geotechnical properties of soil. In these studies, it is stated that biopolymers can be used as an additive (Chang & Cho, 2011; Chang et al., 2015, 2016; Khatami & O'Kelly, 2013; Ayeldeen et al., 2016; Im et al., 2017; Lee et al., 2019; Cabalar et al., 2017; Fatehi et al., 2018; Soldo et al., 2020). However, these studies are generally on improving loose sandy soil. At the same time, the sandy soil used in a few studies had some fine particles. For example, Soldo et al. (2020) performed a study on a soil, SW-SM (well-graded sand with silt), which has fine particles classified as silt with low plasticity. In their study, they stated that biopolymers can significantly increase the strength of the soil. However, the rate of sand in the soil was higher than cohesive soil even if some parts of the soil used in this study contained cohesion. Although biopolymers have grand potential as additives, a remarkable study on cohesive soils related to this topic has not been found. Therefore, the improvement by biopolymers of cohesive soils is still well-unknown.

In this study, the improvement of cohesive soil by the Guar Gum (GG), which is a type of biopolymer and can be used as an additive material, was investigated. Test samples were prepared by mixing the soil with the GG at three different ratios as 1%, 2%, and 3%, and then some samples were cured during six different periods as 1 day, 7 days, 14 days, 21 days, 56 days and 196 days. Subsequently, laboratory tests such as the compaction test, the Atterberg limits test, and the unconfined compressive strength (UCS) test have been conducted on the prepared samples and untreated samples. Also, scanning electron microscopy analyses (SEM analyses) and X-ray fluorescence analysis (XRF analysis) carried out on some prepared samples and cohesive soil, respectively.

2. Materials and methods

2.1 Natural soil

The soil used in the study was collected in Adana, Turkey. The chemical composition and geotechnical properties of this soil have been specified by the laboratory tests. As the result of Atterberg limits tests conducted out on this soil, the liquid limit and plastic limit values of the soil have been determined as 42% and 24%, respectively, according to the Standard ASTM D 4318-00 (ASTM, 2003). Moreover, the particle-size distribution of the soil obtained as a result of hydrometer and sieve analysis is shown in Figure 1. As a result of these tests, the soil has been classified according to ASTM D 2487-06 (ASTM, 2006) as low plasticity clay (CL).

As a result of the pycnometer test, the particle unit weight of the soil has been determined as 27kN/m3 (ASTM, 2018). On the other hand, the optimum moisture content and the maximum dry unit weight, obtained by Proctor test (ASTM, 2009a), were found as 18.1% and 17.40 kN/m^3, respectively. In the result of the unconfined compressive strength (UCS) tests performed on the clay soil (ASTM, 2009b), the UCS value of the clay soil was 128.48 kPa (Kahiyah, 2020). The compaction and unconfined compressive curves of the clay soil are shown in Figure 2. Finally, the chemical composition of this soil has been determined by performing the X-ray fluorescence analysis (XRF analysis), as per ASTM E 2809 (ASTM, 2013). According to the result of the XRF analysis, the soil consists of MgO (6.1%), Al2O3 (18.4%), SiO2 (50.6%), P2O5 (0.65%), K2O (3.1%), CaO (3.2%), MnO (3.1%), Fe2O3 (8.7%), Na2O (2.5%) and LL (3.15%). Accordingly, the soil possesses alumina and silicate in high ratios. Moreover, calcite, quartz and a few groups of clay minerals such as smectite, kaolinite and vermiculite have been detected in the soil.

2.2 Guar Gum (GG)

GG is a biopolymer appropriated in different fields of the industry, mostly due to its structural characteristics, which

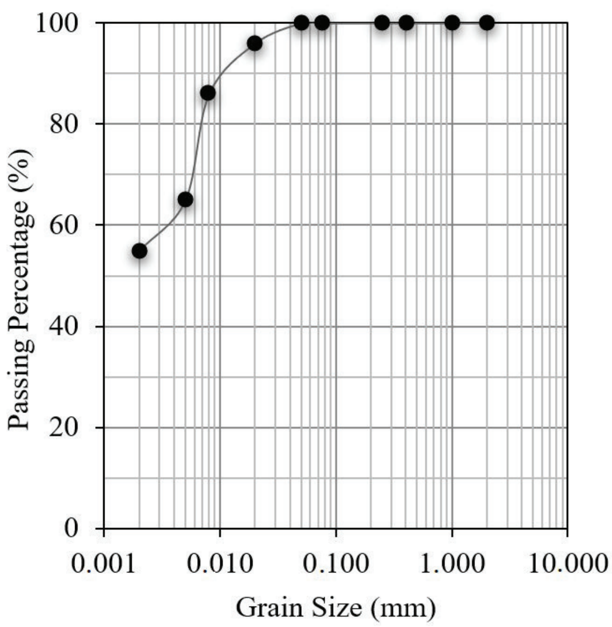

Figure 1. Particle-size distribution of the clay soil (Kahiyah, 2020).

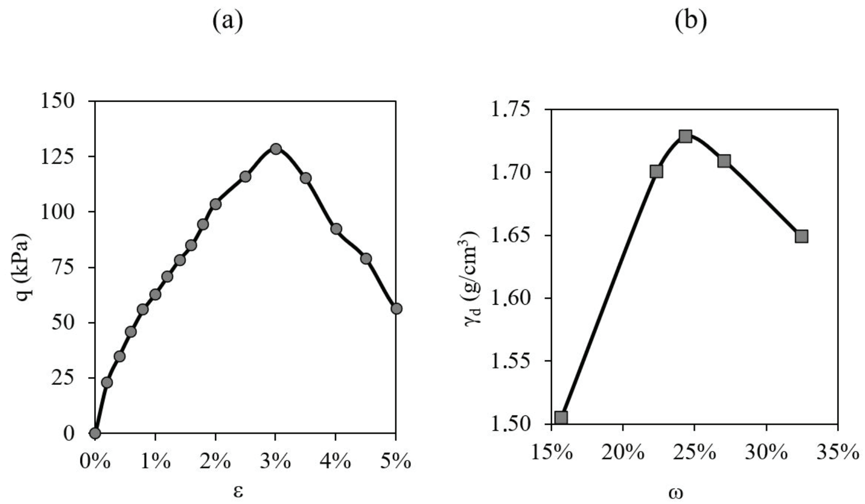

Figure 2. Curves of (a) unconfined compression and (b) compaction tests of the clay soil.

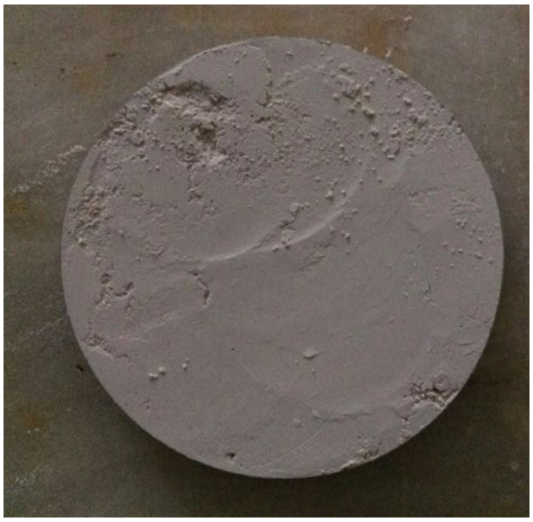

Figure 3. The GG powder.

Figure 4. The wet mixing method (Kahiyah, 2020).

form greatly viscous suspensions at low concentrations. It is a typical non-ionic polysaccharide and composes of mannose and galactose. Commonly-known properties of guar gum can be listed that (1) GG has a pH range of about 1.0 to 10.5 due to its non-ionic and its viscosity also is not affected by the pH, (2) GG can swell and or dissolve in a polar solvent, and also it can form strong hydrogen bonds. It is cheap, easily produced, and available from chemical companies (Whistler & Hymowitz, 1980; Risica et al., 2010; Sharma et al., 2015; Kahiyah, 2020). The GG used in this study was obtained from a chemical company (Figure 3).

2.3 Sample preparation

In this study, GG has been mixed to the soil at three different ratios as 1%, 2%, and 3% by wet mixing method. Accordingly, the quantity of the GG calculated according to the amount of the soil was mixed with a specific quantity of water, which is required for tests, using a mixer. The mixing process was continued until GG soluble in water (Figure 4). Subsequently, the prepared mixture was mixed with the dry soil (Fatehi et al., 2018; Chang et al., 2015; Kahiyah, 2020).

For UCS tests, firstly, soils were placed by tamping in the proctor mold to provide their maximum unit weights and optimum moisture contents obtained from the proctor test. Subsequently, samples, which have a diameter of 50 mm and a length of 100 mm, were removed from this mold with the help of a sampler. Finally, the samples were cured during six different periods. For this, samples, which are obtained mixing soil with GG, were held in isolation bags inside the desiccators at varying times as 1 day, 7 days, 14 days, 21 days, 56 days and 196 days. Then, sequentially, UCS tests were performed on the cured samples. Sujatha & Saisree (2019) stated that after forming gel-like structures (hydrogels) due to the GG, these gels wraps soil grains and form hydrogen bonds. Subsequently, they mentioned that in order to strengthen these hydrogen bonds formed, they should be dehydrated. For this reason, they suggested dry curing at room temperature. Similarly, some researchers stated in their studies that dry curing is more effective (Lee et al., 2019; Chang et al., 2015).

In addition, Sujatha & Saisree (2019) recommended the curing is carried out in an airtight environment to prevent oxidation of the GG. For these reasons, a similar curing method has been carried out in this study.

2.4 Test procedure

Firstly, the Atterberg limits test according to ASTM D 4318-00 (ASTM, 2003) and compaction tests according to ASTM D 698-00 (ASTM, 2009a) has been carried out on samples, mixed with the GG in different ratios. Then, according to ASTM D 2166 (ASTM, 2009b), the UCS test has been performed on the cured samples, which have optimum moisture content. Finally, the Scanning Electron Microscope images (SEM images) of samples obtained from the only GG and the soil-the GG mixture, which contains 1% the GG and is cured for 21 days, have been taken to determine their microstructures (Figure 5). Besides, the Energy Dispersive Spectroscopy (EDS) to specify the elemental composition of samples imaged in the scanning electron microscope has been used. Most elements with concentrations of 0.1% in the sample can be detected with this technique (Moretti et al., 2020). Subsequently, SEM/EDS analyses have been performed by using obtained images.

3. Results and discussion

3.1 Atterberg limits

The liquid limit, plastic limit, and the plasticity index of untreated soil and the soils, which are mixed with the GG, are shown in Figure 6. Increasing the liquid limit value of soil means that it decreases the range where the soil acts like a liquid. Hence, the soil can be more rigid at certain water contents. Furthermore, it has determined from SEM analyses that the GG has been gel-like form after it is mixed with water and this the gel-like structure formed some bonds between the clay soil particles. After adding the GG to the clay soil, the change in consistency limits is thought to be caused by this mechanism.

3.2 Compaction tests

Compaction curves of untreated soil and the soils, which are mixed with the GG, are shown in Figure 7. It is seen in the curves that as the percentage of GG in the soil-GG mixture has increased, the optimum water content has increased and the maximum dry unit weight has decreased. Based on the observation in the tests, it can be said that the GG is a very water-absorbent material. The high water absorption of the GG has been thought to negatively affect the compaction parameters of the soil-GG mixture. Therefore, in fillings by using the GG-soil mixture water consumption might be a

Figure 5. SEM device.

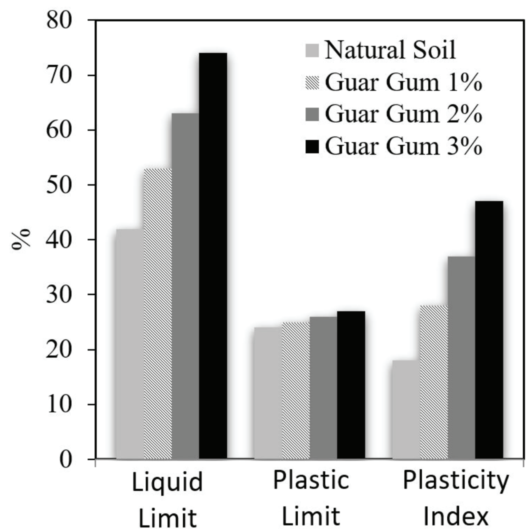

Figure 6. Liquid limit, plastic limit, plasticity index values of the soils.

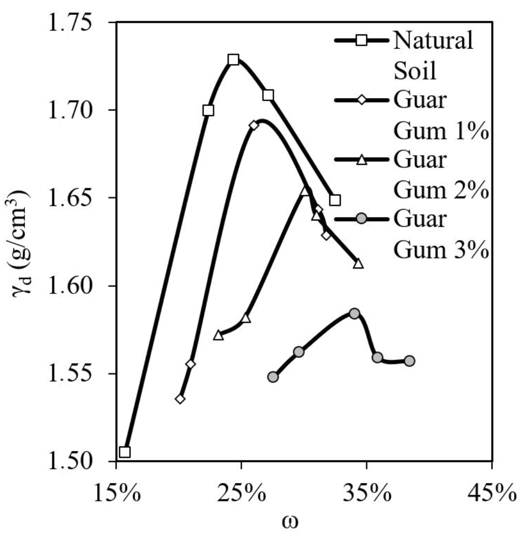

Figure 7. Compaction curves of the soils.

little too much than that of other fillings. In fact, it is thought that this case does not prevent building a filling by using the GG-soil mixture. Nevertheless, water consumption should be taken into account when constructing a filling.

3.3 Unconfined compressive strength (UCS) tests

Results of UCS tests performed on soils that are cured during 1 day and contained 1%, 2%, and 3% GG are presented by comparing with that of untreated soil in Figures 8. As can be seen from the figure, the highest strength was obtained for the soil having 1% GG. This percentage of GG has been accepted as the optimum ratio. As similar to the result in this study, Soldo et al. (2020) determined the optimum percentage of GG in the soil-GG mixture as 1% in their study, which performed on a soil containing a part of silt with low plasticity. Results of UCS tests at different curing periods such as 1 day, 7 days, 14 days, and 21 days in the optimum percentage of the GG are shown in Figure 9. As seen in this figure, the strength of the soil-GG mixture increased as the curing period increased. While the strength of the soil increased approximately 6 times than untreated soil after 1-day of curing, it increased about 9 times after 21 days of curing. It is thought that this increase in strength of the soil-GG mixture occurs in a few steps as the curing time increases. Initially, when the GG is mixed with water, hydrogels start to form due to hydration. Subsequently, when this is mixed with the soil, hydrogels formation continues by absorbing the water in the soil. After that, these hydrogels form hydrogen bonds by coating soil particles. Finally, these bonds become thicker and stronger when the hydrogels are

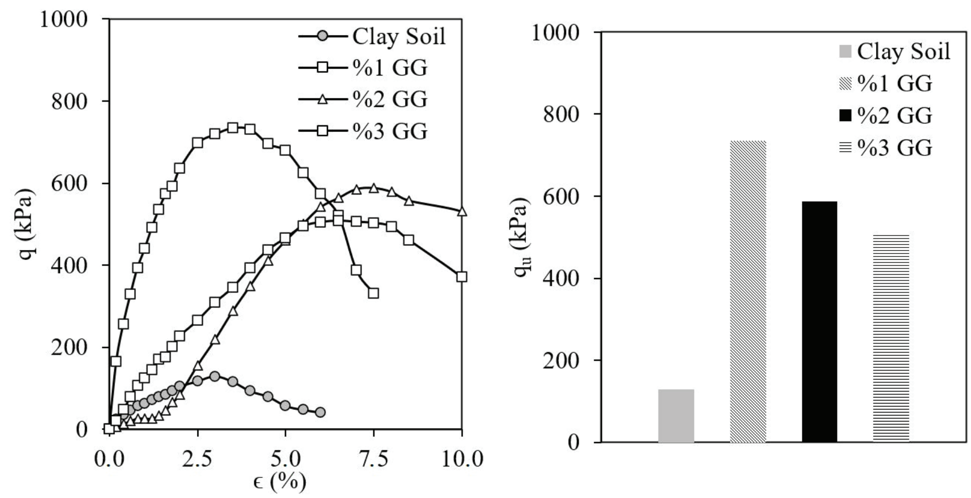

Figure 8. Results of UCS tests for different ratios of GG (the samples were cured during 1 day).

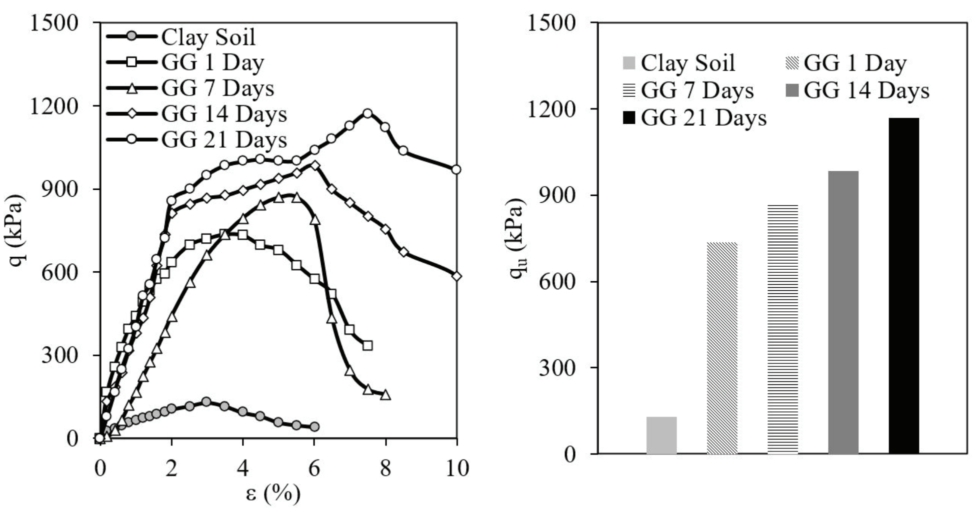

Figure 9. Results of UCS tests for 1% GG at different cure periods.

dehydrated (Sujatha & Saisree, 2019). On the other hands, in the literature, higher increases than this study were obtained at a similar cure period and percentage of biopolymer. However, these studies, unlike this study, performed on the sandy soil as mentioned previously.

3.4 The long-term assessment

The UCS tests have been performed on the soil-GG mixture that is cured for 56 days and 196 days and contained 1% of GG to evaluate the long-term improvement effects of the GG. The results of these tests are given in Figure 10 in comparison with other results of tests. The UCS values of samples which are cured for 56 days and 196 days have been measured as 2.02 and 2.06 times that of sample cured for 1 day, respectively. Therefore, it has been deduced that the UCS value remained approximately constant after the cure period of 56 days.

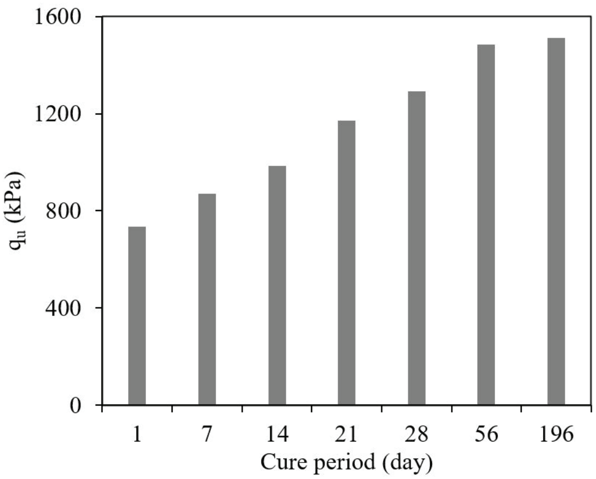

Figure 10. The effects in the long-term of the GG improvement (1% GG).

3.5 Scanning electron microscope analyses

In this study, the dry GG has been mixed with water and then the wet GG has been mixed with soil. SEM images obtained from samples of the dry GG and the soil-the GG mixture, which contains 1% GG and is cured for 21 days, has been used to determine their microstructures. The dry GG has a dispersed form as seen in its SEM image (Figure 11). However, the GG has been gel-like form after it is mixed with water (Figure 4). From the SEM image of soil-the GG mixture, it has been observed that the gel-like structure of wet GG formed some bonds between the clay soil particles (Figure 11). Chang et al. (2016) stated that in clay-biopolymer mixtures, hydrogen and ionic bonds occur between clay particles, which have electrical charges, and biopolymers. Sujatha & Saisree (2019) the increase in strength of guar gum soil mixture correlated with the formation of hydrogen bonds. Besides, they stated that the guar gum coats the soil particles and bridges between them by forming hydrogels. Ultimately, they put forward that the dehydration of the gel with the thickness and strength of the gel bounds increases with age. On the other hand, Ayeldeen et al. (2016) mentioned that guar gum gels fill the voids more than other biopolymers due to being their bonds are thicker and wider. According to the EDS results, it has been thought that the mentioned bonds and hydrogels have occurred as the result of a chemical reaction due to the fact that the peak values of compounds, namely their amount, in dry GG and soil-the GG mixture have changed (Figure 12). Consequently, it is predicted that those bonds and hydrogels have increased the strength of the clay soil.

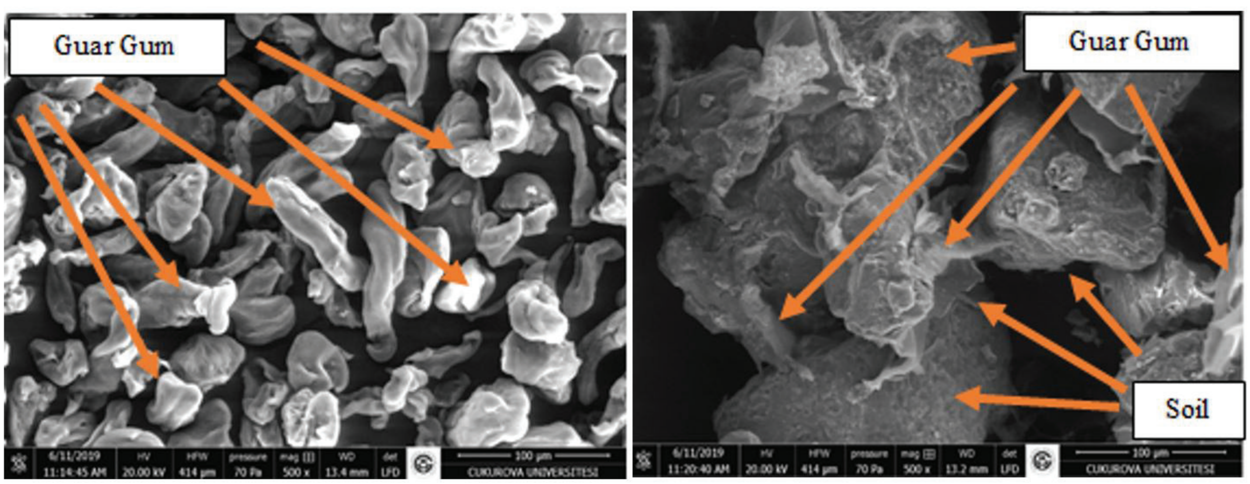

Figure 11. SEM images of the dry GG and soil-the GG mixture.

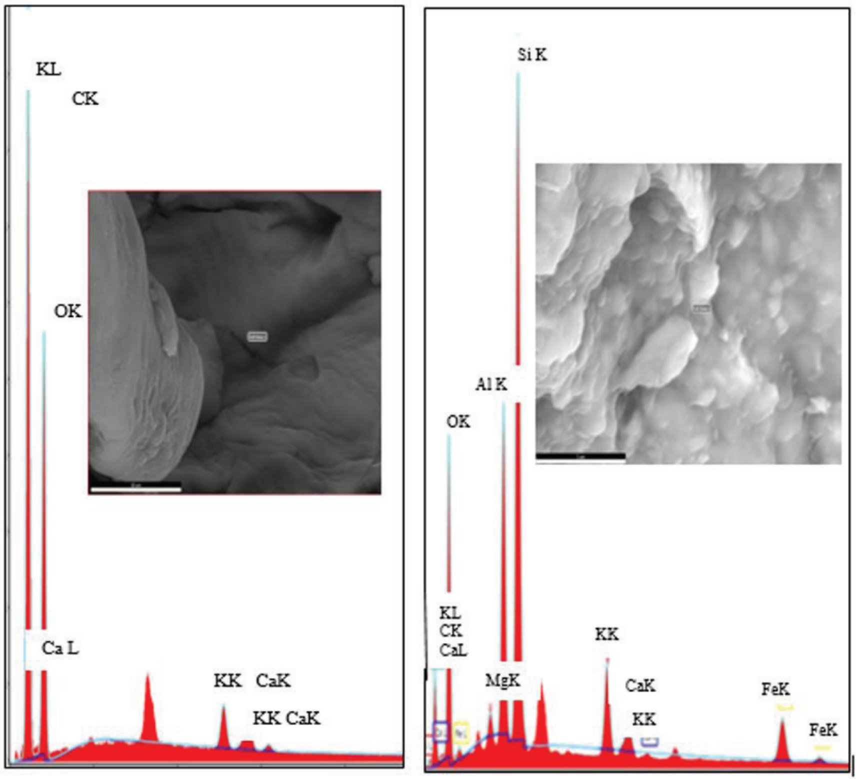

Figure 12. EDS results of the dry GG and soil-the GG mixture.

4. Conclusions

In this study, the improvement of clay soil by using the environmentally friendly GG, which is a type of biopolymer material, has been investigated by laboratory tests, SEM, and XRF analyses. The examined parameters in this research are cure periods and ratios of GG. On the other hand, the mechanism by which the GG improvements the clay soil has been explained with SEM and XRF analyses. The results obtained are presented below.

- It has been determined that in SEM analyses, when the GG is mixed with water, it formed a gel-like structure. Also, in the EDS study, the changes of compound amounts have been thought of as proof of this gel-like structure. In addition, it has been detected that this structure has formed bonds between the clay particles. Therefore, the strength and rigidity of the soil have increased as obtained in the results of the consistency and UCS tests;
- Although the strength of the soil has increased in all percentages of GG, the maximum strength has been obtained when the percentage of the GG is 1%. In this case, the strength of the soil has increased approximately 6 times. Moreover, at this percentage of GG, as the curing time has increased, the rate of improvement has increased. The strength of the soil has determined as approximately 9 times more than untreated soil after 21 days of curing;
- Due to the high water absorption by GG, it has been observed that as the percentage of GG in the soil-GG mixture increased, the compaction parameters of the mixture are negatively affected. During filling construction, it is recommended not to use an excessive amount of GG since the workability can be reduced by affecting the consistency of the soil and the water requirement can be increased;
- According to the results of tests, it is determined as the optimum percentage of GG in the soil-GG mixture in terms of both strength and compressibility for low plasticity clay in this study is 1%;
- According to the results of tests samples that have a long-term curing period, the optimum curing period has been obtained as 56 days;
- It is put forward that the GG can be an alternative to other additives in the soil improvement since it is an environmentally friendly material and the strength of clay soil can be increased even when used at a low percentage;
- The guar gum-soil slurry has the potential to stabilize the walls of trench excavations. Besides, guar gum-soil mixture can provide stability against shallow slope failures and can use in the compacted covers or biopolymer grouts.

Declaration of interest

The authors have no conflicts of interest to declare. All co-authors have observed and affirmed the contents of the paper and there is no financial interest to report.

Author's contributions

Baki Bagriacik: conceptualization, data curation, methodology, visualization, supervision, project administration, formal analysis, writing – original draft. Bahadir Ok: conceptualization, data curation, methodology, validation, writing – original draft, writing – review & editing. Mustafa Tahseen Mohamed Ali Kahiyah: investigation, methodology, resources.

List of symbols

q Unconfined compressive stress of the soil
q_u Unconfined compressive strength of the soil
γ_d Dry unit weight of the soil
ω Water content of the soil
ε Strain of the soil sample

References

Afolabi, A., Francis, F.A., & Adejompo, F. (2012). Assessment of health and environmental challenges of cement factory on Ewekoro community residents, Ogun state Nigeria. *American Journal of Human Ecology*, 1(2), 51-57. http://dx.doi.org/10.11634/21679622150479.

Arulrajah, A., Mohammadinia, A., Phummiphan, I., Horpibulsuk, S., & Samingthong, W. (2016). Stabilization of recycled demolition aggregates by geopolymers comprising calcium carbide, fly ash and slag precursors. *Construction & Building Materials*, 114, 864-873. http://dx.doi.org/10.1016/j.conbuildmat.2016.03.150.

ASTM D 4318-00. (2003). *Standard test method for liquid limit, plastic limit and plasticity index of soils.* ASTM International, West Conshohocken, PA. Retrieved in November 23, 2020, from https://www.astm.org/Standards/D4318

ASTM D 2487-06. (2006). *Standard practice for classification of soils for engineering purposes (Unified Soil Classification System).* ASTM International, West Conshohocken, PA. Retrieved in November 23, 2020, from https://www.astm.org/Standards/D2487.htm

ASTM D 698-00. (2009a). *Standard test method for laboratory compaction characteristics of soil using standard effort.* ASTM International, West Conshohocken, PA. Retrieved in November 23, 2020, from https://www.astm.org/Standards/D698

ASTM D 2166. (2009b). *Standard test method for unconfined compressive strength of cohesive soil.* ASTM International, West Conshohocken, PA. Retrieved in November 23, 2020, from https://www.astm.org/Standards/D2166.htm

ASTM E 2809. (2013). *Standard guide for using scanning electron microscopy/x-ray spectrometry in forensic paint examinations.* ASTM International, West Conshohocken, PA. Retrieved in November 23, 2020, from https://www.astm.org/Standards/E2809.htm

ASTM D 7263-09. (2018). *Standard test methods for laboratory determination of density (unit weight) of soil specimens*. ASTM International, West Conshohocken, PA. Retrieved in November 23, 2020, from https://www.astm.org/Standards/D7263.htm

Ayeldeen, M.K., Negm, A.M., & El Sawwaf, M.A. (2016). Evaluating the physical characteristics of biopolymer/soil mixtures. *Arabian Journal of Geosciences*, 9(5), 371. http://dx.doi.org/10.1007/s12517-016-2366-1.

Cabalar, A.F., Wiszniewski, M., & Skutnik, Z. (2017). Effects of xanthan gum biopolymer on the permeability, odometer, unconfined compressive and triaxial shear behavior of a sand. *Soil Mechanics and Foundation Engineering*, 54(6), 356-361. http://dx.doi.org/10.1007/s11204-017-9481-1.

Chang, I., & Cho, G. (2011). Strengthening of Korean residual soil with β-1,3/1,6-glucan biopolymer. *Construction & Building Materials*, 30, 30-35. http://dx.doi.org/10.1016/j.conbuildmat.2011.11.030.

Chang, I., Prasidhi, A.K., Im, J., & Cho, G. (2015). Soil strengthening using thermo-gelation biopolymers. *Construction & Building Materials*, 77, 430-438. http://dx.doi.org/10.1016/j.conbuildmat.2014.12.116.

Chang, I., Im, J., & Cho, G. (2016). Introduction of microbial biopolymers in soil treatment for future environmentally-friendly and sustainable geotechnical engineering. *Sustainability*, 8(3), 1-23. http://dx.doi.org/10.3390/su8030251.

Cole, D.M., Ringelberg, D.B., & Reynolds, C.M. (2012). Small-Scale mechanical properties of biopolymers. *Journal of Geotechnical and Geoenvironmental Engineering*, 138(9), 1063-1074. http://dx.doi.org/10.1061/(ASCE)GT.1943-5606.0000680.

Cristelo, N., Glendinning, S., Fernandes, L., & Pinto, A.T. (2013). Effects of alkaline-activated fly ash and portland cement on soft soil stabilization. *Acta Geotechnica*, 8(4), 395-405. http://dx.doi.org/10.1007/s11440-012-0200-9.

Dash, S.K., & Hussain, M. (2012). Lime stabilization of soils: reappraisal. *Journal of Materials in Civil Engineering*, 24(6), 707-714. http://dx.doi.org/10.1061/(ASCE)MT.1943-5533.0000431.

Du, Y.J., Horpibulsuk, S., Wei, M.L., Suksiripattanapong, C., & Liu, M.D. (2014). Modeling compression behavior of cement-treated zinc-contaminated clayey soils. *Soil and Foundation*, 54(5), 1018-1026. http://dx.doi.org/10.1016/j.sandf.2014.09.007.

Fatehi, H., Abtahi, S.M., Hashemolhosseini, H., & Hejazi, S.M. (2018). A novel study on using protein based biopolymers in soil strengthening. *Construction & Building*

Materials, 167, 813-821. http://dx.doi.org/10.1016/j.conbuildmat.2018.02.028.

Im, J., Tran, T.P.A., Chang, I., & Cho, G. (2017). Dynamic properties of gel-type biopolymer-treated sands evaluated by Resonant Column (RC) Tests. *Geomechanics and Engineering*, 12(5), 815-830. http://dx.doi.org/10.12989/gae.2017.12.5.815.

Ivanov, V., & Chu, J. (2008). Applications of microorganisms to geotechnical engineering for biologging and biocementation of soil in situ. *Reviews in Environmental Science and Biotechnology*, 7(2), 139-153. http://dx.doi.org/10.1007/s11157-007-9126-3.

Oliveira Júnior, A.I., Jucá, J.F.T., Ferreira, J.A., & Guilherme, L.C. (2019). Geotechnical behavior and soil-fiber interaction of clayey soil mixed with randomly dispersed coconut fibers. *Soils and Rocks*, 42(2), 127-138. http://dx.doi.org/10.28927/SR.422127.

Kahiyah, M.T.M.A. (2020). *Investigation of engineering properties of clayey soils improved with biopolymers* [MSc thesis]. Cukurova University Institute of Natural and Applied Sciences (in Turkish). Retrieved in November 23, 2020, from https://tez.yok.gov.tr/UlusalTezMerkezi/tezSorguSonucYeni.jsp

Kampala, A., Horpibulsuk, S., Prongmanee, N., & Chinkulkijniwat, A. (2014). Influence of wet-dry cycles on compressive strength of calcium carbide residue-fly ash stabilized clay. *Journal of Materials in Civil Engineering*, 26(4), 633-643. http://dx.doi.org/10.1061/(ASCE)MT.1943-5533.0000853.

Khatami, H.R., & O'Kelly, B.C. (2013). Improving mechanical properties of sand using biopolymers. *Journal of Geotechnical and Geoenvironmental Engineering*, 139(8), 1402-1406. http://dx.doi.org/10.1061/(ASCE)GT.1943-5606.0000861.

Kumar, J.K., & Kumar, V.P. (2020). Soil stabilization using E-waste: a retrospective analysis. *Materials Today: Proceedings*, 22(3), 691-693. http://dx.doi.org/10.1016/j.matpr.2019.09.145.

Lee, S., Im, J., Cho, G., & Chang, I. (2019). Laboratory triaxial test behavior of xanthan gum biopolymer treated sands. *Geomechanics and Engineering*, 17(5), 445-452. http://dx.doi.org/10.12989/gae.2019.17.5.445.

Marto, A., Latifi, N., & Eisazadeh, A. (2014). Effect of non-traditional additives on engineering and microstructural characteristics of laterite soil. *Arabian Journal for Science and Engineering*, 39(10), 6949-6958. http://dx.doi.org/10.1007/s13369-014-1286-1.

Mascarenha, M.M.A., Cordão Neto, M.P., Matos, T.H.C., Chagas, J.V.R., & Rezende, L.R. (2018). Effects of the addition of dihydrate phosphogypsum on the characterization and mechanical behavior of lateritic clay. *Soils and Rocks*, 41(2), 157-170. http://dx.doi.org/10.28927/SR.412157.

Menezes, L.C.P., Sousa, D.B., Sukar, S.F., & Ferreira, S.R.M. (2019). Analysis of the physical-mechanical behavior of clayey sand soil improved with coir fiber. *Soils and Rocks*, 42(1), 31-42. http://dx.doi.org/10.28927/SR.421031.

Mitchell, J.K., & Santamarina, J.C. (2005). Biological considerations in geotechnical engineering. *Journal of Geotechnical and Geoenvironmental Engineering*, 131(10), 1222-1233. http://dx.doi.org/10.1061/(ASCE)1090-0241(2005)131:10(1222).

Moretti, L., Conficconi, M., Natali, S., & D'Andrea, A. (2020). Statistical analyses of SEM-EDS results to predict the quantity of added quicklime in a treated clayey soil. *Construction & Building Materials*, 253, 118852. http://dx.doi.org/10.1016/j.conbuildmat.2020.118852.

Najah, L., Ahmed, F.B., & Said, M.A.M. (2013). Influence of polymer on properties of soils. *The Electronic Journal of Geotechnical Engineering*, 18, 1909-1915.

Risica, D., Barbetta, A., Vischetti, L., Cametti, C., & Dentini, M. (2010). Rheological properties of guar and its methyl, hydroxypropyl and hydroxypropyl-methyl derivatives in semi dilute and concentrated aqueous solutions. *Polymer*, 51(9), 1972-1982. http://dx.doi.org/10.1016/j.polymer.2010.02.041.

Sarici, T. (2019). *Evaluation of usability of pozzolan reinforced construction and demolition wastes as a granular fill* [Doctoral thesis]. Inonu University Graduate School of Natural and Applied Sciences (in Turkish). Retrieved in November 23, 2020, from https://tez.yok.gov.tr/UlusalTezMerkezi/tezSorguSonucYeni.jsp

Sharma, R., Kaith, B.S., Kalia, S., Pathania, D., Kumar, A., Sharma, N., Street, R.M., & Schauer, C. (2015). Biodegradable and conducting hydrogels based on Guar gum polysaccharide for antibacterial and dye removal applications. *Journal of Environmental Management*, 162, 37-45. http://dx.doi.org/10.1016/j.jenvman.2015.07.044.

Soldo, A., Miletic, M., & Auad, M.L. (2020). Biopolymers as a sustainable solution for the enhancement of soil mechanical properties. *Scientific Reports*, 10(1), 267. http://dx.doi.org/10.1038/s41598-019-57135-x.

Sujatha, E.R., & Saisree, S. (2019). Geotechnical behaviour of guar gum-treated soil. *Soil and Foundation*, 59(6), 2155-2166. http://dx.doi.org/10.1016/j.sandf.2019.11.012.

Tingle, J.S., & Santoni, R.L. (2003). Stabilization of clay soils with nontraditional additives. *Transportation Research Record: Journal of the Transportation Research Board*, 1819(1), 72-84. http://dx.doi.org/10.3141/1819b-10.

Whistler, R.L., & Hymowitz, T. (1980). *Guar: agronomy, production, industrial use, and nutrition*. Indiana: Purdue University Press. https://doi.org/10.2307/2806779.

Worrell, E., Price, L., Martin, N., Hendriks, C., & Meida, L.O. (2001). Carbon dioxide emissions from the global cement industry. *Annual Review of Energy and the Environment*, 26(1), 303-329. http://dx.doi.org/10.1146/annurev.energy.26.1.303.

Soils and Rocks
An International Journal of Geotechnical and Geoenvironmental Engineering
www.soilsandrocks.com
ISSN 1980-9743
ISSN-e 2675-5475

Proposal for considering the group effect in the prediction of settlements in pile groups through load transfer methods

Francisco Vladson Cardins Gomes Filho[1#], Alfran Sampaio Moura[1]

Article

Keywords
Pile settlements
Load transfer methods
Group effect
Hyperbolic model

Abstract
When designing a foundation project, it is necessary to ensure that all the elements meet both ultimate and serviceability limit states, which call for predictions of settlement and load capacity. The load transfer methods are a widely used alternative to estimate the load-settlement ratio of piles in the design of foundation projects. However, traditional load transfer methods do not consider the interactive effects between the elements in pile groups. This study proposes changes to the load transfer curves developed by Bohn et al. (2016), aiming to incorporate the group effect in the analysis of load-settlement relationships in pile groups. Comparisons between the predicted settlements obtained using the proposed method and the results of load tests performed by Dai et al. (2012) in Jiangsu, China, showed that the modifications proposed in this study agreed well with the experimental results for most of the analyzed groups.

1. Introduction

Settlement prediction is an important task that can be performed using different techniques, such as the load transfer methods, which use load transfer functions (called “t-z” and “q-z” curves) to determine the load-settlement relationship for a pile. These load transfer curves can be developed from theoretical solutions and empirical observations.

Load transfer functions were used to describe relationship between unit skin friction and pile settlement and the relationship between the pile tip resistance and the pile tip displacements. Some examples of this application are present in Zhang & Zhang (2012a, b), Wang et al. (2012) and Lee et al. (2013).

Nowadays most multi-storey buildings use pile groups. Thus, in order to determine the settlements, the interactive effects between them (i.e., group effect) should be considered. However, most of the current methods to estimate settlements analyze the piles separately, without considering the influence of the neighboring ones on the field behavior of the pile group.

Bohn et al. (2016) used the load transfer curves to predict settlement in isolated piles. This study analyzed several load transfer curves, comparing the curves to the results collected in the field. Fellenius (2018) discussed the analyses made by Bohn et al. (2016) and it was concluded that, among the several functions analyzed in the study, the hyperbolic load transfer curves obtained good agreement to the measured results.

The present study aims to propose changes to the load transfer functions for single piles proposed by Bohn et al. (2016) in order to incorporate the group effect in the analysis of load-settlement ratios of pile groups.

2. Development of a t-z load transfer function to predict settlement in pile groups

The hyperbolic t-z load transfer function proposed by Bohn et al. (2016) to calculate the settlement of a single pile can be expressed as shown in Equation 1.

$$\tau_s = \frac{\tau_{s,ult} s_{si}}{M_s D + s_{si}} \tag{1}$$

where τ_s is the mobilized skin friction; $\tau_{s,ult}$ is the ultimate unit resistance; s_{si} is the displacement of the analyzed element (the single pile); D is the pile diameter; and M_s is the deformation parameter, which can be obtained from Bohn et al. (2016).

In order to consider the group effect in the function, the term s_{si} can be isolated, as shown in Equation 2.

[#]Corresponding author. E-mail address: vladson@alu.ufc.br
[1]Universidade Federal do Ceará, Departamento de Engenharia Hidráulica e Ambiental, Fortaleza, CE, Brasil.
Submitted on December 13, 2020; Final Acceptance on May 5, 2021; Discussion open until August 31, 2021.
https://doi.org/10.28927/SR.2021.061320

$$s_{si} = \frac{\tau_s M_s D}{\left(\tau_{s,ult} - \tau_s\right)} \quad (2)$$

Following the procedure suggested by Zhang et al. (2010, 2016), Zhang & Zhang (2012a) and Pan et al. (2018), the term related to the displacement, which is induced by the stress q_s from the neighboring piles, is added to Equation 2. In sequence, the additional settlement is calculated according to the formulations proposed by Randolph & Wroth (1979) and Mylonakis & Gazetas (1998), as shown in Equations 3 and 4.

$$\Delta S_s = \zeta_s \tau_s \quad (3)$$

where ΔS_s is the increase in displacement caused by the group effect; ζ_s is the interaction factor; and τ_s is the mobilized lateral resistance.

$$\zeta_s = \sum_{j\neq 1, j=1}^{n} \frac{r_0}{G_s} \ln\left(\frac{2.5l(1-\upsilon)}{r_{ij}}\right) - \sum_{j\neq i, j=1}^{n} \frac{r_0^2}{G_s r_{ij}} \ln\left(\frac{2.5l(1-\upsilon)}{r_{ij}}\right) \quad (4)$$

where r_0 is the radius of analyzed pile; G_S is the shear modulus of the soil layer where the analyzed element is located; l is the pile length; υ is the Poisson's ratio of the soil layer where the analyzed element is located; and r_{ij} is the distance between axes (centers) of two considered piles.

The total displacement of the shaft that is caused by the applied loads on the analyzed pile plus the neighboring ones can thus be written as in Equation 5, where the additional portion of settlement caused by the group effect is added.

$$s_s = \frac{\tau_s M_s D}{\left(\tau_{s,ult} - q_s\right)} + \zeta_s \tau_s \quad (5)$$

Equation 5 can be rewritten as shown in Equation 6.

$$\tau_s = \frac{\left(M_s D + \tau_{s,ult}\zeta_s + s_s\right) - \sqrt{\left(M_s D + \tau_{s,ult}\zeta_s + s_s\right)^2 - 4\left(-\zeta_s\right)\left(-s_s \tau_{s,ult}\right)}}{2\zeta_s} \quad (6)$$

And Equation 6 can be simplified by defining the terms a_{gs} and b_{gs} as in Equations 7 and 8.

$$a_{gs} = M_s D + \tau_{s,ult}\zeta_s \quad (7)$$

$$b_{gs} = -4\zeta_s \tau_{s,ult} \quad (8)$$

By substituting the values of a_{gs} and b_{gs}, Equation 6 can be rewritten as Equation 9, thus obtaining the expression for the modified t-z load transfer function.

$$\tau_s = \frac{\left(a_{gs} + s_s\right) - \sqrt{\left(a_{gs} + s_s\right)^2 + b_{gs} s_s}}{2\zeta_s} \quad (9)$$

The development described above was implemented by Zhang et al. (2010) for load transfer curves of single piles. The present study implemented a similar procedure but modifying the load transfer functions proposed by Bohn et al. (2016), which were developed based upon a greater number of load tests when compared to Zhang et al. (2010) and also considered load tests carried out in Brazilian soils.

3. Development of a q-z load transfer function to predict settlement in pile groups

The hyperbolic q-z load transfer function developed by Bohn et al. (2016) to calculate settlement of single piles can be written as Equation 10.

$$q_b = \frac{q_{b,ult} s_{bi}}{M_b D + s_{bi}} \quad (10)$$

The term s_{bi} can be isolated, in a similar procedure to that used for the t-z curve, as shown in Equation 11.

$$s_{bi} = \frac{q_b M_b D}{\left(q_{b,ult} - q_b\right)} \quad (11)$$

The additional settlement was calculated according to the formulations proposed by Randolph & Wroth (1979) and can be seen in Equations 12 and 13. The variable q_b is the mobilized resistance, $q_{b,ult}$ is the ultimate resistance, s_{bi} is the pile toe displacement, and M_b is the toe deformation parameter. Values for M_b can be obtained from Bohn et al. (2016).

$$\Delta S_b = \zeta_b q_b \quad (12)$$

$$\zeta_b = \sum_{j=1,\ j\neq i}^{n} \frac{1-\nu_b}{2\pi G_b r_{ij}} \quad (13)$$

The pile tip displacement due to the loading on top of both analyzed pile and neighboring piles can then be expressed as shown in Equation 14.

$$s_b = \frac{q_b M_b D}{\left(q_{b,ult} - q_b\right)} + q_b \zeta_b \quad (14)$$

Isolating the term q_b, the obtained solution (Equation 15) corresponds to the modified q-z load transfer function, with the terms a_{gb} and b_{gb} being defined respectively as in Equations 16 and 17.

$$q_b = \frac{\left(a_{gb} + s_b\right) - \sqrt{\left(a_{gb} + s_b\right)^2 + b_{gb} s_b}}{2\zeta_b} \quad (15)$$

$$a_{gb} = M_b D + q_{b,ult}\zeta_b \quad (16)$$

$$b_{gb} = -4\zeta_b q_{b,ult} \quad (17)$$

Thus, from the expressions proposed in Equations 9 and 15, the group effect can be considered in the prediction of settlements in pile groups.

4. Analyzed case - Dai et al. (2012)

The experimental data used as input in this study were extracted from Dai et al. (2012) and comprised load tests performed on 32 bored piles (single and groups of 2, 4, and 9 piles), in an experimental field located in Jiangsu, China. Table 1 presents a summary with the characteristics of single piles and pile groups.

The compressive strength of the concrete used in pile shafts and caps was 25 MPa, with a Young's Modulus of 29.2 GPa, obtained from compression tests performed in 6 prismatic specimens (100 mm × 100 mm × 300 mm), tested 28 days after casting. According to Bohn et al. (2016), the pile caps could be considered as rigid.

A hole called BH was drilled down to a depth of 29.50 m, aiming to obtain soil samples and the surrounding stratigraphy. In addition, 4 cone penetration tests were carried out (CPT1, CPT2, CPT3, and CPT4). A layout of the experimental field displaying the location of piles, drilled hole BH (stratigraphy), and performed CPTs can be found in Dai et al. (2012).

The stratigraphy showed layers of clay and silt in the upper depths. A layer of soft clay was also identified between the depths of 17.0 m and 29.50 m and water level was located at 2.6 m below ground surface.

The load tests were performed until pile failure. The reaction system consisted of prismatic blocks of precast concrete and a platform supported by 12 m-long reaction piles, installed 5 m away from the center of tested groups. The maximum load applied was 1.2 times the estimated load capacity for each group.

4.1 Method

In order to obtain the load-settlement ratios for the pile groups analyzed by Dai et al. (2012), the modified t-z and q-z curves (Equations 9 and 15) were used. The pile shafts were subdivided into 1 m-long segments, each one of them corresponding to a t-z curve, determined according to the properties of the soil layer in which the segment was located. This same discretization was adopted by Zhang et al. (2016) and Pan et al. (2018).

Values for M_s were obtained based on the chart presented by Bohn et al. (2016) and Poisson's ratio was assumed as 0.45, according to Dai et al. (2012). Table 2 presents the values for the ultimate unitary resistance ($q_{s,ult}$) and M_s per section of the 20-m-long piles (i.e. groups QZ2, QZ4, and QZ9).

Table 1. Characteristics of piles studied by Dai et al. (2012).

Identification	Number of piles	Length (m)	Spacing
DZ1	1	20.0	-
DZ1L	1	24.0	-
QZ2	2	20.0	2.5D
QZ2L	2	24.0	3.0D
QZ4	4	20.0	2.5D
QZ4L	4	24.0	3.0D
QZ9	9	20.0	2.5D
QZ9L	9	24.0	3.0D

Table 2. Values for $q_{s,ult}$ and M_s for the 20 m-long pile groups.

Section (m)	Soil type	Measured $q_{s,ult}$ (kPa)	M_s
0-1	Clay	30.7	0.00280
1-2	Clay	29.6	0.00280
2-3	Clay	52.4	0.00280
3-4	Clay	86.6	0.00280
4-5	Clay and Silt	77.8	0.00300
5-6	Silt	64.8	0.00330
6-7	Silt	64.8	0.00330
7-8	Silt	64.8	0.00330
8-9	Silt	64.8	0.00330
9-10	Silt	64.8	0.00330
10-11	Silt and silty-sand	62.9	0.00330
11-12	Silt and silty-sand	62.5	0.00330
12-13	Silt and silty-sand	62.5	0.00330
13-14	Silt and silty-sand	62.5	0.00330
14-15	Silt and silty-sand	62.5	0.00330
15-16	Silt and silty-sand	62.5	0.00330
16-17	Silt and silty-sand	62.5	0.00330
17-18	Silt, silty-sand and soft clay	44.0	0.00305
18-19	Soft clay	25.5	0.00280
19-20	Soft clay	25.5	0.00280

In this method, the values for ultimate unitary lateral resistances for pile groups – the input parameters – were those regarding single piles, as presented in Table 2. Thus, the values for ultimate unitary lateral resistances obtained for pile DZ1 were used for the 20 m-long pile groups, and the values for pile DZ1L, for the 24 m-long ones.

The t-z and q-z curves for single piles were converted into pile group curves by considering the interactive effects between piles (group effect), according to the development described in Sections 2 and 3 of this study. Table 3 shows the values for ultimate unitary resistance and M_s per section for groups QZ2L, QZ4L, and QZ9L (24 m-long piles).

For both 20 m- and 24 m-long piles, the adopted M_b was 0.0088. The load capacity obtained by Dai et al. (2012) for the single pile DZ1 (20 m) was 1,430 kN and for the single pile DZ1L (24 m), 1,540 kN. Both values were obtained through load tests.

Most of the applied load was absorbed by the shaft. The toe resistance mobilized in failure was 4.73 kN for DZ1 and 78.54 kN for DZ1L. These were the values used in q-z load transfer functions.

In the approach here described, the load-settlement relationships of the piles were obtained through an interactive procedure, similar to that proposed by Coyle & Reese (1966), Zhang & Zhang (2012a) and Zhang et al. (2016).

1. [Step 1] The pile is subdivided into n segments. A displacement S_b is chosen for the pile toe (segment n). From this displacement and using the q-z curve (Equation 15), the mobilized load P_b at pile tip is calculated, multiplying toe stress q_b by the tip area.

Table 3. Values for $q_{s,ult}$ and M_s for the 24 m-long pile groups.

Section (m)	Soil type	Measured $q_{s,ult}$ (kPa)	M_s
0- 1	Clay	32.35	0.0028
1-2	Clay	32.10	0.0028
2-3	Clay	54.90	0.0028
3-4	Clay	89.10	0.0028
4-5	Clay and silt	78.30	0.0030
5-6	Silt	62.10	0.0033
6-7	Silt	62.10	0.0033
7-8	Silt	62.10	0.0033
8-9	Silt	62.10	0.0033
9-10	Silt	62.10	0.0033
10-11	Silt and silty-sand	59.78	0.0033
11-12	Silt and silty-sand	59.20	0.0033
12-13	Silt and silty-sand	59.20	0.0033
13-14	Silt and silty-sand	59.20	0.0033
14-15	Silt and silty-sand	59.20	0.0033
15-16	Silt and silty-sand	59.20	0.0033
16-17	Silt and silty-sand	59.20	0.0033
17-18	Silt, silty-sand and soft clay	40.80	0.00305
18-19	Soft clay	22.40	0.0028
19-20	Soft clay	22.40	0.0028
20-21	Soft clay	22.40	0.0028
21-22	Soft clay	22.40	0.0028
22-23	Soft clay	22.40	0.0028
23-24	Soft clay	22.40	0.0028

2. [Step 2] The displacement of the midpoint of analyzed segment (S_s) is estimated. For the first iteration, $S_s = S_b$.
3. [Step 3] Using the t-z curve (Equation 9) and the displacement S_s, the shear stress q_s mobilized in the lateral area of analyzed segment can be calculated.
4. [Step 4] The force due to friction (ΔP_n) acting on the side of analyzed segment is calculated (Equation 18):

$$\Delta P_n = \tau_s \pi L_i \tag{18}$$

where L_i is the length of analyzed segment; and τ_s is shear stress mobilized in the shaft of analyzed segment.

5. [Step 5] The force acting at the top of analyzed segment (P_{tn}) is determined according to Equation 19.

$$P_{tn} = P_b + \Delta P_n \tag{19}$$

6. [Step 6] The elastic shortening of the lower half of analyzed segment is calculated according to Equation 21, using the axial force which acts at the midpoint of analyzed segment ($P_{n,med}$) and the force acting at its base (P_b).

$$P_{n,med} = \frac{P_{tn} + P_b}{2} \tag{20}$$

$$\Delta e / 2 = \frac{P_{nmed} + P_b}{2} \frac{\left(\Delta L_n / 2\right)}{E_p A_p} \tag{21}$$

where ΔL_n is the variation in the length of analyzed element; E_p is Young's Modulus of the pile; and A_p is pile cross-sectional area.

7. [Step 7] A new displacement for the midpoint of analyzed segment (S_s') is calculated, adding the elastic shortening ($\Delta e/2$) to the displacement of the base of segment S_b, according to Equation 22.

$$S_s^{'} = S_b + \Delta e / 2 \tag{22}$$

8. [Step 8] The value of S_s*'* is compared with S_s. If they differ by more than 10^{-6} m, the procedure from steps 2 to 7 is repeated, assuming S_s*'* as the new value for S_s, until the convergence for analyzed segment is reached.
9. [Step 9] After the convergence is reached, the displacement at the top of analyzed segment (S_{tn}) is calculated, according to Equation 23.

$$S_{tn} = S_b + \Delta e \tag{23}$$

10. [Step 10] The displacement of the top of analyzed segment corresponds to the displacement of the base of the upper segment. Therefore, the procedure is repeated, until load and settlement are obtained for the top segment of pile.

The procedure described above is replicated for several values of S_b until the load-settlement ratio for the range of loads of interest is obtained.

Equations 9 and 15 require the soil shear modulus of each soil layer to be applied, which in this case was estimated for each stress level. For this purpose, the soil shear wave velocity (V_s) was determined using Equation 24 for granular soil layers, proposed by Baldi et al. (1989) and Equation 25 for fine soil layers, proposed by Mayne (1995), which correlate CPT's penetration resistance with V_s.

$$V_s = 277 q_c^{0.13} \sigma_{vo}^{'\,0.27} \tag{24}$$

$$V_s = 1.75 q_c^{0.627} \tag{25}$$

where σ'_{vo} is the effective geostatic stress of soil in the center of analyzed layer.

From the shear wave values for each layer, the maximum shear modulus (G_{max}) can be calculated, according to Equation 26.

$$G_{max} = \frac{\gamma_n}{g} V_s^2 \tag{26}$$

where g is the acceleration of gravity; and γ_n is the soil unit weight.

From G_{max}, the shear modulus (G) is obtained for each analyzed load, using another iterative procedure, as described below (Steps A to E). This geotechnical parameter is obtained using Equations 24 and 25, for each layer, considering the thickness of each layer.

11. [Step A] A load at the top of pile (P_t') is estimated. From the load capacity of the single pile, a factor of safety (*FS*) is determined.
12. [Step B] Using Equation 27 (Fahey & Carter, 1993), the shear modulus (G_s) of each layer can be also determined.

$$\frac{G_s}{G_{máx}} = 1 - \left(\frac{1}{FS}\right)^{0.3} \tag{27}$$

13. [Step C] The iterative procedure described in Steps A and B is performed again, using the calculated values for G. Then, a new load P_t is obtained.
14. [Step D] The obtained P_t is compared with the estimated P_t. If the obtained value is smaller than the estimated one, a larger displacement S_b is used in the beginning of the procedure. If the obtained P_t is greater, a smaller S_b displacement should be used.
15. [Step E] The procedure is repeated until the difference between the estimated P_t' and the obtained P_t is not greater than 0.1 kN.

5. Results of predictions and analyses

5.1 Analyzed case study – Dai et al. (2012)

The case study described by Dai et al. (2012) was used in this study to evaluate the modified t-z and q-z curves and the proposed methodology. At the end of this section, some possible causes for differences between the predicted (calculated) and measured results will be presented.

Figure 1 shows both the predicted and the experimental (obtained by Dai et al., 2012) load-settlement curves for groups QZ2 (2 piles) and QZ2L (2 piles). The method proposed in this study yielded results that agreed quite well with the experimental ones, especially for loads up to 2,500 kN. For higher loads, the predicted settlements were slightly higher than those experimentally measured.

Considering a factor of safety (*FS*) of 2.0 (i.e. an adopted workload of 1,250 kN), a difference of only 1.5 mm (absolute value) was observed between the predicted and the experimentally measured settlements.

As to group QZ2L, the predicted settlements also agreed well with the experimental results for loads up to 1,500 kN. The predicted results were closest to those measured for the load of 1,100 kN. Between 1,500 kN and 2,800 kN, the predicted (calculated) results were slightly lower than those obtained experimentally. Above 2,800 kN, the method yielded higher values for settlement than those obtained experimentally.

Figure 2 shows the predicted and the experimental (Dai et al., 2012) load-settlement curves for groups QZ4 (4 piles, 20-m-long piles) and QZ4L (4 piles, 24-m-long piles). Good agreement was observed between predicted and experimental results up to 1,500 kN. For higher loads, the predicted settlements were smaller than those obtained experimentally. These were the most discordant results (between experimental and predicted) considering all analyzed groups, which might have happened due to differences in stiffness of the soils around the single piles and the pile groups.

Regarding group QZ4L, predicted results were remarkably close to experimental ones, notably for loads below 1,500 kN. Between 1,500 kN and 2,800 kN, experimental results were slightly higher than estimated ones. For load levels above 2,800 kN, the method provided settlements also slightly higher than those experimentally obtained.

Figure 3 shows the load-settlement curves for pile groups QZ9 and QZ9L. For group QZ9, excellent agreement between predicted and experimental results was obtained, especially for loads under 7,500 kN. For higher loads, the predicted results were slightly lower than those experimentally obtained. One of the possible causes for the divergence may be a reduced soil stiffness in the area of installation of this group, in comparison to the area of installation of isolated piles.

For group QZ9L, predicted and experimental results agreed as well. The most consistent results were for loads between 0 and 3,000 kN. Around 6,000 kN, the predicted settlements were slightly higher than the experimental ones.

(a) (b)

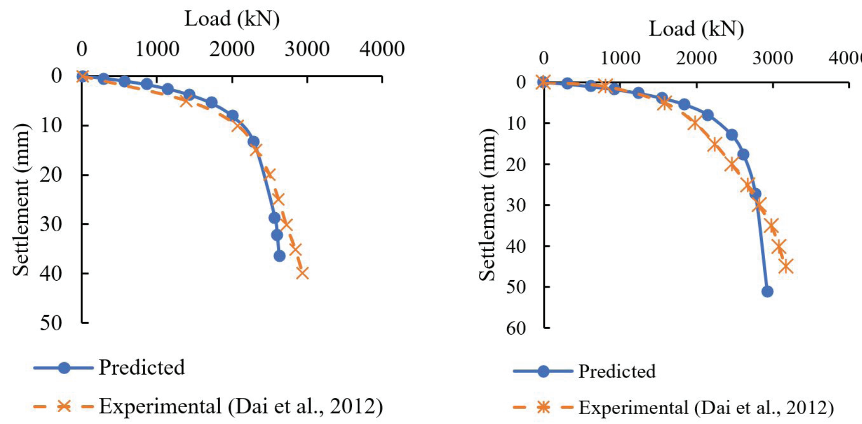

Figure 1. Predicted and experimental load-settlement curves for (a) group QZ2 and (b) group QZ2L.

(a) (b)

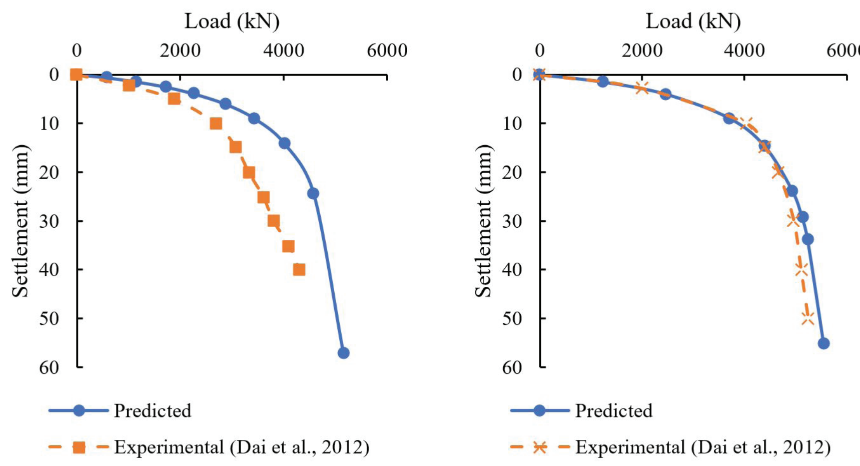

Figure 2. Predicted and experimental load-settlement curves for (a) group QZ4 and (b) group QZ4L.

(a) (b)

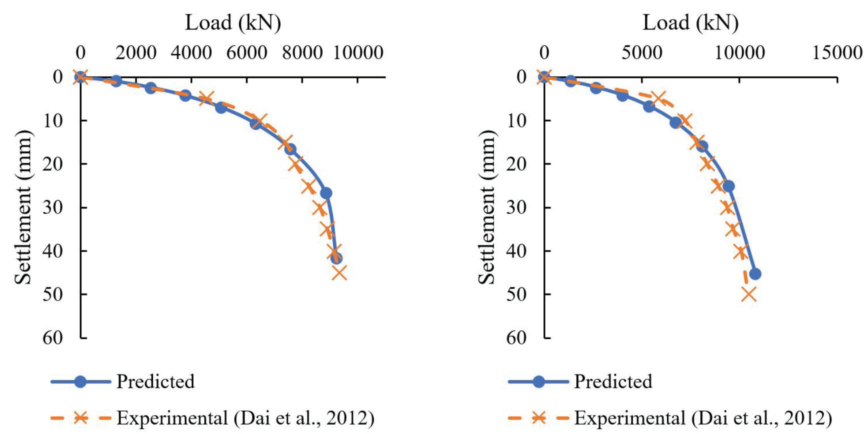

Figure 3. Predicted and experimental load-settlement curves for (a) group QZ9 and (b) group QZ9L.

For loads above 8,000 kN, the experimental results were slightly higher than those predicted.

In general, the method proposed in this study yielded settlements that reasonably agreed with experimental results, notably for groups QZ4L and QZ9. However, some divergences between experimental and predicted results were still observed, particularly for group QZ4.

These small divergences probably happened due to soil heterogeneity, for CPT results showed that soil stiffness was not the same in all assessed locations. Thus, as the used input parameters came both from load tests and CPTs carried out on single piles, it is possible that the stiffness in the regions where the load tests were performed was different from where CPTs were performed.

Another possible reason for the differences in the results reside in the choice for the parameters M_s, M_b, and shear modulus. Although estimated considering the results of 72 load tests, more accurate values for M_s and M_b could have been obtained if a greater number of load tests had been used for each pile and soil types.

As to shear modulus, although the correlations were calibrated considering a large amount of data and showed good adherence to them, it is possible that the values could be a little distant from field reality, which could also be a possible cause for the divergences between predicted and experimental settlements.

6. Conclusions

The present work proposed modifications to the t-z and q-z curves developed by Bohn et al. (2016), in order to consider the group effect in the analysis of load-settlement ratios in pile groups. The modifications were carried out using the interaction factors proposed by Randolph & Wroth (1979) and Mylonakis & Gazetas (1998).

Regarding groups QZ2 and QZ2L, the method proposed in this study yielded results with good agreement with experimental ones, especially for loads up to 2,500 kN. For loads above 2,500 kN, the predicted settlements were slightly higher than those experimentally measured.

For the group QZ4, good agreement was also observed between predicted and experimental results, mainly for loads up to 1,500 kN.

For the group QZ4L, predicted results were quite close to experimental ones, notably for loads below 750 kN. For load levels above 1,400 kN, the predicted settlements were slightly higher than those experimentally obtained.

Regarding groups QZ9 and QZ9L, good agreement between predicted and experimental results was also obtained, especially for loads under 7,500 kN. For higher loads, the predicted results were slightly lower than experimental ones. The geotechnical parameter G_{max} were obtained by correlations with CPT.

Thus, the predictions for load-settlement ratios made according to the modifications proposed in this study for t-z and q-z curves agreed quite well with the experimental data for most analyzed pile groups, even though considerable divergences between experimental and predicted settlements were also obtained (block QZ4), most likely due to soil heterogeneity, evidenced by results from cone penetration tests (CPTs).

Acknowledgements

To the Post-Graduate Program POSDEHA. To the CNPQ - National Council for Scientific and Technological Development and to the Coordination for funding the research. To the CAPES Coordination for the Improvement of Higher Education Personnel.

Declaration of interest

The authors declare no conflict of interest in this research.

Author's contributions

Francisco Vladson Cardins Gomes Filho: data curation, formal analysis, investigation, methodology, software, visualization, validation, writing – original draft, writing – review & editing. Alfran Sampaio Moura: conceptualization, project administration, supervision, validation, writing – review & editing.

List of symbols

τ_s	Mobilized unit lateral resistance
$\tau_{s,ult}$	Ultimate unit lateral resistance
D	Pile diameter
M_s	Deformation parameter for t-z curve
s_{si}	Displacement of the analyzed element
ζ_s	Lateral interaction factor
ΔS_s	Increase in displacement of the analyzed element caused by the group effect
r_0	Radius of pile
G_S	Shear modulus of soil layer where the element is located
υ	Poisson's ratio of soil layer where the element is located
r_{ij}	Distance between axes (centers) of two considered piles
q_b	Mobilized unit base resistance
$q_{b,ult}$	Ultimate unit base resistance
s_{bi}	Base displacement
M_b	Deformation parameter for q-z curve
ΔS_s	Increase in base displacement caused by the group effect
ζ_b	Base interaction factor
G_b	Shear modulus of the base soil layer
υ_s	Poisson's ratio of the base soil layer
ΔP_n	Force due to friction

L_i	Length of analyzed segment
P_{tn}	Force acting at the top of analyzed element
P_b	Force acting at the base of analyzed element
$P_{n,med}$	Axial force which acts at the midpoint of analyzed segment
ΔL_n	Variation in the length of analyzed element
Δe	Elastic shortening
S_s'	Displacement of the midpoint of analyzed segment
S_{tn}	Displacement at the top of analyzed segment
V_s	Soil shear wave velocity
q_c	Cone penetration resistance
G_{max}	Maximum soil shear modulus
g	Acceleration of gravity
γ_n	Soil unit weight
FS	Safety factor

References

Baldi, G., Bellotti, R., Gionna, V.N., Jamiolkowski, M., & Lo Presti, D.C.F. (1989). Modulus of sands from CPT's and DMT's. In *Proceedings of the 12th International Conference on Soil Mechanics and Foundation Engineering* (Vol. 1, pp. 1-6), Rio de Janeiro. Publications Committee of XII ICSMFE.

Bohn, C., Santos, A.L., & Frank, R. (2016). Development of axial pile load transfer curves based on instrumented load tests. *Journal of Geotechnical and Geoenvironmental Engineering*, 143, 2-6. http://dx.doi.org/10.1061/(ASCE)GT.1943-5606.0001579.

Coyle, H.M., & Reese, L.C. (1966). Load transfer for axially loaded piles in clay. *Journal of the Soil Mechanics and Foundations Division*, 92(2), 1-26. http://dx.doi.org/10.1061/JSFEAQ.0000850.

Dai, G., Salgado, R., Gong, W., & Zhang, Y. (2012). Load tests on full-scale bored pile groups. *Canadian Geotechnical Journal*, 49(11), 1293-1308. http://dx.doi.org/10.1139/t2012-087.

Fahey, M., & Carter, J.P. (1993). A finite element study of the pressuremeter test in sand using nonlinear elastic plastic model. *Canadian Geotechnical Journal*, 30(2), 348-362. http://dx.doi.org/10.1139/t93-029.

Fellenius, B.H. (2018). Discussion of "development of axial pile load transfer curves based on instrumented load tests". *Journal of Geotechnical and Geoenvironmental Engineering*, 144(4), 07018005. http://dx.doi.org/10.1061/(ASCE)GT.1943-5606.0001867.

Lee, J., You, K., Jeong, S., & Kim, J. (2013). Proposed point bearing load transfer function in jointed rock-socketed drilled shafts. *Soil and Foundation*, 53(4), 596-606. http://dx.doi.org/10.1016/j.sandf.2013.06.010.

Mayne, P.W. (1995). *Evaluation of foundation response by G/G*$_{max}$ *degradation relationships in soils* (pp. 136-148). Taipei: National Science Council of ROC and NSF of U.S.

Mylonakis, G., & Gazetas, G. (1998). Settlement and additional internal forces of grouped piles in layered soil. *Geotechnique*, 48(1), 55-72. http://dx.doi.org/10.1680/geot.1998.48.1.55.

Pan, D.D., Zhang, Q.Q., Liu, S.W., & Zhang, M.S. (2018). Analysis on response of a single pile and pile groups based on the Runge-Kutta method. *KSCE Journal of Civil Engineering*, 22(1), 92-100. http://dx.doi.org/10.1007/s12205-017-0578-x.

Randolph, M.F., & Wroth, C.P. (1979). An analysis of the vertical deformation of pile groups. *Geotechnique*, 29(4), 423-439. http://dx.doi.org/10.1680/geot.1979.29.4.423.

Wang, Z.J., Xie, X.Y., & Wang, J.J.C. (2012). A new nonlinear method for vertical settlement prediction of a single pile and pile groups in layered soils. *Computers and Geotechnics*, 45(9), 118-126. http://dx.doi.org/10.1016/j.compgeo.2012.05.011.

Zhang, Q.Q., Zhang, Z.M., & He, J.Y. (2010). A simplified approach for settlement analysis of single pile and pile groups considering interaction between identical piles in multilayered soils. *Computers and Geotechnics*, 37(7-8), 969-976. http://dx.doi.org/10.1016/j.compgeo.2010.08.003.

Zhang, Q.Q., & Zhang, Z.M. (2012a). A simplified nonlinear approach for single pile settlement analysis. *Canadian Geotechnical Journal*, 49(11), 11256-11266. http://dx.doi.org/10.1139/t11-110.

Zhang, Q.Q., & Zhang, Z.M. (2012b). Simplified calculation approach for settlement of single pile and pile groups. *Journal of Computing in Civil Engineering*, 26(6), 750-758. http://dx.doi.org/10.1061/(ASCE)CP.1943-5487.0000167.

Zhang, Q.Q., Liu, S.W., Zhang, S.M., Zhang, J., & Wang, K. (2016). Simplified non-linear approaches for response of a single pile and pile groups considering progressive deformation of pile-soil system. *Soil and Foundation*, 56(3), 473-484. http://dx.doi.org/10.1016/j.sandf.2016.04.013.

Soils and Rocks

An International Journal of Geotechnical and Geoenvironmental Engineering

www.soilsandrocks.com

ISSN 1980-9743
ISSN-e 2675-5475

Geogrid mechanical damage caused by recycled construction and demolition waste (RCDW) under in-field cyclic loading

Kátia Regina Monteiro Barbosa[1], Eder Carlos Guedes dos Santos[2#], Alexandre Duarte Gusmão[3]

Article

Keywords
Geosynthetic
Durability
Residues
RCDW
Waste recycling
Unpaved road

Abstract

Despite the advances observed over the last decade, Brazil still suffers from the scarce use of recycled construction and demolition waste (RCDW). On the other hand, most of the roads in the country are unpaved and present low loading support. In this context, the construction of geosynthetic reinforced unpaved roads with RCDW could stimulate the market of recycled materials and increase the performance of these roads. This study aims to evaluate the mechanical damage of two types of geogrids due to in-field cyclic loading of RCDW. The simulation of three scenarios of damage revealed specific reduction factors for each geogrid, which could be easily used in project design. This study reinforces the importance of carrying out investigation of geogrid damage using the specific conditions (material, construction method and loading) of each work. Based on these findings, sustainable development can be implemented using RCDW and provide roads to the society with better operational performance.

1. Introduction

The construction industry is vast and one of the most important industries worldwide due to its role in the growth of the national gross domestic product (GDP) of countries. However, despite being an important economic sector in Brazil, its activities are responsible for over 50% of waste generated in large Brazilian cities (Gusmão, 2008; John, 2000; Pinto, 1999). Nowadays construction and demolition waste (CDW) became a serious problem for the entire society.

A survey, which evaluated 310 recycling plants in Brazil, has shown they were operating at 47% of the maximum capacity, representing a potential to recycle only 16% of the total amount of CDW generated that year (Miranda, 2013). In addition to the low recycling capacity, the country suffers from the irregular dumping of these wastes. About 44.5 million tons of CDW were collected from public places in 2018, representing more than 61% of the total amount of waste collected by the municipal public services (ABRELPE, 2019).

CDW recycling appears as a very promising alternative, given that this waste mainly consists of materials (90% in mass) with the potential to be recycled for the production of new aggregates (Gusmão, 2008). Moreover, choosing materials that allow a simple treatment, such as recycled construction and demolition waste (RCDW), ensures low energy consumption and, as a consequence, low embodied energy. The recycling of CDW could recover from 37% to 42% of the embodied energy of a building (Thormark, 2002).

Bearing in mind that approximately 79% of the Brazilian roads are not paved (CNT, 2019), the proposal to use RCDW in geosynthetic reinforced unpaved roads would be an excellent option to demand great volumes of these materials, and therefore to increase the operational levels of the recycling plants and encourage the establishment of new ones. This could be a strategy to promote a vast market for recycled materials across the country and to preserve its natural resources.

Through laboratory tests, which simulated field conditions of reinforced unpaved roads, a combination of geogrid reinforcement and RCDW significantly increased the number of load repetitions sustained by the road, which could extend the life of the structure and reduce maintenance costs (Góngora & Palmeira, 2012). Large scale studies of unpaved roads (Fannin, 1986; Fannin & Sigurdsson, 1996; Watts et al., 2004; Hufenus et al., 2006; Palmeira & Antunes, 2010; Mekkawy et al., 2011) have shown the effectiveness of geogrid reinforcement related to the reduction of rutting

[#]Corresponding author. E-mail address: edersantos@ufg.br
[1]Universidade Federal de Pernambuco, Recife, PE, Brasil.
[2]Escola de Engenharia Civil e Ambiental, Universidade Federal de Goiás, Goiânia, GO, Brasil.
[3]Escola Politécnica de Pernambuco, Universidade de Pernambuco, Recife, PE, Brasil.

Submitted on August 5, 2020; Final Acceptance on May 19, 2021; Discussion open until August 31, 2021.

https://doi.org/10.28927/SR.2021.056520

formation, and consequently a better condition of supporting compared to non-reinforced roads.

However, geogrids may experience a reduction of their initial strength in both short- and long-term. The short-term effects are caused during the service strains due to the efforts from handling, installation and compaction (Hufenus et al., 2005). Long-term effects are not directly related to short-term effects, but geosynthetics that have suffered installation damage are more susceptible to long-term damage since they are unprotected, presenting higher reduction factors (Greenwood, 2002).

Reduction factor values for geogrid installation damage related to polymer type, protective coating and backfill material were published by Elias et al. (2001). Although important, these values have a relatively wide range. Laboratory and in-field studies have been performed aiming to define more specific reduction factors (Huang & Chiou, 2006; Huang & Wang, 2007; Pinho-Lopes & Lopes, 2014, 2015; Lim & McCartney, 2013). It was observed that they are directly related to the type of geosynthetics used, the nature of the polymer, compaction energy, and filling material.

Fleury et al. (2019) investigated the geogrid mechanical damage caused by RCDW due to installation procedures. The study revealed that, although the dropping heights reduced the tensile strengths, the compaction methods caused more severe damage. Similar results have been reported by Barbosa & Santos (2013) and Barbosa et al. (2016). However, the reduction factors presented by these studies encourage the use of RCDW in geosynthetic reinforced structures.

In a recent study, Domiciano et al. (2020) reported on short-term mechanical damage caused to geogrids by RCDW with different grain size distributions. Laboratory tests were carried out with a steel box and static loading within the magnitudes of values normally observed in the field conditions. The reduction factors calculated revealed the need for proper investigation when using RCDW as backfill material, which could enable them in the design phase.

In this context, given the variability of RCDW characteristics, the use of these materials could cause damage to the geogrids due to presence of coarse and/or angular grains, as well as perforating materials. The damage could also be influenced by the nature of loading processes. Thus, this study aims to investigate the mechanical damage of reinforcement elements when RCDW are used as backfill material and submitted to in-field cyclic loading.

2. Materials and methods

2.1 RCDW production

The RCDW used in this study was collected at a recycling plant located in Camaragibe, PE, Brazil. According to the operational manager, the RCDW is classified as ‘mixed material’, consisting predominantly of soil and, with a lower amount, concrete, ceramic and rock fragments. The recycling process consists of: i) visual inspection to verify if the CDW has up to 30% of contaminants (such as wood, plastic, paper, and metals); ii) if the contaminant limit is acceptable (< 30%), the CDW is crushed (jaw crusher) and sieved – the last of the contaminants are removed during sieving and the metallic elements are removed by a magnetic conveyor belt. The simplicity of this process ensures that production has low energy consumption, and therefore the recycled aggregate presents a low embodied energy.

2.2 Material characterization

To characterize the RCDW, samples were collected in two different periods. Firstly, five samples – codes RCDW 01 to 05 – were collected from March 29th to April 27th, 2016, in 7-day intervals in order to evaluate the mixed RCDW production process and property variability. Finally, two samples – codes RCDW 06 and RCDW 07 – were collected during the experimental section tests (September 6th, 2016). It is worth mentioning that RCDW was always collected from piles which contained the most recently produced materials. The samples were homogenized in the laboratory – according to ABNT (1986a) – and characterized following the procedures prescribed by Brazilian standards.

2.3 Geogrid

Two geogrids commercially used as reinforcement for paving were used in this study: i) uniaxial polyester (PET) geogrid coated with PVC (Figure 1a); and ii) flexible biaxial polypropylene (PP) geogrid (Figure 1b). Table 1 summarizes the main geogrid properties provided by the manufacturer. Specimens were cut according to the following dimensions: 200 mm width and 1,200 mm length, adopting the transversal machine direction for testing, once it would allow similar tensile strengths for both geogrids.

2.4 Description of the experimental section

To evaluate the mechanical damage caused by RCDW in the field, an experimental section of unpaved road (12.0 m long, 5.0 m wide and 0.30 m deep) was constructed in Camaragibe,

Table 1. Geogrid properties (provided by manufacturer).

Properties	PET Geogrid	PP Geogrid
MD ultimate tensile strength (kN/m)	≥ 35	≥ 15
CMD ultimate tensile strength (kN/m)	≥ 20	≥ 24
Stiffness at 5% strain along MD (kN/m)	350	400
Maximum tensile strain (%)	≤ 10	≤ 10
Aperture dimensions (mm)	25 x 25	15 x 15

Note: MD = machine direction; CMD = cross-machine direction.

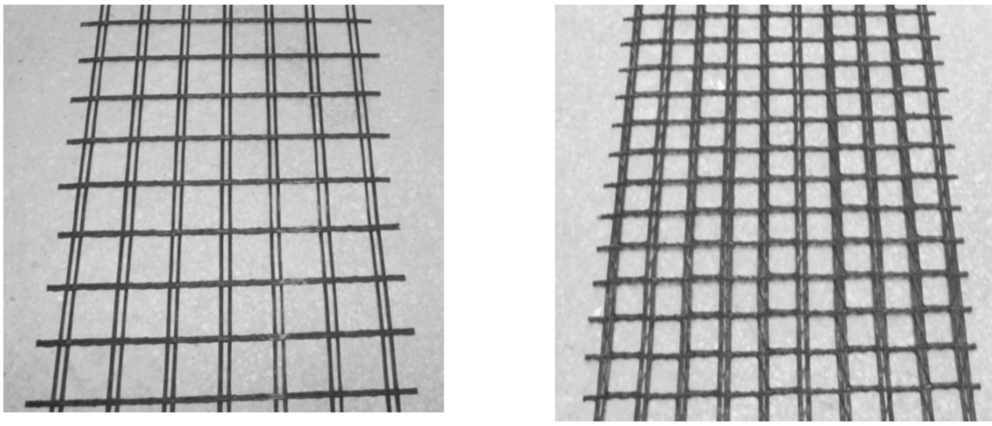

(a) (b)

Figure 1. Visual aspect of virgin geogrid: (a) PET geogrid; (b) PP geogrid.

PE, Brazil. The section consisted of a natural soil subgrade under two structural layers consisting of RCDW: i) base course (100 mm) and ii) surface course (200 mm), exposed to wear. The thickness of the base course was chosen to simulate shallow repair of unpaved road. Between the RCDW layers, specimens of geogrid were installed.

The standard procedure for performing the in-field loading was as follows:

i) excavation of the experimental section (Figure 2a);
ii) subgrade compaction using a vibratory roller (1.2 ton) with previous soil wetting;
iii) launching and spreading the RCDW for base layer construction;
iv) compaction of the base course (100 mm thick) – vibratory roller (1.2 ton);
v) installation of geogrid specimens (Figure 2b);
vi) launching and spreading of RCDW to construct the surface course (Figure 2c);
vii) compaction of the surface course (200 mm thick) – with interest equipment (Figure 2d);
viii) checking in-field density (ABNT, 1986b); and
ix) exhumation of geogrid specimens.

2.5 Damage induced

Geogrid samples were submitted to three damage scenarios: i) installation damage due to compaction with vibratory hammer; ii) installation damage due to compaction using a vibratory roller; and iii) installation damage (vibratory roller) and cyclic loading caused by truck traffic. The compaction degree in the field was intended to be no less than 95% (standard Proctor). More details on the compaction equipment are presented in Table 2.

Five specimens were exhumed for each scenario. Tensile tests were performed according to ISO 10319 (ISO, 2008). The geogrid specimens (virgin and damaged) were tested at the Geosynthetics Laboratory at the São Carlos School of Engineering, University of São Paulo, São Carlos, Brazil.

Table 2. Compaction equipment (provided by manufacturer).

Equipment	Weight	Centrifugal force	Frequency	Compaction depth
	(tf)	(kN)	(Hz)	(mm)
Vibratory plate	0.12	20	98	Up to 300
Vibratory roller	1.2	15	68	150 to 300

To determine the occurrence of damage, the methodology proposed by Santos (2011), which determines a confidence interval by means of Student's *t*-distribution, was used for statistical inferences. The methodology consists of:

i) the determination of mean value of tensile strength of virgin (no damaged) specimens (F_0);
ii) the definition of confidence interval for F_0, which covers all the tensile strength values obtained from virgin specimens (Equation 1);
iii) the determination of mean values of tensile strength for each damage scenario (F_i);
iv) verification if F_i is contained in the confidence interval of F_0. Values of F_i within the confidence interval of F_0 would represent uncertainties about the repercussion of the damage for the adopted reliability and, in this case, value of reduction factor (*RF*) equal to 1.0 was assumed. If values of F_i are presented out of confidence interval of F_0, the *RF* is calculated according to Equation 2.

$$t = \frac{\bar{X} - \mu}{s/\sqrt{n}} \tag{1}$$

where t = Student's *t*-distribution random variable; $\bar{X}$ = sample mean; μ = population mean; s = standard value deviation; n = number of samples.

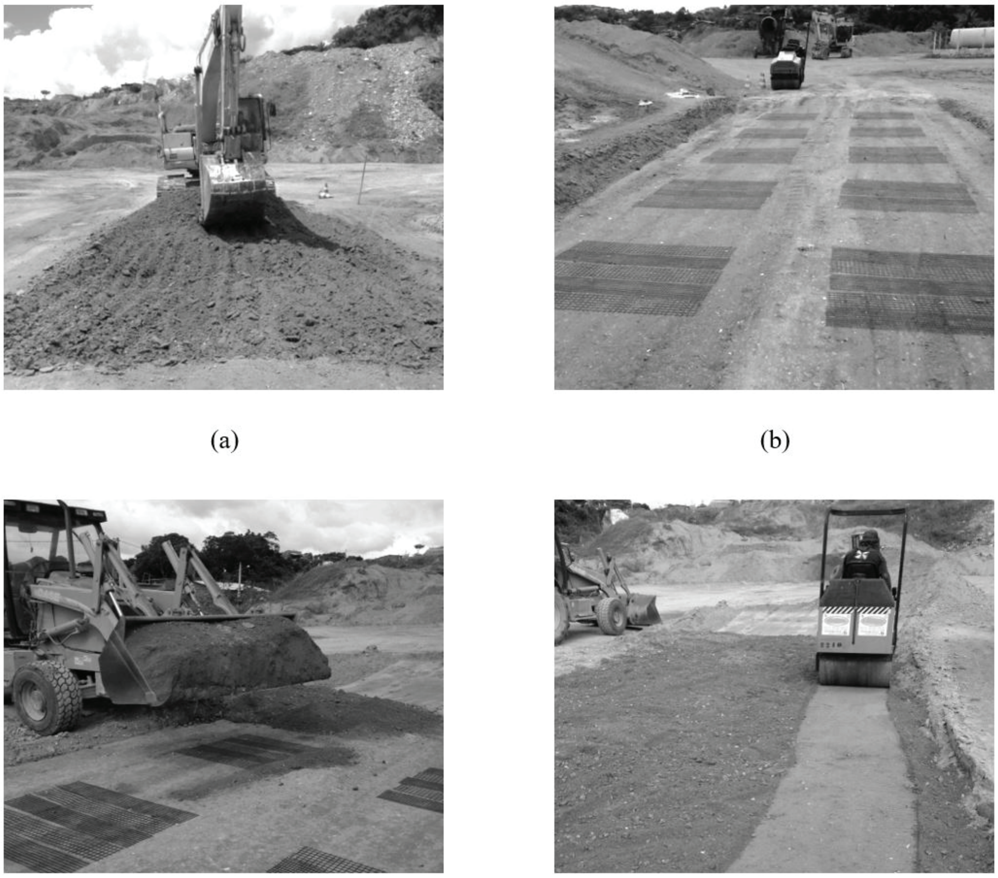

Figure 2. Construction of experimental section: (a) base course excavation; (b) geogrid specimen disposition; (c) RCDW launching; (d) compaction of the surface course with vibratory roller.

$$RF = \frac{F_0}{F_i} \tag{2}$$

where RF = reduction factor; F_0 = tensile strength mean value of virgin specimens; F_i = tensile strength mean value of scenario i.

2.6 Cyclic loading effect

The destructive effects of load per axle or set of axles on pavements can be related to a certain number of passages (N) of a standard axle through the Load Equivalency Factor (LEF). Thus, studies conducted by the American Association of State Highway and Transportation Officials (AASHTO) Road Test, in the late 1950s, defined the standard axle as a single double-axle (SDA) with a load of 18,000 lb or 82 kN (8.2 tf) and 80 psi (552 kPa) tire inflation pressure (Albano, 2005). The equivalence factors adopted in Brazil by the National Department of Transport Infrastructure (DNIT, in Portuguese) through DNER PRO 159/85 (DNER, 1985) based on the general equation of behavior of AASHTO (1972) are presented in Table 3.

Table 3. LEF equations (DNER, 1985).

Axle	Equation (P in tf)	Source
SAAW	$LEF = \left(P/7.77\right)^{4.32}$	(GEIPOT, 1977)
SADW	$LEF = \left(P/8.17\right)^{4.32}$	(AASHTO, 1972)
DTA	$LEF = \left(P/15.08\right)^{4.14}$	(AASHTO, 1972)

In this study, the number of truck passages was obtained from the balance reports of the recycling plant. Each truck passed 2 (two) times through the experimental section; one empty (without CDW) and another loaded (with CDW). Two types of trucks have passed through the experimental section of unpaved road: (i) solo axle truck with simple wheel and solo axle truck with double wheels (SAAW + SADW); and (ii) solo axle truck with simple wheel and dual tandem axle (SAAW + DTA). The Vehicle Factors (VF) adopted in this study were: i) those defined by DNIT (2010), for empty trucks; and ii) the sum of the LEF values with maximum axle load established by Brazilian legislation (see Table 3), for loaded trucks. Table 4 presents a summary of the *VF*.

During the period of exposure to cyclic loading, 39 (SAAW + SADW) and 23 (SAAW + DTA) were recorded, which corresponds to 124 in total, given that each truck passed twice over the experimental section. The total sum of *VF* was 158.452. This means that the total amount of axle loads to which the experimental section was submitted has the same effect (damage) of approximately 158 passes of a standard axle (SADW) loaded with 18,000 lb or 82 kN (8.2 tf). Given that the geogrids were arranged in a way that the wheels of the trucks (left- or right-hand side) passed over the central part of the specimens, it can be considered that each specimen has received an estimated load equivalent to half of the total passes of the SADW, which represents a total number of approximately 79 cycles.

Figure 3a illustrates the traffic of trucks over the experimental section on the second day of cyclic loading (September 9th, 2016). The third day of cyclic loading (September 12th, 2016) was adversely affected by an intense rain precipitation that occurred during the weekend. According to Pernambuco State Agency for Water and Climate (APAC, in Portuguese), an average rain precipitation of 18 mm was recorded on the day before the cyclic loading. Due to the lack of drainage system at the recycling plant area, this precipitation was enough to keep the experimental area flooded during the whole precipitation period. Therefore, in order to prevent additional damage, 5 (five) specimens of each geogrid were exhumed before the recycling plant started its operation. After this, the traffic caused the section failure, which was characterized by the formation of grooves of 45 to 110 mm deep, as illustrated in Figure 3b. However, it should be mentioned that, in general, this level of rut depth would still be acceptable for unpaved roads.

Table 4. Vehicle factors according to DNIT (2010).

Composition	Vehicle factors (VF)	
	Empty	Loaded [1]
SAAW + SADW	0.103	2.722
SAAW + DTA	0.129	1.970

Note: [1] Sum of the LEF values with maximum axle load.

3. Results and discussion

3.1 Recycled CDW

The grain-size distribution curves of RCDW revealed a low variability for samples tested (Figure 4), with predominance of sand and gravel fractions (Table 5). The RCDW presented an average coefficient of uniformity (C_U) equal to 38.86, with coefficient of variation (*COV*) of 40.44%, and coefficient of curvature (C_C) equal to 1.73, with *COV* of 35.76%. The percentage of grains smaller than 0.42 mm was 40.49% (*COV* = 9.80%).

The RCDW also showed low variability for other geotechnical parameters investigated (Table 6), presenting non-expansive and non-plastic behavior (ABNT, 1984b). It is worth mentioning that the recycling plant carries out a standard process to produce recycled materials, with low energy incorporated, by means of a simple treatment (sorting and crushing). This guarantees a RCDW with low embodied energy.

3.2 Tensile tests

The confidence intervals obtained for the average strengths of virgin specimens presented confidence levels of 95%, for both geogrids, and values equal to:

Table 5. Granulometric composition of RCDW.

Classification	Mean (%)
Gravel	31.20
Coarse sand	17.32
Medium sand	23.65
Fine sand	15.39
Silt	3.24
Clay	9.21

(a)

(b)

Figure 3. Experimental section #2: (a) truck traffic; (b) formation of grooves after intense rain precipitation.

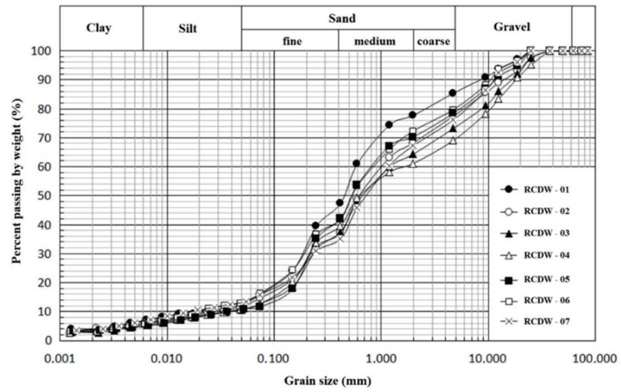

Figure 4. Grain-size distribution curves of RCDW – tested according to NBR 7181 (ABNT, 1984a).

PET geogrid: 16.85 kN/m < F_0 < 19.44 kN/m; and

PP geogrid: 22.82 kN/m < F_0 < 23.86 kN/m.

The *COV* of virgin samples were 5.7% and 1.8%, for PET and PP geogrids, respectively. These values were smaller in comparison to field-damaged geogrid samples – considering all the damage scenarios. The curves of load versus strain of tensile strength tests are shown in Figure 5. The comparative results of the geogrid properties after test with its respective *COV* (presented between parentheses) are shown in Table 7 and 8.

It was observed that the average values of maximum tensile strength (T_{max}) for damaged PET geogrid samples presented values outside the confidence interval of virgin samples, with a reduction factor (*RF*) higher than 1.0 for

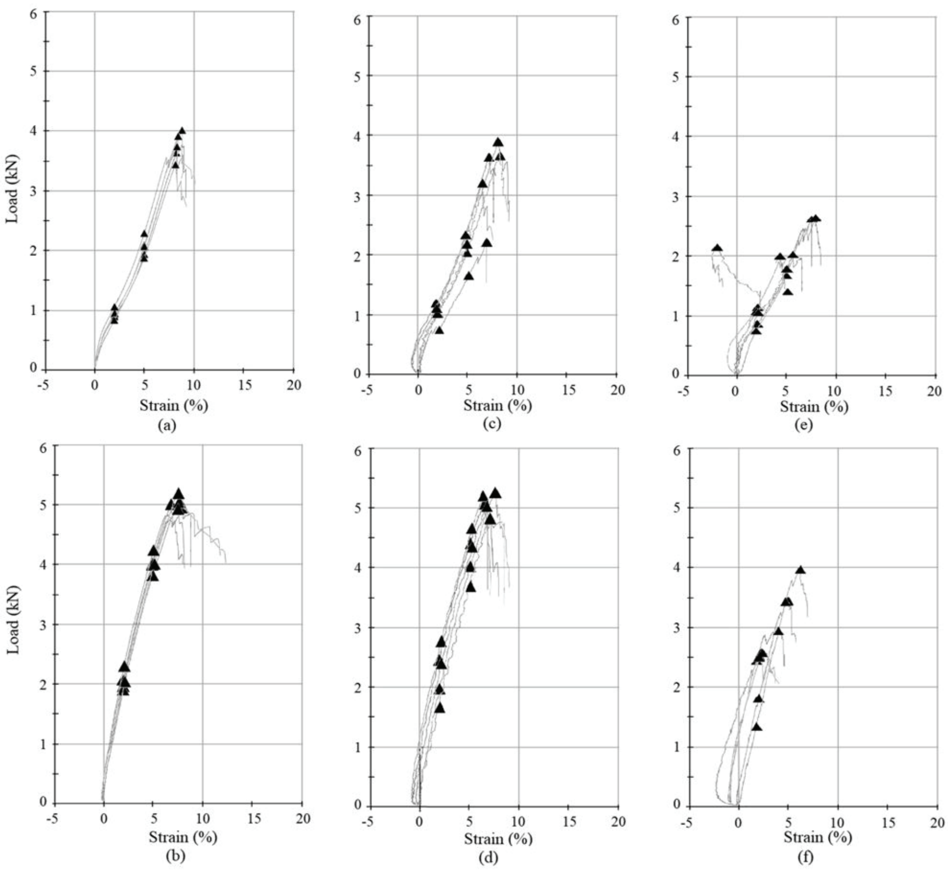

Figure 5. Load versus strain curve (width - 200mm): (a) PET geogrid - virgin; (b) PET geogrid - installation damage; (c) PET geogrid - Installation and loading damage; (d) PP virgin geogrid; (e) PP geogrid - Installation damage; (f) PP geogrid - Installation and loading damage.

Table 6. Summary of the laboratory and the in-field testing program of the RCDW.

	Percent of soil [1]	G_S [2]	$\gamma_{d\,max}$ [3]	w_{ot} [4]	*CBR* [5]	*w* [6]	γ [7]
	(%)		(kN/m³)	(%)	(%)	(%)	(kN/m³)
Mean	78	2.641	18.55	12.62	25	10.33*	18.20*
COV [8] (%)	6.20	3.35	1.39	6.09	24.99	2.28*	0.62*

Note: 1. RCDW smaller than 4.75 mm was classified as ‘soil’; 2. Specific gravity (ABNT, 1984c); 3. Maximum dry unit weight (ABNT, 1986c); 4. Optimum water content (ABNT, 1986c); 5. California Bearing Ratio (ABNT, 1987); 6. Moisture content in the field by Speedy Moisture Test; 7. Density in the field after compaction (ABNT, 1986b); 8. Coefficient of variation; (*) Value obtained from 3 (three) tests.

Table 7. Results of PET geogrid.

Scenario	T_{max} (kN/m)	ε_{rup} (%)	$J_{2\%}$ (kN/m)	$J_{5\%}$ (kN/m)
Virgin specimen	18.15 (5.7)	8.38 (2.8)	227.5 (7.6)	199 (7.1)
Installation damage (VP)	14.73 (15.3)	6.96 (22.6)	224.0 (18.9)	185.6 (9.7)
Installation damage (VR)	16.2 (18.2)	7.5 (9.3)	249 (14.5)	205.4 (11.9)
Installation and loading damage (VR + TT)	11.38* (16.01)	6.23* (26.4)	234.0* (18.8)	163* (10.3)

Note: VP = vibratory plate; VR = vibratory roller; TT = truck traffic; (*) Except sample PET #01 (see Figure 5c).

Table 8. Results of PP geogrid.

Scenario	T_{max} (kN/m)	ε_{rup} (%)	$J_{2\%}$ (kN/m)	$J_{5\%}$ (kN/m)
Virgin specimen	23.34 (1.8)	7.56 (5.3)	479 (6.4)	316 (9.6)
Installation damage (VP)	15.16 (8.2)	6.6 (27.6)	292 (40.5)	226.6 (29.8)
Installation damage (VR)	23.08 (3.0)	6.7 (7.1)	515 (16.8)	384.4 (7.9)
Installation and loading damages (VR + TT)	14.16 (17.2)	4.06 (40.5)	486 (21.9)	313* (0.30)

Note: VP = vibratory plate; VR = vibratory roller; TT = truck traffic; (*) Except sample PET #01, #2 and #4 (see Figure 5f).

Table 9. Reduction factor (*RF*) for geogrids.

Scenario	PET	PP
Installation damage (VP)	1.23	1.54
Installation damage (VR)	1.12	1
Installation and loading damages (VR + TT)	1.44	1.65

both compaction methods (Table 9). It was observed that the compaction with vibratory plate causes more severe damage (*RF* = 1.23) compared to the vibratory roller (*RF* = 1.12). This finding becomes more evident analyzing the results of the PP geogrid, once only the compaction with vibratory plate caused damage to the geogrid (*RF* = 1.54) - the compaction using vibratory roller did not cause damage (*RF* = 1.0). This finding is in accordance with those presented by Fleury et al. (2019).

Geogrid samples that have been subjected to cyclic loading (79 cycles of standard axle) presented a great increment of damage in a short period of time (2 days). An increase of 28.5% has been observed for PET geogrid, which had the *RF* changed from 1.12 to 1.44 (see Table 9). More evidence of the cyclic effect on geogrid mechanical damage was verified for PP geogrid, which has exhibited an increase of 65%, with *RF* presenting a change from 1.0 (no damage) to 1.65. Regarding the conditions investigated in this study, PET geogrid samples were more resistant to damage induced by cyclic loading, with a strength loss of 29.7% in relation to samples damaged by the installation procedure, while the PP geogrid samples showed a loss of 38.6%.

4 Conclusions

This paper showed the effect of RCDW on the short-term mechanical behavior of two types of geogrids. In-field tests were carried out to evaluate the induced installation and cyclic loading damage on tensile strength of the geogrids. The conclusions of this study are presented as follows:

- The RCDW presented excellent values of geotechnical properties, with low variability and non-expansive and non-plastic behaviors, following the recommendations prescribed by the Brazilian standards for unpaved roads;
- The standard procedures adopted by the recycling plant revealed that it is possible to produce a recycled material with high quality and low embodied energy using simple treatments (sorting and crushing);
- The PP geogrid presented resistance to the induced installation procedure (no damage), while the PET geogrid presented loss of tensile strength of 20%;
- The cyclic loading damage was more severe to PP geogrid than PET geogrid, with reductions of tensile strength equal to 38.6% and 29.7%, respectively, compared to samples submitted only to installation damage; and
- This study reinforces the importance of carry out investigation of geogrid damage using the specific conditions (material, construction method and loading) of each work and the need of evaluating the occurrence of damage in short- and long-term.

In addition, the results presented are considered preliminary and further research is needed to better understand the factors affecting the performance of geogrids in unpaved roads constructed with alternative low-cost materials.

Acknowledgements

The authors are indebted to the following institutions that supported the research activities reported in this paper in different ways: University of Pernambuco (UPE), National Council for Scientific and Technological Development

(CNPq), and CAPES – Brazilian Ministry of Education. The authors also thank the manufacturer of geosynthetics and Ciclo Ambiental Ltda, for providing information and materials presented in this paper.

Declaration of interest

The authors have no affiliation with or involvement in any organization with a direct or indirect financial interest in the subject matter discussed in the manuscript that could bias its results. All co-authors have seen and agree with the contents of the manuscript and certify that it has not been submitted to, nor is under review at, another journal or other publishing venue.

Authors' contributions

Kátia R. M. Barbosa: methodology, investigation, validation, writing - original draft preparation. Eder C. G. Santos: conceptualization, methodology, supervision, validation, funding acquisition, writing - reviewing and editing. Alexandre D. Gusmão: funding acquisition, supervision, writing - reviewing and editing.

List of symbols

AASHTO	American Association of State Highway and Transportation Officials
ABNT	Brazilian Association of Technical Standards
ABRELPE	Brazilian Association of Urban Cleaning and Special Solid Waste Companies
ASTM	American Society for Testing and Materials
CBR	California Bearing Ratio (%)
CDW	Construction and demolition waste
C_C	Coefficient of curvature (dimensionless)
CNT	National Confederation of Transport
COV	Coefficient of variation (%)
C_U	Coefficient of uniformity (dimensionless)
DNER	National Department of Roads
DNIT	National Department of Transport Infrastructure
DTA	Dual tandem axle
FEC	Load equivalency factor (tf)
F_i	Tensile strength mean value of scenario i (kN/m)
F_0	Tensile strength mean value of virgin specimens (kN/m)
G_S	Specific gravity (dimensionless)
$J_{2\%}$	Secant tensile stiffness at 2% strain (kN/m)
$J_{5\%}$	Secant tensile stiffness at 5% strain (kN/m)
n	Number of samples (dimensionless)
N	Number of passages of a standard axle (dimensionless)
NBR	Brazilian Standard
P	Weight (tf)
PET	Polyester
PP	Polypropylene
PVC	Polyvinyl chloride
RCDW	Recycled construction and demolition waste
RF	Reduction factor (dimensionless)
s	Standard value deviation (parameter dependent)
SAAW	Solo axle truck with simple wheel
SADW	Solo axle truck with double wheels
SDA	Single double-axle
t	Student's t-distribution random variable (dimensionless)
T_{max}	Tensile strength at rupture (kN/m)
TT	Truck traffic
$\bar{X}$	Sample mean (parameter dependent)
VF	Vehicle Factor (dimensionless)
VP	Vibratory plate
VR	Vibratory roller
w_{ot}	Optimum water content (%)
ε_{rup}	Strain or elongation at rupture mean value (%)
$\gamma_{d\,max}$	Maximum dry unit weight (kN/m^3)
μ	Population mean (parameter dependent)

References

American Association of State Highway and Transportation Officials – AASHTO. (1972). *Interim guide for design of pavement structures.* AASHTO

ABNT NBR 7181. (1984a). *Soil - Grain size analysis*. Associação Brasileira de Normas Técnicas, Rio de Janeiro, RJ (in Portuguese).

ABNT NBR 6459. (1984b). *Soil - Liquid limit determination*. Associação Brasileira de Normas Técnicas, Rio de Janeiro, RJ (in Portuguese).

ABNT NBR 6458. (1984c). *Gravel grains retained on the 4.8 mm mesh sieve - Determination of the bulk specific gravity, of the apparent specific gravity and of water absorption*. Associação Brasileira de Normas Técnicas, Rio de Janeiro, RJ (in Portuguese).

ABNT NBR 6457. (1986a). *Soil samples - Preparation for compaction and characterization tests*. Associação Brasileira de Normas Técnicas, Rio de Janeiro, RJ (in Portuguese).

ABNT NBR 7185. (1986b). *Soil - In situ determination of the apparent specific gravity by sand replacement method using a glass bottle*. Associação Brasileira de Normas Técnicas, Rio de Janeiro, RJ (in Portuguese).

ABNT NBR 7182. (1986c). *Soil - Compaction test*. Associação Brasileira de Normas Técnicas, Rio de Janeiro, RJ (in Portuguese).

ABNT NBR 9895. (1987). *Soil - California bearing ratio (CBR) - Testing method*. Associação Brasileira de Normas Técnicas, Rio de Janeiro, RJ (in Portuguese).

Associação Brasileira de Empresas de Limpeza Pública e Resíduos Especiais – ABRELPE. (2019). *The Panorama of Solid Waste in Brazil 2018/2019*. ABRELPE.

Albano, J.F. (2005). Efeitos dos excessos de carga sobre a durabilidade de pavimentos [Doctoral thesis, Federal University of Rio Grande do Sul]. Federal University of Rio Grande do Sul's repository (in Portuguese). https://lume.ufrgs.br/handle/10183/4498.

Barbosa, F.A.S., & Santos, E.C.G. (2013). Geogrid mechanical damages due to recycled construction and demolition wastes. *Proceedings 14th International Waste Management and Landfill Symposium* (pp. 1-8). Cagliari, International Waste Working Group (IWWG).

Barbosa, F.A.S., Silva, E.M., & Santos, E.C.G. (2016). Redução de resistência de geossintéticos de polipropileno (PP) devido a danos de instalação causados por resíduos de construção e demolição reciclados (RCD-R). In *Anais do 18º Congresso Brasileiro de Mecânica dos Solos e Engenharia Geotécnica* (pp. 1-6). Belo Horizonte. ABMS. (in Portuguese).

ISO 10319. (2008). *Geosynthetics - Wide-width Tensile Test*. ISO - International Organization for Standardization, Geneva.

CNT (2019). *CNT Highway Survey 2019*. CNT - Confederação Nacional do Transporte, Brasília, DF (in Portuguese).

DNER PRO 159/85. (1985). *Project for restoration of flexible and semi-rigid pavements*. Rio de Janeiro, DNER. (in Portuguese).

Departamento Nacional de Infraestrutura de Transportes – DNIT. (2010). *Projeto básico de engenharia para adequação e duplicação de rodovia na travessia urbana de Nova Rosalândia – TO*. DNIT (in Portuguese).

Domiciano, M.L., Santos, E.C.G., & Lins da Silva, J. (2020). Geogrid mechanical damage caused by recycled construction and demolition waste (RCDW): influence of grain size distribution. *Soils and Rocks*, 43(2), 231-246. http://dx.doi.org/10.28927/SR.432231.

Elias, V., Christopher, B.R., & Berg, R.R. (2001). *Mechanically stabilized earth walls and reinforced soil slopes design & construction guidelines*. Department of Transportation, Federal Highway Administration.

Fannin, R.J. (1986). *Geogrid reinforcement of granular layers on soft clay – a study at model and full scale* [Doctoral Thesis, University of Oxford]. University of Oxford's repository. https://ora.ox.ac.uk/objects/uuid:8c860a74-b730-4039-9d5f-383c4156257b.

Fannin, R.J., & Sigurdsson, O. (1996). Field observations on stabilization of unpaved roads with geosynthetics. *Journal of Geotechnical Engineering*, 122(7), 544-553. http://dx.doi.org/10.1061/(ASCE)0733-9410(1996)122:7(544).

Fleury, M.P., Santos, E.G.G., Lins da Silva, J., & Palmeira, E.M. (2019). Geogrid installation damage caused by recycled construction and demolition waste. *Geosynthetics International*, 26(6), 641-656. http://dx.doi.org/10.1680/jgein.19.00050.

Empresa Brasileira de Planejamento de Transportes – GEIPOT. (1977). *Relatório intermediário: resultados e análises preliminares*. GEIPOT, (in Portuguese).

Góngora, I.A.G., & Palmeira, E.M. (2012). Influence of fill and geogrid characteristics on the performance of unpaved roads on weak subgrades. *Geosynthetics International*, 19(2), 191-199. http://dx.doi.org/10.1680/gein.2012.19.2.191.

Greenwood, J.H. (2002). The effect of installation damage on the long-term design strength of a reinforcing geosynthetic. *Geosynthetics International*, 9(3), 247-258. http://dx.doi.org/10.1680/gein.9.0217.

Gusmão, A.D. (2008). *Manual de Gestão de Resíduos da Construção Civil*. CCS Gráfica Publisher (in Portuguese).

Huang, C.C., & Chiou, S.L. (2006). Investigation of installation damage of some geogrids using laboratory tests. *Geosynthetics International*, 13(1), 23-35. http://dx.doi.org/10.1680/gein.2006.13.1.23.

Huang, C.C., & Wang, Z.H. (2007). Installation damage of geogrids: influence of load intensity. *Geosynthetics International*, 14(2), 62-75. http://dx.doi.org/10.1680/gein.2006.13.1.23.

Hufenus, R., Rüegger, R., Flum, D., & Sterba, I.J. (2005). Strength reduction factors due to installation damage of reinforcing geosynthetics. *Geotextiles and Geomembranes*, 23(5), 401-424. http://dx.doi.org/10.1016/j.geotexmem.2005.02.003.

Hufenus, R., Rüegeer, R., Banjac, R., Mayor, P., Springman, S.M., & Brönnimann, R. (2006). Full-scale field tests on geosynthetic reinforced unpaved roads on soft subgrade. *Geotextiles and Geomembranes*, 24(1), 21-37. http://dx.doi.org/10.1016/j.geotexmem.2005.06.002.

John, V.M. (2000). *Reciclagem de resíduos na construção civil: contribuição à metodologia de pesquisa e desenvolvimento* [Thesis for position of Associate Professor]. University of São Paulo (in Portuguese).

Lim, S.Y., & McCartney, J.S. (2013). Evaluation of effect of backfill particle size on installation damage reduction factors for geogrids. *Geosynthetics International*, 20(2), 62-72. http://dx.doi.org/10.1680/gein.13.00002.

Miranda, L.F.R. (2013). *Panorama das usinas de reciclagem de RCD no Brasil: a pesquisa setorial ABRECON 2013*. ABRECON. (in Portuguese).

Mekkawy, M.M., White, D.J., Suleiman, M.T., & Jahren, C.T. (2011). Mechanically reinforced granular shoulders on soft subgrade: laboratory and full-scale studies. *Geotextiles and Geomembranes*, 29(2), 149-160. http://dx.doi.org/10.1016/j.geotexmem.2010.10.006.

Palmeira, E.M., & Antunes, L.G.S. (2010). Large scale tests on geosynthetic reinforced unpaved roads subjected to surface maintenance. *Geotextiles and Geomembranes*, 28(6), 547-558. http://dx.doi.org/10.1016/j.geotexmem.2010.03.002.

Pinho-Lopes, M., & Lopes, M.L. (2014). Tensile properties of geosynthetics after installation damage. *Environmental Geotechnics*, 1(3), 161-178. http://dx.doi.org/10.1680/envgeo.13.00032.

Pinho-Lopes, M., & Lopes, M.L. (2015). Synergisms between laboratory mechanical and abrasion damage on mechanical and hydraulic properties of geosynthetics. *Environmental Geotechnics*, 4, 50-63. http://dx.doi.org/10.1016/j.trgeo.2015.07.001.

Pinto, T.P. (1999). *Methodology for management of urban construction solid waste* [Unpublished doctoral thesis]. University of São Paulo (in Portuguese).

Santos, E.C.G. (2011). Avaliação experimental de muros reforçados executados com resíduos de construção e demolição reciclados (RCD-R) e solo fino [Doctoral thesis], University of Brasília (in Portuguese).

Thormark, C. (2002). A low energy building in a life cycle - its embodied energy, energy need for operation and recycling potential. *Building and Environment*, 37(4), 429-435. http://dx.doi.org/10.1016/S0360-1323(01)00033-6.

Watts, G.R.A., Blackman, D.I., & Jenner, C.G. (2004). The performance of reinforced unpaved sub-bases subjected to trafficking. In *Proceedings 3rd European Geosynthetics Conference*, Munich. Vol. 1, München, Germany: Technische Universität München, 261-266.

Soils and Rocks
An International Journal of Geotechnical and Geoenvironmental Engineering
www.soilsandrocks.com
ISSN 1980-9743
ISSN-e 2675-5475

Hydraulic conductivity and undrained shear strength of clay-construction and demolition solid waste materials mixtures

Mohammed Abdulnafaa[1], Muwafaq Awad[2], Ali Cabalar[3], Nurullah Akbulut[4], Burak Ozufacik[4]

Article

Keywords
Clay
Construction and demolition material
Undrained shear strength
Hydraulic conductivity

Abstract

The study aims to investigate the effects of three different construction and demolition materials (CDMs), including crushed waste asphalt (CWA), crushed waste bricks (CWB), and crushed waste concrete (CWC), on some geotechnical properties of low plastic clayey soil, particularly, the undrained shear strength (S_u) and the hydraulic conductivity (k). A set of experimental tests were performed on clayey soil and on clayey soil-CDM mixtures at mixing ratios of 5%, 10%, 15%, and 20% by dry weight. The results show that the soil plasticity decreases as the CDMs increase. Quantitatively, it is found a maximum of 12%, 6%, and 6% decrease in the liquid limits (LL) and a maximum of 9%, 4%, and 6% decrease in the plasticity limit (PI) of the mixtures with 20% of CWA, CWB, and CWC, respectively. The results of the S_u estimated empirically from the fall cone tests show that the S_u decreases as the CDMs increase. The S_u reduces by approximately 10% and 2% of the mixtures with 20% CWA and CWB, respectively. But the S_u is not affected by the CWC additive for water content lower than approximately 35%. The k value increases as the CDMs increase. The results show that the reported k value increases by 75%, 79%, and 247% of the mixtures with 20% of CWA, CWB, and CWC, respectively. Additionally, the k values obtained from the consolidation test confirm the findings of the effect of the CDMs on the coefficient of hydraulic conductivity.

1. Introduction

The excessive increase in construction activities causes a significant increasing generation of construction and demolition materials (CDMs). Obaid et al. (2019) report that 1.3 billion tons of construction and demolition waste are generated worldwide yearly. This quantity is anticipated to increase up to approximately two times by 2025. Disposing of these materials in landfills will reflect economic and environmental problems. Recently, studies have been done to consider investing and recycling these materials in real projects and studied the engineering properties of these materials (Arulrajah et al., 2011, 2012, 2013; Cristelo et al., 2016; Park, 2003; Yoshizawa et al., 2005). From a geotechnical perspective, studies have been done to investigate the possibility of using these materials additives to enhance the engineering properties of soils and to avoid economic and environmental problems.

Various percentages of crushed bricks, dragged asphalt, and crushed concrete paving slabs were used as additives to reduce the swelling potential of clayey soil (Cabalar et al., 2016). A plasticity index (PI), which is a strong indicator of swelling potential in clayey soils, was found to decrease as the amount of CDMs increases in the mixtures. It was reported that the PI reduced by 28%, 39%, and 43% for an additive of 15% of dragged asphalt, crushed bricks, and concrete paving slabs, respectively. Mohialdeen et al. (2020) investigated the effects of CDMs on expansive soils from Mosul, Iraq, on soil consistency limits. The liquid limit and PI were found to reduce by approximately 16 and 25%, respectively, and the demolition type controls the reduction percent.

Researchers have performed strength tests to investigate the effect of the CMDs on drained shear strength of various soil types (Abdulnafaa et al., 2019; Abhijith et al., 2014; Arulrajah et al., 2014; Jia et al., 2015). In geotechnical design, drained shear strength does not always replicate the field conditions. Therefore, the undrained shear strength should be used in design and analysis. This criterion is applied mainly

#Corresponding author. E-mail address: mohammed1979eng@uomosul.edu.iq
[1]Department of Environmental Engineering, Faculty of Engineering, University of Mosul, Mosul, Iraq.
[2]Department of Civil Engineering, Faculty of Engineering, University of Mosul, Mosul, Iraq.
[3]Department of Civil Engineering, Faculty of Engineering, University of Gaziantep, Gaziantep, Turkey.
[4]Department of Civil Engineering, Faculty of Engineering, Hasan Kalyoncu University, Gaziantep, Turkey.

Submitted on January 9, 2021; Final Acceptance on May 12, 2021; Discussion open until August 31, 2021.
https://doi.org/10.28927/SR.2021.062221

to low permeability soils such as clayey soils. Undrained shear strength can be measured in the laboratory using consolidated undrained (CU) or unconsolidated undrained (UU) triaxial tests, vane shear test, or fall cone test. Very few studies have been performed on the assessment of effects of CDMs on the undrained shear strength of fine-grained soils mixed with CDMs. These studies are limited on assessing the undrained shear strength from unconfined compression tests (Cabalar et al., 2016; Lukiantchuki et al., 2019). The current study used an alternative method for estimating the undrained shear strength (S_u), which is the fall cone testing method. This method has an advantage over other methods (unconfined compression test, direct shear test, triaxial test, and vane shear test) for being a very fast method, using relatively small specimen, and performing over a wide range of water content (Canelas et al., 2018).

Hydraulic properties of soils are as important as the mechanical properties of soils. There are a few research studies on the effects of CDMs on the hydraulic properties of soils, and they are limited to coarse-grained soils. Poon & Chan (2006) studied the effect of self-cementing properties of fine CWC on the properties of unbounded sub-base materials. The results showed that the sub-base aggregate-CWC mixtures exhibited higher hydraulic conductivity than the natural sub-base aggregate by approximately one order of magnitude when it was measured immediately after compaction. Bennert et al. (2000) studied the hydraulic conductivity of natural aggregate and aggregate with varying percentages of CWC and CWA. The results showed that the hydraulic conductivity of aggregate mixed with 75% of CWC became closer to the hydraulic conductivity values of natural aggregate. Kang et al. (2011) evaluated the suitability of four recycled materials with aggregates as base and sub-base layers for roads. They found that the coefficients of hydraulic conductivity of the mixtures were higher than that of the natural aggregates. All the above-mentioned studies have suggested investigating the effects of CDMs on the hydraulic conductivity of fine-grained soils and, it is important to note that they agree that the hydraulic conductivity coefficients of soil-CDM mixtures are generally higher than those of natural soils.

The main objective of the current research was to investigate the impacts of the CDMs on the soil Atterberg limits, the undrained shear strength, and the hydraulic conductivity of low plasticity clayey soil. Undrained shear strength (S_u) was evaluated for various water content and the effect of the CDMs was assess quantitatively. The hydraulic conductivity using two different techniques (falling head tests and consolidation tests) was evaluated for both clayey soil and clayey soil-CDMs mixtures.

2. Materials

The soil used for the current research was classified as a brown clayey soil (ASTM, 2000) with pieces of $CaCo_3$ fragments. Physical properties of the clayey soil were measured according to ASTM standards and the results are tabulated in Table 1.

Three construction and demolition (CDMs) materials illustrated in Figure1 (CWA, CWB, and CWC) were used in this study as additive materials mixed with the clayey soil. The CWA material was produced from the destruction of old and under maintenance crushed asphalt roads and highways, the CWB material was produced from the demolition of buildings, and the CWC material was accumulated in large piles from old plain concrete of building, pavement, and sidewalks.

Atterberg limits tests of clayey soil and clayey soil-CDMs mixtures were performed according to ASTM D4318 (ASTM, 2005) and the results are presented in Table 2. The results of sieve analysis performed on clayey soil and CDMs are shown in Figure 2. Compaction tests following the modified Proctor method were performed on clayey soil and clayey soil-CDMs mixtures according to ASTM D-2216 (ASTM, 1998), and the compaction characteristics were presented in Table 2.

3. Methodology

3.1 Atterberg limits tests

The clayey soil and CDMs were sieved on No. 40 (0.425 mm) for performing the Atterberg limits tests. The tests were performed for both clayey soil and clayey soil-CDM mixtures in accordance with the ASTM D4318 (2005). The liquid limit test was performed using British fall cone equipment according to BS 1377 (BSI, 1990). The results were adopted to empirically estimate the undrained shear strengths (S_u) of soils.

The soil samples of clay and clay-CDM mixtures were prepared using oven-dried clayey soil and CDMs. The required amount of clayey soil and CDMs for each test were weighed and mixed thoroughly in a dry state until homogeneity was achieved. Then the mixture was

Table1. Index properties of clayey soil.

Soil properties Clayey soil		Soil type
Specific gravity, *Gs*		2.7
Atterberg limits	Liquid limit, LL (%) as per BSI standard	42
	Plastic limit, PL (%)	25
	Plasticity index (%)	17
Grain size analysis	Sand (%)	40
	Silt (%)	43
	Clay (%)	17
Classification	Unified soil classification system (USCC)	CL
	AASHTO	A-7-6(14)

Table 2. Atterberg limits and classification of clayey soil and soil-CDMs mixtures.

Mixture type	CDMs (%)	Compaction Characteristics		LL (%)	PL (%)	PI (%)	Classification	
		OMC (%)	$\gamma_{d\,max}$ (kN/m^3)				USCS	AASHTO
Clayey soil	0	18.0	17.30	42	25	17	CL	A-7-6(14)
CWA [a]	5	13.5	17.58	41	27	14	ML	A-7-6(12)
CWA	10	12.6	17.92	40	28	12	ML	A-7-6(11)
CWA	15	12.0	18.00	36	25	11	ML	A-6(9)
CWA	20	11.6	18.26	30	22	8	ML	A-4(5)
CWB [b]	5	18.2	17.25	41	28	13	ML	A-7-6(12)
CWB	10	17.5	17.21	39	27	12	ML	A-6(10)
CWB	15	17.6	17.22	38	28	10	ML	A-6(9)
CWB	20	17.1	17.10	36	27	9	ML	A-4(8)
CWC [c]	5	16.6	17.30	41	29	12	ML	A-7-6(11)
CWC	10	16.3	17.70	40	30	10	ML	A-4(9)
CWC	15	15.8	17.80	37	30	7	ML	A-4(6)
CWC	20	15.2	17.93	36	30	6	ML	A-4(60)

[a] Crushed waste asphalt (CWA), [b] Crushed waste bricks (CWB), [c] Crushed waste concrete (CWC).

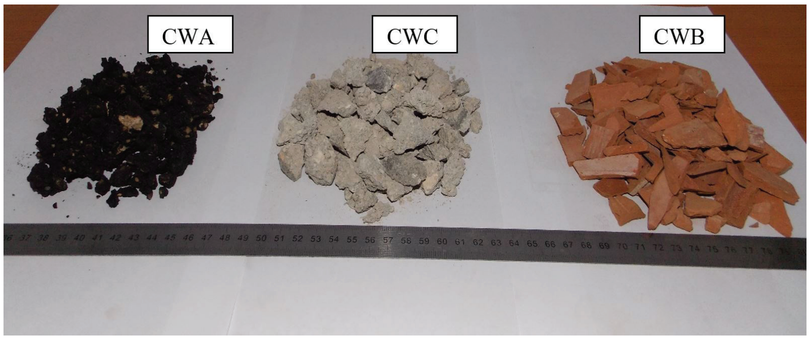

Figure 1. Construction and demolition materials.

mixed with a required amount of water to become like a workable paste and cured for 24 hours in plastic bags before testing.

A British fall cone device with a 30° cone and 0.785 N weight was used. The fall cone cup diameter was 55 mm, and the height was 40 mm. The prepared sample was placed into the fall cone cup using a spatula ensuring no air was trapped during the process. A leveled side of the straight edge was used to remove the excess soil on the cup surface to obtain a smooth surface. Finally, the sample was placed in the device with the cone tip barely touching the surface of the tested sample. After five seconds of penetration, the penetration distance was measured. Three trials were performed to check the repeatability of the tested samples. After test completion, the sample moisture content was determined. The same testing procedure was repeated for all clayey soil and soil-CDMs mixtures at different moisture contents.

The empirical Equation 1, proposed by Hansbo (1957), was adopted to estimate the undrained shear strength (S_u) of soils from the measured consistency limits.

$$S_u = k_{cone} \frac{m}{d^2} \tag{1}$$

where m is the cone mass (in g), d is the cone penetration depth (in mm), and k_{cone} is a constant that is a function of the cone angle (for a cone angle of 30°, k_{cone} = 0.85). This equation was used by many researchers to estimate the undrained shear strength (S_u) for clayey soil and clayey soil mixed with different materials (Cabalar & Mustafa, 2015; Kumar & Muir Wood, 1999; Wood, 1985).

3.2 Hydraulic conductivity test

Hydraulic conductivity measurements on undisturbed samples are commonly performed on samples collected from the field using thin-wall sampling (Shelby) tubes (Clayton et al., 1995). However, because of the inevitable disturbance associated with the process of extracting a sample from the ground and the Shelby tube, remolded specimens were prepared at 90% maximum dry density and the optimum moisture content of premeasured compaction curves. The specimen was prepared in a permeameter with dimensions of 10 cm in diameter and 12.5 cm in height. Four sets of soil specimens were prepared for performing the hydraulic conductivity tests. Each set included five identical specimens prepared for the purpose of repeatability. The first set of specimens was for clayey soil and the other three sets were for clayey soil mixed with 10% of CWA, CWB, and CWC, respectively. The clayey soil was passed through a No. 4 sieve while the additives (CWA, CWB, and CWC) were passed through a 19 mm sieve. The latter represented the maximum particle size identified in the compaction and hydraulic conductivity tests. For each sample, water was added to the dry clayey soil-CDMs mixture until it reached its associated optimum water content. The soil was put in a sealed bag for at least one day before compaction to achieve moisture equalization. The compaction process was carried out in five equal layers; the thickness of each layer was 25 mm to get a uniform density along with the specimen. The density used for preparing hydraulic conductivity specimens in the permeameter was 90% of the maximum dry density of clay and clay-10% CDM mixtures. Before testing, the permeameters were soaked in a water tank for saturation purposes. After assembling, the hydraulic conductivity tests were performed according to ASTM D5084 (ASTM, 2010) specifications.

Another method for measuring the coefficient of hydraulic conductivity was used based on consolidation test results (Das & Sobhan, 2014). A set of compacted specimens of clayey soil and clayey soil-CDMs mixtures were prepared in an oedometer ring with dimensions of 6.2 cm in diameter and 1.92 cm in height. The specimens were compressed in the ring of the oedometer statically, using a constant rate of 0.02 mm/sec. The specimens were prepared at the optimum moisture content and 90% maximum dry density. The CDMs were mixed with clayey soil in different percentages of 5%, 10%, 15%, and 20% to investigate the effect of the CDMs on the coefficient of hydraulic conductivity of clayey soil (Abdulnafaa, 2018). The coefficient of hydraulic conductivity for clayey soil and clayey soil-CDMs mixtures were estimated from the consolidation test results at 400 kPa using Equation 2.

$$k = m_v c_v \gamma_w \tag{2}$$

where k is the coefficient of hydraulic conductivity, m_v is the coefficient of volume compressibility, c_v is the coefficient of consolidation, and γ_w is the unit weight of water.

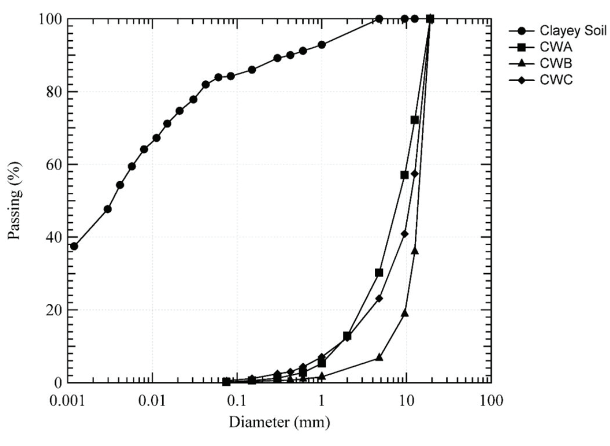

Figure 2. Grain size distributions curves for clayey soil and CDMs used in the study.

4. Results and discussions

4.1 Atterberg limits

The Atterberg limits of clayey soil and clayey soil-CDMs mixture are tabulated in Table 2 and presented in Figures 3 to 5. The table and the figures clearly show that

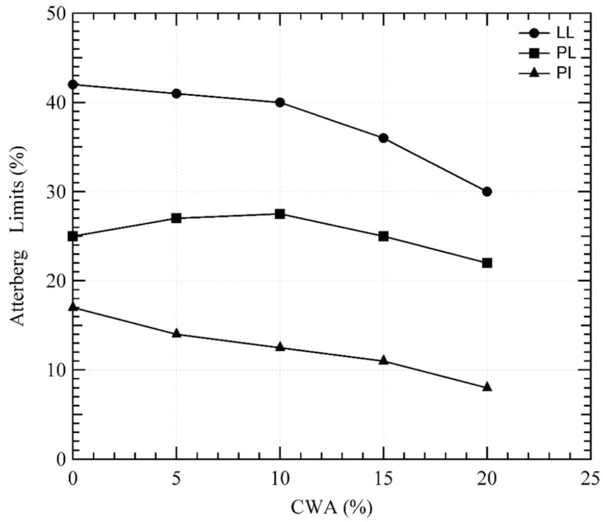

Figure 3. Atterberg limits with CWA content.

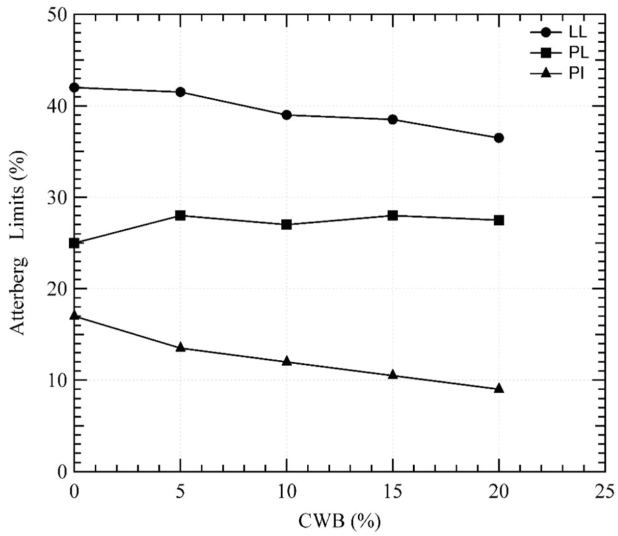

Figure 4. Atterberg limits with CWB content.

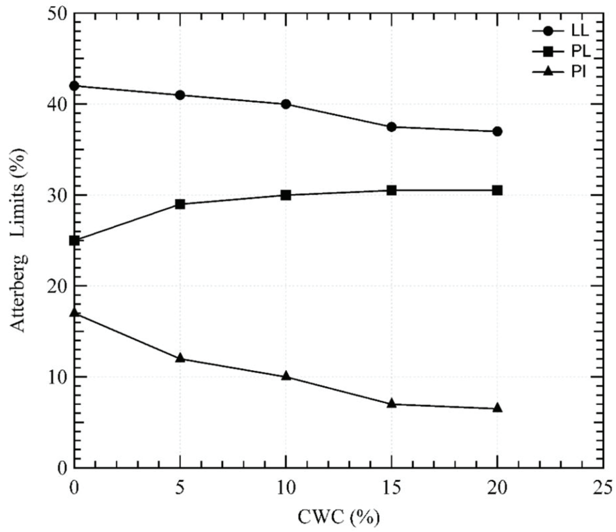

Figure 5. Atterberg limits with CWC content.

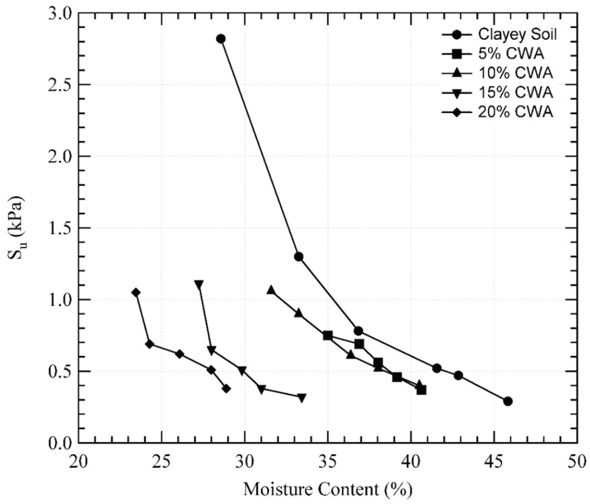

Figure 6. Undrained shear strength with water content for the clayey soil and clay- CWA mixtures.

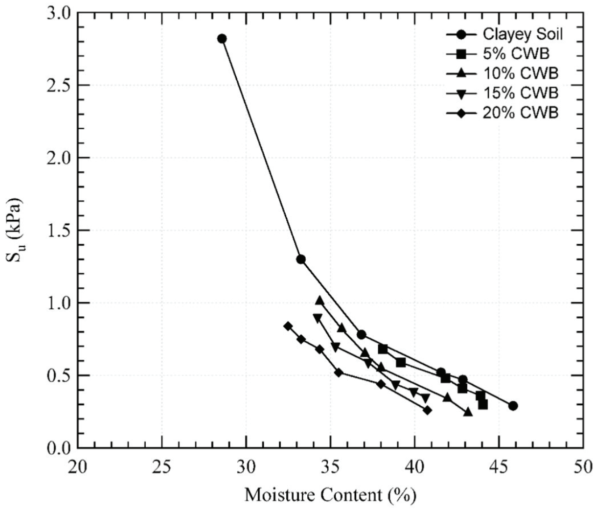

Figure 7. Undrained shear strength with water content for the clayey soil and clay- CWB mixtures.

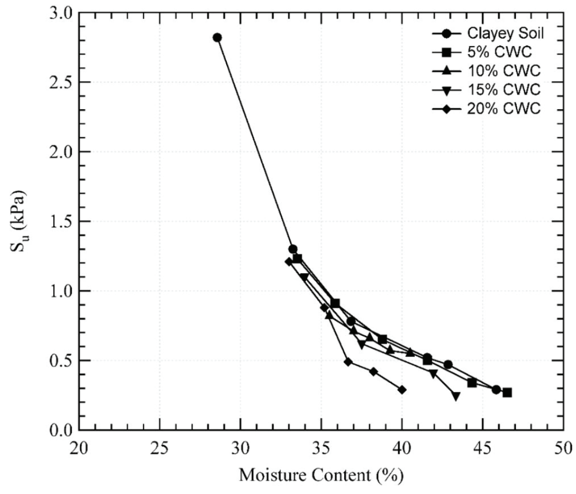

Figure 8. Undrained shear strength with water content for the clayey and clay- CWC mixtures.

the LL decreased as the additive percent increased. For a given additive percent, the reduction in LL varied with the additive type. For instance, for 20% additive, the reduction percentages in the LL were 12%, 6%, and 6% for CWA, CWB, and CWC, respectively. The plasticity index (PI) of the mixtures decreased for all types of additives. The maximum reported reductions in the PI values were 9%, 4%, and 6% when 20% CWA, CWB, and CWC were added, respectively. The reduction in the plasticity indices can be explained by the physical compensation of a ratio of clayey soil (by weight-plasticity materials) to the CDMs (non-plasticity materials).

It is important to note that the CDMs affected the geotechnical classification of clayey soil, as shown in Table 1. The clayey soil used in this study is classified as low plastic clay (CL) according to the Unified Soil Classification System (USCS). The classification changed from CL to low plastic silt (ML) because of the clay-CDM mixtures. An alternative and more common soil classification type used particularly in road design and construction works is the AASHTO classification system. The suitability of the materials could be assessed using such a soil classification system. For instance, it was found that soil classification changed from A-7-6 for clayey soil to A-6 or A-4 for 10% CDMs-clay mixture and the group index (GI) of the mixture was lower than that of clayey soil. This finding showed that the CDM-clay mixtures became more suitable for use as a base or sub-base material than the clayey soil.

4.2 Undrained shear strength

Using Hansbo (1957) empirical equation, the undrained shear strength (Su) was estimated for the fall cone test results of both clayey soil and clayey soil-CDMs mixtures. Figures 6 to 8 display the relationship between the undrained shear strength (S_u) and water content. The results show that the undrained shear strength (S_u) of the clayey soil and clayey soil-CDMs mixtures generally decreased as the water content increased. Results presented in Figure 6 show that the undrained shear strength (S_u) decreased significantly as the CWA increased especially for the 15 and 20% of CWA and the range of water content used. For instance, in comparison to the clayey soil, the undrained shear strength (S_u) of clayey soil-20% CWA mixture reduced by 10% at moisture content near the LL. Figure 7 shows the effect of the CWB on the undrained shear strength (S_u) of the clayey soil. It was observed that the undrained shear strength (S_u) decreased only slightly as the CWB increased. For instance, for LL, the reduction of undrained shear strength (S_u) was only 2% for the clayey soil-20% CWB mixture compared to the clayey soil. Practically, this amount of reduction can be ignored as it is minimal. Figure 8 showed the effect of the CWC on the undrained shear strength (S_u) of clayey soil and the clayey soil-CWC mixtures. The results showed an insignificant different behavior between the clayey soil and the clayey soil mixed with 5%, and 10% of CWC additive for all the range of moisture content used. However, for 15% and 20% additive, the effect of CWC was significant for the range of water content higher than 35% while the effect of the CWC on the undrained shear strength (S_u) disappear for the water content lower than approximately 35%. In other words, the undrained shear strength (S_u) of clay and clayey soil-CDM mixtures merged into one curve for water content lower than 35%.

The change in undrained shear strength (S_u) of a composite matrix of cohesive and cohesionless soils can be affected by the nature of the interaction between sand-like grains and clay grains (Mitchell & Soga, 2005). The non-plastic materials (CDMs) which have a similar nature to cohesionless materials (i.e. sand) can easily reduce the undrained shearing strength (S_u) of clayey soils. From the fact that the cohesionless soil causes the plasticity of the cohesive soil to reduce when they are mixed, the cohesion between soil particles will be reduced. The undrained shear strength (S_u) is a function of soil cohesion; thus, undrained shearing strength (S_u) will be reduced. Similar findings can be found in Al Rawi et al. (2018) and Cabalar & Mustafa (2015).

4.3 Hydraulic conductivity

The hydraulic conductivity (k) for clayey soil and clayey soil-10% CDMs mixtures are shown in Table 3 and Figures 9 and 10, which show the change in k with three different additives. Because the hydraulic conductivity test is highly influenced by the variation of void ratio, pore size and pore size distribution, soil density, and additive distribution along with the soil specimens, as commented by Das & Sobhan (2014), five identical specimens of each soil type were tested to examine repeatability. The results for clayey soil show that the variations in the value of k for specimen numbers 2, 3, and 4 were minimal. However, there was some variation by approximately -10% and +10% in specimen numbers 1 and 5, respectively. The variation could be due to the non-homogeneity of the additive in the specimens, and the non-uniformity of the density along with the soil specimens. The results showed that there was no variation in the values of k for the CWA and

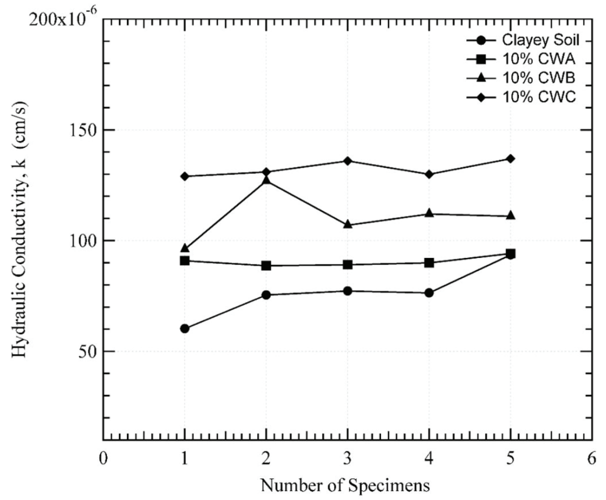

Figure 9. Hydraulic conductivity (k) for the clayey soil and clayey soil- CDMs mixtures.

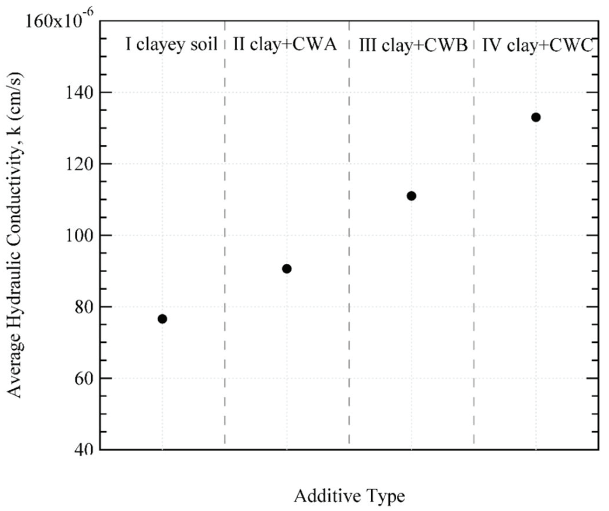

Figure 10. Average values of hydraulic conductivity, k for the clayey soil and clayey soil- CDMs mixtures.

Table 3. Coefficient of hydraulic conductivity, k of clayey soil and clay-10% CDMs using falling head test.

Specimen No.	Coefficient of hydraulic conductivity, k, (cm/sec)			
	Clayey soil	CWA	CWB	CWC
1	6.03E-05	9.09E-05	9.62E-05	1.29E-04
2	7.55E-05	8.87E-05	1.27E-04	1.31E-04
3	7.73E-05	8.91E-05	1.07E-04	1.36E-04
4	7.64E-05	9.00E-05	1.12E-04	1.30E-04
5	9.36E-05	9.42E-05	1.11E-04	1.37E-04
Average	7.66E-05	9.06E-05	1.11E-04	1.33E-04

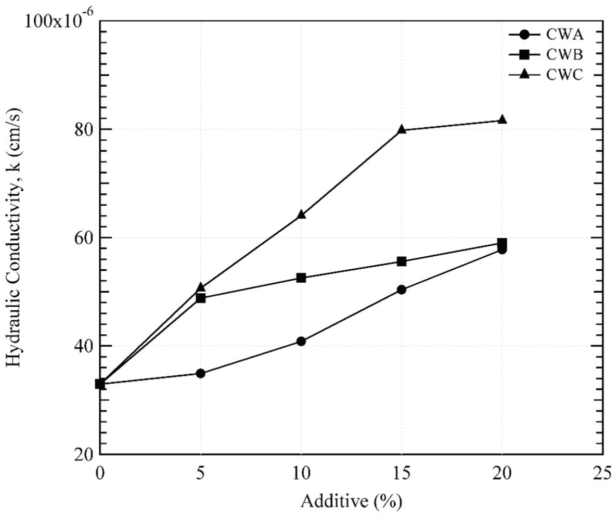

Figure 11. Hydraulic conductivity k for the clayey soil and clayey soil-CDMs mixtures.

CWC tested specimens. Except for specimen number 2, the values of k of CWB specimens were approximately the same. This finding implies that the soil specimens were well uniform and homogenous, and the additives were well distributed in the soil sample during mixing and compacting processes.

Table 3 and Figure 10 show the average values of k. The plot is divided into four zones I, II, III, IV for clayey soil, clayey oil-CWA, clayey soil-CWB, and clayey soil-CWC, respectively. It was observed that k varied with the additive type. In comparison to the clayey soil, it was noted that k increased by approximately 18%, 44%, and 73% for the clayey soil mixed with 10% of CWA, CWB, and CWC, respectively. The explanation for increasing the value of k when adding CDMs to the clayey soil was that adding materials with high granular gradients, and high hydraulic conductivity to clayey soil with very low hydraulic conductivity would increase the hydraulic conductivity of the new mixtures in proportions depending on the type and quantity of the additive.

The hydraulic conductivity levels of clayey soil and the clayey soil-CDM mixtures estimated indirectly from the consolidation tests are presented in Figure 11. The figure clearly shows that k increased as the additive percent increased. For instance, at 20% additive, a maximum reported incremental percentage in k was 75%, 79%, and 247% for CWA, CWB, and CWC, respectively. Similarly, the increments in the hydraulic conductivity can be explained by the physical compensation of a ratio of clayey soil (by weight) (cohesive materials) to the CDMs (cohesionless materials). This finding confirms the finding of the k values measured by the falling head method. It is observed that the two methods exhibited the same trend but different magnitudes of k values, which is because the testing conditions are different between the two testing techniques.

5. Conclusions

This experimental study examined the influences of three types of CDMs (CWA, CWB, and CWC) on the engineering properties of natural clayey soil. The conclusions are the following:

- The LL and PI of clayey soil decrease as the CDMs percentages increase. A maximum of 13%, 37%, and 30% decrease in the LL of the mixtures with 20% content of CWA, CWB, and CWC, respectively, and a maximum of 13%, 37%, and 30% decrease in the PI of the mixtures with 20% content of CWA, CWB, and CWC, respectively.
- The classification of the clayey soil changes from CL for clayey soil to ML for clay-CDM mixtures.
- Results indicate that the clayey soil-CDMs mixtures are more suitable for use as base or sub-base materials than the clayey soil under paving or parking area.
- The undrained shear strength (S_u) of both clayey soil and clayey soil-CDMs mixtures decreases as the moisture content increases. The greatest reduction in the undrained (S_u) of clayey soil was 10% for clayey soil- 20% CWA mixtures.
- The hydraulic conductivity (k) of the CDMs is higher than that of clayey soil by 75%, 79%, and 247% for CWA, CWB, CWC, respectively.
- The coefficient of hydraulic conductivity measured from the consolidation test confirms the k values measured by the falling head test.

Declaration of interest

The authors declare that there are no known conflicts of interest associated with this publication and there has been no significant financial support for this work that could have influenced its outcome.

Authors' contributions

Nurullah Akbulut: investigation. Ali Cabalar: methodology, validation. Mohammed Abdulnafaa: data curing, writing - original draft preparation. Muwafaq Awad: writing - reviewing and editing. Burak Ozufacik: experimental work.

List of symbols

CDMs	Construction and Demolition Materials
CWA	Crushed Waste Asphalt
CWB	Crushed Waste Bricks
CWC	Crushed Waste Concrete
k	Hydraulic conductivity
S_u	Undrained shear strength
$\gamma_{d\,max}$	Maximum dry unit weight

References

Abdulnafaa, M., Cabalar, A., & Karabash, Z. (2019). Shear strength characteristics of clay with waste solid construction and demolition materials. *Proceedings International Conference on Innovation, Sustainability, Technology and Education in Civil Engineering (iSTE-CE'2019)* (pp. 303-313). Iskenderun. ISTE.

Abdulnafaa, M.T. (2018). *Use of construction and demolition materials to improve geotechnical properties of a clay* [Doctoral thesis, Civil Engineering Department, Gaziantep University]. Gaziantep University's repository. https://tez.yok.gov.tr/UlusalTezMerkezi/tezSorguSonucYeni.jsp.

Abhijith, B.S., Murthy, V.S., & Kavya, S.P. (2014). Study of the effectiveness in improving montmorillonite clay soil by construction and demolition waste. *Journal of Civil Engineering and Environmental Technology*, 1(5), 1-4.

Al Rawi, O.S., Assaf, M.N., & Hussein, N.M. (2018). Effect of sand additives on the engineering properties of fine grained soils. *Journal of Engineering and Applied Sciences (Asian Research Publishing Network)*, 13(9), 3197-3206.

Arulrajah, A., Piratheepan, J., Aatheesan, T., & Bo, M.W. (2011). Geotechnical properties of recycled crushed brick in pavement applications, *Journal of* Materials in Civil Engineering, 23(10), 1444-1452. https://doi.org/10.1061/(ASCE)MT.1943-5533.0000319.

Arulrajah, A., Piratheepan, J., Bo, M.W., & Sivakugan, N. (2012). Geotechnical characteristics of recycled crushed brick blends for pavement sub-base applications. *Canadian Geotechnical Journal*, 49(7), 796-811. http://dx.doi.org/10.1139/T2012-041.

Arulrajah, A., Piratheepan, J., Disfani, M.M., & Bo, M.W. (2013). Geotechnical and geoenvironmental properties of recycled construction and demolition materials in pavement subbase applications. *Journal of Materials in Civil Engineering*, 25(8), 1077-1088. http://dx.doi.org/10.1061/(asce)mt.1943-5533.0000652.

Arulrajah, A., Disfani, M.M., Horpibulsuk, S., Suksiripattanapong, C., & Prongmanee, N. (2014). Physical properties and shear strength responses of recycled construction and demolition materials in unbound pavement base/subbase applications. *Construction & Building Materials*, 58, 245-257. http://dx.doi.org/10.1016/j.conbuildmat.2014.02.025.

ASTM D-2216. (1998). *Standard test method for laboratory determination of water (moisture) content of soil and rock by mass*. ASTM International, West Conshohocken, PA. https://doi.org/10.1520/D2216-10.N.

ASTM D2487. (2000). *Standard practice for classification of soils for engineering purposes (Unified Soil Classification System)*. ASTM International, West Conshohocken, PA. https://doi.org/10.1520/D2487-11.

ASTM D4318. (2005). *Standard test methods for liquid limit, plastic limit, and plasticity index of soils*. ASTM International, West Conshohocken, PA. https://doi.org/10.1520/D4318-10E01.

ASTM D5084. (2010). *Standard test methods for measurement of hydraulic conductivity of saturated porous materials using a flexible wall permeameter*. ASTM International, West Conshohocken, PA. https://doi.org/10.1520/D5084-10.

Bennert, T., Papp Jr, W., Maher, A., & Gucunski, N. (2000). Utilization of construction and demolition debris under traffic-type loading in base and subbase applications. *The Transportation Research Board*, 1714(1), 33-39. https://doi.org/10.3141%2F1714-05.

BSI 1377. (1990). *Methods of test for soils for civil engineering purposes*. BSI – British Standards Institution, London.

Cabalar, A., Abdulnafaa, M., & Karabash, Z. (2016). Influences of various construction and demolition materials on the behavior of a clay. *Environmental Earth Sciences*, 75(9), 841-900. http://dx.doi.org/10.1007/s12665-016-5631-4.

Cabalar, A., & Mustafa, W. (2015). Fall cone tests on clay-sand mixtures. *Engineering Geology*, 192, 154-165. http://dx.doi.org/10.1016/j.enggeo.2015.04.009.

Canelas, D., Fernandes, I., & Lopes, M.D.G. (2018). Use of fall cone test for the determination of undrained shear strength of cohesive soils. *MATEC Web of Conferences*, 251, 1-8. https://doi.org/10.1051/matecconf/201825104067.

Clayton, C.R.I., Matthews, M.C., & Simons, N.E. (1995). *Site investigation: a handbook for engineers*. Blackwell Science.

Cristelo, N., Vieira, C.S., & Lurdes Lopes, M. (2016). Geotechnical and geoenvironmental assessment of recycled construction and demolition waste for road embankments. *Procedia Engineering*, 143(June 2017), 51-58. https://doi.org/10.1016/j.proeng.2016.06.007.

Das, B., & Sobhan, K. (2014). *Principles of geotechnical engineering*. Cengage Learning.

Hansbo, S. (1957). New approach to the determination of the shear strength of clay by the fall-cone test. Royal Swedish Geotechnical Institute Proceedings. Retrieved in January 9, 2021, from http://www.diva-portal.org/smash/get/diva2:1300142/FULLTEXT01.pdf

Jia, X., Ye, F., & Huang, B. (2015). Utilization of construction and demolition wastes in low-volume roads for rural areas in China. *Transportation Research Record: Journal of the Transportation Research Board*, (2474), 39-47. http://dx.doi.org/10.3141/2474-05.

Kang, D.H., Gupta, S.C., Ranaivoson, A.Z., Siekmeier, J., & Roberson, R. (2011). Recycled materials as substitutes for Virgin Aggregates in Road Construction: I. Hydraulic and mechanical characteristics. *Soil Science Society of America Journal*, 75(4), 1265-1275. http://dx.doi.org/10.2136/sssaj2010.0295.

Kumar, G.V., & Muir Wood, D. (1999). Fall cone and compression tests on clay-gravel mixtures. *Geotechnique*, 49(6), 727-739. http://dx.doi.org/10.1680/geot.1999.49.6.727.

Lukiantchuki, J.A., Oliveira, J.R.M.S., Almeida, M.S.S., Janeiro, R.D., Silva, T.B., & Guideli, L.C. (2019). Construction and demolition waste (CDW) used in reinforced soil mixtures for pavement applications. In

Proceedings XVII European Conference on Soil Mechanics and Geotechnical Engineering (pp. 1-7.). Reykjavik. Icelandic Geotechnical Society. https://doi.org/10.32075/17ECSMGE-2019-0613.

Mitchell, J.K., & Soga, K. (2005). *Fundamentals of soil behavior*. John Wiley & Sons Inc.

Mohialdeen, O.K., Khattab, S.I.A., & Al–ahmady, K.K. (2020). Utilization of mosul city demolition waste to improve some soil engineering properties. *Key Engineering Materials*, 857, 374-382. http://dx.doi.org/10.4028/www.scientific.net/KEM.857.374.

Obaid, A.A., Rahman, I.A., Idan, I.J., & Nagapan, S. (2019). Construction waste and its distribution in Iraq: an ample review. *Indian Journal of Science and Technology*, 12(17), 1-10. http://dx.doi.org/10.17485/ijst/2019/v12i17/144627.

Park, T. (2003). Application of construction and building debris as base and subbase materials in rigid pavement. *Journal of Transportation Engineering*, 129(5), 558-563. http://dx.doi.org/10.1061/(ASCE)0733-947X(2003)129:5(558).

Poon, C.S., & Chan, D. (2006). Feasible use of recycled concrete aggregates and crushed clay brick as unbound road sub-base. *Construction & Building Materials*, 20(8), 578-585. http://dx.doi.org/10.1016/j.conbuildmat.2005.01.045.

Wood, D.M. (1985). Some fall-cone tests. *Geotechnique*, 35(1), 64-68. http://dx.doi.org/10.1680/geot.1985.35.1.64.

Yoshizawa, S., Tanaka, M., & Shekdar, A.V. (2005). Global trends in waste generation. In I. Gaballah, B. Mishar, R. Solozabal & M. Tanaka (Eds.), *Recycling, waste treatment and clean technology* (pp. 1541-1552). TMS Mineral, Metals and Materials Publishers.

Soils and Rocks

An International Journal of Geotechnical and Geoenvironmental Engineering

www.soilsandrocks.com

ISSN 1980-9743
ISSN-e 2675-5475

Comparative analysis of Piled Raft Foundation System (PRFS) settlements placed on soft soils via geotechnical centrifuge

Edgar Rodríguez Rincon[1#], Bernardo Caicedo Hormaza[2],
Juan Felix Rodríguez Rebolledo[3]

Article

Keywords
Centrifuge modelling
Clays
Subsidence
Piled Raft Foundation System
Settlement

Abstract

The use of Piled Raft Foundations Systems (PRFS) has been extended to different types of soils, including soft clay soils. In this type of soil it is possible that, in addition to the consolidation process due to the presence of loads, a subsidence process is generated, associated with variations in pore pressure with depth. In many cases, these variations are associated with the loss of recharge of the aquifers or with the extraction of water from deep soil layers. In this work, the behaviour of some PRFS built on soft clay soils, which are subjected to the double consolidation process, are evaluated, both by loading and by the extraction of water from deep soil layers. The research is based on the implementation of reduced-scale models in a geotechnical centrifuge; the influence of the separation and number of piles on the deformation or settlement of the system is analysed. It is shown that, normally, groups of piles with greater separation control settlement more effectively. However, the settlements are greater when the soil is subjected to the weight of the structure in addition to a process of depletion of the pore pressure, because the settlement depends on the distribution of the piles, which is described using the Filling Factor (FF).

1. Introduction

The use of Piled Raft Foundation Systems (PRFS) as a foundation system has been extended to different types of soils, including soft clay soils in which consolidation phenomena occur due to load and/or due to changes in the pore pressure condition. The behaviour of PRFS in soils that suffer consolidation due to variations in pore pressure (subsidence) have not been studied comprehensively (Rodríguez-Rincón, 2016).

Cities like Shanghai, Bangkok, Mumbai, Kuala Lumpur, Jakarta, Singapore, Bogotá, and Mexico are underlain by soft clay soils. In these cities, the use of PRFS has been expanded. These systems have presented damage associated with subsidence processes because the normal working conditions of PRFS vary (Banerjee, 2009; Bareño & Rodríguez-Rincon, 1999). In piles built under these conditions, negative friction can be generated, which induces additional vertical loads and settlements. In extreme conditions, this can lead to pile failure (Leung et al., 2004; Auvinet-Guichard & Rodríguez-Rebolledo, 2017).

In the traditional design approach of PRFS, the raft is able to withstand the imposed loads however, the piles are additional elements designed to control deformations, especially differential settlements. With more up-to-date approaches, piles are added both to control settlement and to support part of the load imposed on the system; the PRFS is a geotechnical composition of three elements: raft, piles and soil (Burland, 1977).

Rodríguez-Rebolledo et al. (2015) mentioned that, worldwide, several field studies have been carried out on individual piles that are arranged in a soft soil and consolidated by reducing pore pressures. However, only some of these consider the use of piles working only by friction and almost none of them consider the three-dimensional effects. Rodríguez-Rincón (2016) indicated that some studies have been carried out on groups of piles and PRFS that present piles working by friction, but they do not consider the variations that can occur due to the extraction of water from deep layers and the consequent variations in pore pressure.

This research aims to advance the understanding and evaluation of the influence of subsidence (by extracting water from deep layers) on PRFS that are built on soft soils and include piles that work by shaft friction. This type of

[#]Corresponding author. e-mail: erodriguezr@unal.edu.co
[1]Universidad Nacional de Colombia, Departamento de Ingeniería Civil y Agrícola, Sede Bogotá, Bogotá, Colombia.
[2]Universidad de Los Andes, Departamento de Ingeniería Civil y Ambiental, Bogotá, Colombia.
[3]Universidade de Brasília, Programa de Pós-graduação em Geotecnia, Brasília, DF, Brasil.

Submitted on January 11, 2021; Final Acceptance on May 5, 2021; Discussion open until August 31, 2021.
https://doi.org/10.28927/SR.2021.062321

knowledge will allow the adjustment of analytical and numerical models that better represent the behaviour of this type of foundation, under the conditions presented here.

The main characteristics and the results obtained from experimental work are presented; this was carried out by implementing 10 models of PRFS on a reduced scale and tested in two types of geotechnical centrifuge. As a result of the investigation, the influence of the number, separation and distribution of the piles on the collapse of the PRFS (when the medium is consolidated) was determined, both by the weight of the structure and by the reduction of the pore pressure due to the extraction of water from deep permeable layers.

2. Background and concepts

2.1 Piled Raft Foundations Systems (PRFS)

One of the first practical works using the PRFS concept was developed by Zeevaert (1957), using a pile group system working by friction, with the aim of reducing the settlements of a 43-storey building (Torre Latinoamericana) placed in the lacustrine clays of Mexico City. From a theoretical point of view, one of the first works that includes the concept of a shallow foundation supported on piles is attributed to Poulos in the 1960s. In this work, the author concluded that the settlement of very long piles ($L/d > 25$) is controlled by the soil-raft contact (Poulos & Mattes, 1971).

According to Janda et al. (2009), the PRFS corresponds to a three-element geotechnical composition in which two structural components (piles and raft) interact with each other and with the surrounding soil, to support the loads (vertical, horizontal or moments) that come from the superstructure. This system can be designed to present an adequate Safety Factor according to the relevant state limits, guarantee its load capacity, guarantee the control of settlements, or guarantee the two conditions simultaneously (Mandolini et al., 2013).

In the traditional design process of groups of piles, the number of piles is determined by dividing the total load placed on the group by the individual load capacity, considering a minimum Safety Factor (average) for all piles. When the influence of group stiffness is analysed, in this case, it is found that the peripheral piles support more load, which generates an increase in the number of piles to guarantee the minimum safety factor for all piles (Sales et al., 2002).

The load-settlement curve (Figure 1) may not be linear under design conditions however, the system has an adequate Safety Factor and the maximum allowable settlement criterion is met. Thus, the design represented by curve 3 in Figure 1 is acceptable and will likely be less expensive than the designs represented by curves 1 and 2.

According to Chow (2007), in PRFS design it is necessary to understand the load transfer mechanism of the raft to the piles and to the soil, considering:

- The behaviour of the raft, including settlements, moments and proportion of load assumed by this element;
- The transfer mechanism involves a complex interaction between the raft and the piles, in addition to the surrounding soil, taking into account that the stress-strain response of the system is controlled by several factors, such as soil properties, group geometry, the type of load and the execution process.

In the literature, some authors (e.g. Poulos, 1993; Durán, 2003), established load proportions assumed by the raft (up to 80% of the load) and the piles (up to 20%), under external load conditions and without variation of the soil water conditions. Mandolini et al. (2013) presented a graph (Figure 2) in which the variation of the proportion of total load taken by the raft is established as a function of the Filling Factor (FF). The FF establishes that the behaviour of a PRFS depends on parameters related to both the piles and the raft, as defined by Equation 1.

$$FF = \frac{A_G}{A_R}\frac{d}{s} \tag{1}$$

where A_G is the piles group area, defined by De Sanctis et al. (2002), as shown in Equation 2.

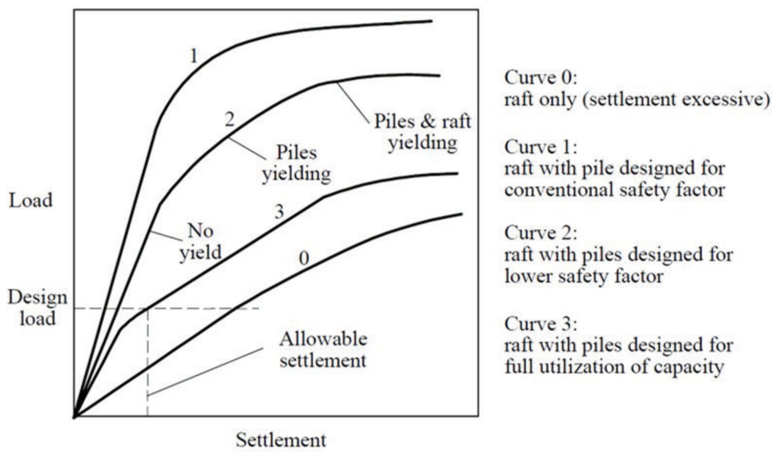

Figure 1. Load settlement curves for piled rafts according to various design philosophies (adapted from Van Impe, 2001).

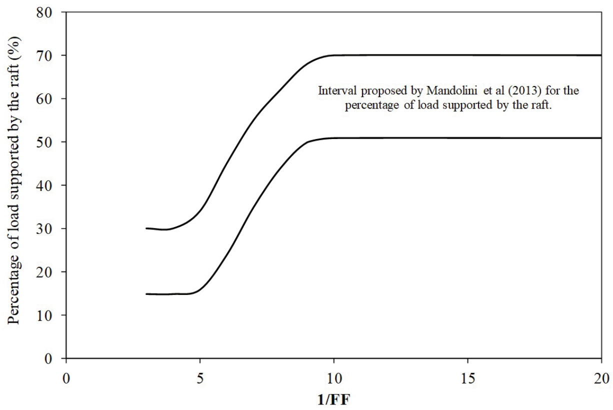

Figure 2. Proportion of load assumed by the raft (adapted from Mandolini et al., 2013).

$$A_G = \left[\left(\sqrt{N_p} - 1 \right) s \right]^2 \tag{2}$$

where A_R is the raft area; s the piles spacing; d the pile diameter and N_p the number of piles in the group.

Determining the settlement of the PRFS turns out to be the critical point (Chung Nguyen et al., 2013). One way to evaluate the influence of the inclusion of piles under a raft was proposed by Bajad & Sahu (2008), through the settlement reduction ratio (Sr) defined in Equation 3.

$$S_r = \frac{d_{ri} - d_r}{d_{ri}} \tag{3}$$

According to the authors, this parameter makes it possible to relate the settlement of the raft without piles (d_{ri}) and the settlement of the PRFS (d_r). Thus, when the settlement of the piles increases, the raft supports a greater load. In this case, the piles act as elements that reduce settlement. If the load taken by the piles increases, this increase is low and the pile group can take up to 60% of the load. The settlement in the system decreases when the number of piles increases; there is a critical settlement value from which the piles do not contribute to the resistance of the system.

2.2 PRFS in soft soils

For Poulos & Davis (1980), the most suitable sites for PRFS to be implemented are those where relatively rigid clays, dense sands and stratigraphic profiles without soft strata prevail below the tip of the piles. Poulos (1993) presented some situations in which the use of PRFS would not be recommended, including profiles of soils with soft clays or loose sands close to the surface, or those that presented compressible, collapsible or expansive soils.

Balakumar & Anirudhan (2011) mention that the use of PRFS is optimal when they are built on over-consolidated clays with loads from tall buildings, in which the raft is deepened, generating relief from stress conditions at the edges, which influences the settlements.

In more recent years, the use of PRFS in soft soils has increased in areas where there are soft clays or with different non-rigid material behaviour, just as more research and developments have been presented. Some analytical methods for studying the behaviour of PRFS have been presented by Kuwabara & Poulos (1989), Lee (1993), Teh & Wong (1995), De Sanctis & Mandolini (2006), Roy et al. (2011), and Rodríguez-Rebolledo & Auvinet (2019), among others. These have focused on the influence of negative friction on induced loads (drag loads) on the piles, due to the consolidation of soft soils.

Numerical methods were implemented by Katzenbach et al. (1998), Chow et al. (2001), Reul (2002), Lee et al. (2002), Lee & Ng (2004), El-Mossallamy (2011), Cho et al. (2012), Rodríguez-Rebolledo et al. (2015), Khanmohammadi & Fakharian (2018) and Mali & Singh (2018), among others. These studies focused on analysing the soil-structure interaction, the load distribution, the potential failure surfaces along the shaft and the settlements of the PRFS or group of piles. They used material response models that were not the usual Mohr-Coulomb type, including the influence of the subsidence phenomenon on the behaviour of the PRFS or groups analysed.

In Brazil, Cunha et al. (2000), Sales (2000) and Ayala (2013), have shown that PRFS can be implemented in collapsible clayey soils, such as those in the city of Brasilia, presenting adequate behaviour, in terms of load support and settlement control, decreasing the costs of the foundations. With a study that analysed the behaviour of PRFS in the city of Bogotá, Durán (2003) concluded that these systems present an adequate response when piles that work by friction are included to support the secondary compression and subsidence processes generated by the change in the pore pressure conditions.

With 1g scale models, Shibata et al. (1982), Ergun & Sonmez (1995) and Bajad & Sahu (2008) analysed the distribution of loads and settlements in PRFS or groups of piles subjected to vertical loads and arranged on soft soils, including the influence of negative friction on their behaviour.

Thaher & Jessberger (1991) presented the results of an experimental model on a 50*g* scale, evaluating the effect of the number of piles, and their diameter and length, on the behaviour of a PRFS subjected to axial load. They concluded that the geometry is one of the variables that most influences the behaviour of the system, when it is placed on soft clay-type material. Horikoshi & Randolph (1996) used a 100*g* model to evaluate the bearing capacity of a PRFS in soft soils and the effect of lateral confinement, for variable vertical loads. Tran et al. (2012) analysed the influence of subsidence in a PRFS system using a 50*g* scale model, concluding that the load supported by the piles, as well as their effectiveness as settlement controllers, decreased with time as a function of the subsidence processes.

Cui et al. (2010) mentioned that few studies have been carried out to analyse the three-dimensional and time-dependent behaviour of PRFS, due to the fact that it is easy to represent the variation of pore pressure in the soil. Normally, linear stress-strain behaviour is assumed, which does not correspond to the real behaviour of the system, making it necessary to develop more realistic models that reproduce these interaction phenomena and the effects of subsidence.

3. Experimental program

In this research, we analysed the effects of the consolidation of a soil by an external load and by variations in pore pressure due to the extraction of water from deep soil layers, in the response of a PRFS. Specifically, the response of the PRFS is evaluated by the settlements measured on the raft and in the soil near the raft.

3.1 Testing facilities

The testing facilities used in this research consisted of two beam geotechnical centrifuges with the characteristics shown in Table 1 and Figure 3 (the largest capacity equipment) and in Table 2 and Figure 4 (the smallest equipment), The facilities were located at the Geotechnical Models Laboratory of Los Andes University in Bogota, Colombia.

3.2 Scale, materials, and geometry of the PRFS models

To scale the models, is necessary to guarantee the similarity between models and prototypes based on the flexural modulus, as shown in the Equation 4 (Taylor, 1995).

$$E_m^{mm} I_m^{mm} = E_m^c I_m^c \tag{4}$$

where E_m^{mm} is the elastic modulus of the material in the model; E_m^c is the elastic modulus of concrete; $I_m = \left(bt^3\right)/12$ is the moment of inertia, where b is the base of the element and t is the thickness of the element.

As a specific prototype was not taken, it was sought to guarantee that at least the values of the modulus (E) were consistent with the typical values recommended in the literature. Equation 4 was applied to the raft, as it was the main element subjected to flexural stress, for all of the other elements, conversion of the dimensions was proportional to the scale factor.

Table 1. Large geotechnical centrifuge characteristics.

Turning radius (m)	1.90
Model boxes dimensions (cm)	40 × 50 × 60
Gravitational field maximum (g)	200
Maximum model weight (kN)	4.0
Nominal power (HP)	400
Channels for data acquisition	50

Note: g = earth's gravity; 1HP = 745.7 W.

Table 2. Small geotechnical centrifuge characteristics.

Turning radius (m)	0.56
Model boxes dimensions (cm)	7 × 14 × 12
Gravitational field maximum	300*g*
Maximum model weight (N)	50
Nominal power (HP)	3
Channels for data acquisition	40

Note: *g* = earth's gravity; 1HP = 745.7 W.

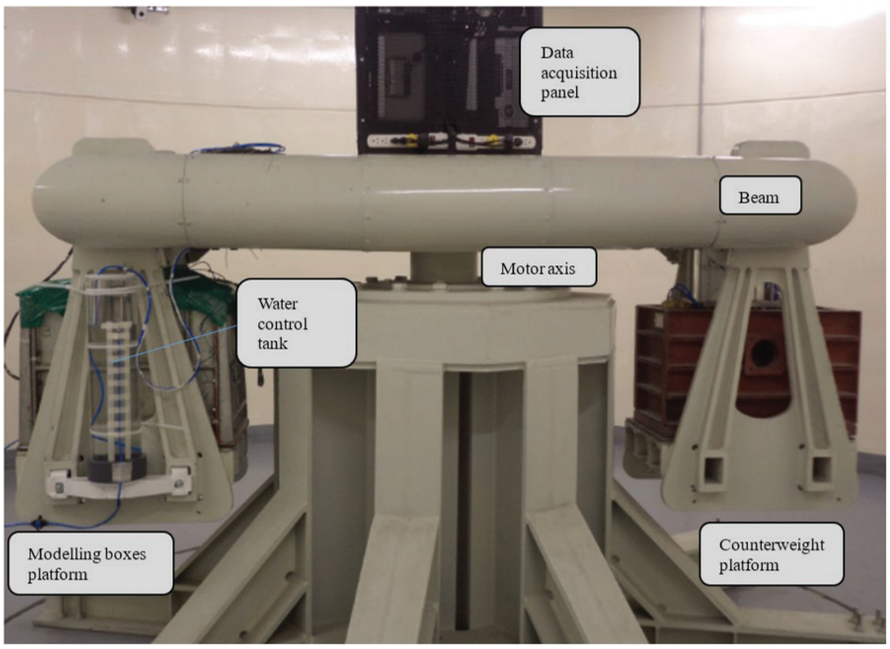

Figure 3. Large beam geotechnical centrifuge.

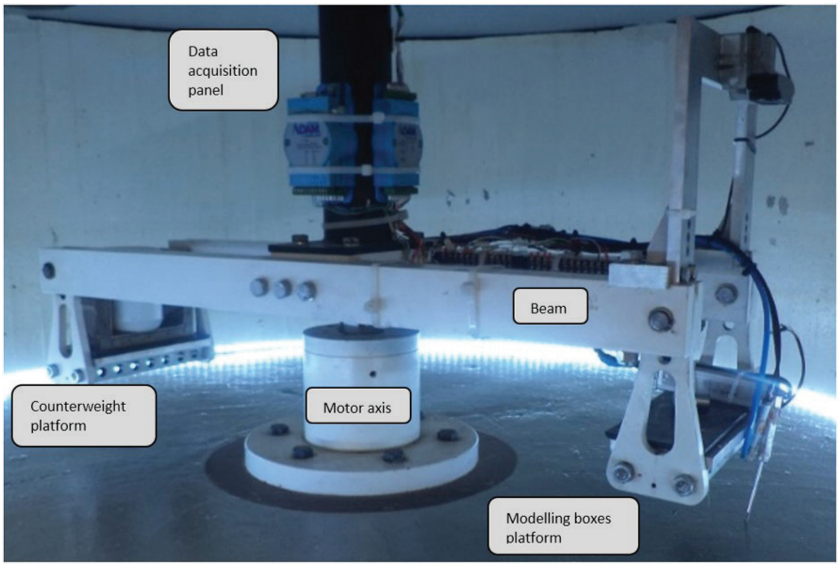

Figure 4. Small beam geotechnical centrifuge.

Table 3. Dimensions and materials for model elements and prototype equivalences.

Element	Parameter	---- 70g ----		---- 200g ----	
		Model characteristic	Prototype characteristic (equivalent)	Model characteristic	Prototype characteristic (equivalent)
Raft	Material	Aluminium	Concrete	Acrylic	Concrete
	Thickness, e_R	13 mm	1.147 m	9 mm	1.0 m
	*Elasticity modulus, E	70000 MPa	35000 MPa	6000 MPa	35000 MPa
	Width, B	200 mm	14 m	40 mm	8 m
	Length, L	200 mm	14 m	40 mm	8 m
Piles	Material	Aluminium	Concrete	Wood	Concrete
	Diameter, D	9 mm	63 cm	3 mm	63 cm
	*Elasticity modulus, E	70000 MPa	30000 MPa	18000 MPa	30000 MPa
	Length, L	320 mm	22.4 m	80 mm	16.0 m

*Parameter value based on supplier's information and the literature.

Taking the Equation 4 and considering a unit base width, the dimensions of the raft-type elements are determined from Equation 5.

$$t_p^c = \frac{t_m^{mm} n_l}{\sqrt[3]{\dfrac{E_m^c}{E_m^{mm}}}} \tag{5}$$

where t_p^c is the concrete thickness in the prototype, t_m^{mm} is the thickness of the element made from the corresponding material in the model, n_l is the scale factor, E_m^{mm} is the elastic modulus of the material in the model, and E_m^c is the elastic modulus of concrete. Table 3 presents the dimensions and equivalences between the models and the prototypes.

The scale factor in this work was selected based on the dimensions of the modelling boxes, being 70 times the value of the force of gravity (70g) for the models to be implemented in the larger centrifuge, and 200 times the force of gravity (200g) for the models in the smallest centrifuge. Table 3 presents the dimensions and equivalences between the models and prototypes.

The models included piles with 3 × 3, 4 × 4 and 5 × 5 group distributions under the raft, with distributions centred (C) or distributed over the entire raft area (T). The models are specified in Table 4, where the denomination M corresponds to the largest models (at 70g scale) and the denomination m corresponds to the smallest models (at 200g scale).

3.3 Soil profile

According to the principles of geotechnical modelling, the model must duplicate the factors that influence the soil response: level of stresses and resistance. In the case of clays, it is necessary to control the void ratio and the pressure applied in manufacturing the soil, to comply with these requirements.

The soil profile selected to represent the behaviour of soft clay soils was that proposed by Rincón & Rodríguez-Rincón (2001), which corresponds to a clay profile of variable

Table 4. Pile distribution and geometric configuration of the models.

Model	Raft dimensions (cm × cm)	Raft thickness (cm)	Piles diameter (cm)	Piles length (cm)	Distribution	Spacing (cm)	Piles number
M3	20 × 20	1.3	0.9	32	3 × 3 C	1.8	9
M4	20 × 20	1.3	0.9	32	4 × 4 C	1.8	16
M6	20 × 20	1.3	0.9	32	3 × 3 T	8.1	9
m1	4 × 4	0.9	s/p	s/p	s/p	s/p	s/p
m2	4 × 4	0.9	0.3	8	3 × 3 C	0.6	9
m3	4 × 4	0.9	0.3	8	4 × 4 C	0.6	16
m4	4 × 4	0.9	0.3	8	5 × 5 C	0.6	25
m5	4 × 4	0.9	0.3	8	3 × 3 T	1.7	9
m6	4 × 4	0.9	0.3	8	4 × 4 T	1.13	16
m7	4 × 4	0.9	0.3	8	5 × 5 T	0.85	25

Table 5. Kaolin properties.

Parameter	Value
Specific gravity, *Gs*	2.68
Liquid limit, w_L (%)	54
Plasticity index, I_P (%)	33
Plasticity limit, w_P (%)	21
Compression index, *Cc*	0.37
Swelling index, *Cs*	0.09
Vertical consolidation coefficient, *Cv* (m^2/s) × 10^{-6}	0.49-0.62

resistance with depth, from 10 kPa at the surface to 40 kPa in the bottom of the thickness to be modelled. This is typical for the city of Bogotá DC. Commercial kaolin was used in the soil profile construction, with the characteristics shown in Table 5. Kaolin characterisation was performed in the laboratory from reconstituted samples.

The soil was manufactured inside or outside the geotechnical centrifuge. In the latter case, it was necessary to perform testing to ensure uniformity of the stress with depth and pore pressures inside the soil (Thaher & Jessberger, 1991; Taylor, 1995; Rincón & Rodríguez-Rincón, 2001; Dallos, 2007). For the present investigation, manufacturing outside the centrifuge field was implemented, executing the procedure presented by Rincón & Rodríguez-Rincón (2001) and described by Rodríguez-Rincón et al. (2020). This procedure consists of manufacturing several layers of soil, starting of a mixture of kaolin with water (slurry with water content of 1.5 times the liquid limit), applying a pressure (or equivalent load) value, based on the load-undrained shear correlation curve determined in laboratory and controlling the degree of consolidation. The samples were manufactured outside the centrifuge (1*g*), subjecting it to pressures of the same magnitude as the vertical stresses to which it would be subjected when the test was carried out at 70*g* or 200*g*.

3.4 Model testing

The objective of this research was to analyse the settlement of PRFS subjected to a double consolidation process. The models were placed inside soil in the modelling boxes, subjected to an initial consolidation process by an external load and then to a double consolidation process, by an external load and extraction of water from deep layers.

To guarantee outflow of water during the testing (or 'flights') of the modelling boxes, for the two scales used, a filter material was placed in the lower part. In the case of the 70*g* scale models, this corresponded to a sand filter embedded in layers of geotextile and, for the 200*g* scale models, the filter comprised porous stone, approximately 0.5 cm in thickness. For the boxes of the larger models (70*g*), two intermediate 0.7 cm thick filters (sand embedded in filter paper) were implemented throughout the area of the model box, with the objective of reducing testing times, by reducing the effective drain length. For the 200*g* scale models, these filters were not necessary.

The extraction of water effectively represented the phenomenon of subsidence in soft soils. To carry out this process in the models, the lower part of the modelling boxes had a water outlet connected, internally, to the lower filter material (sand filter or porous stone) and, externally, to a water level control tank (Item 3 in Figure 3). The lower filter materials guaranteed equilibrium pore pressure conditions in the soil, when evaluating the response of PRFS subjected to consolidation due to external load. The function of the external tank was to control the pressure of the water inside the soil or to allow it to escape.

The proposed test stages are outlined in Figure 5, considering that some stop times had to be carried out during the tests (when it was necessary to modify the drainage condition or for the construction of the PRFS in the model), due to the inability to make modifications during the test. The three stages defined for the test correspond to:

- Stage 1 - Self-weight reconsolidation step;
- Stage 2 - Consolidation by load application over the PRFS, keeping the hydraulic external condition (maintaining the water level in the external control tank);
- Stage 3 - Consolidation by load and extraction of water from deep soil layers (lower layer of sand).

During the first two stages of the test, the water level in the external tank was maintained up to the same height as

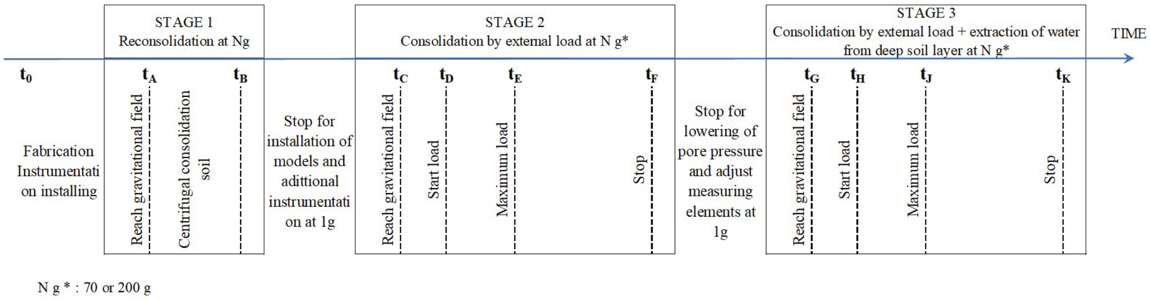

Figure 5. Stages and model's time-line.

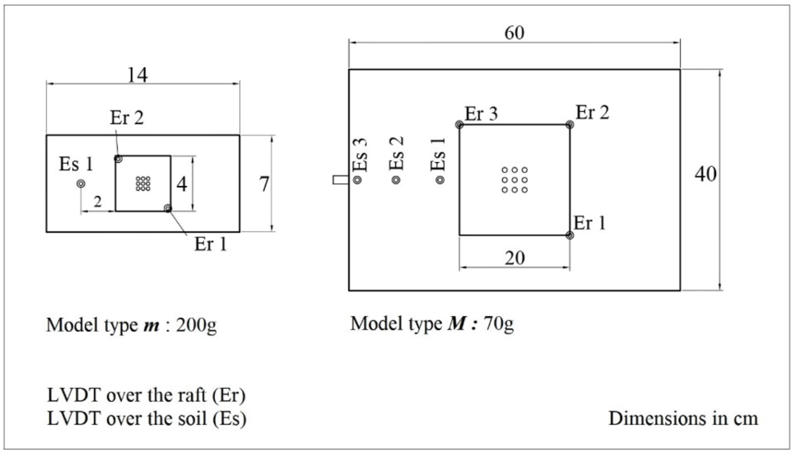

Figure 6. LVDTs distribution in the Model.

Table 6. Testing times.

Activity	Range*	Flight time to 70*g* Model (h:mim)	Flight time to 200*g* Model (h:mim)
Model soil preparation	t_0 - t_A		
Stage 1	t_A - t_B	1:54	1:20
Stop for instrument and model installation	t_B - t_C		
Stage 2	t_C - t_F	2:54	1:45
Stop for external water tank disconnection	t_F - t_G	0:30	0:15
Stage 3	t_G - t_K	2:54	1:45

Range*: time ranges referred to Figure 5.

the ground surface in the model, guaranteeing the pressure balance and that the volume changes were generated by the flow of water due to increased stresses.

In the models, to measure the settlements, Linear Variable Differential Transformers (LVDTs) were implemented at various points of the raft and the soil, as shown in Figure 6, also load cells in the two type of models and, pore pressure gauges on the 1:70 scale models. However, this paper focuses on the analysis of the models' settlements. Additionally, from the resistance profile assumed for the soil and through Meyerhoff's bearing capacity equation for a raft without piles, the load value to be applied on the raft was determined. The load was applied by pneumatic actuators and corresponded to 92 kPa (1.46 kN multiplied by the area) for the 70*g* scale models and 37 kPa (60 N if the area is considered) for the 200*g* models.

From the values of the vertical consolidation coefficient (*Cv*) of the material and based on the drainage lengths for each model, the test times that would guarantee a minimum degree of consolidation of 90% were determined. The calculated times are presented in Table 6.

In Table 6 was included a stop between stages. This stopping time was short, compared to the test time, and the soil rebound was controlled. Although the stress conditions may vary with the stop of the test, when the test is restarted, the conditions are recovered elastically. In any case, between stage 2 and stage 3, the modification of the pore pressure condition is carried out, generating that the rebound deformations are less important than the deformation associated with the double process of loading and extraction of water in deep layers.

Table 7. Filling factors to the models (FF).

Parameter	Model								
	M3	M4	m2	M6	m3	m5	m4	m6	m7
Diameter - d (cm)	63	63	60	63	60	60	60	60	60
Piles number - N_p	9	16	9	9	16	9	25	16	25
Piles spacing - s (cm)	126	126	120	567	120	340	120	226	170
Raft area - A_R (m^2)	196	196	64	196	64	64	64	64	64
Piles group area - A_G (m^2)	63.5	14.3	5.8	12.9	13.0	46.2	23.0	46.0	46.2
FF	0.02	0.04	0.05	0.07	0.10	0.13	0.18	0.19	0.26

4. Results and discussion

In this section, the results obtained in the models are presented and discussed. All measurements were converted to prototype values. To carry out a comparative analysis of the settlements of the PRFS, the Filling Factor (FF) presented in Equation 1 was used. The FFs were determined for each model based on the respective geometric conditions, as summarised in Table 7. The models are organised according to the increasing FF, considering that the FF is taken as being nil for a raft without piles.

As mentioned above, the measured displacements, both on the ground and on the raft, were scaled to the equivalent prototype dimensions. For all flight stages, the results obtained at the end of the stage were analysed without consideration to the climb ramp, i.e. the acceleration time of the equipment until the gravitational field was reached.

The settlements measured at the end of each stage, in which the respective model was implemented according to its arrangement (on the soil or on the raft), are averaged and presented in Table 8. These settlements are representative of the long-term behaviour of PRFS.

From Table 8 in general, for Stage 3, the settlement of the soil (*Es*) is higher when compared to the settlement of the PRFS (*Er*). As a consequence, there may be separation of the raft and the ground, as was indeed verified in the models made at a 200*g* scale and as illustrated in Figure 7.

The reported settlements were normalised with respect to the thickness of the equivalent raft in the prototype, which represents the stiffness of the raft, in such a way that an adequate parametric analysis can be performed. Figure 8 represents the general trend of the PRFS settlements (measurement over the raft - *dr*) normalised by the raft thickness (e_R) for the 200*g* scale models. It can be seen that systems that have piles grouped in the centre of the raft present greater settlement, when compared to those that have piles distributed throughout their area. Chow et al. (2001), Balakumar (2008) and Chung Nguyen et al. (2013) confirmed that there is only a reduction in differential settlements when the piles are concentrated in the central area, since the effects of spacing and pile number influences the overall settlement of the system.

Table 8. Average settlements measured in each model.

Model	Stage 2		Stage 3	
	Es	*Er*	*Es*	*Er*
m1*	16.1	50.1	61.9	47.2
M3	29.4	34.1	34.1	33.5
M4	25.4	29.3	42.0	37.9
m2	27.2	21.1	71.8	27.8
M6	44.6	47.0	22.8	20.6
m3	31.1	12.3	71.9	21.0
m5	28.3	14.9	68.1	24.0
m4	31.3	7.3	74.8	17.0
m6	28.3	6.5	66.7	19.8
m7	32.3	4.5	62.3	15.2

m1*: raft without piles at 200*g* scale. M1 has failed and is not included.

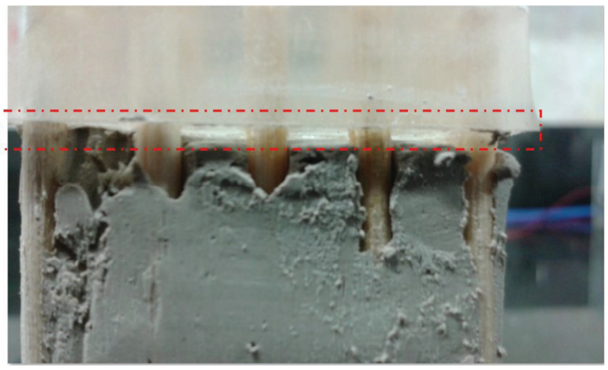

Figure 7. Raft-soil separation on model type m.

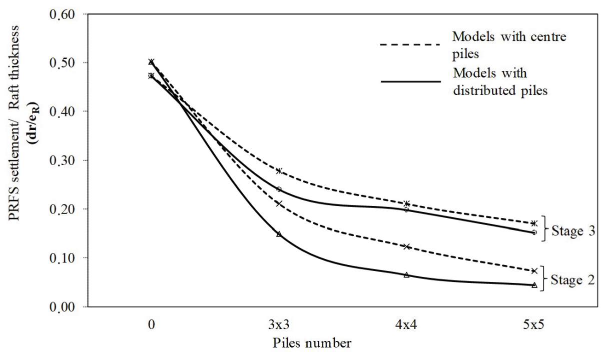

Figure 8. Comparison of PRFS settlement normalised in 200*g* models.

Figure 9 presents the PRFS settlement values measured over the raft (*dr*), normalised for all models, allowing the establishment of a trend of settlement behaviour, as a function of the Filling Factor (FF) and the consolidation condition, with and without water extraction. Bajad & Sahu (2008) indicated that when the number of piles increases, the reduction of the settlements of PRFS is greater. In fact, it can be seen that if the number of piles exceeds a certain value, the increase in the efficiency of the PRFS over the reduction of settlements is marginal, as reported by Rodríguez-Rebolledo et al. (2015). Figure 10 shows that the settlements generally decrease while the FF increases, with a certain tendency to stabilise. This may be because, for low separations, the influence of the group effect is increased, decreasing the capacity of the group.

Figure 9 suggests that the efficiency in decreasing settlements is lower for higher values of FF. The trend of the two lines allows us to observe that the percentage of difference in the settlements for the two situations, with and without water extraction, can be up to 20%.

According to Rodríguez-Rebolledo et al. (2015), the difference between the settlement measured over the raft (*dr*) and the settlement measured on the soil (*ds*), indicates the effective displacement of the PRFS. When the difference is positive, it can be said that the system settles, otherwise, the system presents emersion. Figure 10 presents the effective displacement evaluated for the prototypes represented by the studied models. From Figure 10 one can observe that the 70*g* scale models, with FF values less than 0.07, show settlement in the two stages. The 200*g* scale models mostly present emersions. Emersions are higher in Stage 3 and are influenced by deep water extraction processes and the consequent change in the pore pressure condition; this is confirmed by the separation of the raft, observed in Figure 8. It can also be seen that the relative settlement tends to be stable in Stage 3, showing the greatest influence of the water extraction processes on the behaviour of all the evaluated systems. In this case, the general settlement will depend to a greater extent on the actual settlement of the soil.

Another parameter presented in Equation 3, which allows analysis of the influence of the inclusion of piles in the PRFS, is the settlement reduction ratio (*Sr*), which is graphically presented in Figure 11.

The reduction of the settlements appears to be greater as the FF increases; high FF values are normally associated with a greater number of piles and greater separations between them. From Figure 11, it should be noted that even when the presence of piles reduces the settlements of the PRFS, the reduction efficiency is lower, when the soil is subjected to the double consolidation process by external loads and extraction of water from deep layers (subsidence). The efficiency of the piles can be up to 29% lower in this case, compared to the conditions of a PRFS subjected only to consolidation by external load.

For higher FF, the piles offer greater resistance to settlement due to the presence of the load. However, when there is additional abatement to the loading process, the largest settlements are influenced by the general displacement of the soil layer and, thus, the PRFFS system sinks together with the soil.

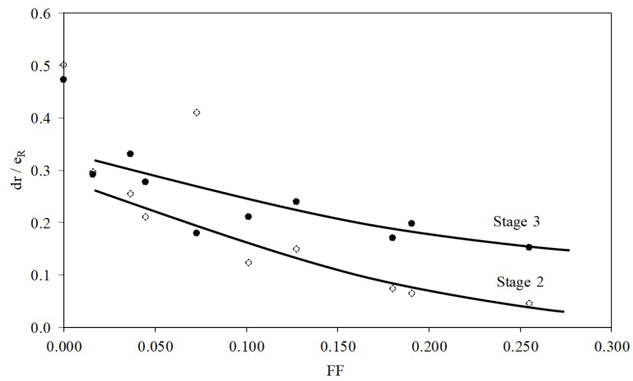

Figure 9. Settlement trend for the PRFS evaluated.

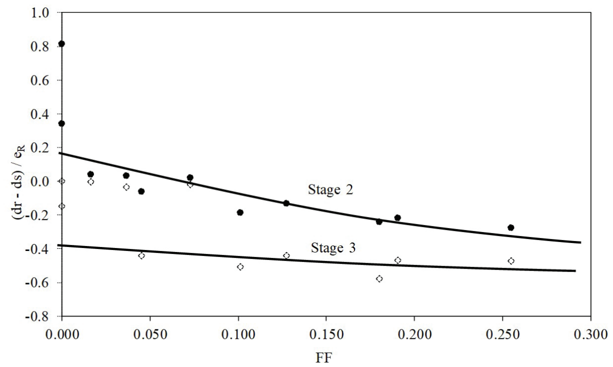

Figure 10. Effective settlement of the PRFS evaluated.

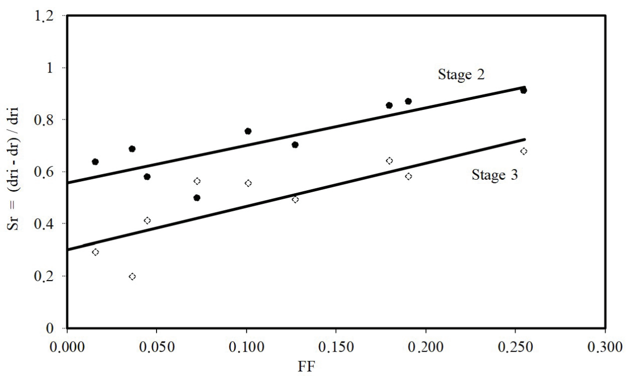

Figure 11. Settlement reduction ratio of the PRFS evaluated.

5. Conclusions

In this work, a physical model via geotechnical centrifuge simulating the complex behaviour of a Piled Raft Foundation System (PRFS) founded in soft soils undergoing regional subsidence was developed to understand the induced settlements by the consolidation process and the double process of consolidation and extraction of water from deep layers.

With the settlement results of this models, it was shown that PRFS that have piles grouped in their central zone present greater settlement when compared to those systems that have piles distributed throughout the entire area of the raft, since the settlements are influenced by both the spacing between the piles and the quantity of piles in the system.

To analysing the settlement response, the Filling Factor (FF) of a PRFS was used. The FF represents the influence of the geometry or geometric distribution over the behaviour of PRFS response. This work shows when the Filling Factor (FF) increases, the reduction in settlement of the PRFS system is greater. However, the percentage at which the piles reduce the settlement decreases, because there must be an optimal number of piles, above which the inclusion of new piles does not have a significant influence on settlement control.

The settlements induced in PRFS founded on soft clays are not necessarily controlled by placing a greater number of piles under the raft or with greater spacing, since, as shown, as the Filling Factor (FF) increases, the effectiveness of the piles decreased.

The reduction in settlements is less when there are additional consolidation processes due to the extraction of water from deep levels, with differences of up to 20% between the condition with and without water extraction.

This work shows that in the subsidence processes represented by the extraction of water from deep soil layers, the settlements of PRFS are greater, mainly because the PRFS system is embedded in a double consolidation process by the loading and reduction of pore pressures. In the reduction of pore pressure process, the greater settlements of the soil, if compared with those of the PRFS system, cause a gradual loss of contact between the soil and the raft, with the consequent possibility of reducing the load capacity of the system.

The results presented can be useful either for future design scenarios or for adjusting analytical methodologies of this same system, since it optimises the performance of this type of foundation structure when undergoing a regional subsidence phenomenon.

Acknowledgements

The authors would like to acknowledge the Los Andes University, the Universidad Nacional de Colombia, COLCIENCIAS in Colombia and the University of Brasilia and the CNPq in Brazil, which collectively funded the doctoral research from which the information for the present article was extracted.

Declaration of interest

The authors wish to confirm that there are no known conflicts of interests associated with this publication and there has been no significant financial support for this work that could have influenced its outcome.

Authors' contributions

Edgar Rodríguez Rincón: conceptualization, methodology, investigation, validation, writing - original draft. Bernardo Caicedo Hormaza: supervision, conceptualization, methodology and resources. Juan F. Rodríguez Rebolledo: supervision, conceptualization, methodology.

List of symbols

A_G	Piles group area
A_R	Raft area
B	Width raft
Cc	Compression index
Cs	Swelling index
Cv	Vertical consolidation coefficient
d	Diameter pile
dr	Settlement of PRS
dri	Settlement of raft without piles
ds	Soil displacement
E	Elasticity Modulus
Es	Settlement measured for the LVDT over the soil
Er	Settlement measured for the LVDT over the raft of the PRFS
e_R	Raft thickness
FF	Filling factor
g	Gravitational acceleration
Gs	Specific gravity
I_P	Plasticity index
L	Raft Length or pile length
N_p	Piles number in the group
$PRFS$	Piled Raft Foundation System
s	Piles spacing
Sr	Settlements Reduction Radio
w_L	Liquid limit
w_P	Plasticity limit

References

Auvinet-Guichard, G., & Rodríguez-Rebolledo, J.F. (2017). Criteria for the design of friction piles subjected to negative skin friction and transient loads. *Ingeniería, Investigación y Tecnología*, 18(3), 279-292. http://dx.doi.org/10.22201/fi.25940732e.2017.18n3.025.

Ayala, D.J. (2013). *Use of the pile draft technique for small buildings supported on collapsible soil* [Master thesis, University of Brasilia]. University of Brasilia's repository (in Portuguese). Retrieved in January 11, 2021, from https://repositorio.unb.br/handle/10482/13840

Bajad, S.P., & Sahu, R.B. (2008). An experimental study on the behaviour of vertically loaded piled raft on soft clay.

In *Proceedings of the 12th International Conference of International Association for Computer Methods and Advances in Geomechanics (IACMAG)* (pp. 84-91), Goa, India. Red Hook, NY: Curran Associates.

Balakumar, V. (2008). *Experimental studies of model pile rafts on sand and field study of prototype behavior* [Doctoral thesis, Anna University]. Anna University's repository. Retrieved in January 11, 2021, from http://hdl.handle.net/10603/27622

Balakumar, V., & Anirudhan, I.V. (2011). Piled raft behaviour-model studies and field performance. In *Proceedings of the Indian Geotechnical Conference* (pp. 947-950), Kochi. New Delhi: Indian Geotechnical Society.

Banerjee, S. (2009). *Centrifuge and numerical modelling of soft clay pile raft foundations subjected to seismic shaking* [Doctoral thesis, National University of Singapore]. National University of Singapore's repository. Retrieved in January 11, 2021, from https://scholarbank.nus.edu.sg/handle/10635/16909

Bareño, E.E., & Rodríguez-Rincon, E. (1999). *Clays shrinkage* [Unpublished undergraduate final course thesis]. Department of Civil and Agricultural Engineering, National University of Colombia (in Spanish).

Burland, J. (1977). Piles as settlement reducers. In *Proceedings of the 19th National Italian Geotechnical Conference* (Vol. 2, pp. 21-34), Pavia, Italy. Italy: AGI.

Cho, J., Lee, J.H., Jeong, S., & Lee, J. (2012). The settlement behavior of piled raft in clay soils. *Ocean Engineering*, 53, 153-163. http://dx.doi.org/10.1016/j.oceaneng.2012.06.003.

Chow, H.S. (2007). *Analysis of piled raft foundations with piles of different lengths and diameters* [Doctoral thesis, University of Sidney]. University of Sidney's repository. Retrieved in January 11, 2021, from https://sydney.primo.exlibrisgroup.com/permalink/61USYD_INST/1c0ug48/alma991027064869705106

Chow, Y.K., Yong, K.Y., & Shen, W.Y. (2001). Analysis of piled raft foundations using a variational approach. *International Journal of Geomechanics*, 1(2), 129-147. http://dx.doi.org/10.1061/(ASCE)1532-3641(2001)1:2(129).

Chung Nguyen, D.D., Kim, D.-S., & Jo, S.-B. (2013). Settlement of piled rafts with different pile arrangement schemes via centrifuge tests. *Journal of Geotechnical and Geoenvironmental Engineering*, 139(10), 1690-1698. http://dx.doi.org/10.1061/(ASCE)GT.1943-5606.0000908.

Cui, C., Luan, M., & Li, M. (2010). A study on time-effects of piled raft system by using computational methods. In *Proceedings of the GeoShanghai 2010 International Conference* (pp. 42-51), Shanghai. Reston: ASCE. http://dx.doi.org/10.1061/41106(379)4.

Cunha, R.P., Soares, J.M., & Mota, N.M.B. (2000). Otimização de um projeto de fundações, através do uso de radier estaqueado. In Anais do Simpósio Interação Estrutura-Solo em Edifícios (pp. 1-10). São Carlos: EESC-USP (in Portuguese).

Dallos, V.F. (2007). *Modelación en centrifuga de asentamientos en tubería de red matriz de acueducto por extracción de agua debida a excavaciones aledañas* [Master's thesis, Los Andes University]. Los Andes University's repository (in Spanish). Retrieved in January 11, 2021, from http://hdl.handle.net/1992/9757

De Sanctis, L., & Mandolini, A. (2006). Bearing capacity of piled rafts on soft clay soils. *Journal of Geotechnical and Geoenvironmental Engineering*, 132(12), 1600-1610. http://dx.doi.org/10.1061/(ASCE)1090-0241(2006)132:12(1600).

De Sanctis, L., Mandolini, A., Russo, G., & Viggiani, C. (2002). Some remarks on the optimum design of piled raft. In In *Proceedings of the International Deep Foundations Congress* (pp. 405-425), Orlando. Reston: ASCE. http://dx.doi.org/10.1061/40601(256)30.

Durán, J.E. (2003). Optimización de un sistema de cimentacionplaca: pilotes en el deposito lacustre de bogotá. In *III Encuentro Nacional de Ingenieros de Suelos y Estructuras* (pp. 1-65). Bogotá: Escuela Colombiana de Ingeniería "Julio Garavito" (in Spanish).

El-Mossallamy. Y. (2011). *Modelling the behaviour of piled raft applying Plaxis 3D Foundation Version 2* (pp. 10-13). Plaxis Practice.

Ergun, M.U., & Sonmez, D. (1995). Negative skin friction from surface settlement measurements in model group tests. *Canadian Geotechnical Journal*, 32(6), 1075-1079. http://dx.doi.org/10.1139/t95-105.

Horikoshi, K., & Randolph, M.F. (1996). Centrifuge modelling of piled raft foundations on clay. *Geotechnique*, 46(4), 741-752. http://dx.doi.org/10.1680/geot.1996.46.4.741.

Janda, T., Cunha, R.P., Kuklk, P., & Anjos, G.D. (2009). Three dimensional finite element analysis and back-analysis of CFA standard pile groups and piled rafts founded on tropical soil. *Soils and Rocks*, 32(1), 3-18.

Katzenbach, R., Arslan, U., Moormann, C., & Reul, O. (1998). Piled raft foundation–interaction between piles and raft. *Darmstadt Geotechnics*, 4(2), 279-296.

Khanmohammadi, M., & Fakharian, K. (2018). Evaluation of performance of piled raft foundations on soft clay: a case study. *Geomechanics and Engineering*, 14(1), 43-50. http://dx.doi.org/10.12989/gae.2018.14.1.043.

Kuwabara, F., & Poulos, H.G. (1989). Downdrag forces in group of piles. *Journal of Geotechnical Engineering*, 115(6), 806-818. http://dx.doi.org/10.1061/(ASCE)0733-9410(1989)115:6(806).

Lee, C.J., & Ng, C.W. (2004). Development of downdrag on piles and pile groups in consolidating soil. *Journal of Geotechnical and Geoenvironmental Engineering*, 130(9), 905-914. http://dx.doi.org/10.1061/(ASCE)1090-0241(2004)130:9(905).

Lee, C.J., Bolton, M.D., & Al-Tabbaa, A. (2002). Numerical modelling of group effects on the distribution of dragloads in pile foundations. *Geotechnique*, 52(5), 325-335. http://dx.doi.org/10.1680/geot.52.5.325.38704.

Lee, C.Y. (1993). Pile groups under negative skin friction. *Journal of Geotechnical Engineering*, 119(10), 1587-1600. http://dx.doi.org/10.1061/(ASCE)0733-9410(1993)119:10(1587).

Leung, C., Liao, B., Chow, Y., Shen, R., & Kog, Y. (2004). Behavior of pile subject to negative skin friction and axial load. *Soil and Foundation*, 44(6), 17-26. http://dx.doi.org/10.3208/sandf.44.6_17.

Mali, S., & Singh, B. (2018). Behavior of large piled raft foundation on clay soil. *Ocean Engineering*, 143, 205-216. http://dx.doi.org/10.1016/j.oceaneng.2017.12.029.

Mandolini, A., Di Laora, R., & Mascarucci, Y. (2013). Rational design of piled raft. *Procedia Engineering*, 57, 45-52. http://dx.doi.org/10.1016/j.proeng.2013.04.008.

Poulos, H.G. (1993). Piled raft in swelling or consolidating soils. *Journal of Geotechnical Engineering*, 119(2), 374-380. http://dx.doi.org/10.1061/(ASCE)0733-9410(1993)119:2(374).

Poulos, H.G., & Davis, E.H. (1980). *Pile foundations analysis and design*. New York: John Wiley & Sons.

Poulos, H.G., & Mattes, N.S. (1971). Settlement and load distribution analysis of pile groups. *Australian Geomechanics Journal*, 1, 18-28.

Reul, O. (2002). Study of the influence of the consolidation process on the calculated bearing behaviour of a piled raft. In *Proceedings of the 5th European Conference on Numerical Methods in Geotechnical Engineering (NUMGE 2002)* (pp. 383-388). Paris: Presses de l'ENPC.

Rincón, C.L., & Rodríguez-Rincón, E. (2001). *Centrifuge physical modelling of a wall without anchors in a soft clay* [Unpublished master's thesis]. Los Andes University (in Spanish).

Rodríguez Rebolledo, J.F., Auvinet-Guichard, G.Y., & Martínez-Carvajal, H.E. (2015). Settlement analysis of friction piles in consolidating soft soils. *Dyna*, 82(192), 211-220. http://dx.doi.org/10.15446/dyna.v82n192.47752.

Rodríguez Rincón, E., Cunha, R.P., & Caicedo Hormaza, B. (2020). Analysis of settlements in piled raft systems founded in soft soil under consolidation process. *Canadian Geotechnical Journal*, 57(4), 537-548. http://dx.doi.org/10.1139/cgj-2018-0702.

Rodríguez-Rebolledo, J.F., & Auvinet, G.Y. (2019). Analytical model for friction piles in consolidating soft soils. *Ingeniare*, 27(2), 295-303. http://dx.doi.org/10.4067/S0718-33052019000200295.

Rodríguez-Rincón, E. (2016). *Análise experimental do comportamento de sistemas radier estaqueado em solos moles em processos de adensamento* [Doctoral thesis, University of Brasilia]. University of Brasilia's repository (in Portuguese). Retrieved in January 11, 2021, from https://repositorio.unb.br/handle/10482/21438

Roy, S., Chattopadhyay, B.C., & Sahu, R.B. (2011). Piled-raft foundation behavior on consolidating soft soil. In *Proceedings of the Indian Geotechnical Conference* (pp. 879-882), Kochi. New Delhi: Indian Geotechnical Society.

Sales, M.M. (2000). *Análise do comportamento de sapatas estaqueadas* [Unpublished doctoral thesis]. University of Brasilia (in Portuguese).

Sales, M.M., Cunha, R.P., Carvalho, J.C., & Silva, C.M. (2002). Previsões de Comportamento de um radier estaqueado no Distrito Federal. In *Anais do XII Congresso Brasileiro de Mecânica de Solos e Engenharia Geotécnica (COBRAMSEG)* (pp. 1-8). São Paulo: ABMS (in Portuguese).

Shibata, T., Sekiguchi, H., & Yukitomo, H. (1982). Model test and analysis of negative friction acting on piles. *Soil and Foundation*, 22(2), 29-39. http://dx.doi.org/10.3208/sandf1972.22.2_29.

Taylor, R.N. (1995). Centrifuges in modelling: principles and scale effects. In R.N. Taylor (Ed.), *Geotechnical centrifuge technology* (pp. 20-34). London: Blackie Academic & Professional. http://dx.doi.org/10.4324/9780203210536_chapter_2.

Teh, C.I., & Wong, K.S. (1995). Analysis of downdrag on pile groups. *Geotechnique*, 45(2), 191-207. http://dx.doi.org/10.1680/geot.1995.45.2.191.

Thaher, M., & Jessberger, H.L. (1991). The behavior of pile-raft foundatios, investigated in centrifuge model tests. In *Proceedings of the International Conference Centrifuge* (pp. 225-234). Boulder. ISMFE.

Tran, T.V., Teramoto, S., Kimura, M., Boonyatee, T., & Vinh, L.B. (2012). Effect of ground subsidence on load sharing and settlement of raft and piled raft foundations. *World Academy of Science, Engineering and Technology*, 6(2), 120-127. http://dx.doi.org/10.5281/zenodo.1074345.

Van Impe, W.F. (2001). *Methods of analysis of piled raft foundations: a report prepared on behalf of technical committee TC 18 on piled foundations*. London: ISSMGE.

Zeevaert, A. (1957). Foundation design and behaviour of tower Latino Americana in Mexico City. *Geotechnique*, 7(3), 115-133. http://dx.doi.org/10.1680/geot.1957.7.3.115.

TECHNICAL NOTES

Soils and Rocks
v. 44, n. 2

Soils and Rocks

An International Journal of Geotechnical and Geoenvironmental Engineering

www.soilsandrocks.com

ISSN 1980-9743
ISSN-e 2675-5475

Limitations of the Danish driving formula for short piles

Silvio Heleno de Abreu Vieira[1#], Francisco R. Lopes[2]

Technical Note

Keywords
Foundations
Piles
Dynamic formulae
Dynamic tests
Load tests

Abstract

Dynamic formulae are a widely used expedient for the control of driven piles to ensure load capacity. These formulae have considerable limitations when used in the prediction of the load capacity on their own, but are very useful in the control of a piling when combined with other tests. This technical note presents an evaluation of the Danish Formula for 54 precast concrete piles, comparing its results with High Strain Dynamic Tests (HSDTs), Static Load Tests (SLTs) and predictions by a semi-empirical static method (Aoki & Velloso, 1975). The data used in the comparison come from three works in the city of Rio de Janeiro, Brazil. All piles were driven with free-fall hammers and in one particular work the piles were relatively short. The predictions of the Danish Formula were evaluated in relation to the pile length/diameter ratio. It was concluded that for short piles - with lengths less than 30 times the diameter - this formula indicates bearing capacities higher than the actual ones. A correction for a safe use of the Danish Formula for short piles is suggested.

1. Introduction

Dynamic formulae are based on elementary laws of Physics, such as those that govern the conservation of energy or the shock between bodies. However, driving a pile is a more complex phenomenon. The pile is not a free body, but an elongated element inserted into the ground, with which it interacts under a hammer blow. An alternative to these formulae is the solution of the Wave Equation, introduced by Smith (1960).

Dynamic formulae basically require the hammer and pile data and provide the set (permanent penetration of the pile per blow). On the other hand, a Wave Equation solution requires, in addition to these data, those related to the driving accessories and the soils (in terms of rigidity, resistance and viscosity), and outputs not only the set, but also the dynamic stresses (stresses along the pile under driving). In their use to estimate pile capacity, the dynamic formulae are fed simply by the measured set, while the Wave Equation solution requires more extensive measurements of the pile response to driving, in what is called the High Strain Dynamic Test (HSDT).

The use of either of the two dynamic methods, however, pose a few questions, such as (e.g., Alonso, 1988):

(i) the energy of the hammer blow is not always sufficient to bring about the maximum resistance of the soil;

(ii) the resistance presented by the soil depends on the time between driving and the measurement of the set or the HSDT, with soil resistance usually increasing with time, hence this phenomenon being known as "set-up" (very rarely, resistance decreases over time, in this case, called "relaxation");

(iii) the energy losses in the accessories and the viscous response of soil are not properly incorporated in most dynamic formulae.

The first two aspects are inherent to any dynamic method, leading to different load capacities obtained (i) with different driving energies and (ii) with set measurements or HSDTs made at different times after driving. As a consequence of aspect (i), it is common practice to refer to load capacity obtained in HSDTs – performed with a given driving equipment – as *mobilized load capacity*, implying that a higher capacity could be obtained with a higher energy.

Despite the above issues, dynamic formulae are very useful in the control of a piling, especially if combined with HSDTs and static load tests (SLTs) − ideally executed right at the beginning of the construction −. The dynamic formulae serve to ensure homogeneity in load capacity, leading to different lengths of piles driven in heterogeneous soils.

[#]Corresponding author. E-mail address: silvioheleno@gmail.com
[1]Vale, Nova Lima, MG, Brasil.
[2]Universidade Federal do Rio de Janeiro, Rio de Janeiro, RJ, Brasil.

Submitted on September 5, 2020; Final Acceptance on March 24, 2021; Discussion open until August 31, 2021.

https://doi.org/10.28927/SR.2021.057320

There are more than one hundred formulae. In the evaluation of Agerschou (1962), the Dutch and the Engineering News Record Formulae presented values with a very large scatter, therefore, were considered unreliable. The Hiley, Janbu and Danish Formulae showed close and reliable values. In the review by Poulos & Davis (1980), the Engineering News Record Formula was considered to be unreliable, with a weak correlation with load test results, while the Janbu and Danish Formulae presented a good correlation. Likins et al. (2012) summarizes the discussions that followed a report by the ASCE "Committee on Pile Driving Formulas and Tests", published in the 1940s after a decade-long study (Greulich, 1941). In these discussion, several very prominent engineers expressed opposing views on the formulae available at the time.

The Danish Formula has been widely used worldwide, both for steel and precast concrete piles. In the evaluation of Danziger & Ferreira (2000), this formula presented a good correlation with results of a Wave Equation solution for steel piles. In another evaluation (Silva et al., 2020), the Danish Formula proved to be suitable for the control of a large piling.

The present technical note aims to evaluate the Danish Formula in the verification of the load capacity of precast concrete piles. Comparisons are made with HSDTs, SLTs and predictions by a semi-empirical static method (based on SPT results). For the latter type of comparison, the Aoki & Velloso (1975) method was chosen for its common use in Brazilian practice. The predictive capacity of this formula is evaluated in particular in relation to the pile length, resulting in the recommendation of a range for its safe use.

2. Construction data used in the study

Data from three works in the city of Rio de Janeiro were used: Metallurgical Laboratory of the Federal University of Rio de Janeiro (UFRJ), located in Fundão Island, Athletes Village for the Pan-American Games (Vila Pan-Americana) and Shopping MAP-Car, the last two located in Barra da Tijuca. Altogether there are 54 precast concrete piles, some with a hollow circular cross-section and others with a full square section. The piles passed through different sediments and had their tips driven into gneissic residual soil. Site investigations were conducted with SPTs.

The present evaluation used pile set measurements, HSDTs and SLTs, as summarized in Table 1 (with more details can be seen in Vieira, 2006). The piles had very different lengths, which allowed an evaluation of this effect.

3. A preliminary evaluation of the Danish Formula

According to Sorensen & Hansen (1957), the pile driving resistance depends on 5 factors: the pile driver efficiency (η); hammer weight (W); hammer drop height (h); set or permanent penetration of the pile per blow (s); pile length (L); pile cross-section area (A) and pile modulus of elasticity (E_p). The driving resistance is given by (Danish Formula):

$$R_{Dan} = \frac{\eta\ W\ h}{s + \frac{1}{2}\sqrt{\frac{2\ \eta\ W\ h\ L}{A\ E_p}}} \tag{1}$$

The second part of the denominator corresponds to the elastic (recoverable) compression of the pile under the energy of the blow. The authors suggest an efficiency factor of the driving system equal to 0.70 for free-fall hammers and 0.90 for diesel hammers.

The set and the cross-section area have their influences on driving resistance easy to perceive in the formula. On the other hand, an increase in its cross-section is known to require greater energy to drive the pile into the ground.

Figure 1 shows, for a pile with a cross-section area of 895 cm^2 (for example, a hollow pile 42 cm in diameter, 10 cm thick wall), how the driving resistance varies with pile length and net energy, considering two final sets: 0 and 3mm/blow (or 0 and 30 mm/10 blows). It can be observed that the load capacity is influenced by pile length and that, for relatively short piles, driving resistance varies very sharply as the set varies.

It can be observed in Figure 1 that short piles with small sets (sets that approach 0) would have exceptionally high resistances, according to the formula; furthermore, as pile length tends to 0, driving resistance tends to infinity. For piles with lengths greater than 10 m (typically 30 diameters in this case), the variation in set has little effect on driving resistance, as does driving energy.

Table 1. Summary of pile data.

Work	Number of Piles	HSDTs	SLTs	Pile length (m)
Metallurgical Lab.	20	7	-	3.70 to 8.40
Vila Pan-Americana	11	10	4	23.00 to 32.20
Shopping MAP-Car	23	7	-	20.50 to 22.20

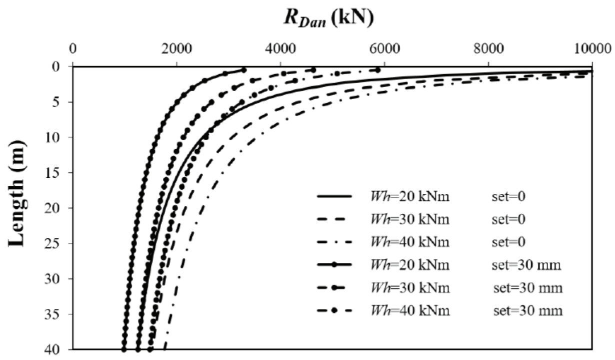

Figure 1. Pile resistance variation with pile length and set by the Danish Formula (Vieira, 2006).

4. Evaluation of the Danish Formula in three foundation works

4.1 Important clarifications and assumptions

In this section, Danish Formula results will be compared to results of HSDTs, SLTs and a static method (Aoki-Velloso method). In the interpretation of a HSDTs it is possible to separate the dynamic resistance and the static resistance (e.g., by the CAPWAP method), the latter corresponding to the static load capacity. However, as HSDTs are often made during the driving process or shortly after, the static resistance usually increases over time, due to set-up, until reaching the load capacity of a SLT or a prediction by static method, Q_{ult}. Thus, it is common practice to use the notation R_u for the static resistance obtained in the HSDT. If there were no set-up, $R_u = Q_{ult}$.

The Danish Formula does not provide, strictly speaking, the static load capacity, Q_{ult}, but the driving resistance, R_{Dan}. To obtain the service load, Sorensen & Hansen (1957) recommend a factor of 2.0 (i.e., $Q_{ser} = R_{Dan} / 2.0$). Since the overall safety factor to be applied to the static load capacity to obtain the service load is 2.0, it can be assumed that the driving resistance given by the formula corresponds to the static load capacity, Q_{ult}.

In the analysis of the data from three foundation works using the Danish Formula, the piles were supposed to have an excess of 2.0 m in length at the end of the driving, that is, above ground level, which is common (later demolished). The hammer efficiency factor, η, was based on the net energies measured in the HSDTs, and were: 0.80 for the Metallurgical Laboratory, 0.70 for the Vila Pan-Americana and 0.60 for the Shopping MAP-Car.

4.2 Comparison between Danish Formula and HSDT results

Figure 2 shows that, for short piles (Metallurgical Laboratory), the Danish Formula indicates load capacities much higher than those measured in HSDTs; the ratio between these values varied between 1.75 and 3.95. On the other hand, for long piles (Shopping MAP-Car and Vila Pan-Americana), values obtained by HSDTs were higher.

Figure 3 shows that, for relatively short piles, the Danish Formula indicates load capacities much higher than those predicted by the Aoki-Velloso static method. The ratio between these values varied between from 1.81 to 3.83. For long piles, load capacities were close, with a ratio ranging from 0.75 to 1.67. Two piles in that figure were not included in this evaluation, as they had a very low load capacity predicted by the static method, probably due a flaw in the SPT.

From Figures 2 and 3, it can be concluded that the Danish Formula greatly overestimates the driving resistance or load capacity of relatively short piles.

Figure 4 shows in more detail the relation between load capacities indicated by the Danish Formula and by

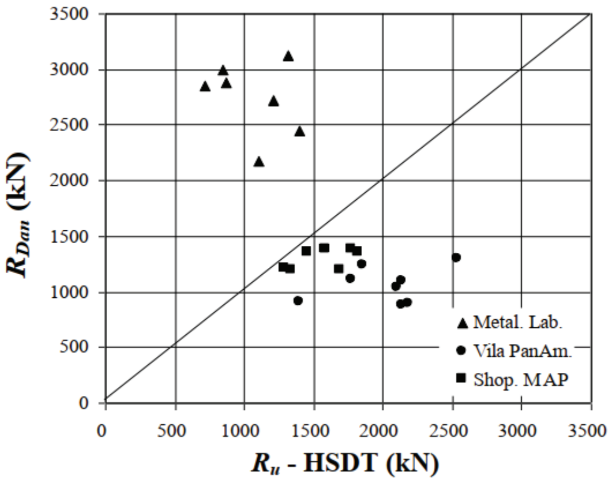

Figure 2. Danish Formula vs. HSDTs – all piles.

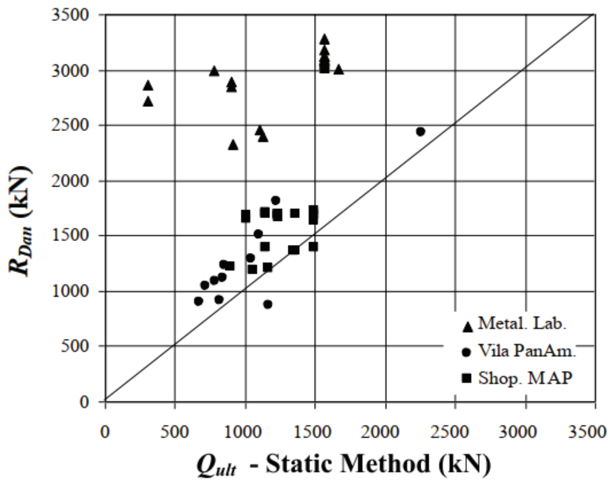

Figure 3. Danish Formula vs. static method (Aoki-Velloso).

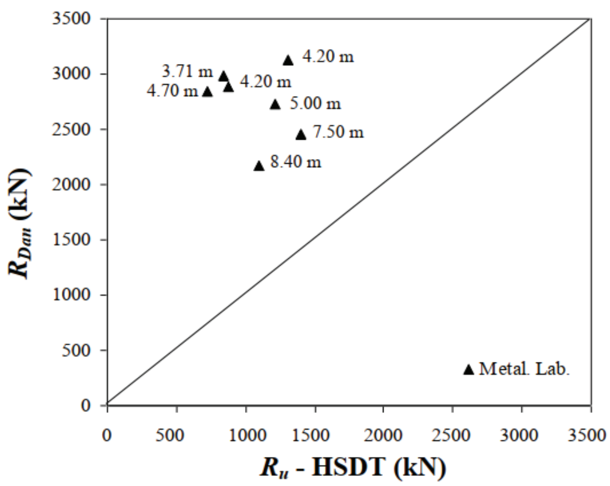

Figure 4. Danish Formula vs. HSDTs - Metallurgical Laboratory.

HSDTs for short piles in the Metallurgical Laboratory. The numbers next to the dots indicate the pile lengths in meters. Note that, as the piles are longer, the results of the dynamic formula approach those of the HSDT.

Figures 5 show how the ratio between the load capacities predicted by the Danish Formula and HSDTs varies with the aspect ratio of the pile (*L/B*). In this figure, a trend curve − with solid line − was fitted, showing how the predictability of the Danish Formula is influenced by pile length. A second line – dashed – was introduced, suggesting that this formula can be used for pile lengths greater than 30 diameters, and that its results need adjustments for lengths below this value.

The ratio between load capacities indicated by the Danish Formula and the HSDT for the Metallurgical Laboratory, with shorter piles, varied between 0.25 to 0.57, while for the Vila Pan-Americana, with longer piles, the ratio varied between 1.50 to 2.45. For MAP-Car, with long piles (but not so much as in the Vila Pan-Americana), the ratio remained between 1.06 and 1.41.

The data in Figure 5 indicates that piles with up to 30 diameters need some adjustment in the application of the Danish Formula − and these piles will be considered here as relatively short −. Based on this figure, it is suggested that the Danish Formula needs the following correction for safe use if *L/B* < 30 (assuming $Q_{ult} = R_{Dan}$ for longer piles):

$$Q_{ult} = 0.033 R_{Dan} \left(L / B \right) \tag{2}$$

4.3 Comparison between dynamic and static methods

Figure 6 shows the results of 4 Static Load Tests (SLTs) compared to those of the Danish Formula. These static tests were performed on long piles in the Vila Pan-Americana, where results of the Danish Formula were lower than those obtained in the HSDTs. The failure loads in the SLTs are higher than those obtained by the Danish Formula, a possible explanation being the occurrence of a significant set-up after driving.

Figure 7 presents a comparison between static load capacities obtained in HSDTs and given by the Aoki-Velloso static method. In the Metallurgical Lab., where piles were shorter, HSDTs static load capacities are close to those provided by the static method. At the other two sites, where long piles passed through very soft clay layers, HSDTs results are higher than those of the Aoki-Velloso method, most likely because the latter does not consider any shaft friction in clays with $N_{SPT} = 0$. In fact, a skin friction of about 10 kN/m^2 develops in soft clays after consolidation which follows pile driving (e.g., Décourt & Quaresma, 1978).

Figure 8 presents a comparison between static load capacities obtained in HSDTs and SLTs. These tests were carried out on long piles at Vila Pan-Americana. Two HSDTs results were close to those obtained in SLTs, while another was considerably lower.

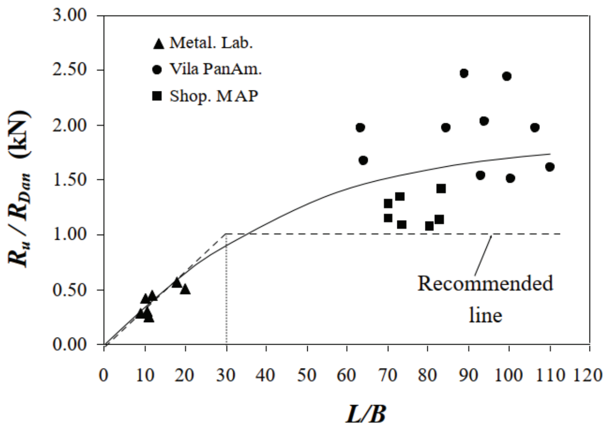

Figure 5. Predictive capacity of the Danish Formula as a function of pile aspect ratio (*L/B*).

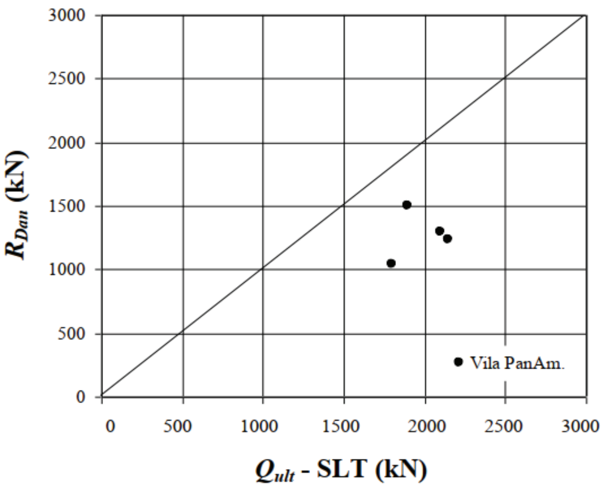

Figure 6. Danish Formula vs. SLTs - Vila Pan-Americana.

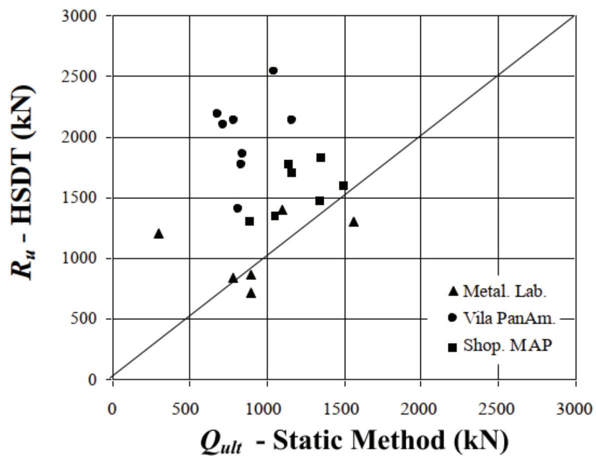

Figure 7. Static method (Aoki-Velloso) vs. HSDTs.

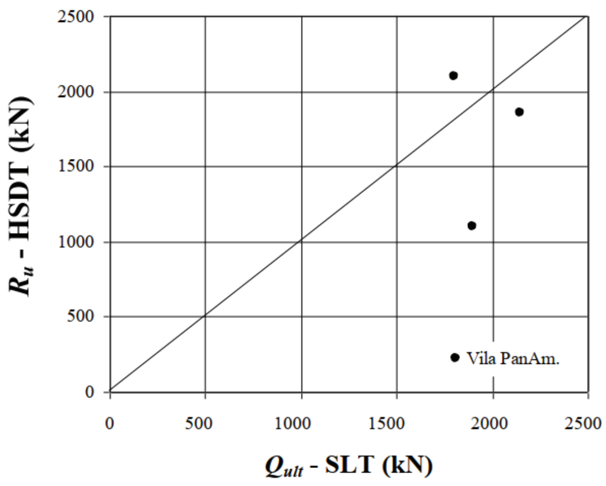

Figure 8. HSDTs vs. SLTs.

5. Concluding remarks

The development of quality control techniques based on measurements of pile response to driving should be encouraged, either by the simple set measurements or by the acquisition of more complete data in a dynamic test HSDTs. In any dynamic method, special attention should be given to the question of soil recovery after driving − set-up −, a phenomenon capable of considerably altering the load capacity of driven piles, especially in fine grained soils. The assessment of set-up can be made by carrying out HSDTs or even set measurements on two or three occasions after driving.

The comparison of the pile load capacities indicated by the Danish Formula with those of other methods, in particular HSDTs, showed that this formula overestimates the load capacity of relatively short piles (length less than 30 times the diameter). For longer piles, the results of the Danish Formula were consistent with those of dynamic and static tests (HSDTs and SLTs). The results of the present paper for this particular formula must be confirmed with a larger data base.

In view of the natural heterogeneity of the subsoil, the control of a piling through set measurements and dynamic formulae is quite efficient to ensure homogeneity in terms of load capacity. However, the use of these formulae should be restricted to the piling control process and not as a predictive tool. The best practice suggestion is: (i) prediction of pile depths by static methods (based on SPT, CPT, etc.) in the design stage, (ii) confirmation of pile depths and capacities during actual construction by HSDTs and SLTs, performed right at the beginning of the works, and (iii) adjustment of the selected dynamic formula (using measured pile response to driving – set – and capacities) to control the homogeneity of the pilling.

Acknowledgements

Thanks are due to Prof. Bernadete Ragoni Danziger, Rio de Janeiro State University, for her kind review of the manuscript.

Declaration of interest

There is no conflict of interests in the material presented.

Author’s contributions

Silvio Heleno de Abreu Vieira: Conceptualization, Methodology, Formal analysis. Francisco R. Lopes: Discussion of results, Writing - Reviewing and Editing.

List of symbols

A = pile cross-section area
B = pile cross dimension (diameter if circular pile)
E_p = modulus of elasticity of the pile material
h = hammer drop height
η = efficiency factor of the driving system
L = pile length
Q_{ult} = pile (static) load capacity
Q_{ser} = pile service load
R_{Dan} = pile driving resistance by the Danish Formula
R_u = static load capacity or static resistance obtained in HSDT
s = pile set (permanent penetration per blow)
W = weight of hammer
HSDT = High Strain Dynamic Test
SLT = Static Load Test
CAPWAP = Case Pile Wave Analysis Program (Pile Dynamics, Inc.)

References

Agerschou, H.A. (1962). Analysis of the engineering pile formula. *Journal of the Soil Mechanics and Foundations Division*, 88(5), 1-11. http://dx.doi.org/10.1061/JSFEAQ.0000450.

Alonso, U.R. (1988). *Previsão e controle das fundações* (1. ed.). São Paulo: Edgar Blucher.

Aoki, N., & Velloso, D.A. (1975). An approximate method to estimate the bearing capacity of piles. In *Proceedings of the 5th Panamerican Conference on Soil Mechanics and Foundation Engineering* (pp. 367-376), Buenos Aires.

Danziger, B.R., & Ferreira, J.S. (2000). Back-analyses of steel pile driving records for quality assurance. In *Proceedings of the International Conference on the Application of Stress-Wave Theory to Piles* (pp. 657-663), São Paulo.

Décourt, L., & Quaresma, A.R. (1978). Bearing capacity of piles from SPT values. In *Proceedings of the 6th Brazilian Conference on Soil Mechanics and Foundation Engineering* (pp. 45-53). Rio de Janeiro.

Greulich, G.G. (1941). Progress report of the committee on the bearing value of pile foundations. *Proceedings of the American Society of Civil Engineers*, 67(7), 1391-1396.

Likins, G.E., Fellenius, B.H., & Holtz, R.D. (2012). Pile driving formulas: past and present. In *Proceedings of the GeoCongress 2012* (pp. 737-753), Oakland, California. http://dx.doi.org/10.1061/9780784412084.0051.

Poulos, H.G., & Davis, E.H. (1980). *Pile foundation analysis and design.* New York: John Willey.

Silva, E.R., Danziger, B.R., & Pacheco, M.P. (2020). Comparação entre critérios de controle de estacas cravadas. *Geotecnia*, 149, 3-16. http://dx.doi.org/10.24849/j.geot.2020.149.01.

Smith, E.A.L. (1960). Pile-driving analysis by the wave equation. *Journal of the Soil Mechanics and Foundations Division*, 86(4), 35-61. http://dx.doi.org/10.1061/JSFEAQ.0000281.

Sorensen, T., & Hansen, J.B. (1957). Pile driving formulae, an investigation based on dimensional considerations and a statistical analysis. In *Proceedings of the 4th International Conference on Soil Mechanics and Foundation Engineering* (pp. 61-65), London.

Vieira, S.H.A. (2006). *Controle da cravação de estacas pré- moldadas: avaliação de diagramas de cravação e fórmulas dinâmicas* [MSc dissertation]. Federal University of Rio de Janeiro.

Soils and Rocks
An International Journal of Geotechnical and Geoenvironmental Engineering
www.soilsandrocks.com
ISSN 1980-9743
ISSN-e 2675-5475

Physical, chemical and microstructural characterization of two problematic soils from the Paraguayan Chaco

Hugo Carlos Scheuermann Filho[1#], Gustavo Dias Miguel[1], Lucas Festugato[1], Rubén Alejandro Quiñonez Samaniego[2], Eduardo José Bittar Marín[2]

Technical Note

Keywords
Sulfate-rich soils
Dispersive soils
Problematic soils
Soil characterization

Abstract

It is not uncommon for Geotechnical Engineering works to be carried out under unfavorable conditions that compromise the earth-stability. In this context, the Paraguayan Region of Chaco is notably known owing to the presence of problematic soils that possess dispersive characteristics and/or present high amounts of soluble-sulfates content. Geomaterials of such nature affect mainly the road infrastructure earthworks due to, respectively, their promptness to erosive phenomena when in contact with water and swelling owing to the grown and hydration of expansive minerals such as ettringite and thaumasite, when treated with calcium-based materials. Therefore, present research presents a detailed characterization of a dispersive soil and a sulfate-rich dispersive soil, both collected in the Western Region of Paraguay. Physical, chemical and microstructure tests were carried out in order to verify and explain the deleterious behavior observed in both soils.

1. Introduction

It is not atypical for engineering earthworks to be carried out under adverse geotechnical conditions due to the existence of problematic soils (Ingles & Metcalf, 1972; Mitchell, 1981; Behnood, 2018). That is, soils which are not suitable for a particular purpose without the application of any kind of improvement/stabilization technique. Distinct issues may lead soils of different natures to earth-stability problems, such as high swell or shrinkage potential, dispersibility tendency, amongst others. Those drawbacks are usually related to the soil' overall structure (fabric, composition and interparticle forces) and the way it interacts to the medium (Mitchell & Soga, 2005; Miguel et al., 2020).

In this sense, the Paraguayan region of Chaco (Western Region) is notably known for the presence of soils that may present either dispersive characteristics and/or sulfate-rich expansive soils (Quiñónez Samaniego, 2015; Consoli et al., 2016, 2019, 2020, 2021; Rocha et al., 2016; Scheuermann Filho, 2019; Miguel, 2020, Miguel & Festugato, 2021). These imply constant damage to local infrastructure, especially on road embankments which require persistent maintenance interventions owing to erosive and swell related issues. Generally, dispersive soils are distinguished by its high amounts of monovalent cations (mostly Na^+) adhered to the surface of the clay particles (Ryker, 1977; Elges, 1985). This yields in the predisposition of such soils to phenomena of external and internal erosion (piping) when in contact with water, since the level of electrochemical forces of attractive character is low as sodium is lightly charged and weakly adhered to the clay minerals (CRC, 2001). Thus, it is not uncommon to observe severe erosive phenomena, such as tunnel erosion, in sodic soil areas (Sparks, 2003).

The complications related to sulfate-rich soils, in turn, are associated to the presence of sulfates that may interact with calcium-based stabilizers and yield the precipitation of hydrated calcium alumino-sulfate minerals, which might grow, hydrate and expand, causing the heaving of the treated soil (Sherwood, 1962; Hunter, 1988; Kota et al., 1996; Roy et al., 2003; Little & Nair, 2009; Knopp & Moormann, 2016; Consoli et al., 2019; Scheuermann Filho et al., 2020). This happens in a hydrated alkaline environment, through the reaction between the calcium ions (from the stabilization agent), the available sulfates and the aluminates from the clay minerals. Thus, the stabilization of such soils with conventional materials (e.g. Ordinary Portland Cement and hydrated lime) may lead to inconvenient pathologies. Moreover, sodium sulfate (Na_2SO_4), magnesium sulfate ($MgSO_4$) and calcium sulfate ($CaSO_4 \cdot H_2O$ – gypsum) are commonly encountered in such soils and may be natural compounds or secondary sources from the oxidation of sulfides (Puppala et al., 2003; Talluri, 2013; Talluri et al., 2013; Harris et al., 2004).

[#]Corresponding author. E-mail address: hugocsf@gmail.com
[1]Universidade Federal do Rio Grande do Sul, Programa de Pós-graduação em Engenharia Civil, Porto Alegre, RS, Brasil.
[2]Universidad Nacional de Asunción, Asunción, Paraguay.

Submitted on July 27, 2020; Final Acceptance on January 27, 2021; Discussion open until August 31, 2021.

https://doi.org/10.28927/SR.2021.056420

Therefore, the present research intends to comprehensively characterize two problematic soils from the Paraguayan Chaco. The first is a highly dispersive soil and the second is a sulfate-rich soil which also presents an intermediate dispersibility propensity. For this, both soils were assessed by means of its standard physical properties (i.e. grain size distribution, Atterberg limits, compaction characteristics, amongst others), chemical composition and mineralogical constitution. In addition, regular tests aiming to determine the dispersibility potential and the soluble sulfates content were also performed.

2. Experimental program

The experimental program was carried out on three parts. First, the physical properties of both soils were characterized. Next, the total soluble salts (TDS) and water-soluble sulfate contents were determined. Finally, the microstructure of both soils was assessed by means of X-Ray diffraction tests and scanning electron microscope images (SEM). Both soils come from the Paraguayan Chaco region, which is located in the Western Region of Paraguay. The dispersive soil was collected nearby the Villa Hayes town, which is 31 km from the north of Asunción (capital of Paraguay). The sulfate-rich dispersive soil, in turn, was collected in the city of Filadelfia, which is 467 km northwest from Asunción.

2.1 Physical properties

Table 1 summarizes the physical properties of the studied soils, while Figure 1 presents the grain size distribution obtained for both soils via the hydrometer method (ASTM, 2017a). Both soils can be classified as a lean clay (CL) accordingly to the Unified Soil Classification System (ASTM, 2017b). The compaction curves of the soils are presented in Figure 2 and were obtained through the employment of the standard effort accordingly to the ASTM D698 standard (ASTM, 2012). Hence, the maximum dry unit weight attained for the dispersive soil was equal to 18.05 kN/m^3, at a moisture content of 15.70%, while the greatest dry unit weight was 18.20 kN/m^3 for an optimum moisture content of 13.50% for the sulfate-rich dispersive soil.

In order to determine the dispersive characteristics of both soils, the Crumb Test and the Pinhole test were performed in either. The first was carried out in according to the ASTM D6572 standard (ASTM, 2020) and basically consists in observe the turbidity of a portion of distilled water due to the presence of crumbs of soil. That is, if the soil possesses dispersive features its particles deflocculate and go into suspension as the crumbs begin to adsorb water. Therefore, the dispersive grade (I to IV) is based upon the turbidity of the water attained once the test is finished. The dispersive soil was classified as a highly dispersive soil (grade IV) as a dense and profuse cloud of suspended clay colloid was seen along the test. The sulfate-rich soil, in turn, was classified as an intermediate dispersive soil (grade II) since

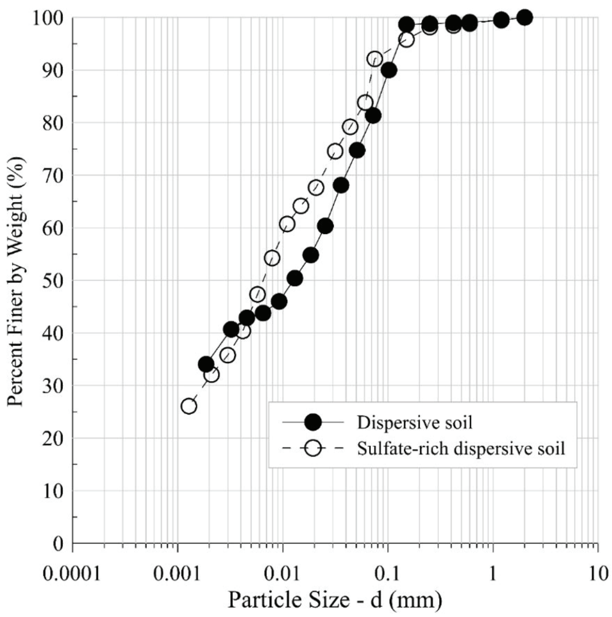

Figure 1. Grain size distribution of the studied soils.

Table 1. Physical properties of the soils.

Parameter	Sulfate-rich dispersive soil	Dispersive soil
Liquid limit (%)	32	43
Plastic limit (%)	16	19
Plastic index (%)	16	24
Unit weight of the soil grains (g/cm^3)	2.69	2.74
Percent finer by weight sieve #200	92%	91%
Mean particle diameter, D_{50} (mm)	0.0064	0.013
Maximum dry unit weight (kN/m^3)	18.2	18.05
Optimum moisture content (%)	13.5	15.7
USCS classification	CL	CL
Organic matter (%)	1.24%	0.20%
Crumb Test	Grade 2 (intermediate)	Grade 4 (highly dispersive)
Pinhole Test	D1	D2

only a slight reaction took place, which resulted in a barely visible colloidal suspension.

The pinhole test was performed according to NBR 14114 standard (ABNT, 1998) on soil samples molded to the maximum dry unit weight (at the optimum moisture content) attained in the compaction tests (Figure 2). The test consists in opening a small hole (1 mm of diameter) at the entire length of cylindrical specimens (38 mm in diameter and 38 mm in height) of the compacted soil. These specimens are then subjected to constant hydraulic heads during time intervals equal to 5 minutes. After each interval, the average flow rate and turbidity of the water is checked. Hydraulic heads of 50 mm, 180 mm, 380 mm and 1020 mm are employed. For instance, the test firstly initiates with a hydraulic head of 50 mm that is subjected to the sample during a defined volume and time, after either elapsed time or volume collected, is able to classify the soil according to its effluent turbidity and flow rate. Additionally, the hole enlargement must be verified, highly dispersive soils tend to easily erode, therefore, enlarge the initial hole size. In case of results do not fit with the NBR 14114 requirements, then the hydraulic head must be raised and the procedure repeated with the next hydraulic head. Consequently, as greater is the dispersibility of the soil, greater is the flow rate and the turbidity of the water. Namely, the soil particles in dispersive soils tend to be carried by the water flowing, which is responsible to increase the diameter of the hole and, as a consequence, the flow rate and the turbidity of the water. Accordingly, the dispersive soil was classified as a dispersive soil (D2), while the sulfate-rich dispersive soil was classified as a highly dispersive soil (D1).

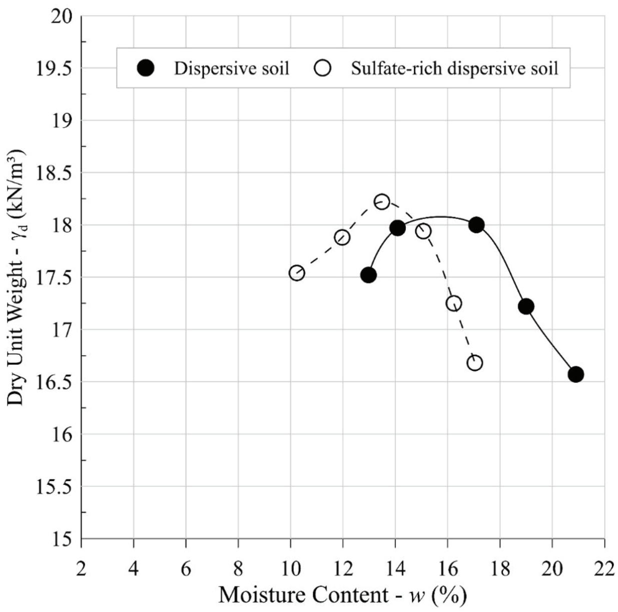

Figure 2. Compaction curves.

Table 2. Soluble salts content.

Parameter/Elements	Sulfate-rich dispersive soil	Dispersive soil
Na (cmol/kg)	44.91	13.90
K (cmol/kg)	0.21	0.50
Ca (cmol/kg)	15.80	0.60
Mg (cmol/kg)	4.53	0.20
TDS (*Total Dissoluble Salts*)	65.45	15.20
PS (*Percent Sodium*)	68.60	91.40
SAR (*Sodium Adsorption Ratio*)	14.09	21.98
pH	8.54	8.52

2.2 Chemical properties

Table 2 present the results of the soluble salts contained in the pore water of the studied soils. The pore water extraction and the determination of the soluble salts content was carried out in according to ASTM D4542 (ASTM, 2015a) standard. The total dissoluble salts (TDS) is the sum between the content of the soluble salts, while the percent sodium (PS) and the sodium adsorption ration (SAR) were determined, respectively, with the following Equations 1 and 2:

$$PS\ (\%) = \left(\frac{Na}{TDS}\right) x100 \quad (1)$$

$$SAR = \frac{Na}{\sqrt{0.5\ x\left(Ca + Mg\right)}} \quad (2)$$

Those parameters are an indicative of the soil' dispersive potential, as the presence of sodium cations can be seen as the main reason for the dispersion observed amongst clays. Thus, both soils can be classified as dispersive accordingly to Sherard et al. (1976) diagram, which is illustrated in Figure 3 and relates the dispersibility to the TDS and PS. Moreover, soils that present SAR values greater than 13 are defined as dispersive by the United States Department of Agriculture (2017), which is the case for both soils studied herein.

Table 3 presents the water-soluble sulfates content for the sulfate-rich dispersive soil. The determination of the sulfates content followed the recommendations of the ASTM C1580 standard (ASTM, 2015b), and yielded a total of 14229 ppm. There is not exactly a precise value of sulfates content that can be taken as critical, as the researches on the area point out that there are other important factors that affect the ettringite formation in the stabilized soil, such as availability of water and soil mineralogy (Hunter, 1988; Mitchell & Dermatas, 1992; Dermatas, 1995). However, based upon previous researches, was stated that soluble sulfate contents higher than 3000 ppm may require special attention for soil stabilization purposes (Mitchell & Dermatas, 1992; Dermatas, 1995; Berger et al., 2001; Harris et al., 2004; Little & Nair, 2009a, b; Jones et al., 2010). Furthermore, it's a consensus that amounts higher than 10000 ppm are serious and demand specific considerations (Hunter, 1988; Berger et al., 2001;

Table 3. Soluble salts content.

Soluble salts	Sulfate-rich dispersive soil
$CaSO_4$ (ppm)	5372
K_2SO4 (ppm)	93
$MgSO_4$ (ppm)	1351
Na_2SO_4 (ppm)	7576
$NaHCO_3$ (ppm)	215
NaCl (ppm)	7396
Total of salts (ppm)	22003
Total of sulfate salts (ppm)	14229

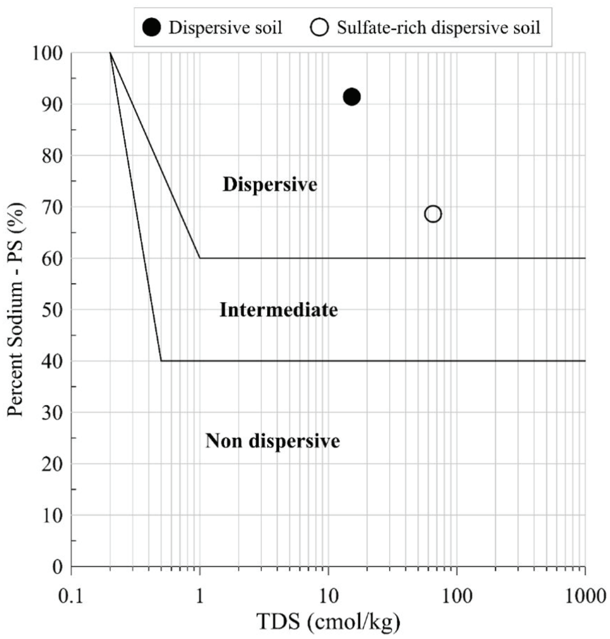

Figure 3. Diagram of identification.

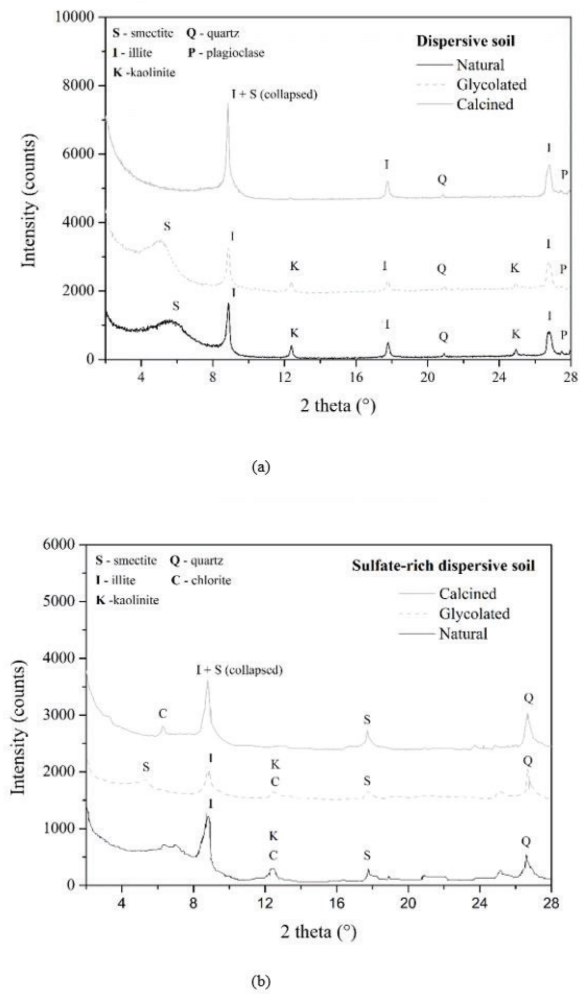

Figure 4. (a) XRD of the dispersive soil (b) XRD of the sulfate-rich dispersive soil.

Little & Nair, 2009a, b), which is the case of the sulfate-rich dispersive soil studied herein.

2.3 Microstructure

In order to assess the soils' mineralogy, with emphasis to the clay minerals, X-Ray diffraction tests (XRD) were carried out on the fractions finer than 4 µm of both. Therefore, for each soil, this fraction was isolated by means of a special process that encompassed (i) the disintegration using an orbital mixer along 14 hours, (ii) disintegration via ultrasonic tip during 5 minutes in a liquid solution and (iii) separation of the finer portion via decantation during a pre-defined time which was calculated based on the Stokes' law. Right after, plain slides were prepared by pipetting the soil on them. In order to precisely check for expansive minerals and/or minerals from the kaolinite group, three samples were tested within each soil. Namely, a sample with the natural soil, a glycolated sample aiming to verify the existence of expansive minerals (smectites) and a calcined sample (calcined at 550°C) intending to assure the existence of minerals that collapse its structure at that temperature. The tests were conducted on a Siemens (Bruker AXS) D-5000 diffractometer, equipped with copper anode tube and operated at 40 kV and 35 mA. The angular range adopted varied from 2° to 28° 2θ at rate of 0.02°/s.

The XRD results for the dispersive soil are depicted in Figure 4a, while the results for the sulfate-rich dispersive soil are exhibited in Figure 4b. For the first, the following minerals were identified: quartz (47.6%), illite (4.1%), kaolinite (3.4%), plagioclase (14.8%), K-Feldspar (19.3%) and smectite (10.8%). For the second, in turn, the presence of quartz (33.9%), albite (24.5%), chlorite (17.4%), illite (14.5%), barium orthoclase (5.5%) and gypsum (4.2%) were attested. However, those quantities are merely semi-quantitative as they were based upon the Reference Intensity Ratio method (RIR).

Moreover, intending to visually assess the fabrics of both soils in a disintegrated state, scanning electron microscope (SEM) tests were carried out. Hence, Figure 5 presents the

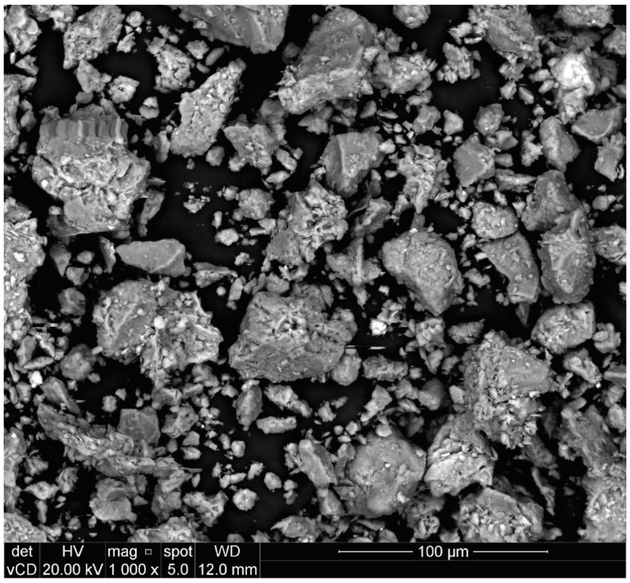

Figure 5. SEM image of the dispersive soil magnified 1000x.

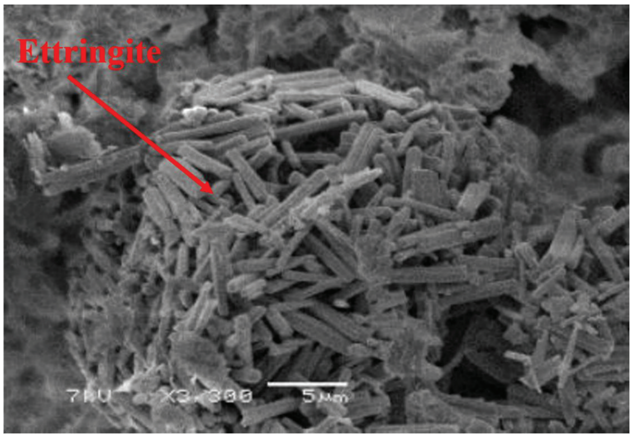

Figure 6. SEM image of the sulfate-rich dispersive soil magnified at 3300x.

SEM images of the dispersive soil, whereas Figure 6 exhibits SEM images of the sulfate-rich dispersive soil. In case of Figure 5, from dispersive soil, this figure focus on particle size and structure of clay minerals. The same approach was made to sulfate-rich dispersive soil, however, was also magnified the expansive minerals formation through calcium-based stabilizers addition, where ettringite crystals were depicted.

3. Conclusions

The present research intended to characterize in detail two problematic soils encountered in the region of the Paraguayan Chaco, from the data presented herein, the following assertions can be made:

- the results of the physical, chemical and mineralogical characterizations, when analyzed in conjunction, corroborate and explain the adverse behavior of the dispersive soil and of the sulfate-rich dispersive soil;
- the sulfate-rich dispersive soil is highly susceptible to ettringite/thaumasite formation when stabilized with calcium-based stabilizers as it possesses great quantities of soluble-sulfates and, as well, clay minerals that serve as an alumina source;
- both soils contain smectite, which is highly reactive and presents an elevated specific surface area, thus being capable to adsorb great quantities of sodium ions.

Acknowledgements

The authors wish to explicit their appreciation to FAPERGS/CNPq 12/2014 – PRONEX (grant # 16/2551-0000469-2), MCT-CNPq (INCT, Universal & Produtividade em Pesquisa) and MEC-CAPES (PROEX) for the support to the research group.

Declaration of interest

The authors declare that there is no conflict of interest.

Authors' contributions

Hugo Carlos Scheuermann Filho: data curation, writing-original draft preparation. Gustavo Dias Miguel: conceptualization, methodology, validation. Lucas Festugato: supervision. Rubén Alejandro Quiñonez Samaniego: writing-reviewing and editing. Eduardo José Bittar Marín: writing-reviewing and editing.

List of symbols

TDS	Total soluble salts
SEM	Scanning electron microscope
CL	Lean clay
PS	Percent sodium
SAR	Sodium adsorption ratio
ppm	Parts-per-million
XRD	X-ray diffraction
RIR	Reference intensity ratio

References

ABNT NBR 14114. (1998). *Solos argilosos dispersivos: identificação e classificação por meio do ensaio do furo de agulha (pinhole test).* Associação Brasileira de Normas Técnicas, Rio de Janeiro.

ASTM D698-12e2. (2012). *Standard test methods for laboratory compaction characteristics of soil using standard effort (12,400 ft-lbf/ft³ (600 kN-m/m³)).* ASTM International, West Conshohocken, PA. https://doi.org/10.1520/D0698-12E02.

ASTM D4542-15. (2015a). *Standard test method for pore water extraction and determination of the soluble salt content of soils by refractometer.* ASTM International, West Conshohocken, PA. https://doi.org/10.1520/D4542-15.

ASTM C1580-15. (2015b). *Standard test method for water-soluble sulfate in soil.* ASTM International, West Conshohocken, PA. https://doi.org/10.1520/C1580-15.

ASTM D7928-17. (2017a). *Standard test method for particle-size distribution (gradation) of fine-grained soils using the sedimentation (hydrometer) analysis*. ASTM International, West Conshohocken, PA. https://doi.org/10.1520/D7928-17.

ASTM D2487-17e1. (2017b). *Standard classification of soils for engineering purposes.* ASTM International, West Conshohocken, PA. https://doi.org/10.1520/D2487-17E01.

ASTM D6572-20. (2020). *Standard test method for determining dispersive characteristics of clayey soils by the crumb test.* ASTM International, West Conshohocken, PA. https://doi.org/10.1520/D6572-20.

Behnood, A. (2018). Soil and clay stabilization with calcium- and non-calcium-based additives: a state-of-the-art review of challenges, approaches and techniques. *Transportation Geotechnics*, 17, 14-32. http://dx.doi.org/10.1016/j.trgeo.2018.08.002.

Berger, E., Little, D.N., & Graves, R. (2001). *Guidelines for stabilization of soils containing sulfates* (p. 16). Arlington: National Lime Association.

Consoli, N.C., Bittar Marin, E.J., Samaniego, R.A.Q., Scheuermann Filho, H.C., Miranda, T., & Cristelo, N. (2019). Effect of mellowing and coal fly ash addition on behavior of sulfate-rich dispersive clay after lime stabilization. *Journal of Materials in Civil Engineering*, 31(6), 04019071. http://dx.doi.org/10.1061/(ASCE)MT.1943-5533.0002699.

Consoli, N.C., Samaniego, R.A.Q., & Villalba, N.M.K. (2016). Durability, strength, and stiffness of dispersive clay-lime blends. *Journal of Materials in Civil Engineering*, 28(11), 4016124. http://dx.doi.org/10.1061/(ASCE)MT.1943-5533.0001632.

Consoli, N.C., Festugato, L., Miguel, G.D., Moreira, E.B., & Scheuermann Filho, H.C. (2021). Fatigue life of green stabilized fiber-reinforced sulfate-rich dispersive Soil. *Journal of Materials in Civil Engineering*. In press.

Consoli, N.C., Festugato, L., Miguel, G.D., & Scheuermann Filho, H.C. (2020). Swelling prediction of green stabilized fiber-reinforced sulfate-rich dispersive soils. *Geosynthetics International*. In press. http://dx.doi.org/10.1680/jgein.20.00050.

CRC. (2001). *Diagnosis and management of sodic soils under sugarcane* (Technical Report). Townsville, Australia: Cooperative Research Center for Sustainable Sugar Production.

Dermatas, D. (1995). Ettringite-induced swelling in soils: state-of-the-art. *Applied Mechanics Reviews*, 48(10), 659-673. http://dx.doi.org/10.1115/1.3005046.

Elges, H.F.W.K. (1985). Problems in South Africa: state of the art: dispersive soils. *The Civil Engineer in South Africa*, 27(1), 347-353. Retrieved in July 27, 2020, from https://hdl.handle.net/10520/EJC25000

Harris, P., Scullion, T., & Sebesta, S. (2004). *Technical report documentation page: hydrated lime stabilization of sulfate-bearing soils in Texas* (p. 36). Texas, US: Texas Department of Transportation, Texas Transportation Institute and Federal Highway Administrations.

Hunter, D. (1988). Lime-induced heave in sulfate-bearing clay soils. *Journal of Geotechnical Engineering*, 114(2), 150-167. http://dx.doi.org/10.1061/(asce)0733-9410(1988)114:2(150).

Ingles, O.G., & Metcalf, J.B. (1972). *Soil stabilization: principles and practice*. Sidney, Australia: Butterworths.

Jones, D., Rahim, A., Saadeh, S., & Harvey, J. (2010). *Guidelines for the stabilization of Subgrade Soils in California* (Research report – UDC-ITS-RR-10-38, p. 97). California: Institute of Transportation Studies, University of California.

Knopp, J., & Moormann, C. (2016). Ettringite swelling in the treatment of sulfate-containing soils used as subgrade for road constructions. In *Proceedings of the 3rd International Conference on Transportation Geotechnics (ICTG 2016)* (pp. 128-137), Guimarães, Portugal.

Kota, P.B.V.S., Hazlett, D., & Perrin, L. (1996). Sulfate-bearing soils: problems with calcium-based stabilizers. *Transportation Research Record: Journal of the Transportation Research Board*, 1546(1), 62-69. http://dx.doi.org/10.1177/0361198196154600107.

Little, D.N., & Nair, S. (2009). *Recommended practice for stabilization of sulfate-rich subgrade soils* (Document, No. 145, p. 54). United States: American Association of State Highway and Transportation (AASHTO), Transportation Research Board (TRB): The National Academies: National Cooperative Highway Research Program (NCHRP).

Miguel, G.D. (2020). *Desempenho e comportamento mecânico de um solo dispersivo e sulfatado tratado com uma pozolana artificial, cal de carbureto e reforçado com fibras de vidro* [Unpublished master's dissertation]. Federal University of Rio Grande do Sul. https://doi.org/10.13140/RG.2.2.27481.67687/1.

Miguel, G.D., & Festugato, L. (2021). Uso de resíduos e subprodutos na estabilização sustentável de um solo dispersivo e sulfatado. *Holos Environment*, 21(1), 23-46. http://dx.doi.org/10.14295/holos.v21i1.12411.

Miguel, G.D., Scheuermann Filho, H.C., Festugato, L., & Corte, M.B. (2020). Cement, lime, and fly ashes in stabilizing expansive soils: performance evaluation and comparison. *Journal of Materials in Civil Engineering*. In press.

Mitchell, J.K., & Soga, K. (2005). *Fundamentals of soil behavior*. Hoboken: John Willey & Sons.

Mitchell, J.K. (1981). Soil improvement: state-of-the-art report. In *Proc. 10th International Conference on Soil Mechanics and Foundation Engineering* (pp. 509-565), Stockholm, Sweden.

Mitchell, J., & Dermatas, D. (1992). Clay soil heave caused by lime-sulfate reactions. In D. Walker, T. Hardy, D. Hoffman & D. Stanley (Eds.), *Innovations and uses for lime* (pp. 41-64). West Conshohocken, PA: ASTM International. https://doi.org/10.1520/STP15529S.

Puppala, A.J., Wattanasanticharoen, E., & Punthutaecha, K. (2003). Experimental evaluations of stabilisation methods for sulphate-rich expansive soils. *Proceedings of the Institution of Civil Engineers - Ground Improvement*, 7(1), 25-35. http://dx.doi.org/10.1680/grim.2003.7.1.25.

Quiñónez Samaniego, R.A. (2015). *Estabilização de um solo dispersivo com adição de cal* [Unpublished master's dissertation]. Federal University of Rio Grande do Sul.

Rocha, C.G., Passuello, A., Consoli, N.C., Samaniego, R.A.Q., & Kanazawa, N.M. (2016). Life cycle assessment for soil stabilization dosages: a study for the Paraguayan Chaco. *Journal of Cleaner Production*, 139, 309-318. http://dx.doi.org/10.1016/j.jclepro.2016.07.219.

Roy, A., Wang, L., Seals, R.K., & Metcalf, J.B. (2003). *Stabilization techniques for reactive aggregates in soil-cement base course* (Technical Report No. FHWA/LA. 03/366, p. 69). Louisiana Department of Transportation and Development, Louisiana Transportation Research Center.

Ryker, N.L. (1977). Encountering dispersive clays on soil conservation projects in Oklahoma. In *Proceedings of the Symposium of Dispersive Clays, Related Piping, and Erosion* (pp. 370-389), Chicago. https://doi.org/10.1520/STP27001S.

Scheuermann Filho, H.C. (2019). *Dispersive soil stabilization with ground glass and carbide lime* [Unpublished master's dissertation]. Federal University of Rio Grande do Sul. (in Portuguese).

Scheuermann Filho, H.C., Miguel, G.D., Festugato, L., & Corte, M.B. (2020). Suppressing ettringite-induced swelling of gypseous soil by using magnesia-activated ground granulated blast-furnace slag. *Journal of Geotechnical and Geoenvironmental Engineeringt*, 146(7), 1-46.

Sherard, J.L., Decker, R.S., & Dunnigan, L.P. (1976). Identification and nature of dispersive soils. *Journal of the Geotechnical Engineering Division*, 102(4), 287-301.

Sherwood, P.T. (1962). Effect of sulfate on cement and lime-stabilized soils. In *Proceedings of the 41st Annual Meeting of the Highway Research Board* (pp. 98-107), Washington DC, United States.

Sparks, D.L. (2003). The chemistry of saline and sodic soils. In D.L. Sparks (Ed.), *Environmental soil chemistry* (pp. 285-300). San Diego: Elsevier. https://doi.org/10.1016/b978-012656446-4/50010-4.

Talluri, N. (2013). *Stabilization of high sulfate soils* [Doctoral thesis]. University of Texas. Retrieved in July 27, 2020, from https://rc.library.uta.edu/uta-ir/bitstream/handle/10106/23923/Talluri_uta_2502D_12312.pdf?sequence=1

Talluri, N., Puppala, A.J., Chittoori, B.C.S., Gaily, A.H., & Harris, P. (2013). Stabilization of high-sulfate soils by extended mellowing. *Transportation Research Record: Journal of the Transportation Research Board*, 2363(1), 96-104. http://dx.doi.org/10.3141/2363-11.

United States Department of Agriculture – USDA. Natural Resources Conservation Service Wisconsin. (2017). *Soil mechanics note no. 13: Eng.: dispersive clays* (p. 24). Washington: Federal Government of United States.

Soils and Rocks

An International Journal of Geotechnical and Geoenvironmental Engineering

www.soilsandrocks.com

ISSN 1980-9743
ISSN-e 2675-5475

A simple approach to predict settlement due to constant rate loading in clays

Raphael F. Carneiro[1#], Denise M. S. Gerscovich[2], Bernadete R. Danziger[2]

Technical Note

Keywords
Consolidation
Settlement prediction
Soft clays
Linearly increasing load

Abstract

Classical theory of consolidation was conceived considering loads instantaneously applied. Since then, researchers have addressed this issue by suggesting graphical and/or analytical solutions to incorporate different time-depending load schemes. The simplest alternative is to assume a linearly increasing load. Another approach to predict the average degree of consolidation caused by a constant rate loading is based on instantaneous excess pore pressures during and at the end of construction. This technical note explains why and how this approach leads to substantial errors after the end of construction. A corrected solution is then proposed, based on the concept of superposition of effects. The final set of equations agree with the theoretical ones. A new simple approximate methodology is also presented. Numerical examples using the proposed approach showed an excellent agreement with the analytical solution. The validity of this new approach was also proven by reproducing oedometer test results with a good agreement.

1. Introduction

Consolidation is one of the most relevant and most studied phenomena in Geotechnical Engineering. The process involves volume change due to water flow in response to stress increase and it is particularly relevant with saturated clayey soils. Due to the extremely low permeability of clays, consolidation can last for decades.

Terzaghi and Fröhlich's (1936) one-dimensional consolidation theory is based on Darcy's law and uses a set of simplifying hypotheses. One of the main assumptions imposes that load is applied instantaneously. The average degree of consolidation U is given by

$$U(T) = 1 - \sum_{m=0}^{\infty} \frac{2}{M^2} e^{-M^2 T} \tag{1}$$

where

$$M = (2m+1)\pi / 2 \tag{2}$$

for m = 1, 2, 3… and the Time Factor T is defined as

$$T = c_v t / H_d^2 \tag{3}$$

Where t is time, H_d is the maximum length of the drainage path and c_v is the coefficient of consolidation.

The consideration of instantaneous load is unlikely to occur in engineering practice. Loading is generally carried out gradually, in stages, during a given construction period. Therefore, consolidation takes place while loading is still in progress.

Several methods have addressed the time-dependent loading issue (Terzaghi, 1943; Schiffman, 1958; Schiffman and Stein, 1970; Olson, 1977; Zhu and Yin, 1998; Conte and Troncone, 2006; Liu and Ma, 2011, Hanna et al. 2013; Gerscovich et al., 2018). The two most worldwide known approaches for linearly increasing loading are Terzaghi's (1943) graphical method and Olson's (1977) theoretical solution.

Terzaghi's (1943) empirical method is a graphical procedure performed differently before and after construction. After the end of construction, the settlement curve is shifted by half the construction period t_c. During construction, the calculation considers only a fraction of the total load as if applied instantaneously in half the time. Despite being a graphical method, whose accuracy is subject to the operator expertise, it can be expressed by the following set of equations (Gerscovich et al., 2018):

$$U'(T) = \begin{cases} \dfrac{T}{T_c} U\left(\dfrac{T}{2}\right) \ldots\ldots\ldots\ldots T \le T_c \\ U\left(T - \dfrac{T_c}{2}\right) \ldots\ldots\ldots\ldots T \ge T_c \end{cases} \tag{4}$$

[#]Corresponding author. E-mail address: raphaelfc@esp.puc-rio.br
[1]Pontifícia Universidade Católica do Rio de Janeiro, Rio de Janeiro, RJ, Brasil.
[2]Universidade do Estado do Rio de Janeiro, Departamento de Estruturas e Fundações, Rio de Janeiro, RJ, Brasil.

Submitted on September 01, 2020; Final Acceptance on February 11, 2021; Discussion open until August 31, 2021.

https://doi.org/10.28927/SR.2021.057120

Where $U'(T)$ is the corrected average degree of consolidation, $U(T)$ is the corresponding value for instantaneous loading (Equation 1) and T_c is the Time Factor corresponding to the end of construction t_c.

Olson (1977) developed a mathematical solution for a linearly increasing loading as an extension of Terzaghi and Fröhlich's (1936) theory. The ramp load was discretized into small instantaneous incremental loads. Using the principle of superposition, Olson (1977) could express the average degree of consolidation (U') both during and after construction. The solution is divided into two equations:

$$U'(T) = \begin{cases} \dfrac{T}{T_c}\left[1-\dfrac{1}{T}\sum\limits_{m=0}^{\infty}\dfrac{2}{M^4}\left(1-e^{-M^2T}\right)\right] \ldots\ldots\ldots T \le T_c \\ 1-\dfrac{1}{T_C}\sum\limits_{m=0}^{\infty}\dfrac{2}{M^4}\left(e^{M^2T_c}-1\right)e^{-M^2T} \ldots\ldots T \ge T_c \end{cases} \quad (5)$$

where M and T were formerly defined in Equations 2 and 3, respectively.

Mota (1996) and Hanna et al. (2013) showed that Terzaghi's (1943) empirical method tends to overestimate the average degree of consolidation when compared with Olson's (1977) solution; the higher the value of T_c, the higher the error. The maximum divergence occurs at $T = T_c$. The method overestimates the average degree of consolidation by approximately 10%.

For this reason, Hanna et al. (2013) proposed a new approach to construct the consolidation curve due to a ramp load. During construction, the analytical development agrees with Olson's (1977). After construction, a simple equation is proposed, assuming that the remaining excess pore water pressure at the end of construction T_c is an instantaneous load applied at $T = T_c$.

This technical note reveals that Hanna et al.'s approach (2013) may lead to considerable errors in predicting the average degree of consolidation after the construction period. A corrected solution to the development is then proposed. Besides, a new simple approximate method is suggested, aiming to be more accurate than Terzaghi's (1943).

2. Method based on instantaneous excess pore pressures

2.1 Hanna et al.'s (2013) proposition

Hanna et al. (2013) discretized the ramp load into infinitesimal increments at a rate of λ per unit of time. As shown in Figure 1, Hanna et al. (2013) assume that after an infinitesimal increment dt, the loading is increased by λdt. At the end of construction, the total applied load (q_C) is λt_c. Each load increment results in an infinitesimal increase in pore pressure (Δu_0), which is assumed constant with depth. At the end of construction (t_c), only part of each increment of pore pressure will have been dissipated.

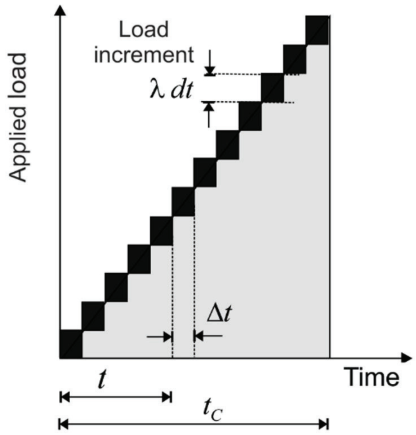

Figure 1. Discretization of the applied load into infinitesimal increments (adapted from Hanna et al., 2013).

Each infinitesimal load increment is applied instantaneously. The dissipation of each excess pore pressure may be expressed by Terzaghi and Fröhlich's (1936) theory. The dissipated excess pore water pressure at the end of loading is $U(t_c - t)\lambda dt$. Considering all intervals, the average degree of consolidation at a time t_c is given by:

$$U'(T_c) = \frac{1}{\lambda t_c}\int_0^{t_c} U(t_c - t)\lambda dt = \frac{1}{t_c}\int_0^{t_c} U(t_c - t)dt \quad (6)$$

Due to loading linearity (Figure 1), Equation 6 can also be expressed as:

$$U'(T_c) = \frac{1}{t_c}\int_0^{t_c} U(t)dt = \frac{1}{T_c}\int_0^{T_c} U(T)dT = 1-\frac{1}{T_c}\sum_{m=0}^{\infty}\frac{2}{M^4}\left(1-e^{-M^2T_c}\right) \quad (7)$$

By taking T as T_c, Hanna et al. (2013) extended Equation 7 for any time during construction. Thus, the final equation is given by:

$$U'(T \le T_c) = \frac{1}{T_c}\int_0^{T} U(T)dT = \frac{T}{T_c}\left[1-\frac{1}{T}\sum_{m=0}^{\infty}\frac{2}{M^4}\left(1-e^{-M^2T}\right)\right] \quad (8)$$

which agrees with Olson's (1977) solution during construction (Equation 5).

After the end of construction, Hanna et al. (2013) proposed another methodology. The remaining excess pore pressure $\overline{u_e}$ at the end of construction $T = T_c$ is expressed as a fraction of the final load by:

$$\overline{u_e} = \left[1 - U'(T_c) \right] q_c \tag{9}$$

If $\overline{u_e}$ is interpreted as the excess pore pressure due to an instantaneously applied load, the average degree of consolidation after the end of construction becomes the sum of the corresponding value at the end of loading and the one due to $\overline{u_e}$ dissipation:

$$U'(T \geq T_c) = U'(T_c) + \left[1 - U'(T_c) \right] U(T - T_c) \tag{10}$$

Hanna et al. (2013) applied their method to a practical example of an embankment on a 4 m thick, single-drained clay deposit, with a coefficient of consolidation c_v of 2.0 m^2/year and a coefficient of volume change m_v of 1.2 MPa^{-1}. The construction period was nine months ($T_c = 0.0938$). At the end of construction, the loading achieved 120 kPa. Hanna et al. (2013) calculated the average degrees of consolidation *U' (T)* equal to 12,5% after six months of construction, and equal to 57% after two years.

Figure 2 compares Hanna et al.'s (2013) method with the analytical solutions. After the end of loading, the curve quickly deviates and approaches Terzaghi and Fröhlich's (1936) consolidation curve for instantaneous loading. The results revealed that Hanna et al.'s (2013) proposition is inappropriate after the end of construction.

The error is due to an overestimation of the consolidation rate at the end of construction. Each infinitesimal increase of pore pressure is associated with a different value of the average degree of consolidation. The dissipation of the remaining excess pore pressure at $T = T_c$ is certainly slower than if it was applied instantaneously at that moment.

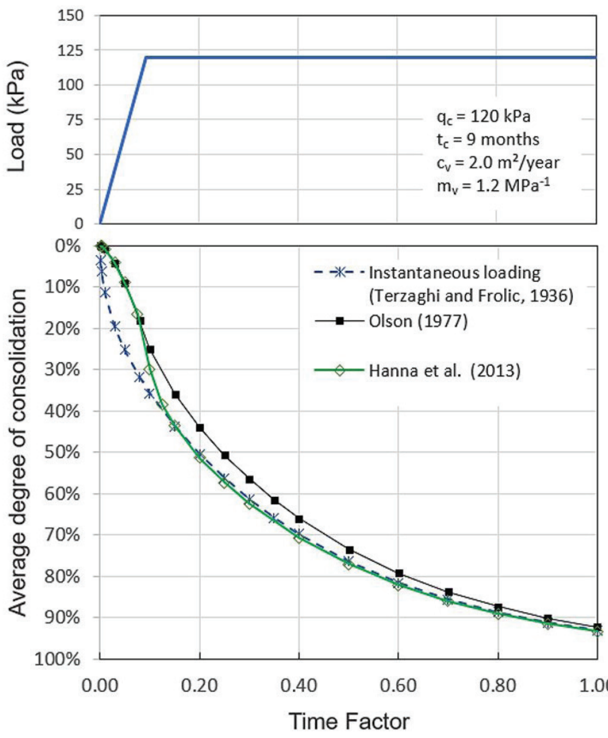

Figure 2. Predictions of the average degree of consolidation due to the construction of an embankment on a 4 m thick, single-drained clay deposit.

2.2 Correcting post-construction consolidation prediction

Hanna et al. (2013)'s procedure may be corrected by the simple application of superposition principle. As shown in Figure 3, the first step consists in a loading extrapolation beyond the end of construction ($t' \geq t_c$) to q'_t. Then, the average degree of consolidation is computed by subtracting from $U'_1(t')$ the corresponding value $U'_2(t')$ due to the excess load; i.e.:

$$U'(t') = U'_1(t') - U'_2(t') \tag{11}$$

The first term $U'_1(t')$ comprises all the real and the virtual infinitesimal load increments. The fraction of the excess pore pressure that is dissipated at any time $t' \geq t_c$ is $U(t' - t)\,\lambda dt$. Thus, for all time intervals, the average degree of consolidation at time t' is given by:

$$U'_1 = \frac{1}{\lambda t_c} \int_0^{t'} U(t' - t)\,\lambda dt = \frac{1}{t_c} \int_0^{t'} U(t)\,dt \tag{12}$$

The second term contains only the virtual load increments. The average degree of consolidation $U'_2(t')$ is determined similarly by shifting the origin of the Cartesian axis. The fraction of excess pore water pressure that is dissipated at time $t' \geq t_c$ is $U(t' - t_c - t)\,\lambda dt$; so:

$$U'_2 = \frac{1}{\lambda t_c} \int_0^{t'-t_c} U(t' - t_c - t)\,\lambda dt = \frac{1}{t_c} \int_0^{t'-t_c} U(t)\,dt \tag{13}$$

Thus, the average degree of consolidation at any time after the end of loading is given by:

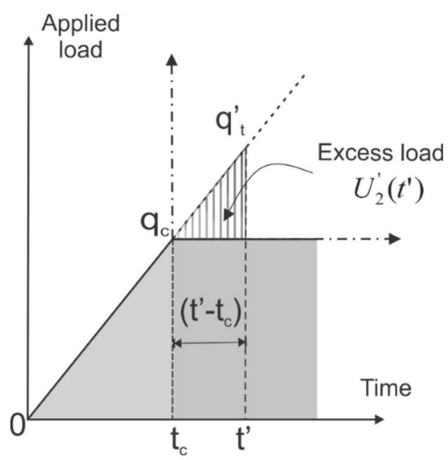

Figure 3. Calculation scheme for $t > t_c$.

$$U'(t') = \frac{1}{t_c}\left[\int_0^{t'} U(t)\,dt - \int_0^{t'-t_c} U(t)\,dt\right] = \frac{1}{t_c}\int_{t'-t_c}^{t'} U(t)\,dt \tag{14}$$

Finally, the average degree of consolidation at any time after the end of construction is expressed by:

$$U'(T \geq T_c) = 1 - \frac{1}{T_c}\sum_{m=0}^{\infty}\frac{2}{M^4}\left[e^{-M^2(T-T_c)} - e^{-M^2 T}\right] \tag{15}$$

This equation is analogous to Olson's (1977) solution (Equation 5) for $t \geq t_c$.

3. A new simple approach to predict the average degree of consolidation

Alternatively, a new simple procedure is proposed to calculate the average degree of consolidation. Its goal is to be as simple and accurate as possible.

3.1 During construction

An approximate solution for the definite integral in Equation 7 can be obtained by numerical integration methods, such as Simpson's rule (Davis and Rabinowitz, 1984). Given three points, Simpson's rule approximates the integrand into a quadratic function.

Applying Simpson's rule on Equation 7, the approximated average degree of consolidation can be expressed by the function values at the lower limit, midpoint, and upper limit:

$$\int_{t_a}^{t_b} U(t)\,dt \approx \frac{T_b - T_a}{6}\left[U(T_a) + 4U\left(\frac{T_b + T_a}{2}\right) + U(T_b)\right] \tag{16}$$

The loading process initiates at $t_a = 0$. Thus, at any Time Factor (T) during construction, the approximate value of the average degree of consolidation is given by:

$$U'(T \leq T_c) = \frac{1}{T_c}\int_0^T U(T)\,dT \approx \frac{T}{T_c}\left[\frac{U(0) + 4U\left(\frac{T}{2}\right) + U(T)}{6}\right] \tag{17}$$

It is worth noting that Equation 17 incorporates an error that increases with the decrease in the rate of loading. If T_c tends to infinity, the average degree of consolidation at the end of construction should be 100%, since consolidation and loading would occur simultaneously. However, Equation 17 gives $U'(T_c)$ = 5/6(83.3%) , since $U(0) = 0$.

To overcome this inherent error, a slight adjustment on the first term in Equation 16 is recommended, as shown in Equation 18. This correction improves the accuracy of Equation 17 and it has no significant influence on predicting the average degree of consolidation for any speed of construction.

$$U'(T \leq T_c) \approx \frac{T}{T_c}\left[\frac{U\left(\frac{T}{24}\right) + 4U\left(\frac{T}{2}\right) + U(T)}{6}\right] \tag{18}$$

It is worth noting that Equation 18 is close to Terzaghi's (1943) graphical method for $T \leq T_c$ (Equation 4), but it provides average degrees of consolidation that are always lower. As shown in Figure 4, the higher the value of T_c, the higher the difference between Terzaghi's (1943) curve and both Olson's (1977) and the method herein proposed.

The error of the approximate propositions relative to Olson's (1977) theoretical solution can be expressed by:

$$Relative\,error = \frac{\text{Ä}U'}{U'_{theoretical}} = \frac{U'_{approximate} - U'_{theoretical}}{U'_{theoretical}} \tag{19}$$

Figure 5 compares the relative error of the two approximate methods. The relative error of Terzaghi's (1943) method reaches magnitudes that cannot be neglected, exceeding 10% for Time Factors T_c higher than 1.0. The proposed approach is less sensitive to the construction duration, with an acceptable error close to 1%.

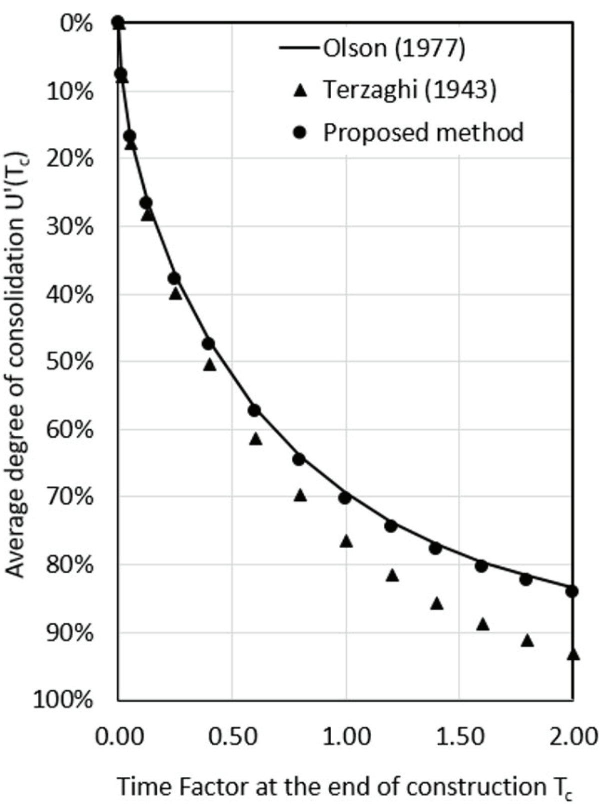

Figure 4. Influence of the construction period on the average degree of consolidation prediction at the end of construction $U'(T_c)$ for ramp loads.

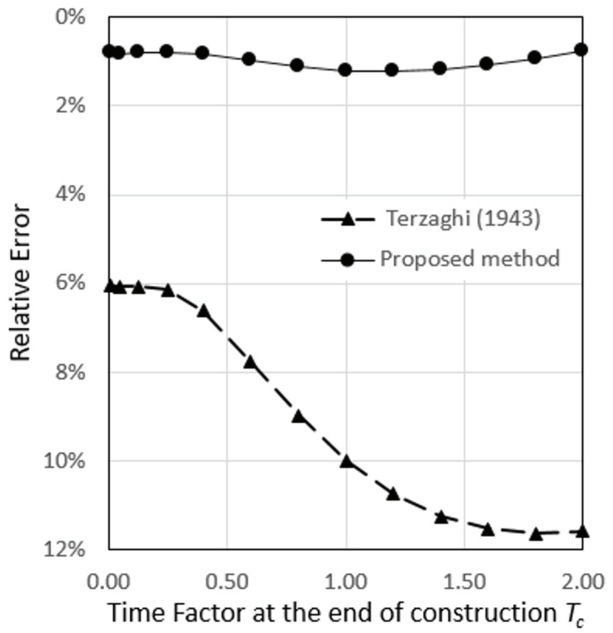

Figure 5. Relative error of the approximate propositions for ramp load.

3.2. After the end of construction

Since the load no longer varies, a procedure similar to Terzaghi's (1943) can be used. The consolidation is approximated considering that the load was instantaneously applied at a Time Factor $T \leq T_c$. Thus, the corrected average degree of consolidation can be estimated by determining which Time Fator $T^* \leq T_c$ would provide the same average degree of consolidation at the end of construction. In other words, according to Equation 18, $U(T^*)$ is given by:

$$U\left(T^*\right) = U'(T_c) = \left[\frac{U\left(\frac{T_c}{24}\right) + 4U\left(\frac{T_c}{2}\right) + U\left(T_c\right)}{6}\right] \tag{20}$$

This equivalent instantaneous loading was therefore applied at $T = T_c - T^*$. After the end of construction, the instantaneous loading settlement curve is always shifted by $T_c - T^*$. This procedure leads to:

$$U'(T > T_c) \approx U\left(T + T^* - T_c\right) \tag{21}$$

As expected, both Equation 18 and Equation 21 predict the same average degree of consolidation at the end of construction $T = T_c$.

The proposed method was applied to Hanna et al.'s (2013) example (embankment on a 4 m thick, single-drained clay deposit). After six months ($T = 0.0625$), one has:

$$U'(0.0625) = \frac{0.0625}{0.0938}\left[\frac{28.2\% + 4 \cdot 19.9\% + 5.8\%}{6}\right] = 12,6\%$$

After nine months, at the end of construction ($T_c = 0.0938$), one has:

$$U'(0.0938) = \frac{0.0938}{0.0938}\left[\frac{34,5\% + 4 \cdot 24.4\% + 7.1\%}{6}\right] = 23.2\%$$

And after two years ($T = 0.25$), one has:

$$U\left(T^*\right) = 23.2\% \rightarrow T^* = 0.0423$$

$$U'(0.25) = U\left(0.25 + 0.0423 - 0.0938\right) = 50.2\%$$

Olson's (1977) exact solution for $T_c = 0.0938$ gives $U'(0.0625) = 12.5\%$, $U'(0.0938) = 23.0\%$ and $U'(0.25) = 50.7\%$.

4. Predicting laboratory test results

The accuracy of the proposed method was also verified in its ability to predict the experimental oedometer test curves.

Sivakugan et al. (2014) carried out laboratory oedometer tests with ramp loading on an artificially mixed kaolinite/sand blend. The ramp loading was performed by filling a bucket, located on the loading arm, with sand scoops over varying periods.

Figure 6 shows the oedometer test data for a 2 hours loading test. The specimen was 18.241 mm thick, and the coefficient of consolidation was $c_v = 0.6$ m^2/year, determined by conventional oedometer tests on the same soil with instantaneous loading. Total stress increase was 215.1 kPa, and settlement at the end of loading was $\rho_c = 0.22$ mm. Experimental normalized settlement was defined as the ratio of vertical displacement ρ to final settlement ρ_c. Estimated normalized settlement, based on the estimations from the distinct propositions shown in previous sections, was calculated as the ratio of estimated average degree of consolidation U' to U'_c at the end of loading ($T_c = 1.6$). It worth noting that the average degree of consolidation U'_c is around 80% for both methods.

There is a reasonable agreement, despite the slight difference between the experimental and numerical results. Olson's (1977) theory and the proposed method only include primary consolidation. If the specimen develops secondary consolidation, the final settlement is higher than the primary compression value. As a result, the experimental normalized settlement becomes lower than the predicted ones. The maximum difference is 5.25%, at $T/T_c = 0.45$.

Mota (1996) performed laboratory tests with ramp loading on 2 cm thick specimens of very soft clay from Barra da Tijuca, Rio de Janeiro, Brazil. Soil characterization revealed natural water content ranging from 132% to 626%. Liquid and plastic limits range from 64% to 488% and 36% to 214%, respectively. The ramp loading test was performed

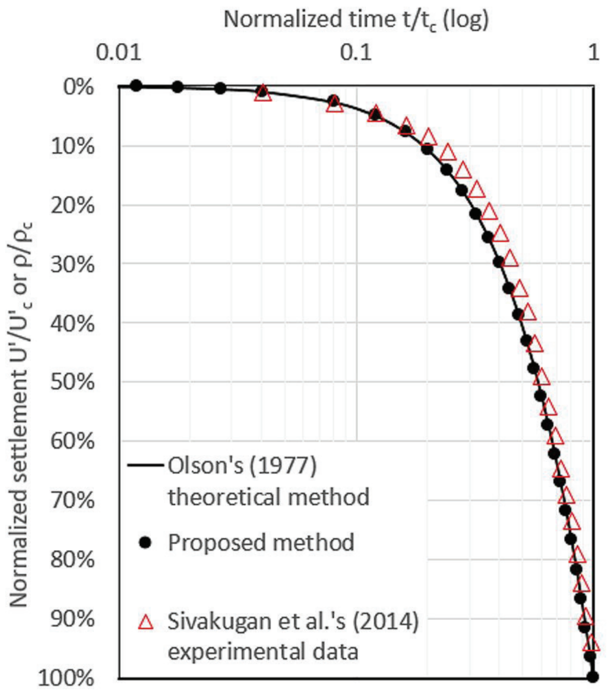

Figure 6. Predicted and measured normalized settlements versus normalized time.

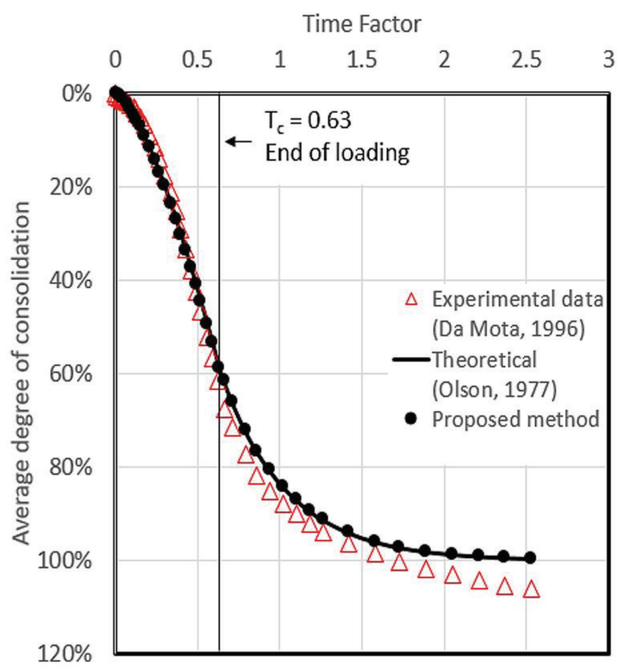

Figure 7. Predicted and measured average degree of consolidation versus Time Factor for ramp load.

by filling a bucket on the loading arm in steps of 1% of the total load at each 1% of the total period of loading.

The coefficient of consolidation was $c_v = 4.3 \cdot 10^{-5}$ cm^2/s. Both the coefficient of consolidation and the vertical displacement corresponding to the end of primary (U' = 100%) were determined via Taylor's method in a conventional oedometer test.

Figure 7 compares the experimental data with Olson's (1977) theoretical solution and the proposed method for a 2 hours loading test (T_c = 0.63) and a total stress increase of 100 kPa. The analytical and proposed methods agreed with the experimental results, although small deviations are observed after approximately 60% of primary consolidation. The differences are attributed mainly due to secondary consolidation. At a Time Factor of 2.5, the experimental curve reaches an average degree of consolidation of 106%.

5. Conclusions

This technical note revisited some approximate methods for predicting consolidation settlements due to ramp loading. Terzaghi's method (1943) has shown to be accurate only for small values of T_c values ($T_c < 0.2$). Hanna et al.'s (2013) approach provides exact results during construction, but it leads to significant errors after the end of construction.

Two procedures have been proposed herein to overcome these issues. The first one improved Hanna et al.'s (2013) approach by combining the applied load discretization with the concept of superposition effects. The correction solved the inaccuracies. The new set of equations was identical to Olson's (1977) solution for any construction time.

Finally, a new approximate method was developed. Simple and easy to apply, it revealed to be much more accurate than Terzaghi's (1943) method when compared to Olson's (1977) solution. Numerical examples have shown that the difference between the proposed method and Olson's (1977) theory is negligible for the whole time range.

The approximate method was also validated by very good reproductions of oedometer tests results in clayey soils subjected to ramp loading. The differences were mainly due to secondary consolidation.

Acknowledgements

The authors thank the Brazilian research agency CAPES and the Pontifical Catholic University of Rio de Janeiro (PUC-Rio) for their support.

Declaration of interest

The authors declare no conflict of interest.

Author's contributions

Raphael F. Carneiro: conceptualization, data curation, formal analysis, investigation, methodology, validation, writing – original draft. Denise M. S. Gerscovich: investigation, validation, visualization, writing – review & editing. Bernadete R. Danziger: validation, writing – review & editing.

References

Conte, E., & Troncone, A. (2006). One-dimensional consolidation under general time-dependent loading. *Canadian Geotechnical Journal*, 43, 1107-1116. http://dx.doi.org/10.1139/t06-064.

Davis, P.J., & Rabinowitz, P. (1984). *Methods of numerical integration* (2nd ed.). New York: Academic Press.

Gerscovich, D., Carneiro, R., & Danziger, B. (2018). Extension of Terzaghi's graphical method to predict settlement due to stepped load. *International Journal of Geomechanics*, 18(12), 06018033. http://dx.doi.org/10.1061/(ASCE)GM.1943-5622.0001266.

Hanna, D., Sivakugan, N., & Lovisa, J. (2013). Simple approach to consolidation due to constant rate loading in clays. *International Journal of Geomechanics*, 13(2), 193-196. http://dx.doi.org/10.1061/(ASCE)GM.1943-5622.0000195.

Liu, J., & Ma, Q. (2011). One-dimensional consolidation of soft ground with impeded boundaries under depth-dependent ramp load. In *Proceedings of First International Symposium on Pavement and Geotechnical Engineering for Transportation Infrastructure* (pp. 127-134), Nanchang, China. https://doi.org/10.1061/9780784412817.015.

Mota, J.L.C.P. (1996). *Study of one-dimensional consolidation under gradual application of load* [Master's thesis]. Federal University of Rio de Janeiro. (in Portuguese).

Olson, R. (1977). Consolidation under time dependence loading. *Journal of the Geotechnical Engineering Division*, 103(1), 55-60.

Schiffman, R.L. (1958). Consolidation of soil under time dependent loading and varying permeability. *Proceedings of the Highway Research Board*, 37, 584-615.

Schiffman, R.L., & Stein, J.R. (1970). One-dimensional consolidation of layered systems. *Journal of the Soil Mechanics and Foundations Division*, 96(4), 1499-1504. http://dx.doi.org/10.1061/JSFEAQ.0001453.

Sivakugan, N., Lovisa, J., Ameratunga, J., & Das, B.M. (2014). Consolidation settlement due to ramp loading. *International Journal of Geotechnical Engineering*, 8(2), 191-196. http://dx.doi.org/10.1179/1939787913Y.0000000017.

Terzaghi, K. (1943). *Theoretical soil mechanics*. New York: Wiley.

Terzaghi, T., & Fröhlich, A. (1936). *Theorie der Setzung von Tonschichten*. Leipzig-Wein: Franz Deutick. (in German).

Zhu, G., & Yin, J. (1998). Consolidation of soil under depth-dependent ramp load. *Canadian Geotechnical Journal*, 35, 344-350. http://dx.doi.org/10.1139/t97-092.

List of symbols

H_d	maximum length of drainage path;
M	count parameter;
T	Time factor;
T'	Time factor at time t';
T_c	Time factor at the end of construction;
T^*	a Time Factor such that $U(T^*) = U'(T_c)$;
U	average degree of consolidation (instantaneous loading);
U'	average degree of consolidation (non-instantaneous loading);
U'_c	average degree of consolidation at the end of loading;
c_v	coefficient of consolidation;
dt	time increment;
m_v	coefficient of volume change;
q_c	total load;
t	time;
t_a	lower integral limit;
t_b	upper integral limit;
t_c	time at the end of construction;
t'	any time after the end of construction;
$\overline{u_e}$	remaining excess pore pressure at the end of construction;
λ	rate of loading;
ρ	settlement;
ρ_c	settlement at the end of loading.

Soils and Rocks
An International Journal of Geotechnical and Geoenvironmental Engineering
www.soilsandrocks.com
ISSN 1980-9743
ISSN-e 2675-5475

Interpretation of bi-directional tests on piles with the evaluation of stress relief at the pile toe

Thais Lucouvicz Dada[1#], Faiçal Massad[2]

Technical Note

Keywords
Bi-directional test
Expansive cell
Equivalent top-down curve
Elastic shortening
Stress relief

Abstract
This paper presents the interpretation of bi-directional load tests performed on three auger piles, in the city of São Paulo, Brazil, using a method based on transfer functions for the shaft and toe. Elastic shortenings of the shaft were directly measured through a displacement indicator at the pile top and two telltales at the upper and bottom plates of the expansive cell. The equivalent top-down load-settlement curves were estimated and compared with two other methods from the literature, one which considers the pile infinitely rigid; and the other, which takes the pile elastic shortening into account. The curves resulted in good agreement considering the pile compressibility. Yet for the infinitely rigid pile, the settlements resulted in up to 75% smaller. Furthermore, the influence of stress relief on the toe behavior due to shaft lifting was investigated. For the cases studied, involving bored and auger piles with the slenderness ratio (L_s/r) greater than 20, the percentage of this effect was generally small, up to 5% of the toe load, being negligible for practical uses.

1. Introduction

To perform the pile bi-directional load test, one or more expansive cells (or O-cells) are usually installed near the pile toe. They are hydraulically expanded, pushing the shaft upward and the toe downward. Load-displacement curves are obtained for the pile shaft and toe separately.

The resulting force in the shaft corresponds to the load applied by the expansive cell minus the buoyant weight of the pile shaft (Fellenius, 2021). At the pile segment below the cell, taken as a “fictitious” toe, acts the force applied by the cell plus the pore pressure at the cell level.

This paper presents a modification of the method described in Dada & Massad (2018b), based on the model of Coyle & Reese (1966), which can be used to estimate the equivalent top-down load-settlement curve, simulating a conventional static load test.

A practical application of the method is made on continuous flight auger (CFA) piles installed in São Paulo City, Brazil. Displacement measurements were made at the pile top, by a displacement indicator, and at the upper and bottom cell plates, by means of displacement gauges and two telltales.

In addition, the possible influence of the stress relief on the toe behavior, due to the shaft lifting, was evaluated.

2. Methods of interpretation

To obtain the equivalent top-down load-settlement curve, a modified version of the method based on the model of Coyle & Reese (1966) will be used. Two other methods will also be applied for comparisons, namely: a) the Elísio-Osterberg’s method (Silva, 1986; Osterberg, 1998), which considers the pile infinitely rigid; and b) the method of Massad (2015), which contemplates pile elastic shortening.

Coyle & Reese (1966) developed a model to predict the load-settlement curve of a pile axially loaded at the top, based on known load transfer functions for the shaft and the toe. The pile is divided into n elements and the soil is replaced by independent springs that interact with the pile in the centers of each element.

For the bi-directional test, a hyperbolic (Chin, 1970) or an elastoplastic (Cambefort, 1964) relation is fitted to the load-displacement curve, measured at the bottom cell plate, and is used as the load transfer function of the “fictitious toe”. Figure 1 illustrates the use of a hyperbolic relation.

[#]Corresponding author. E-mail address: thaisldada@gmail.com
[1]LPC Latina Ltda., Projetos – Geotecnia, São Paulo, SP, Brasil.
[2]Universidade de São Paulo, Escola Politécnica, PEF – Engenharia de Estruturas e Geotécnica, São Paulo, SP, Brasil.

Submitted on January 7, 2021; Final Acceptance on May 19, 2021; Discussion open until August 31, 2021.

https://doi.org/10.28927/SR.2021.062021

For the shaft, first, a hyperbola is fitted to the test curve measured at the pile top, as shown in Figure 1. Then, the hyperbola is translated to the center of compression, i.e., to the level at which half of the total shaft elastic shortening occurs. The soil surrounding the shaft pile is assumed to consist of an equivalent layer of homogeneous soil; the subsoil heterogeneity is incorporated by means of the coefficient *c* of Leonards & Lovell (1979).

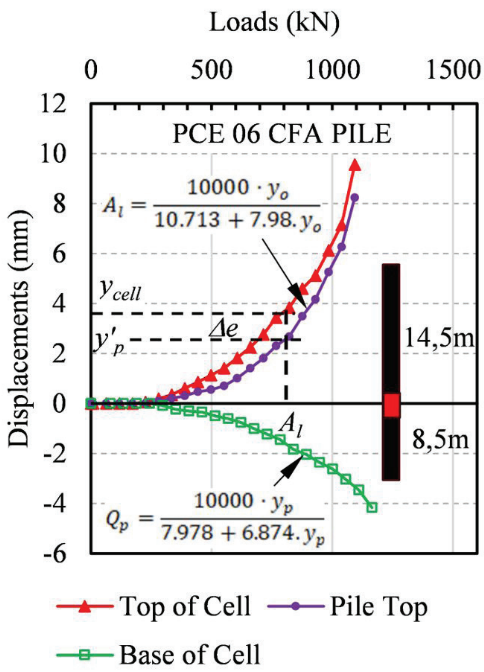

Figure 1. Example of bi-directional test results (see the list of symbols).

In effect, to obtain the translated hyperbola simulating a pile loaded on top, the upward movement measured at the pile top, y'_p, should be increased by half of the elastic shortening for top-down loads, as given in Equation 1.

$$y_f = y'_p + \frac{1}{2}\left(\frac{cA_l}{K_r} + \frac{Q'_p}{K_r}\right) \tag{1}$$

where y_f is the shaft displacement at the center of compression. A_l and Q'_p are respectively the shaft and the toe load for the same displacement y'_p, as shown in Figure 1. For K_r and c, see the list of symbols.

The translated hyperbola $A_l = f(y_f)$ can be used as the load transfer function of the shaft. It corresponds to the modification of the method originally proposed by Dada & Massad (2018b).

Finally, the equivalent top-down load-settlement curve can be obtained using the model of Coyle & Reese (1966), with the load transfer functions described above.

3. Case studies

Six continuous flight auger (CFA) piles, installed in São Paulo, Brazil, were submitted to bi-directional tests. Table 1 presents the general data and some parameters related to the shaft. The typical subsoil profile is shown in Figure 2.

The bi-directional test results for the CFA Pile PCE06 are presented in Figure 1 as an illustration. Note that the displacements were measured at three levels. The difference between the measurements at the cell top and the pile top gives the shaft elastic shortening Δe, which varies with A_l.

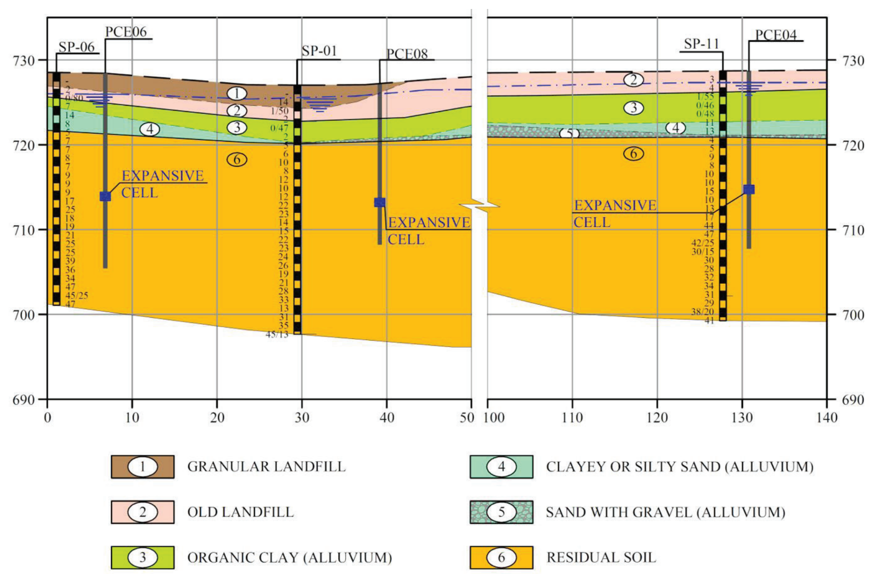

Figure 2. CFA piles: subsoil profile inferred from SPT tests near piles PCE04, PCE06 and PCE08. A similar profile was observed for the entire workplace.

Table 1. Bi-directional tests on 6 CFA piles - general data (adapted from Dada et al., 2019; Dada, 2019).

Pile	D	L_s	L_{toe}	Pile shaft parameters		
	(m)	(m)	(m)	K_r (kN/mm)	c_{eq}	$c'_{eq}=1-c_{eq}$
PCE03	0.5	14	7	393	0.74	0.26
PCE04	0.5	14	7	393	0.7	0.3
PCE05	0.5	14.7	7.3	374	0.74	0.26
PCE06	0.5	14.5	8.5	379	0.53	0.47
PCE07	0.5	16	7	344	0.72	0.28
PCE08	0.4	14	5	251	0.72	0.28

See list of symbols.

For each pile, Massad's (2015) coefficients c' were estimated with Equation 2.

$$\Delta e = \frac{c' A_l}{K_r} \tag{2}$$

The average values (c'_{eq}) are indicated in Table 1.

To simulate the download conventional test by the Method of Massad (2015), $y_{'p}$ related to A_l is settled equals to the toe movement y'_p, associated with Q'_p, as indicated in Figure 1 for CFA Pile PCE06. A pair y_o - P_o of the equivalent curve is determined by Equations 3 and 4.

$$y_o = y'_p + \Delta e \frac{c}{c'} + \frac{Q'_p}{K_r} \tag{3}$$

$$P_o = A_l + Q'_p \tag{4}$$

As far as the method based on Coyle & Reese's model is concerned, the application of Equation 1 to the results given in Figure 1 leads to the translated hyperbola of Equation 5, which was used as the load transfer function of the shaft for CFA Pile PCE06. For its toe, the hyperbolic transfer function is shown in Figure 1.

$$A_l = \frac{10000 y_f}{23.348 + 6.995 y_f} \tag{5}$$

The equivalent top-down curves, given by these two methods, are shown in Figure 3 for three CFA Piles of Table 1, revealing good convergence when compared to each other.

The application of the Elísio-Osterberg method (Silva, 1986; Osterberg, 1998), which assumes the pile as infinitely rigid, resulted in settlements up to 75% smaller, as shown in Figure 3 for the PCE06.

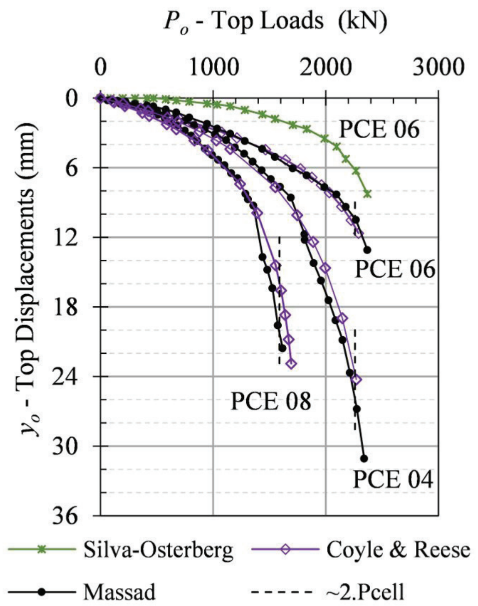

Figure 3. Equivalent top-down curves - CFA piles: PCE04, PCE06 and PCE08.

4. Evaluation of stress relief

Next, the influence of stress relief on the toe behavior due to shaft lifting during the bi-directional test (up-top loads) was evaluated.

4.1 Loading at the pile top (top-down loads)

For loads applied at the pile top, Martins (1945) and Geddes (1966) developed elastic solutions to obtain the load increase at the pile toe, due to shaft load ($\Delta Q_{p,f}$), by integrating Mindlin's (1936) influence factors. Vargas (1978) adopted Martins's (1945) solutions, which assumed uniform skin friction (f) and Poisson's ratio $\nu = 0.5$ for the soil. Poulos & Davis (1974) suggested the use of Geddes' (1966) solutions, which in turn considered a linear variation of f and $\nu = 0.3$.

Vargas (1978) proposed the following equation, rewritten for this paper:

$$\frac{\Delta Q_{p,f}}{Q_p} = K_{zz} \pi \alpha \left(\frac{1}{L_s/r} \right)^2 \tag{6}$$

where $\alpha = A_l/Q_p$; L_s is the pile shaft length; r is the pile radius and, therefore, L_s/r is the slenderness ratio.

The term K_{zz} is an influence factor at a depth $1.05 \cdot L_s$, proposed by Vargas (1978), and is equal to 4.73 or 6.70, according to Martins (1945) or Geddes (1966) solutions, respectively. Vargas concluded that the $\Delta Q_{p,f}$ is usually small and may be disregarded. Randolph & Wroth (1978) made a similar statement: the stress changes at the pile toe would be uncoupled from the shaft load, adding the condition $L_s/r \geq 20$, that is, slenderness ratio not less than 20.

4.2 Bi-directional tests (up-top loads)

Analogous analyses were made for the bi-directional tests performed on the CFA piles plus 3 others, as indicated in

Table 2, together with some parameters (see list of symbols). Note that the shaft loads take a negative signal in the elastic analysis since they are upward loads.

The load relief ratios were estimated using Equation 6. Figure 4 presents the results for Martins (1945) solutions, highlighting the ratio L_s/r = 20 and α = 1. The concept of "fictitious toe" was considered in the analysis.

From Figure 4, when L_s/r = 20, the ratio $\Delta Q_{p,f}$ / Q_p assumes a value of 3.7%. For Geddes's (1966) solution, this ratio is 5.2% (Dada, 2019). About 75% of the studied piles had $L_s/r \geq 40$; hence, in these cases, the load relief percentages resulted in a maximum of 1%.

Table 2. Case studies - L_s/r ratio, maximum loads reached in bi-directional tests and α parameter (adapted from Dada, 2019).

Pile type	L_s/r	$A_{l,max}$ (1) (kN)	$Q_{p,max}$ (1) (kN)	α (3)	Data source
Root (E-B3)	44	-1218	1264	-1	Dada & Massad (2018a)
Omega (PC-02)	24	-931 (2)	931 (2)	-1	Fellenius (2014)
Omega (PC-07)	21	-761 (2)	761 (2)	-1	
CFA (PCE03)	56	-1095	1163	-0.9	Dada et al., (2019)
CFA (PCE04)	56	-1095	1164	-0.9	
CFA (PCE05)	59	-1187	1260	-0.9	
CFA (PCE06)	58	-1093	1165	-0.9	
CFA (PCE07)	64	-1087	1165	-0.9	
CFA (PCE08)	70	-772	816	-0.9	

(1) Sign convention: upward load negative; downward load positive; (2) Data as presented by Fellenius (2014); (3) α ≅ 1, because the expansive cell applies almost the same load to shaft and toe, due to the above-mentioned corrections. $A_{l,max}$ and $Q_{p,max}$ are compression loads.

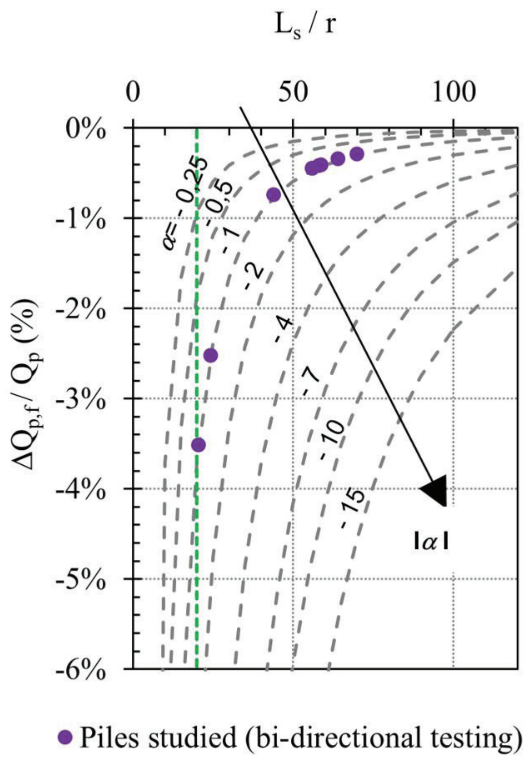

Figure 4. Load relief ratio ($\Delta Q_{p,f}$ /Q_p), estimated with Martins's (1945) solution. The studied piles, subjected to bi-directional tests, are indicated with circles.

5. Conclusions

The method for the interpretation of bi-directional test results presented herein, based on the model of Coyle & Reese (1966), lead to equivalent top-down curves with good agreement with the method of Massad (2015), which considers pile elastic shortening. The application of the Elísio-Osterberg Method (Silva, 1986; Osterberg, 1998), which assumes the pile as infinitely rigid, resulted in settlements up to 75% smaller, as was the case of CFA Pile PCE06.

Finally, load reliefs at the pile toe, due to shaft lifting, were estimated for the CFA piles plus 3 others from the literature. The load relief ratios ($\Delta Q_{p,f}$ /Q_p) resulted in less than 1% for 75% of the piles, and up to 5% for all of them. These values are not significant for practical purposes and could be neglected.

Acknowledgements

The authors acknowledge the EPUSP (Escola Politécnica da Universidade de São Paulo), and CAPES (Coordenação de Aperfeiçoamento de Pessoal de Nível Superior) for the support given to the research, and engineers Werner Bilfinger, Fernando Perez and Alysson Resende, for providing the data.

Declaration of interest

The authors declare that there are no known conflicts of interest associated with this publication.

Authors' contributions

Thais Lucouvicz Dada: conceptualization, data curation, methodology, writing – original draft, writing – review and editing. Faiçal Massad: conceptualization, data curation, methodology, supervision, validation, writing – review and editing.

List of symbols

A_l	Total lateral (shaft) load.
$A_{l,max}$	Maximum lateral (shaft) load reached in the bi-directional test.
c	Leonards & Lovell (1979) coefficient.
c_{eq}	Value of c related to the average of elastic shortening measurements.
c'	Correlate of c for bi-directional tests (Massad, 2015).
c'_{eq}	Value of c' related to the average of elastic shortening measurements.

D Pile diameter.
F Unit skin friction.
K_r Pile stiffness, as a structural piece.
K_{zz} Influence factor of the shaft load at the pile toe.
L_s Pile shaft length embedded in soil up to the toe (real or "fictitious") level.
L_{toe} Length of pile "fictitious toe".
n Number of pile subdivision elements for iterative calculation.
P_{cell} Load applied by the expansive cell.
P_o Axial load at the pile head.
Q_p Total toe load (real toe or "fictitious" toe).
Q'_p Total toe load of the bi-directional test ("fictitious toe"), related to y'_p.
$Q_{p,max}$ Maximum toe load reached in the bi-directional test ("fictitious toe").
r Pile radius.
y_o Displacement of the pile at the head (pile top).
y_f Displacement at the center of compression of the pile shaft.
y_{cell} Upward displacement at the expansive cell upper plate.
y'_p Upward displacement of the pile head (bi-directional test) = downward displacement of the pile toe (downward test).
α Ratio of A_l to Q_p.
Δe Pile elastic shortening.
$\Delta Q_{p,f}$ Load increase or decrease at the pile toe (real toe or "fictitious toe").
ν Poisson's ratio of subsoil.

References

Cambefort, H. (1964). *Essai sur le Comportement en Terrain Homogène des Pieux Isolés et des Groupes de Pieux*. Paris: Éditions Eyrolles. (in French).

Chin, F.K. (1970). Estimation of the ultimate load of piles not carried to failure. In *Proceedings of the 2nd Southeast Asian Conference on Soil Engineering* (pp. 81-90), Singapore. Singapore: Southeast Asian Society of Soil Engineering/ AIT/ IES/ University of Singapore.

Coyle, H.M., & Reese, L.C. (1966). Load transfer for axially loaded piles in clay. *Journal of the Soil Mechanics and Foundations Division*, 92(2), 1-26. http://dx.doi.org/10.1061/JSFEAQ.0000850.

Dada, T.L. (2019). *Bi-directional load testing on bored cast-in-situ piles: technical procedures and methods of interpretation, including case studies* [Master's thesis, University of São Paulo]. University of São Paulo's repository (in Portuguese). https://doi.org/10.11606/D.3.2019.tde-21102019-153221.

Dada, T.L., & Massad, F. (2018a). Ensaio bidirecional: características, interpretação e estudos de casos de estacas moldadas in loco no Brasil. *Geotecnia*, 143, 29-54. http://dx.doi.org/10.24849/j.geot.2018.143.03.

Dada, T.L., & Massad, F. (2018b). Proposta de novo método para obtenção da curva equivalente do ensaio bidirecional em estacas escavadas. In *Proceedings of the 19th Brazilian Conference on Soil Mechanics and Geotechnical Engineering* (pp. 1-10), Salvador. São Paulo: ABMS. (in Portuguese).

Dada, T.L., Resende, A.S., & Massad, F. (2019). Análise de ensaios bidirecionais com medida de encurtamento elástico em estacas hélice contínua. In *Proceedings of the 9th Seminar on Special Foundations Engineering and Geotechnics* (pp. 1-10), São Paulo. São Paulo: ABEF. (in Portuguese).

Fellenius, B.H. (2014). Analysis of results from routine static loading tests with emphasis on the bidirectional test. In *Proceedings of the 17th Brazilian Conference on Soil Mechanics and Geotechnical Engineering* (pp. 1-22), Goiânia. São Paulo: ABMS.

Fellenius, B.H. (January, 2021). *Basics of foundation design.* Retrieved in January 7, 2021, from www.fellenius.net/papers.html

Geddes, J.D. (1966). Stresses in foundation soils due to vertical subsurface loading. *Geotechnique*, 16(3), 231-255. http://dx.doi.org/10.1680/geot.1966.16.3.231.

Leonards, G.A., & Lovell, D. (1979). Interpretation of load tests on high-capacity driven piles. In R. Lundgren (Ed.), *Behavior of deep foundations* (pp. 388-415). West Conshohocken: ASTM International. https://doi.org/10.1520/STP33741S.

Martins, H.A. (1945). Stresses transmitted to the subsoil by the pile: integral of the Mindlin's formula for the hypothesis of constant friction along the pile. *Revista Politécnica*, 41, 365-372. (in Portuguese).

Massad, F. (2015). On the interpretation of the bidirectional static load test. *Soils and Rocks*, 38(3), 249-262.

Mindlin, R.D. (1936). Force at a Point in the Interior of a Semi-Infinite Solid. *Journal of Applied Physics*, 7(5), 195-202. http://dx.doi.org/10.1063/1.1745385.

Osterberg, J.O. (1998). The Osterberg load test method for bored and driven piles: the first ten years. In *Proceedings of the 7th International Conference & Exhibition on Piling and Deep Foundations* (pp. 1-17), Vienna. Rickmansworth: Westgrade Group.

Poulos, H.G., & Davis, E.H. (1974). *Elastic solutions for soil and rock mechanics*. New-York: John Wiley & Sons Inc.

Randolph, M.F., & Wroth, C.P. (1978). Analysis of deformation of vertically loaded piles. *Journal of the Geotechnical Engineering Division*, 104(12), 1465-1487.

Silva, P.E.C.A.F. (1986). Célula expansiva hidrodinâmica: uma nova maneira de executar provas de carga. In *Proceedings of the 8th Brazilian Conference on Soil Mechanics and Foundation Engineering* (Vol. 6, pp. 223-241), Porto Alegre. São Paulo: ABMS. (in Portuguese).

Vargas, M. (1978). Uma experiência brasileira em fundações por estacas: 1ª Parte - Teoria das estacas verticais carregadas axialmente. *Geotecnia*, 23, 3-33. (in Portuguese).

CASE STUDY

Soils and Rocks

An International Journal of Geotechnical and Geoenvironmental Engineering

www.soilsandrocks.com

ISSN 1980-9743
ISSN-e 2675-5475

Assessment of seismic vulnerability index of RAJUK area in Bangladesh using microtremor observations

Abdul L. Helaly[1], Mehedi A. Ansary[2#]

Case Study

Keywords
H/V peak amplitude
Frequency
H/V spectral ratio
Nakamura technique
Seismic vulnerability index

Abstract

Microtremor Horizontal to Vertical spectral ratio technique, also known as the Nakamura's method is growing in status for site response analysis. 500 locations in RAJUK area (1530 km^2) have been selected for microtremor observations. Microtremor data have been compiled and studied to estimate the predominant resonance frequency and *H/V* peak amplitude following the SESAME (2004) guideline. Finally, seismic vulnerability index of site soil using Nakamura's technique has been determined from predominant resonance frequency and *H/V* peak amplitude parameter. The calculated seismic vulnerability index for the studied 500 locations varies between 0.16 and 7.28. The low seismic vulnerability index (K_g) value means that the areas are relatively stiff and underlain by substantial deposit of sediments. The relatively higher K_g values are spread in the soft alluvial deposit areas. The areas with high K_g values are considered as fragile zones that may initiate significant damage to infrastructure situated in those areas during an earthquake.

1. Introduction

A large number of environmental studies have revealed that the majority of the Asian regions are exposed to seismic risks, which is mostly significant for South East Asia (Shah et al., 2018, 2019). Bangladesh has been damaged by great earthquakes in the past although it has not faced any significant great earthquakes in the recent years. In this region, most of the significant recent earthquakes have happened outside the important cities, and have damaged moderately less densely populated areas (Ansary & Rahman, 2013; Ansary & Arefin, 2020). Dhaka Metropolitan Development Plan (DMDP) area, which is mainly represented by RAJUK (Capital Development Authority) is the most populated city and the Capital of Bangladesh having a population of approximately 20 millions. Most of the policy makers and population do not recognize earthquake risk to be significant, although Bangladesh is situated in an area of major earthquake activity. It is a source of immense anxiety that significant damage to infrastructures may happen during a large earthquake occurring in this region.

Finn et al. (2004) has defined microzonation as the mapping of the earthquake hazards at local scales to integrate the effects of local geological environment. The term microzonation does not necessarily means a scale of mapping, while the prerequisite for defining local geological environment tends to state the more thorough scale maps (Roca et al., 2006). Building codes use the countrywide earthquake zonation maps in defining the minimum design requirements (DRM, 2004).

There are two sides of seismic safety: i) structural safety and ii) safety of a location based on the geotechnical conditions, such as site intensification, slope failures, and liquefaction. Effects of vibration have been taken care of in building codes all over the world to guarantee the safety of structures under seismic loading. Though, little attention in the form of land use guideline has been provided to the safety evaluation of individual sites (ISSMGE, 1999).

The purpose of the following review is to show the variety of methodologies applied for preparation of earthquake risk maps and the fundamental philosophies of zonation for ground motion with respect to diverse scales. Under this circumstance, necessary advancement is presented in the Manual for Zonation on Seismic Geotechnical Hazards, which is developed by the ISSMGE (1999). According to Mihalic et al. (2011), microzonation can be classified into three grades. Microtremor study together with simplified geotechnical studies have been placed in grade 2. Evaluation of ground motions is based on local seismicity, reduction of ground motion amount and local soil conditions. The local

#Corresponding author. E-mail address: ansary@ce.buet.ac.bd
[1]Rajdhani Unnayan Kartripakkha, Urban Resilience Project, Dhaka, Bangladesh.
[2]Bangladesh University of Engineering and Technology, Department of Civil Engineering, Dhaka, Bangladesh.

Submitted on September 6, 2020; Final Acceptance on April 16, 2021; Discussion open until August 31, 2021.
https://doi.org/10.28927/SR.2021.057420

soil condition is the most significant issue in defining surface ground motions. Therefore, evaluation of the soil conditions is based on the ranking of the zonation.

Among empirical methods for site response analysis, the popularity of HVSR (H/V spectral ratio method), also commonly known as the Nakamura's method (Parolai et al., 2001; Del Monaco et al., 2013) has been gradually increasing for the past three decades. The HVSR method is effective to estimate site response by removing source effects by dividing the horizontal component of ambient noise by the vertical component. This method has been applied by many researchers in many countries such as Mexico, Turkey, India, Pakistan, USA and Japan, to determine fundamental frequency, amplification and depth of basin (Qadri et al., 2015a, b, 2017, 2018; Rehman et al., 2016; Raymond, 2017; Singh et al., 2017).

The main aim of the paper is to determine the dynamic factors of alluvium including resonance frequency, resonance period, peak values of *H/V* ratio and seismic vulnerability index (*Kg*) at 500 locations of the RAJUK area using microtremor.

2. Geology of the RAJUK area

Dhaka is the capital, literary of Bangladesh; also it is the political and economic hub of the country. It is one of the most heavily populated cities in the South Asia. Microtremor observations have been carried out within the Dhaka city (around 250 km^2 area) by several researches (Ansary & Rahman, 2013; Ansary & Arefin, 2020; CDMP, 2009). In this research, the measurement sites will be selected within the entire Dhaka city and DMDP/RAJUK (Capital Development Authority) area (around 1530 km^2) (Figure 1). The use of microtremor investigation in this research is to estimate the seismic vulnerability index (K_g), by using the *HVSR* technique. The location of the 500 observation points is shown in Figure 2.

According to Reimann (1993), more than 80% of Bangladesh is underlain by Quaternary sediments consisting of deltaic and alluvial deposits of the Ganges, Brahmaputra and Meghna rivers and their tributaries. The sediments of Bangladesh geology have been classified into five major groups, which are Coastal deposits, Deltaic deposits, Paludal deposits, Alluvial deposits and Residual deposits. Dhaka is located between the Meghna and Brahmaputra Flood Plains. Forty four boreholes are drilled in the first stage of geotechnical field investigation along with the field microtremor investigation as shown in Figure 3 to get an overall idea of the soil profile of RAJUK/DMDP area. Figure 4 shows the lithology of the east – west cross-section between borehole numbers 20 to 185 and Figure 5 shows the lithology of the north – south cross-section between borehole numbers 400 to 62. The Madhupur Clay Residuum is the main soil deposit in the top (which is part of Pleistocene terrace deposit: very stiff soil shown by red color in Figures 4 and 5) and then Alluvial Sand, Silt and Clay and their various combinations. According to the CDMP (2009), the engineering bedrock of Dhaka city (Shear-wave velocity ≥ 400 m/s) is situated around 70 m below the existing ground level.

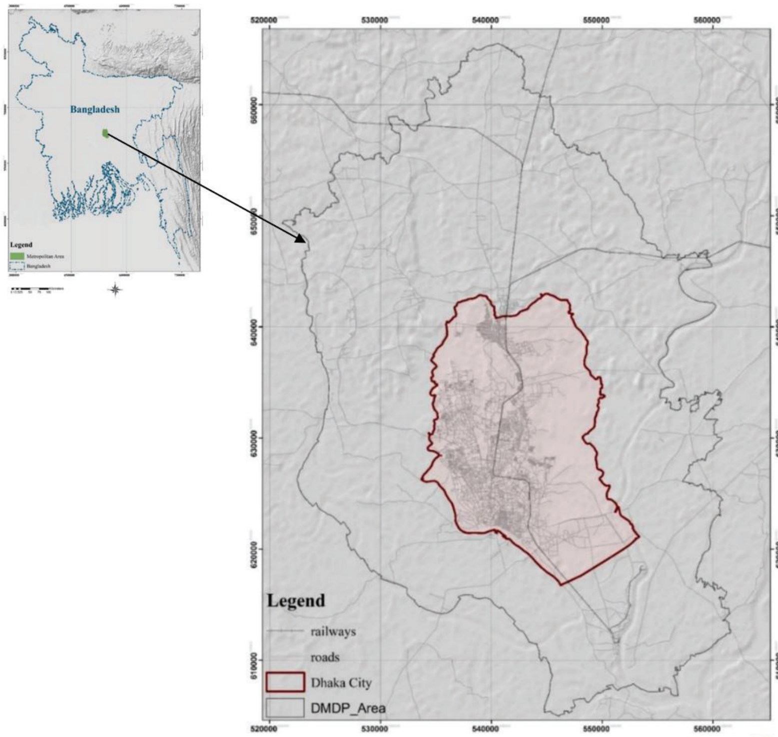

Figure 1. RAJUK/DMDP area with respect to the country Bangladesh.

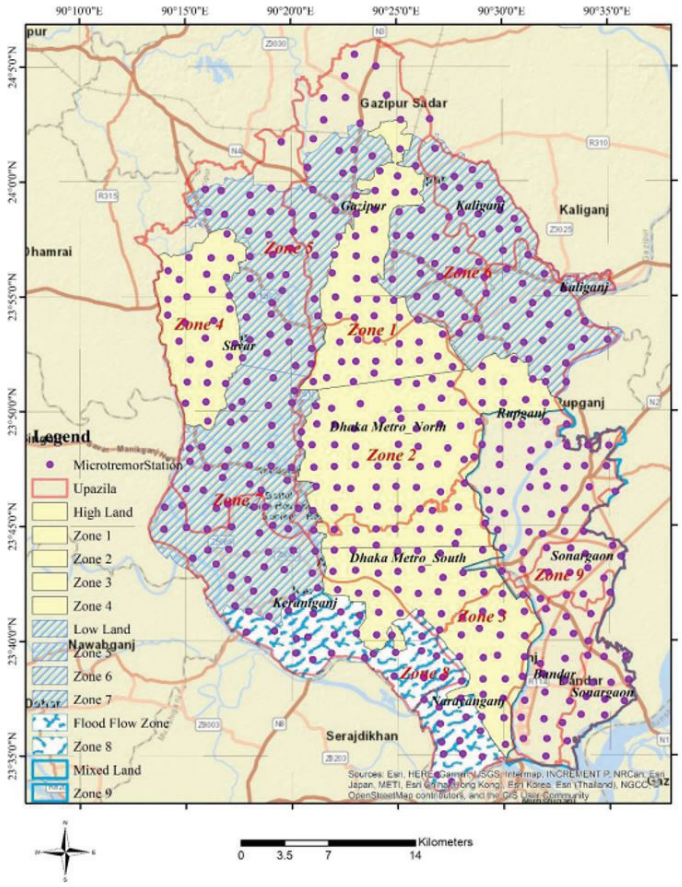

Figure 2. Location of the microtremor observation point within RAJUK area.

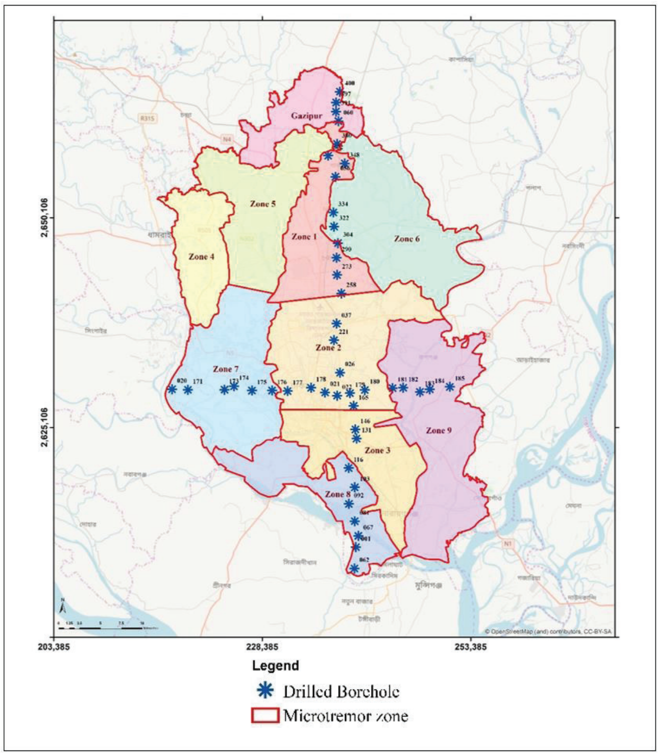

Figure 3. Location of 44 drilled boreholes for phase 1 of field investigation.

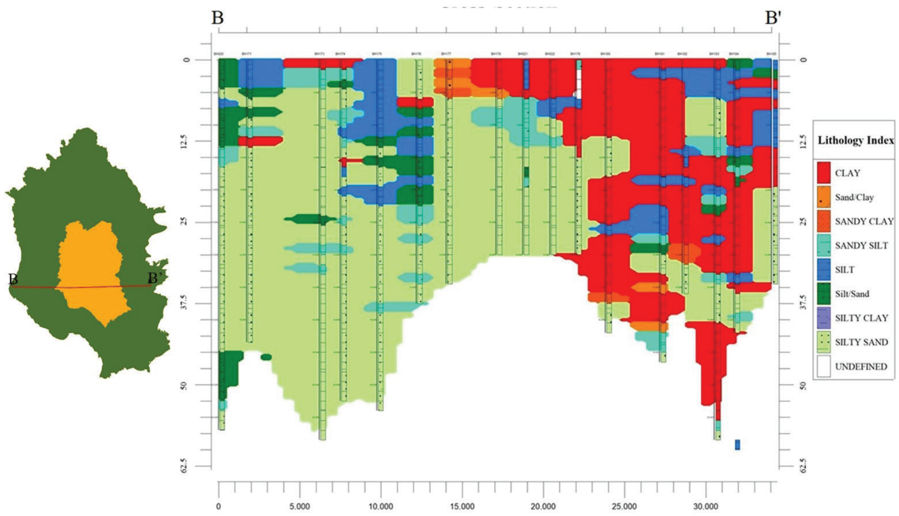

Figure 4. The lithology of the east-west cross-section between boreholes no. 20 to 185.

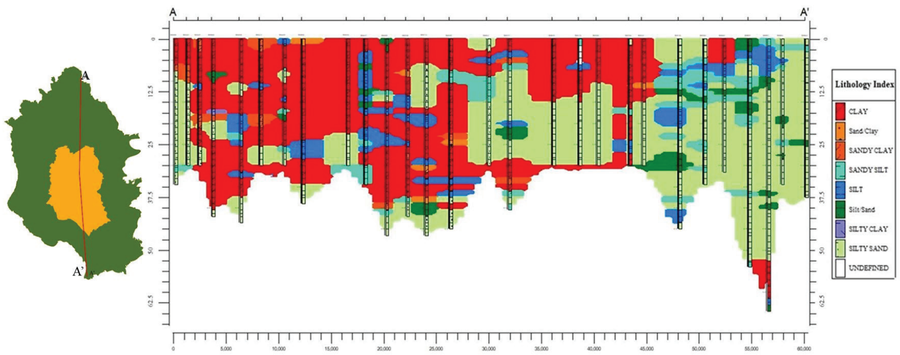

Figure 5. The lithology of the north-south cross-section between boreholes no. 400 to 062.

3. Microtremor survey method

The microtremors are generated by the movement of machinery in industries, vehicles, pedestrian, the flow of water in rivers, rain, wind, deviation of atmospheric pressure, and oceanic waves. The majority of the sources of microtremors generally originate from human activities.

Ambient noise has been put into use to glean information of the soil amplification since 1950s. Nogoshi & Igarashi (1970, 1971) are among the first to implement the horizontal to vertical spectral ratio (HVSR) to microtremor measurements, however the practice of this technique has faced many condemnation due to the uncertainty about microtremor sources. Many researchers (Ansary & Arefin, 2020; Qadri et al., 2015a, 2017; Raymond, 2017; Singh et al., 2017) have paid a renewed interest for estimating dynamic properties of soils and structures using microtremor, since lucid and dependable information can be obtained by very easy and less costly noise measurements.

Nakamura has developed the *H/V* technique for various geological site environments in Japan along with borehole investigations, as well as with the analysis of strong ground motion. It has been assumed that the vertical component of ambient noise that maintains the uniqueness of source to sediments of the ground surface is comparatively biased to Rayleigh wave on the sediments. Thus, the vertical component can be applied to eliminate the Rayleigh wave and the source effects from the horizontal components. On soft ground, vertical motion is smaller than the horizontal motion. On stiff ground, vertical and horizontal vibrations are comparable to each other both on the value and shape. Horizontal to vertical ratio has been estimated from each maximum value and has been judged against the softness of ground and the *H/V* peak amplitude. For this reason, the value of horizontal to vertical ratio greatly matches with these soil characteristics. The *H/V* spectral ratio shows the amplification characteristics by the multiple reflections of the *SH* wave at least around F_0, the predominant frequency of sedimentary layer, and shows the characteristics has been baffled by the Rayleigh wave around $2F_0$. Where the effect of the Rayleigh wave is smaller, it is possible to determine preliminary as well as the secondary peak of amplification due to multiple reflections with the *H/V* spectral ratio.

H/V technique has been regularly applied in seismic microzonation investigation due to its relatively small cost. The main feature of the *H/V* method is its stability: an identical result may be found if one replicates measurements for a week (Volant et al., 1998), after a month (Mucciarelli & Monachesi, 1998) or after a year (Bour et al., 1998). This method is most useful in determining the natural frequency of soft soil sites where there is a large contrast with the underlying bedrock. The technique is particularly suitable in locations of reasonable seismicity, due to the lack of considerable seismic recordings, in contrast to high seismic regions.

The main suggested application of the *H/V* method in microzonation studies is to delineate the fundamental period of the location and assist limit the geotechnical and geological models used for numerical estimations. *H/V* method, alone or collectively with other techniques, has been used for the seismic zonation of many cities.

The *H/V* technique has been established to be helpful to determine the fundamental period of soil deposits. However, measurements and the study should be executed with care. The endeavor of this study is to obtain the increase of ground motion over as broad a frequency range as possible, for the elastic (low-deformation) soil behavior as well as compute the natural frequency.

4. Data collection and analysis method

Within the RAJUK area, at 500 locations, microtremor observations have been done as shown in Figure 2. A standard square network with approximately 1.7 kilometers sides has been considered; one station has been placed within each square.

4.1 Data acquisition

Microtremor data have been gathered on three-component sensors of GS11D Geospace Technology. The system has an internal 12V rechargeable battery having the ability to record 5 hour continuously. Surveys have been carried out at 100 samples per second for about 20 minutes. Figure 6 shows a GS11D sensor with an internal 12V rechargeable lead battery connected to a laptop. All the data have been collected during night time.

Figure 6. Setup illustration of GS11D sensor with an internal 12V rechargeable lead battery connected to a laptop.

4.2 Analysis of the data and development of the *H/V* curve

All 500 microtremors have been recorded as three components velocity data. In order to obtain *H/V* ratio from the recorded microtremor data, Geopsy software has been used with a 21-s time window. In order to reduce the effects of the noises and obtaining the best possible results, a band pass filter between 0.05 to 6 Hz is implemented on the records. H/V ratios have been estimated eliminating the time windows infected with transients (after Qadri et al., 2015b, 2017) often associated to built-up sources or other noises. A conventional approach to detect the infected transients is based on a comparison between the short-term average (*STA*) and the long-term average (*LTA*). The *H/V* computation has been applied to only those windows with an STA/LTA ratio lying between 0.20 and 2.50. A Konno & Ohmachi (1998) filter and cosine taper with 5% width have been applied to every window to smooth the Fourier amplitude spectra along with a coefficient of 40 for bandwidth. The waveform of microtremor record in station 23 is shown in Figure 7.

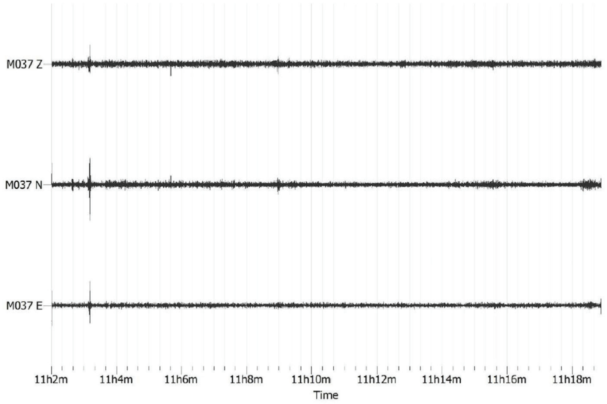

Figure 7. The microtremor component's waveform in the station 23.

This method estimates *H/V* ratio of the ambient noise which has been observed at a single point. *H/V* ratio is the proportion between the Fourier amplitude spectra of the horizontal (*H*) to vertical (*V*) components. For computing this ratio, the first step is to record the ambient signal using a three-component system; the next step is to pick the most stable time windows; then for each time windows, estimate the Fourier amplitude spectra by smoothing; then average the two-horizontal component (using a quadratic mean); in the next step for each window, *H/V* ratio is estimated; finally, the average *H/V* ratio is estimated. European Commission (2004) parameters and criteria have been used in order to obtain a reliable *H/V* curve.

The *H/V* method is applied to obtain the resonance frequency and the *H/V* peak amplitude. The curves derived from all the records are shown in Figure 8. To avoid the effect of probable environmental noises, time windows can be selected in Geopsy software. The *H/V* technique is applied on the selected windows. The selected windows and the graph after noise removal in station 23 are shown in Figure 9 and Figure 10 respectively. The assessed parameters including resonance frequency, *H/V* peak amplitude and vulnerability index in station 23 are presented in Table 1. Figure 11 shows *H/V* curves for six more stations.

4.3 Comparison of microtremor data with 1D response analysis using the program shake

From the existing borelogs, and PS-loggings, soil model at each site has been established for theoretical analysis. The transfer function of the shear wave (the surface motion versus the incidental motion at depth) has been calculated using the soil models. Figure 12 shows the four typical graphs for comparison of amplitude ratio between the transfer function of shear wave and microtremor *H/V* ratio. The 1D response analysis using the program SHAKE has helped to estimate the characteristics transfer function curve. Microtremor *H/V* ratio graph has been obtained from the Horizontal to Vertical spectral ratio (*H/V*) of Fourier spectra as discussed earlier.

These figures show that the amplitude values of the ratios and the predominant resonance frequency for the two cases slightly vary. The cause of this variation is that microtremor is composed of various types of waves, but the theoretical transfer function is based on shear-wave only.

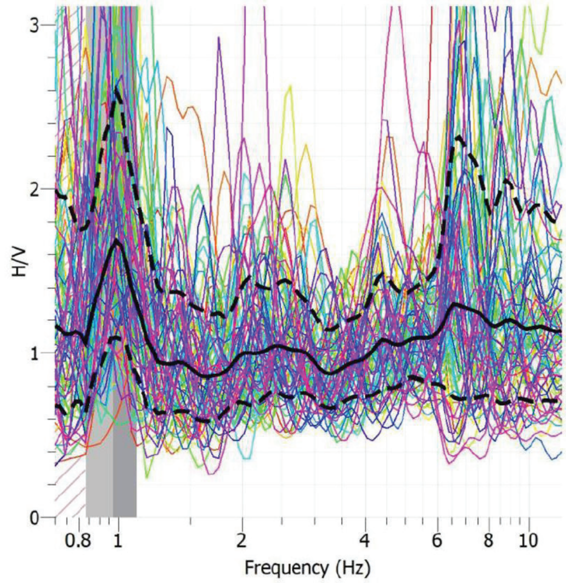

Figure 8. The plot of H/V curve for all records in the station 23.

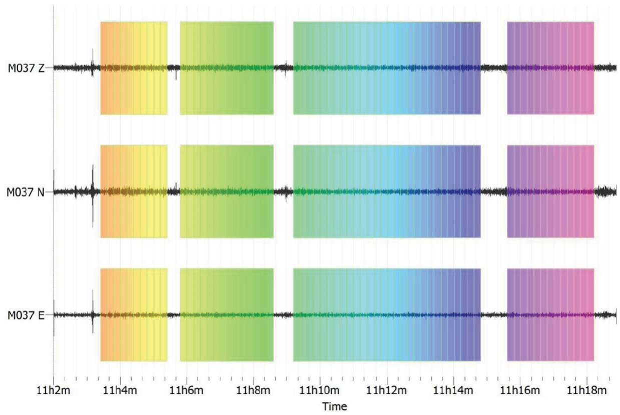

Figure 9. The selected windows from station 23 record.

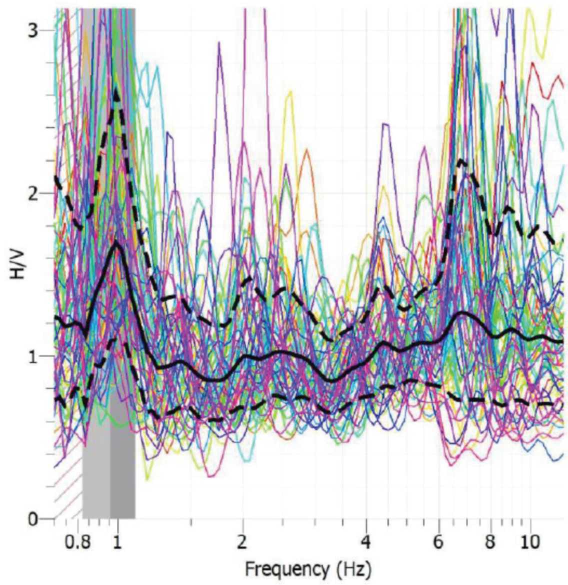

Figure 10. The plot of *H/V* curve after noise removal at the station 23.

5. Results and discussions

The microtremor investigations have been conducted at 500 locations within the RAJUK area. The location of every station has been determined by hand held GPS. Around twenty minutes of data acquisition has been done on average when the noise level has been low. The outputs of the study have been presented in the form of resonance frequency, *H/V* peak amplitude and seismic vulnerability index distribution within the RAJUK area.

5.1 The resonance frequency

The resonance frequency has been classified from less than 0.23 Hz to more than 6.6 Hz (0.23-7.67). The resonance frequency distribution within RAJUK area has been presented in Figure 13. Most areas of RAJUK show the resonance frequency of less than 1.2 Hz. It means that, the RAJUK is mostly covered by soft soil with a high resonance period. It should be noted that, to avoid the resonance phenomenon during a major earthquakes, the number of building floors should not be consonant with the resonance period of the soil.

Table 1. The results of *H/V* graph for station 23.

Station No.	Longitude	Latitude	Resonance Frequency f_0 (Hz)	*H/V* Peak Amplitude (A_0)	Resonance Period (s)	Vulnerability Index ($K_g = A_0^2/f_0$)	Remarks
23	90.4372	23.6236	0.96	1.64	1.04	2.80	low

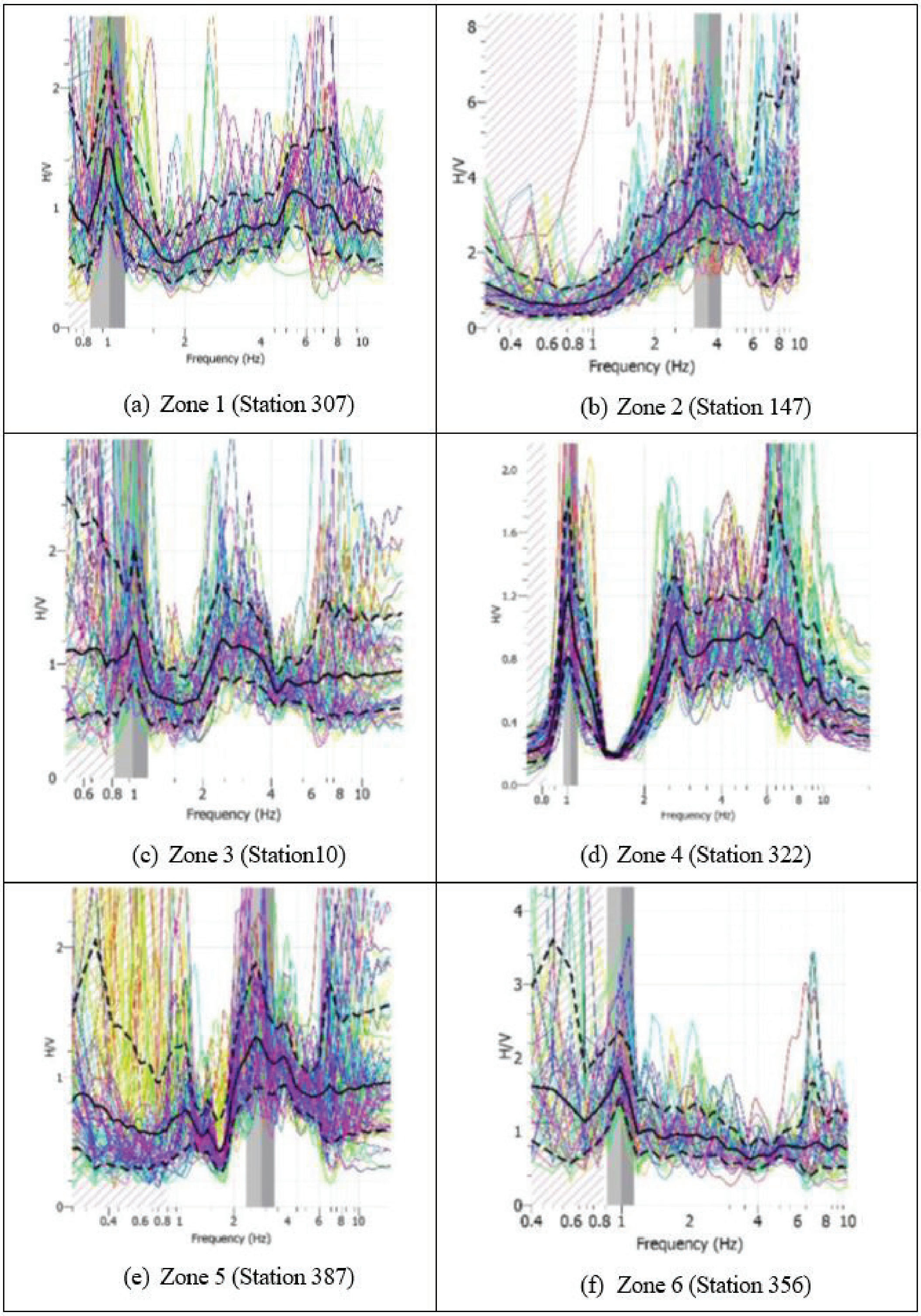

(a) Zone 1 (Station 307)
(b) Zone 2 (Station 147)
(c) Zone 3 (Station10)
(d) Zone 4 (Station 322)
(e) Zone 5 (Station 387)
(f) Zone 6 (Station 356)

Figure 11. The H/V graphs for several stations located in different zones of Dhaka city.

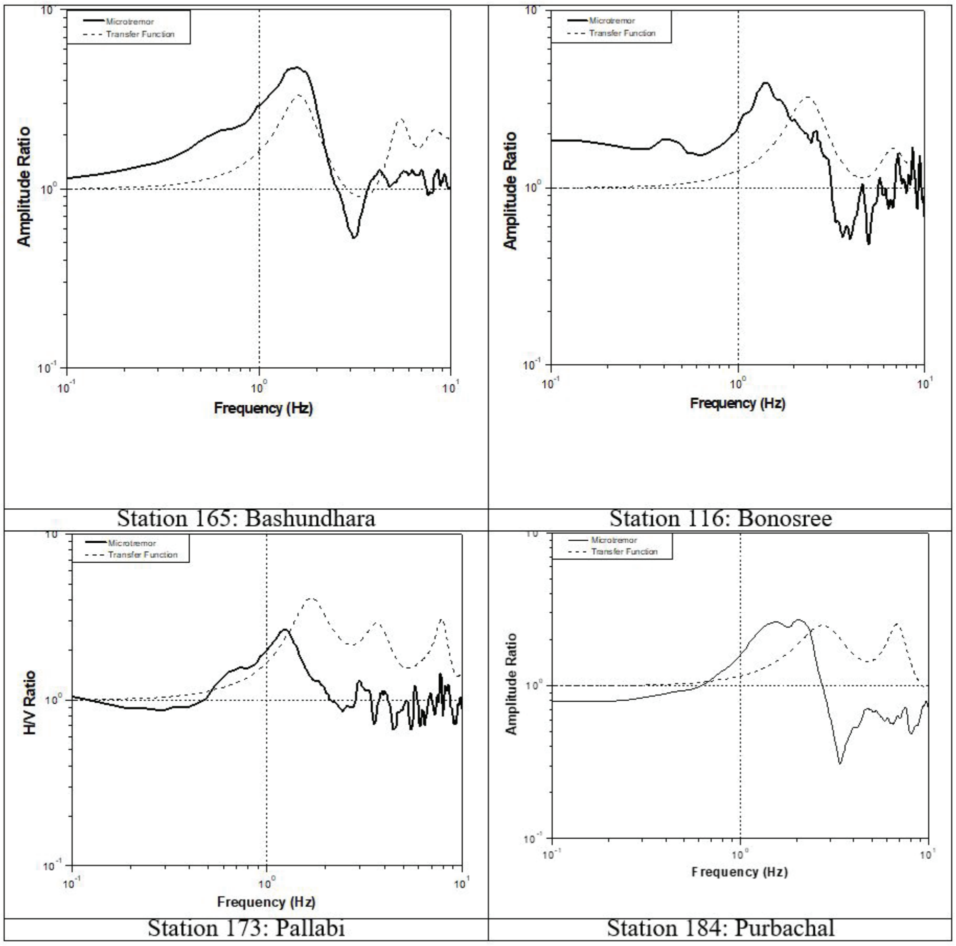

Figure 12. Comparison of *H/V* peak amplitude of microtremor and theoretical transfer function from numerical 1D response analysis for various locations in Dhaka city.

A minor part of RAJUK area shows high resonance frequencies. These anomalies are mostly observed in the middle part and some areas of the northern part of RAJUK area. The remarkable point of the distribution of high-frequency areas in RAJUK area is its compatibility with the local geology; these areas are underlain by Pleistocene terrace deposits (Ansary & Arefin, 2020) which are also represented by red Madhupur clay deposits in Figures 4 and 5. Therefore, the areas with high frequency probably consist of compact soils where the land subsidence rate is low (Higgins et al., 2014). The high frequency (low period) areas can be used for high-rise constructions considering the local geotechnical properties (such as lateral spreading, *H/V* peak amplitude, and liquefaction).

5.2 *H/V* peak amplitude

The *H/V* peak amplitude is classified from around 0.85 to more than 4 (0.85-6.54). Figure 14 shows the H/V peak amplitude variation within RAJUK area. Fortunately, most parts of RAJUK area show a *H/V* peak amplitude around 1. Consequently, the probability of soil amplification during an earthquake is not very high. Anyhow, there are areas with *H/V* peak amplitude of more than 1 which need special attention in designing the development plan. The most areas with a high *H/V* peak amplitude locate in the middle part of the city where, unfortunately, most of the constructions have been already placed.

5.3 Seismic vulnerability index

Seismic vulnerability index (*Kg*) is a parameter which shows the level of vulnerability of a soil layer to collapse. Therefore, this index is useful for identifying areas that are relatively weak during incidence of seismic events. Nakamura (2000) have demonstrated that a high-quality correspondence exists between seismic vulnerability index (*Kg*) and the distribution of damage due earthquakes. This index can be estimated by squaring from the peak value of *HVSR* curve and dividing it by the value of the predominant frequency. Four major classifications of the seismic vulnerability index have been recommended, these are Low (0–5), Moderate (6–10), High (11–20), and Very High (>20).

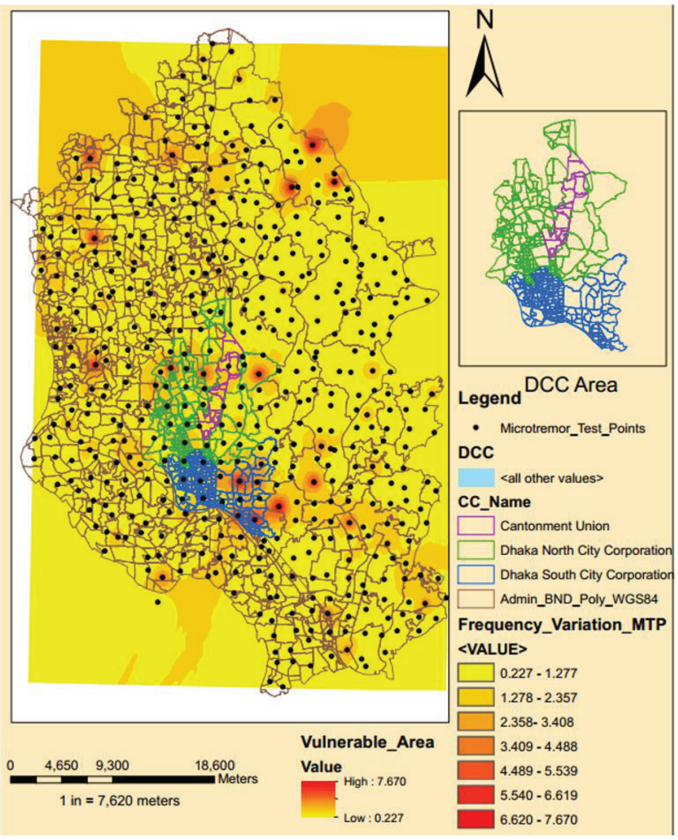

Figure 13. Resonance frequency variation in RAJUK area.

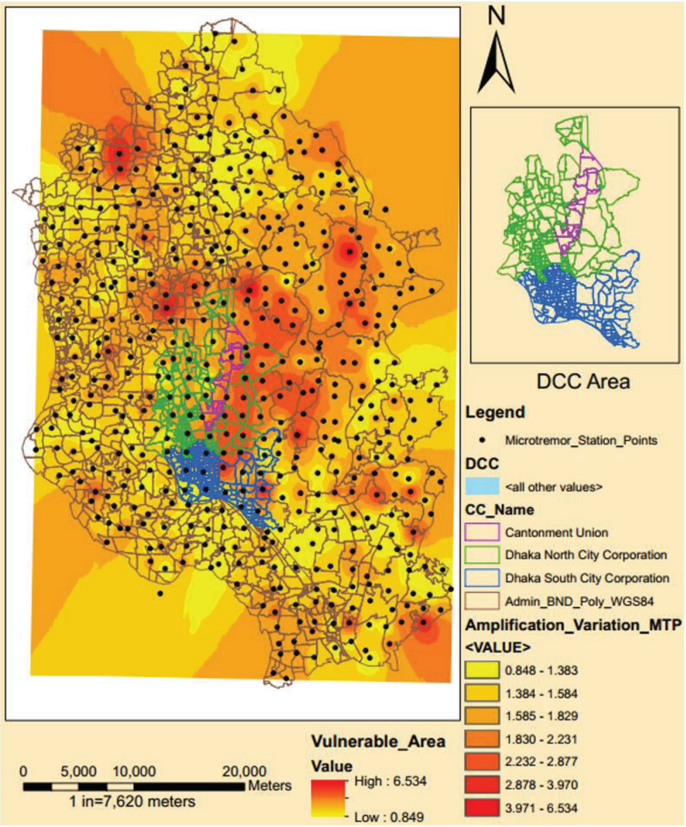

Figure 14. *H/V* peak amplitude variation in RAJUK area.

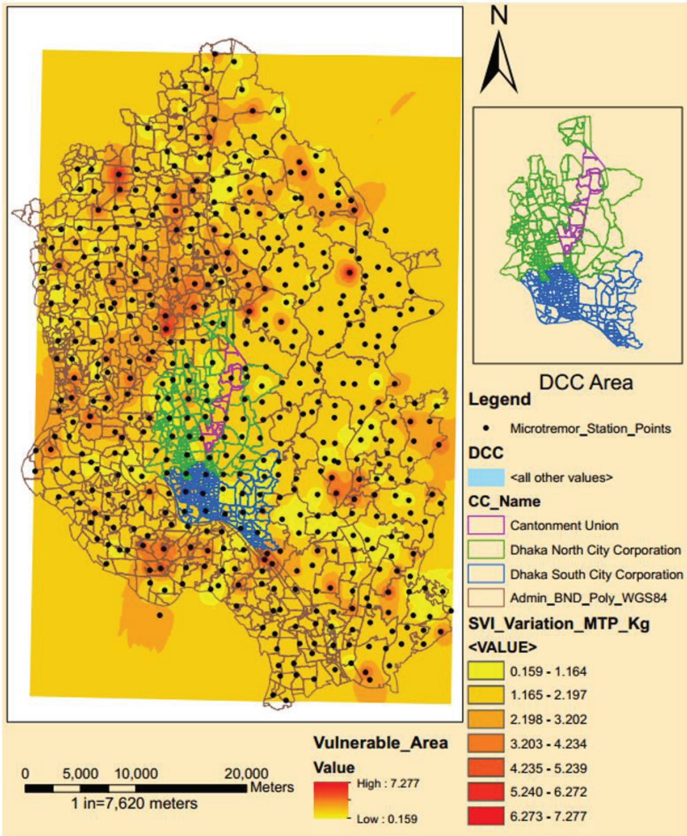

Figure 15. Seismic vulnerability index variation in RAJUK area.

The seismic vulnerability index is classified from around 0.16 to more than 6 (0.16-7.28). Figure 15 shows the seismic vulnerability index variation within RAJUK area. Fortunately, most parts of RAJUK area show low seismic vulnerability index. Consequently, the probability of soil amplification during an earthquake is not very high.

6. Conclusions

This is the first time 500 microtremor observations have been conducted within the RAJUK area. The locations are selected considering the flood plains, restricted areas, roads, and sensitive centers. The findings of this research have been presented with respect to resonance frequency, *H/V* peak amplitude and seismic vulnerability index distribution. The predominant frequencies within RAJUK area are comparatively homogeneous, ranging from 0.23 to 7.67 Hz. In most of the soft soil locations, the frequencies are low and in a few stiff soil locations, the frequencies are high. The *H/V* peak amplitude or peak of *H/V* spectral ratio in investigation sites vary from 0.85 to 6.54. For stiff soil sites, small spectral values are observed and for soft soil sites, high spectral values are observed. The seismic vulnerability index varies between 0.16 and 7.28. The small seismic vulnerability index signifies that the areas are relatively stiff as well as underlain by thick sediment deposit. The findings of microtremor observations can be applied as an input for a lot of investigations, for instance the site selection of geotechnical boreholes or designing the city development plans, etc.

Declaration of interest

On behalf of all the authors, the corresponding author states that there is no conflict of interest

Author's contributions

Abdul L. Helaly: conceptualization, data collection, methodology. Mehedi A. Ansary: Writing- reviewing and editing.

References

Ansary, M. A. & Rahman, M. S. (2013). Site amplification investigation in Dhaka, Bangladesh, using H/V ratio of microtremor. *Environmental Earth Sciences*, 70, 559–574. https://doi.org/10.1007/s12665-012-2141-x.

Ansary, M.A. & Arefin, M.R. (2020). Assessment of predominant frequencies in Dhaka city, Bangladesh using ambient vibration. *Asian Journal of Civil Engineering,* 21, 91–104. https://doi.org/10.1007/s42107-019-00194-2.

Bour, M., Fouissac, D., Dominique, P., & Martin, C. (1998). On the use of microtremor recordings in seismic microzonation. *Journal of Soil Dynamics and Earthquake Engineering*, 17, 465-474. https://doi.org/10.1016/S0267-7261(98)00014-1.

Comprehensive Disaster Management Program – CDMP. (2009). *Seismic hazard and vulnerability mapping of Dhaka, Chittagong, and Sylhet city corporation areas*. Bangladesh: CDMP.

Del Monaco, F., Tallini, M., De Rose, C. & Durante, F. (2013). HVNSR survey in historical downtown L'Aquila (central Italy): site resonance properties vs. subsoil model. *Engineering Geology,* 158, 34–47. https://doi.org/10.1016/j.enggeo.2013.03.008

European Commission. SESAME European Research Project. (2004). *Guidelines for the implementation of the h/v spectral ratio technique on ambient vibrations, measurements, processing and interpretation* (European Commission-Research General Directorate Project no. CT2000--00026 SESAME). Luxembourg.

Finn, L W. D., Onur, T. & Ventura, C. E. (2004). Microzonation: developments and applications. In A. Ansal (Ed.), *Recent advances in earthquake geotechnical engineering and microzonation* (pp. 3-26). Dordrecht: Kluwer Academic Publishers.

Higgins, S.A., Overeem, I., Steckler, M.S., Syvitski, J.P.M., Seeber, L., & Akhter, S.H. (2014). InSAR measurements of compaction and subsidence in the Ganges-Brahmaputra Delta, Bangladesh. *Journal of Geophysical Research & Earth Surface*, 119, 1768–1781. https://doi.org/10.1002/2014JF003117.

International Society for Soil Mechanics and Geotechnical Engineering – ISSMGE. (1999). *Manual for zonation on seismic geotechnical hazards* (209 p.). Tokyo: The Japanese Geotechnical Society.

Konno, K. & Ohmachi, T. (1998). Ground-motion characteristics estimated from spectral ratio between horizontal and vertical components of microtremor. *Bulletin of SeismolOgical Society of America*, 88, 228-241.

Mihalic, S., Ostric, M. & Krkac, M., (2011). Seismic microzonation: a review of principles and practice. *Geofizika*, 28, 5-20.

Mucciarelli M. & Monachesi G. (1998). A quick survey of local amplifications and their correlation with damage observed during the Umbro-Marchesan (Italy) earthquake of September 26, 1997. *Journal of Earthquake Engineering*, 2, 1-13.

Nakamura, Y. (2000). Clear identification of fundamental idea of Nakamura's Technique and its applications. In *Proceedings of the 12th World Conference on Earthquake Engineering* (pp. 2656-2664). Auckland, New Zealand.

Nogoshi, M. & Igarashi, T. (1970). On the propagation characteristics of microtremors. *Journal of the Seismological Society of Japan*, 23, 264-280. In Japanese with English abstract.

Nogoshi, M., & Igarashi, T. (1971). On the amplitude characteristics of microtremor (Part 2). *Journal of the Seismological Society of Japan*, 24: 26-40.

Parolai, S., Bormann, P. & Milkereit, C. (2001). Assessment of the resonance frequency of the sedimentary cover in the Cologne area (Germany) using noise measurements. *Journal of Earthquake Engineering*, 5(4), 541-556.

Qadri, S.M.T., Islam, A., Raza, A., & Sheikh, R.A. (2018). Utilization of microtremor measurements to evaluate fundamental frequency in Urban settlement of Taxila-Pakistan. In *Proceedings of the 7th Brunei International Conference on Engineering and Technology*, Bandar Seri Begawan, Brune. https://doi.org/10.1049/cp.2018.1608.

Qadri, S.M.T., Islam, A., Shalaby, M., Rehman, K., & Sajjad, S.H. (2017). Characterizing site response in the Attock Basin, Pakistan, using microtremor measurement analysis. *Arabian Journal of Geosciences*, 10, 267. https://doi.org/10.1007/s12517-017-3057-2.

Qadri, S.M.T., Nawaz, B., Sajjad, S.H. & Sheikh, R.A. (2015a). Ambient noise H/V spectral ratio in site effects estimation in Fateh jang area, Pakistan. *Seismological Society of China*, 28(1), 87-95. https://doi.org/10.1007/s11589-014-0105-9.

Qadri, S.M.T., Sajjad, S.H., Sheikh, R.A., Rehman, K., Rafi, Z., Newaz, B., & Haider, W. (2015b). Ambient noise measurements in Rawalpindi-Islamabad, twin cities of Pakistan: a step towards site response analysis to mitigate impact of resonance hazard. *Resonance Hazards*, 78(2). https://doi.org/10.1007/s11069-015-1760-4.

Raymond, Ng. (2017). *Site characterization of the Los Angeles basin using ambient noise spectral ratio measurements from a high density temporary broadband deployment* [[Unpublished master's thesis]. California State Polytechnic University.

Rehman, K., Qadri, S. M., Ali, A., Ali, A. & Ahmed, S. (2016). Analysis of the devastating Kashmir earthquake 2005 aftershocks. *Arabian Journal of Geosciences*, 9, 379. https://doi.org/10.1007/s12517-016-2418-6.

Reimann, K.U. (1993). *Geology of Bangladesh*. Stuttgart: Schweizerbart Science Publishers.

Roca, A., Oliveira, C. S., Ansal, A. & Figueras, S., (2006). Local site effects and microzonation. In C. S. Oliveira, A. Roca & X. Goula (Eds.) *Assessing and managing earthquake risk* (pp. 67-89). Dordrecht: Springer.

Shah A. A., Navakanesh, B., Sheeba, K., Reduan, Q., Jawi, Z., Shah, B.A., Singh, A.R.T., & Malik, J.N. (2019). Making living with earthquake hazards a culture. In *Proceedings of the Geoscience & Society Summit*. Sweden: American Geophysical Union.

Shah, A.A., Qadri, T., & Sheeba, K. (2018). Living with earthquake hazards in South and South East Asia. *ASEAN Journal of Community Engagement*, 2(1), 15-37. https://doi.org/10.7454/ajce.v2i1.105.

Singh, A.P., Parmar, A. & Chopra, S. (2017). Microtremor study for evaluating the site response characteristics in the Surat City of western India. *Natural Hazards,* 89(3),1145–1166. https://doi.org/10.1007/s11069-017-3012-2.

Volant P., Cotton F. & Gariel J.C. (1998). Estimation of site response using the H/V method. Applicability and limits of this technique on Garner Valley Downhole Array dataset (California). In *Proceedings of the 11th European Conference on Earthquake Engineering.* Rotterdam: Balkema. CD-ROM.

World Institute for Disaster Risk Management – DRM. (2004). *Seismic microzonation for municipalities, pilot studies: Adapazarý, Gölcük,* Ýhsaniye *and Deðirmendere* (270 p.). Republic of Turkey: Ministry of Public Works and Settlement, General Directorate for Disaster Affairs.

List of symbols

K_g	seismic vulnerability index
H/V	horizontal to vertical ratio
f_0	Resonance frequency
A_0	H/V Peak Amplitude

Soils and Rocks
An International Journal of Geotechnical and Geoenvironmental Engineering
www.soilsandrocks.com
ISSN 1980-9743
ISSN-e 2675-5475

Combined analysis of landslide susceptibility and soil water dynamics in a metropolitan area, northeast Brazil

Cristiane Ribeiro de Melo[1#], Paulo Abadie Guedes[2], Samuel França Amorim[3], Fellipe Henrique Borba Alves[4], José Almir Cirilo[5]

Case Study

Keywords
SINMAP
HYDRUS
Landslide susceptibility
Water balance
Barreiras Formation

Abstract

Landslide susceptibility and water balance in the soil, in the community of Lagoa Encantada, Recife Metropolitan Area, Brazil, were assessed using the computational models SINMAP and HYDRUS-1D. The SINMAP input parameters were the physical and hydrodynamic characteristics of the soil, evidence of landslides and the DEM; and for the HYDRUS-1D model, the hydraulic parameters of the soil. For both programs, simulations were also carried out, based on the rain recorded in the area. The soil was classified using the Unified Soil Classification System (USCS). To assess infiltration processes that cause landslides, HYDRUS-1D was used, under the same scenarios simulated by the SINMAP model and also in the evaluation of the infiltrated volume, in real landslides. The SINMAP results (susceptibility maps) show a 71% increase in the susceptible area ($SI < 1$; SI = stability index) between the two precipitation scenarios, and are consistent with evidence of landslides. The HYDRUS-1D results complement SINMAP results and suggest that infiltration values for simulated scenarios were similar to those of real landslides. It is concluded that it is possible to map areas of greater instability and to predict possible landslides in different precipitation scenarios, by quantitatively assessing the infiltrated volume that contributes to the destabilization of the soil.

1. Introduction

In Brazil, the most frequent mass movements are the shallow rotational and translational landslides, triggered by the decrease in the shear resistance of surface soils subjected to intense rains (Sausen & Lacruz, 2015). The critical rainfall volumes that trigger mass movements vary with the soil infiltration regime, the dynamics of groundwater in the massif, the type of material and the instability under study (Gusmão Filho et al., 1997). Landslides related to human interference occur with much less rainfall than natural landslides (Santos, 2012). In the city of Recife, the highest incidence of landslides is observed in the Barreiras Formation. This formation consists of sandy-clayey sediments, poorly consolidated: it is environmentally unstable (Silva et al., 2010). The sandy material has a high content of feldspars, which, under the hot and humid weather, favor landslides (CONDEPE/FIDEM, 2019).

The area chosen for study was the Lagoa Encantada community, with an area of approximately 6 km^2, located in the Recife Metropolitan Area (RMA), in the Ibura neighborhood, 15 km from downtown Recife. In this place, the relief is steep, unstable and with several human interventions: it has many areas of risk.

For disaster prevention, important information must be generated and updated to determine various levels of threat; indeed, the reliability of the process is limited by factors such as the availability and quality of the data (Dragićević et al., 2015). The minimum database for the preparation of landslide forecasts are: maps of susceptibility or risk of landslides (to indicate which areas are exposed to the problem), previous levels of groundwater in the soil, intensity and duration of rain that are needed to trigger processes and meteorological data and forecasts (Baum & Godt, 2010).

There are computational models that allow assessing the propensity for landslides due to previous precipitation events of known magnitudes and soil characteristics, such as: TRIGRS (Baum et al., 2009), SHALSTAB (Dietrich & Montgomery, 1998), SINMAP (Pack et al., 2005), among others. However, few have the characteristic of a free and

#Corresponding author. E-mail address: cristiane.melo@cprm.gov.br
[1]Serviço Geológico do Brasil, Recife, PE, Brasil.
[2]Instituto Federal de Educação Ciência e Tecnologia de Pernambuco, Recife, PE, Brasil.
[3]Universidade Federal de Pernambuco, Recife, PE, Brasil.
[4]Agência Pernambucana de Águas e Clima, Recife, PE, Brasil.
[5]Universidade Federal de Pernambuco, Centro Acadêmico do Agreste, Caruaru, PE, Brasil.

Submitted on May 12, 2020; Final Acceptance on May 12, 2021; Discussion open until August 31, 2021.
https://doi.org/10.28927/SR.2021.051420

open source program, for broad access to the scientific community and management institutions that are interested in studying areas susceptible to landslides.

The use of physical models to assess the spatial susceptibility of superficial landslides has proved to be very promising, starting from an analysis of distributed slope stability (Baum & Godt, 2010). The TRIGRS is an open-source program designed for physically-based modeling of the timing and distribution of shallow landslides, caused by rainfall (Alvioli & Baum, 2016). SHALSTAB and SINMAP are also open-source programs. Both combine a hydrological model with an infinite slope stability model for predicting landslide occurrence (Michel et al., 2014). Zizioli et al. (2013) compared the stability models TRIGRS, SHALSTAB, SINMAP and SLIP. The research demonstrates that the four physically based models, although they use different hydrological models, present a close performance regarding prediction of shallow landslide areas. However, according to Witt (2005), SINMAP has the advantage of being able to use transmissivity and recharge values in the calculation so that the precipitation limits can be tested. This characteristic was important when choosing SINMAP for this study.

Combined assessments between susceptibility assessment models are observed in the literature (e.g. Pradhan & Kim, 2016); and methods that assess susceptibility using relief, soil properties and infiltration (e.g. Baum et al., 2010). An alternative is to evaluate the results of susceptibility models and infiltration models in a combined way, aiming to better evaluate the sliding processes. An example is Silva & Zuquette (2013) who calculated the three-dimensional safety factor (3D) and related the results to the wetting depths using HYDRUS-1D.

In this work, the proposed methodology aims to use, in a combined way, a model that is based on geotechnical and climatological information, the accumulation of water in situations of intense precipitation (water balance in the soil) and high resolution digital models of the terrain, in an area not yet studied. The assessment of landslide susceptibility and water balance in the soil were simulated using the following two free access computational models: SINMAP, which computes and maps areas of potential slope instability based on digital elevation data and locations of observed landslides, and HYDRUS-1D, which analyzes the movement of water and solute in porous unsaturated, partially saturated or fully saturated media. It was also decided to use input data that are exclusively public and accessible free of charge. Based on these tools, a general methodology was proposed that aimed at zoning areas by level of susceptibility and understanding the accumulation of water, in the soil, in situations favorable to earth movements caused by the action of rain. Therefore, our objective was to contribute to the techniques of assessing susceptibility to landslides, providing a method of combined analysis, which uses exclusively free software and open data, and which can be useful for future risk analyses and for the creation of warning systems in the studied community.

2. Characterization of the area

The term Barreiras Formation is used to name little or unconsolidated sediments, with varied colors, lithologically varying between clay and conglomerates, with irregular and very indistinct sedimentary structures. It can occur in a discordant way on the crystalline basement or on cretaceous and tertiary sedimentary units. The Lagoa Encantada community was built on this geological unit. According to Pfaltzgraff (2007), covering the crystalline basement and the Cretaceous sedimentary units, the formation is characterized by deposits of coarse sand, interspersed with rhythmic strata of fine sand and/or very friable and easily erodible clay. When subjected to precipitation, water infiltrates the sandy layer and finds the clay layer, which is impermeable. Water accumulates in the sandy area, which becomes more fragile due to poor cohesion, increasing the risk of landslides.

As usual in these occupations, in Lagoa Encantada the decrease in natural vegetation caused by human action, for the construction of houses, is observed everywhere. This behavior of the population results in the exposure of the soil to intense rains, which weakens its resistance to shear and increases the active stresses. Souza et al. (2012) classified the accumulated precipitation intensity in 24 hours for Recife as: heavy rain with values between 18.6 mm and 55.3 mm; and very heavy rain above 55.3 mm.

According to the records provided by the Civil Defense Coordination of Recife (CODECIR), 2,141 requests were met in the 2013-2017 period. There were 65 landslides, 04 damaged walls, 1,755 new plastic sheeting placed and 317 existing plastic sheeting were replaced. Throughout the community, the photointerpretation of high-resolution satellite images and field visits confirmed the existence of scars from past landslides; these certainly were the motivation for the construction of restraint walls and application of plastic tarpaulins, as documented during a field visit. The orthophoto and slope map for this region, where the community is located (Figure 1), shows a hill region with high slopes. The slope classification follows the SiBCS - Brazilian Soil Classification System (EMBRAPA, 2018). Bandeira (2010) showed that in the Southern Area of Recife metropolitan area, in the Barreiras Formation, 69% of slope instability was recorded, with accumulated rainfall values greater than 60 mm in 72 hours. From the total unstable areas in the mentioned area, 75% of the landslides occurred in the Lagoa Encantada community. The majority of landslides in the area occurred until the beginning of 2016, when they declined. Preventive actions implemented by the institutions in charge and awareness raising work with the community have contributed to the reduction of disasters.

3. Materials and methods

An overview of the work structure is presented next. Initially, the type of soil was evaluated, in order to determine

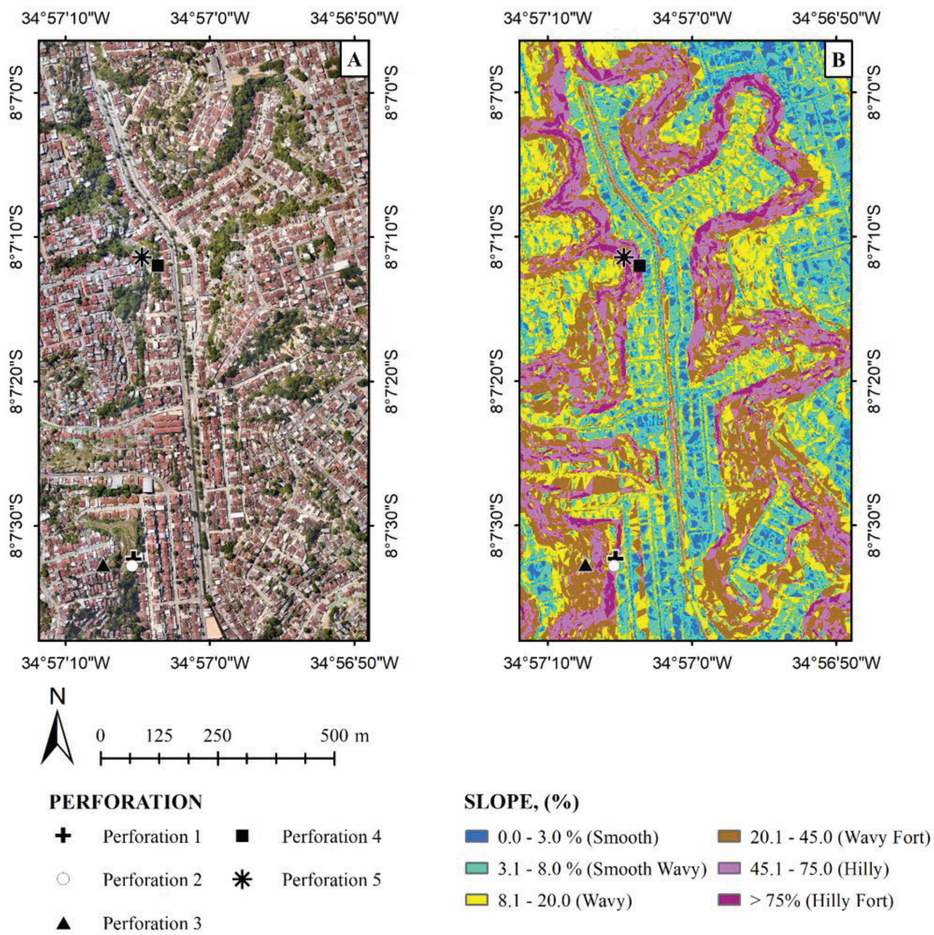

Figure 1. (A) orthophoto, and (B) slope map of Lagoa Encantada.

its physical and hydrodynamic characteristics. In addition, precipitation data, data on previous landslides and the terrain elevation model were also obtained. With this information, the area's behavior regarding landslides was evaluated for two different scenarios: one representing the situation of little rain and the other, the situation of a lot of rain (winter) in the region. The combined assessment was carried out using two separate open source programs: SINMAP and HYDRUS. The assessment carried out by SINMAP determines the map of susceptibility to landslides in the area. It considers rain, but it does not model the infiltration over time. The assessment carried out by HYDRUS complements the previous one, providing data of infiltration over time.

The work structure is depicted in Figure 2. The soil type was determined by prospection with manual auger, and classification by the Unified Soil Classification System (USCS) (steps 1 and 2; items A and B). The rain records used in the study make up item C.

The susceptibility analysis is as follows. The records of landslides that occurred at the site (item D) were used to calibrate the SINMAP model (step 3). This work also used high quality images of the terrain, produced by LIDAR (item E). The cited data (items A to E) were used as input to the SINMAP model, for the assessment of susceptibility to landslides in two scenarios (item F). SINMAP can work with only a single type of soil.

The infiltration analysis was performed with the HYDRUS-1D model (step 4) from the hydraulic parameters of the soil (item B) and the rainfall data (item C). The soil water balance (step 4) was simulated with precipitation (item C) and infiltration data (HYDRUS-1D), for two situations (item G).

The combined evaluation between the analysis of the models (steps 3 and 4) allows to verify the areas susceptible to landslide, and to evaluate the accumulation of water in the soil in such situations. Unlike SINMAP, HYDRUS-1D can handle more than a type of soil.

3.1 SINMAP model

The computational model denominated "Stability INdex MAPping" (SINMAP) is a deterministic mathematical model that enables the classification of areas that are susceptible to shallow translational landslides; it is configured and manipulated in a GIS environment. SINMAP is related to hydrological factors, as well as factors related to soil fragility, precipitation, soil type and relief as input parameters. The

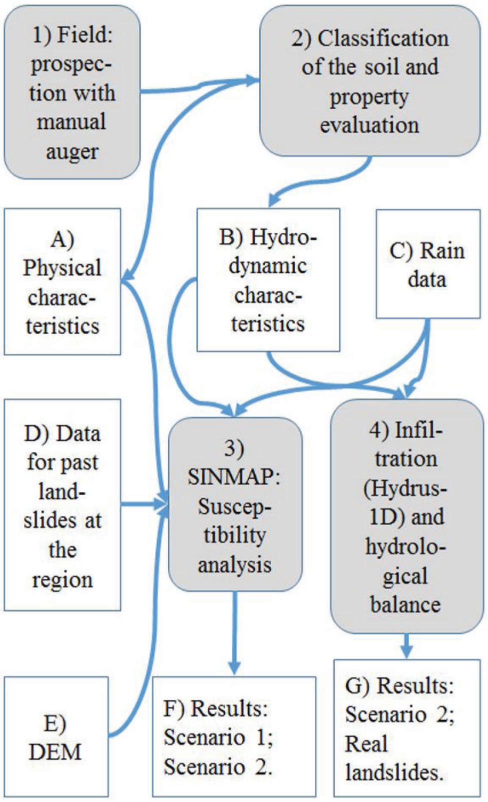

Figure 2. Work structure overview.

model was applied in a region that experiences shallow translational and rotational landslides.

The accuracy of the program results is strongly dependent on the quality of the digital elevation model (DEM) that is used (Pack et al., 2005). The validation of the model depends on the verification of the spatial coincidence between the previously mapped slip scars, and the areas designated as unstable by the model. The results are presented based on the stability index (*SI*), or safety factor, which is the probability that an area be considered stable, assuming uniform distributions of the parameters, in the uncertainty ranges. This probabilistic result is of great importance for usage in future risk analyzes. The safety factor presented here does not correspond to the safety factor calculated by limit equilibrium models like the slice methods; they just have the same name.

The *SI* can vary from 0 (most unstable situation) to 1.5 (most stable situation). SINMAP is simulated for 6 *SI* classes, as shown in Table 1. One advantage of the model is that it is not restricted to a specific program and operating system. Rather, it presents the option of being used on the MapWindow platform (open source GIS software). More information about SINMAP can be obtained in USU (2017).

3.1.1 SINMAP input parameters

The DEM used in the model is one of the products of the Pernambuco Three-Dimensional Program (PE3D),

Table 1. Slope stability classes (Menon-Júnior, 2016).

SI range	Suggested classes	Possible influences of non-modeled factors
SI > 1.5	Stable	Significant destabilizing factors are required for instability
1.5 > *SI* > 1.25	Moderately stable	Moderate destabilizing factors are required for instability
1.25 > *SI* > 1.0	Little stable	Destabilizing factors are required for instability
1.0 > *SI* > 0.5	Little unstable	Destabilizing factors are not required for instability
0.5 > *SI* > 0.0	Moderately unstable	Stabilizing factors may be responsible for stability
0.0 > *SI*	Unstable	Stability factors are required for stability

which provides products generated through Light Detection and Raging (LiDAR) technology. The DEM provided by PE3D is generated after classification of point clouds with a density of approximately 1 point/m^2, removal of elevation points related to treetops and buildings, and finally the surface interpolation through kriging. The matrix file used has a spatial resolution of 1m, and an altimetric accuracy greater than 25 cm. For more information about the PE3D program, see Governo do Estado de Pernambuco (2017). For DEM validation, see Governo do Estado de Pernambuco (2018).

Another input for SINMAP was a set of records from highly susceptible points, including past landslides occurred in the community, with and without victims. These records were used in the calibration and validation of the SINMAP model. This information was provided by the Coordination of Civil Defense of Recife (CODECIR), from 2013 to 2017. The location of Lagoa Encantada has rainfall monitored by the Ibura and Alto da Bela Vista automatic stations, which are operated by the Pernambuco Water and Climate Agency (APAC, 2017).

The physical parameters of the soil and its hydrodynamic characteristics were obtained from Santana (2006), who analyzed the same type of soil in nearby areas (2 km). Ebel et al. (2018) suggested that estimates of unsaturated hydraulic parameters, based on field data *in situ*, in contrast to laboratory measurements, can lead to a more accurate simulation of the hydrological response to rain. However, it was not possible to carry out more specific experiments due to financial cost, poor accessibility, and the lack of security in the community.

The identification of the type of soil in Lagoa Encantada was made based on the prospecting test with a manual auger, carried out *in situ* and later in laboratory tests to characterize the deformed samples according to the USCS classification. With the soil defined, the parameters presented by Santana (2006) were used, which identified the same type of soil in the UR2 community, located approximately 2 km from the area studied here. In the study, Santana (2006) collected deformed samples for characterization tests, granulometry tests with sedimentation, Atterberg limits and densities; undisturbed samples for direct shear tests; permeability tests "Tri-Flex" and *in situ* permeability "Guelph".

For the Barreiras Formation, in Recife, studies showed that the humidity profiles, both in winter and summer, differ only over the first three meters of depth, delimiting the potential landslide surface in the studied area (Gusmão-Filho et al., 1997). Normally, depending on the intercalations of draining sandy layers and impermeable clay layers, as well as the characteristic of the superficial layer, in most cases very deep water tables and fringes of variable surface moistening are founded. Such information served as the basis for determining the average rupture depth, which was visually estimated as 2 m, in the field.

3.1.2 Physical parameters of the soil and hydrodynamic characteristics

The field estimations took place in September 2017, just after the rainy season for the region. During the previous 10 days, as well as in the work day there were no rains of significant volume, which could interfere with the results. The daily rainfall recorded were considered according to Souza et al. (2012) dry day (rainfall < 2.2 mm) or very light rain (2.2 mm ≤ rainfall < 4.2 mm). For recognition of the soil profile, five perforations were made with manual auger, at different levels of elevation, in two locations in the community: Point 1, where there is no record of landslides; and Point 2, where there is a record of a landslide, which occurred on 06/28/2011. The locations for the perforation points are depicted in Figure 1. The coordinates and depths reached in each one of the perforations are presented in Table 2.

At Point 1, the depths reached by prospecting for the three levels were up to 8.9 m, and for the two levels of Point 2, up to 7.50m. The subsoil profile for each perforation can be seen in Figure 3.

In the holes made, samples were taken at every meter of depth, or visual change of layer, to be subsequently subjected to laboratory analysis. The deformed samples were sieved and the granulometric classification was performed for use by USCS. No tests were carried out to determine the percentage of clay and silt particles. The Atteberg limits (liquid limit and plastic limit) were determined using a prepared sample with prior drying.

According to the Unified Soil Classification System, the particle size and boundary analyzes showed variations for the samples between clayey sand (SC), low plasticity clay (CL) and silty sand (SM). However, it was observed that the predominant soil in the sampling is of the SC (clayey sand) type. This type was considered to be characteristic of the whole local soil profile. The parameters used for the soil

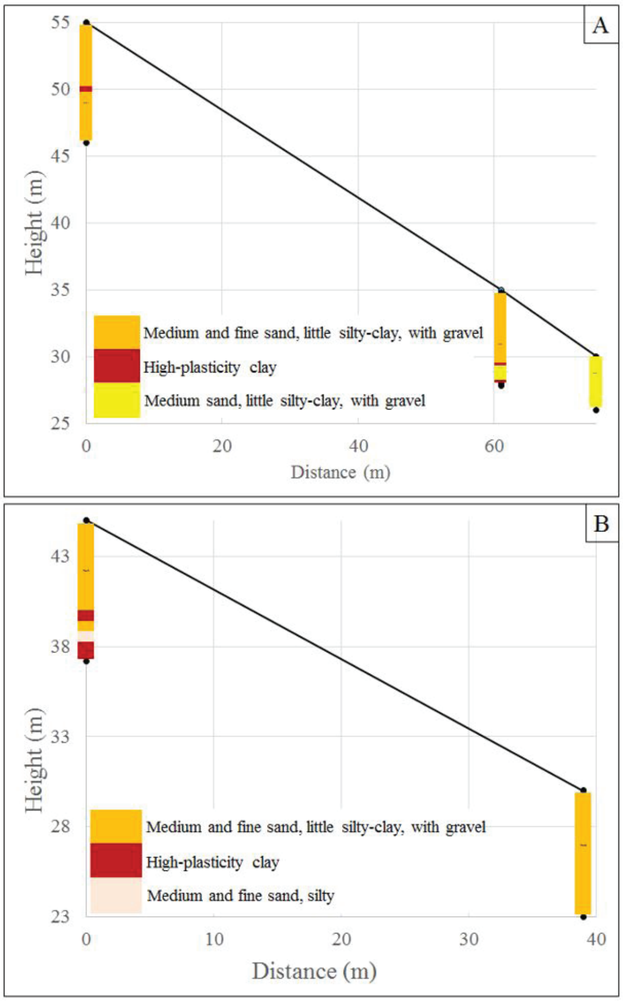

Figure 3. Sub-soil profile: (A) point 1: perforations 1 to 3; (B) point 2: perforations 4 and 5.

Table 2. Perforation points made in Lagoa Encantada.

Point	Perforation	Coordinate		Altitude (meters)	Depth reached (meters)
		Latitude	Longitude		
1	1	8º 7' 32,32"	34º 57' 5,29"	30.00	3.70
	2	8º 7' 32,80"	34º 57' 5,40"	35.00	7.05
	3	8º 7' 32,70"	34º 57' 7,40"	55.00	8.90
2	4	8º 7' 12,00"	34º 57' 3,60"	30.00	7.00
	5	8º 7' 11,40"	34º 57' 4,70"	45.00	7.50

type SC, considered as the only soil for entering parameters in SINMAP, were presented by Santana (2006), who studied and identified the soil from the UR2 Community, located approximately 2 km from Lagoa Encantada, within an area of the Barreiras Formation. The basic soil parameters that were used in the model are shown in Table 3.

The dimensionless cohesion, or the contribution of cohesion to stability slope, necessary for the model, unlike the classic cohesion of soil mechanics, is the ratio between the cohesive strength of the soil and the root zone in relation to the weight of a saturated layer of soil, as shown in Equation 1.

$$C = \frac{(Cr + Cs)}{(h \, . \, \rho_s \, . \, g)} \tag{1}$$

Where the symbols and units used in SINMAP are: C = dimensionless cohesion; Cr = root cohesion (N/m^2); Cs = soil cohesion (N/m^2); h = perpendicular thickness of the soil (m); ρ_s = density of wet soil (kg/m^3); and g = acceleration of gravity (m/s^2). For use into the model, Cr was considered null, due to homogenization and considering the worst scenario of complete removal of vegetation, and h as 2 m depth.

The soil hydrodynamic characteristics in Lagoa Encantada were performed by correlation, as performed for the physical characteristics. The transmissivity value (T = 0.1526 m^2/h) is the product between the hydraulic conductivity determined for the SC soil (k = 0.07632 m/h) (presented by Santana, 2006), and the depth of the soil susceptible to sliding (h = 2 m) determined visually in the area. The T/R ratio, transmissivity over groundwater recharge (incident rain) that was used by the program, depends on the recharge capable of causing slippage, as considered in the analysis. Two scenarios were evaluated for soil recharge: scenario 1, for rains occurring in a period of low precipitation; and scenario 2, for a rainy season with high rainfall.

3.1.3 Hydrological data

For the simulation of scenario 1 (low rain incidence), the precipitated volume in November, recorded by the Data Collection Platform (PCD), "Alto da Bela Vista", was used as the groundwater recharge value. Considering that the month of November had the lowest daily rainfall in the available data series, with values close to zero, it was decided to use, in the referred Scenario 1, the monthly total precipitated occurred in the month, as the maximum and minimum recharge. The situation of daily maximum rains, in the studied region, occurs on average in the rainiest quarter, between the months of May and July, with June being normally the most critical month. For scenario 2, the highest rainfall that occurred in 48 consecutive hours was used, in all rain series recorded in the PCD. The evaluated scenarios, their respective recharges and the T/R values are shown in Table 4.

Table 3. Physical soil parameters for entry into the SINMAP model.

Parameter	Value
Type of soil	SC (clayey sand)
Soil density (ρ_s)	2,670 kg/m^3
Internal friction angle (ϕ)	29° (min) and 36.1° (max)
Cohesion (C_s)	0 kPa (min) and 8.88 kPa (max)
Dimensionless cohesion	0 (min) and 0.17 (max)

3.2 HYDRUS-1D model

The prediction of a landslide event depends on the pore water pressure, a consequence of the incident rain that is deterministically quantified by the Richards Equation (van Genuchten, 1980). The water balance in the soil was simulated trying to determine the accumulation of water in a situation that could slide, assisting in the assessment of risk areas and situations, based on the joint analysis of the relief and the infiltration of water in the soil. The HYDRUS-1D software (Šimunek et al., 2013), which aims simulating the one-dimensional movement of water, was selected. The model numerically solves the Richards equation for variable water flow, offering the option of four analytical hydraulic models that describe water retention in the soil, as a function of hydraulic conductivity. More information at PC-progress (2019).

HYDRUS-1D (version 4.17) was used by Feltrin et al. (2013) to simulate the dynamic of water in the soil, in an area under vegetation cover in a native field. Feltrin et al. (2013) compared the simulated results with results obtained in field measurements; they concluded that the results presented by the program are compatible with the drainage obtained in a lysimeter. Zhang et al. (2017) applied the SINMAP model to Zhouqu County, successfully identifying areas susceptible to landslides, and determined the saturated hydraulic conductivity for use in the model, using the HYDRUS-1D software. Therefore, it is reasonable to assume that HYDRUS-1D can be used to adequately simulate infiltration in the studied region. It is also an open source program, hence it was chosen.

In this work, the HYDRUS-1D model was used to reproduce the water balance in the soil in the same simulated situation for the use of SINMAP, in the winter period, making possible a joint evaluation of the results. In a second analysis,

Table 4. Groundwater recharge considered for precipitation and T/R ratio scenarios.

Scenarios	Recharge (mm)		Period of the occurrence		T/R	
	Maximum	Minimum	Maximum	Minimum	Maximum	Minimum
Scenario 1	20.31	9.09	November/2016	November/2015	12,090	5,411
Scenario 2	120.59	57.73	June 03 and 04, 2016	June 28 and 29, 2017	127	61

the model was used to simulate the water balance in real situations of landslide in the Lagoa Encantada area.

The analysis of water accumulation in the soil was carried out by hydrological balance. This decision aimed to better represent the accumulation of water in the soil and maintain consistency in relation to the analysis using SINMAP. This analysis considered Scenario 2 SINMAP, which includes the maximum rainfall observed throughout the series, over a period of 48 hours. The maximum rain occurred between 3 and 6 April, 2016.

Unfortunately, because the free version of the program was initially thought for use in agriculture, it disregards topography. The disregard of the slope of the terrain, which would contribute to the decrease of infiltration and increased runoff, brings, as a consequence, an overestimated simulation for the infiltration.

3.2.1 HYDRUS-1D input parameters

To determine the water balance in the soil of Lagoa Encantada, the standard module of the HYDRUS-1D program was used to calculate the infiltration of water, in a profile of two layers of the soil. Groundwater recharge estimation was not considered in our calculations because, during prospecting, the presence of groundwater was not found. It was assumed, for the model, that the water table was located far below the bottom of the soil domain, and therefore it would not affect the flow processes, in the adopted soil profile. As no specific tests were performed to determine the parameters necessary for the model, it was decided to use the hydraulic parameters of the soils provided by the program, which are very approximate averages for the different texture classes (PC-progress, 2020).

Soil was reclassified as required by the model, and it was necessary to adapt and use the United States Department of Agriculture (USDA) soil texture classification system. Considering that the soil found during prospection was classified by the USCS as SC (clayey sand) type, the Loamy Sand soil option in the soil catalog was used as the best alternative to represent the studied area. It is important to note that in the area under study, as the topsoil is subjected to transformations caused by weather, sun exposure and other agents, a thin impermeable or semi-permeable layer is formed above the ground. Thus, in order to better represent the real soil conditions, the soil was considered as being divided into two layers: 1) an initial layer of Sandy Clay Loam soil from 0 to 12 cm deep; and 2) a second layer from 13 cm to 200 cm thickness of Loamy Sand soil. The depth of the two layers representing the soil profile totalized 2 m of the rupture surface, the same depth considered for SINMAP. The analytical hydraulic model, chosen at HYDRUS to assess infiltration in the pilot area, was that of van Genuchten (1980). The flow of water that penetrates through the soil surface increases, as the pressure of the surface water layer increases. According to the program manual, this flow into the soil stabilizes when the depth of the surface water layer reaches 3 cm (Šimunek et al., 2013).

3.2.2 Rain period used in the simulation

To assess the water balance in the soil, all simulations, from January 1th to September 30th, of each year were evaluated. This means that the simulated period corresponded to 250 consecutive days of observation. The assessment begins in the dry period, passing through the most humid quarter, which occurs between the months of May to June, until the recession of rains in September. Unfortunately, in the Lagoa Encantada and its surroundings (up to a maximum of 7 km), there were no PCD or rain gauges with hourly precipitation records, with a series prior to May 2015. In order to observe the gradual accumulation of water in the soil, prior to the landslide events that occurred in 2015, a significant series of data was needed. Thus, the infiltration analysis was performed on a daily basis (accumulated for 24 hours), using data from the CPRM/Recife rainfall station, monitored by the Geological Service of Brazil (SGB). It belongs to the National Hydrometeorological Network, located 11 km from the studied area. The data series that was used for the referred study can be accessed at the National Water Agency (ANA, 2019).

4. Results

4.1 SINMAP simulation and scenario assessment

The results show the SINMAP susceptibility classes for the simulation of the two proposed scenarios: scenario 1 - groundwater recharge for one month, during the summer, where the monthly total precipitation is low; and scenario 2, for a maximum rain of 48 hours, which occurred during winter, for the entire series recorded by the PCD station "Alto da Bela Vista". The maps for stability and saturation index for scenarios 1 and 2 are in Figure 4.

The calculation was performed over a total area of 0.791 km^2 using DEM with a spatial resolution of 1 meter. However, the area effectively calculated by the model corresponded to 0.614km^2. In other words, an amount of 22.4% of the total area was classified by the program as "no data". Of all the susceptible points plotted, only 75 of them were presented on the area with calculated *SI* and the others on the area not calculated, classified as "no data". Thus, the results of this work consider only the 75 points with calculated *SI* by SINMAP.

When compared, the maps of scenarios 1 and 2 show that, in the situation of lower rainfall, the region that is in low humidity and has a stable or moderately stable factor of security is greater. In this case, the zones at the threshold of saturation and total saturation occupy very few areas. In scenario 1, even though the groundwater recharge is very

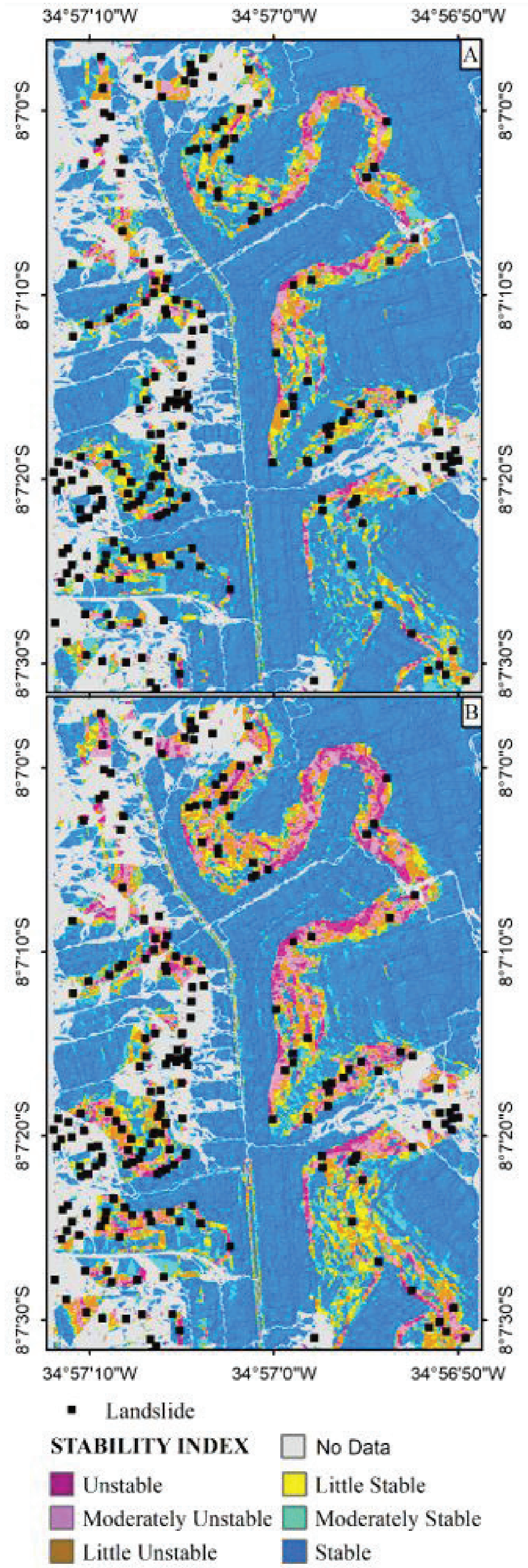

Figure 4. Stability and saturation index for (A) scenario 1 and (B) scenario 2.

low, there is instability on the slope, at the steepest points. With the simulation of increased recharge (scenario 2), and a significantly increased number of unstable zones, a smaller recharge was observed (Table 4), which is more diluted in time, in relation to the constant transmissivity. With the increase in precipitation in winter, there was a transformation from "moderately stable" and "little stable" classes, at steep places, to "little stable" and "little unstable" classes, respectively.

The graph that was generated from the validation model for the two scenarios can be seen in Figure 5. According to the results for the two scenarios, the slip points provided for the validation are distributed in the areas of least stability in the *SI* value and are located in a region with steeper slopes, with a contribution area of up to 100 m^2. In Figure 5, it was noted, for scenario 1, that a considerable part of the landslides

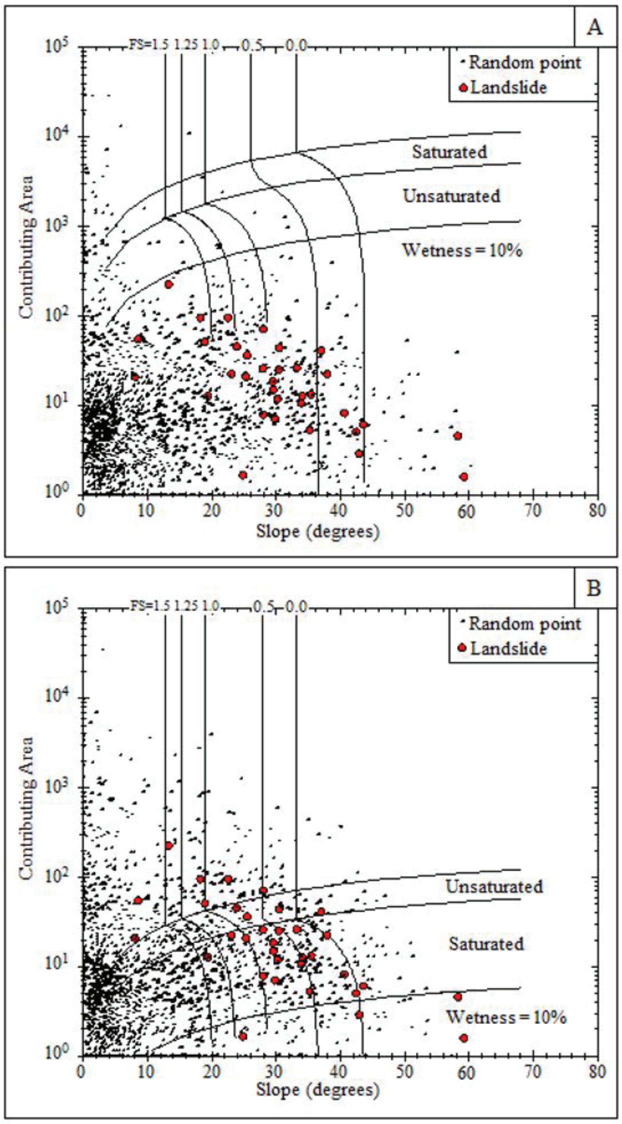

Figure 5. Results of the SINMAP validation model (sliding scars mapped by CODECIR in red and model calibration points) for (A) scenario 1 and (B) scenario 2.

occurred in slope intervals between 20º and 44º. The same is presented for scenario 2. For the low rainfall situation, most of the mapped risk points were in conditions of low humidity, and with a stability index (*SI*) below 1.25. However, in the situation of greater humidity, the mapped risk points were mostly in the zone with the highest saturation, with a stability index (*SI*) below 1.0. The evaluation of the two scenarios showed that, in case of landslide, this will not be caused only by rain, but also by the excessive slope of the terrain and other associated factors.

Following the same methodology presented here, simulations were carried out for maximum rainfall of 12 and 24 hours in the studied region. For these groundwater recharges, SINMAP predicted, as expected, that for the Lagoa Encantada community the most stable areas can be found in the flatter regions, regardless of the soil and hydraulic parameters used. The areas of greatest instability combined well with the steeper terrain, provided that it was in a certain range of slope of the terrain. For all recharge simulations, the results showed that massive precipitation is not necessarily required for the landslides to start; furthermore, the topographic factor is an important trigger for the occurrence of landslides.

Table 5 show the statistics of the areas simulated by SINMAP for each scenario, according to the risk class. In these tables, the following three terms are presented: 1) "#Landslides", which corresponds to the number of landslides inserted in each stability zone, based on the points susceptible to landslides supplied to the program by the user (total of 75 points); 2) "% of slides", which is the percentage distribution of the referred points; and 3) "LS Density (#/km^2)", which corresponds to the relationship between the number of landslide points and the respective area for each stability index.

The analysis of Table 5 show that, for Scenario 1 (little rain), 55% of the studied cases are in an unstable situation, with 41 landslide points reported in CODECIR's history (total of 75) that are inserted in such areas. With the increased precipitation for scenario 2, which presents the highest reload, there is an increase of percentage of landslide cases in the areas of instability to 77%, which corresponds to the insertion of 58 mapped points in an unstable area. Significant changes in the precipitation threshold showed that SINMAP was particularly sensitive to changes in the amount of groundwater recharge, with an increase in the expected areas of instability. This is expected because the recharge rate certainly is one of the most important factors in triggering landslides.

4.2 Soil water balance using HYDRUS-1D

The accumulation of water in the soil in the days prior to landslides is an important destabilizing factor. In this way, the water balance in the soil was modeled in order to try to understand how the infiltrated water contributes to the risk of landslide in the region. The water balance was simulated for two situations: 1) scenario 2 simulated by SINMAP, where the maximum rain per 48 hours, of the whole series recorded in the community, was used as a groundwater recharge; 2) simulation of the volume of water accumulated on the ground in real landslide situations that occurred in 2014.

4.2.1 HYDRUS-1D simulation for real landslide situations

In the studied location, the rainiest quarter usually is between the months of May and July, a period in which, on average, 50% of the annual rainfall is concentrated. In 2014, when the total precipitous of 202.20cm was recorded, the landslides occurred on June 26 and July 12. During the mentioned winter months, the total precipitated corresponded to 42% of the annual precipitation. The volume infiltrated in 2014 was simulated by HYDRUS-1D. The rains that occurred during the year and the infiltrated volume are shown in Figure 6. Based on the results, the accumulated infiltration was calculated (Figure 6).

In the studied area, the landslides that occurred in winter are more common because this is a period of intense precipitation. Table 6 shows the numerical values involved in the water balance, on the day of the mentioned landslides. The soil types present in Lagoa Encantada were also studied by Schilirò et al. (2019), in another region. This study concluded that the soil types SC and CL were the most influenced by the rainfall events evaluated, and that they are very susceptible to landslides. It also showed that humidity conditions are an important triggering factor.

Table 5. SINMAP statistics for scenarios 1 (S1) and scenarios 2 (S2).

SI	*SI* > 1.5	1.5 > *SI* > 1.25	1.25 > *SI* > 1.0	1.0 > *SI* > 0.5	0.5 > *SI* > 0	0 > *SI*
#Landslides (S1)	14	6	14	19	16	6
% of slides (S1)	18.67	8	18.67	25.33	21.33	8
Area (km^2) (S1)	0.47	0.03	0.04	0.04	0.02	0.01
LS Density (#/km^2) (S1)	29.91	193.09	356.78	442.61	732.87	553.05
#Landslides (S2)	9	0	8	27	21	10
% of slides (S2)	12	0	10.67	36	28	13.33
Area (km^2) (S2)	0.43	0.03	0.04	0.06	0.04	0.02
LS Density (#/km^2) (S2)	21	0	202.22	431.52	573.35	570.48

Table 6. Water balance in the soil on the day of the landslides in 2014.

Landslide date	Precipitation on the day of the landslide (cm)	Accumulated from January 1 until the day of the landslide		
		Precipitation (cm)	Infiltration (cm)	Overland flow (cm)
06/26/2014	8.4	115.9	78.6	28.9
07/12/2014	0	129.2	87.1	42.1

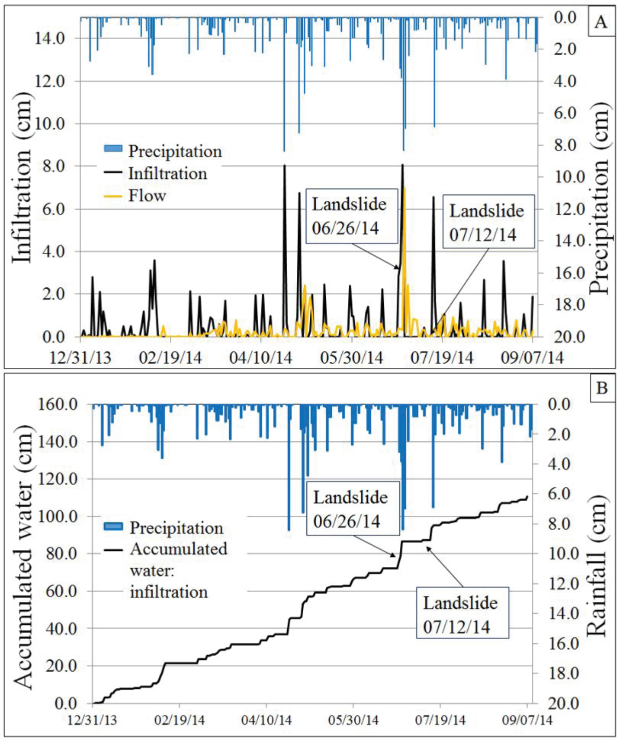

Figure 6. (A) simulated soil water balance from 01/01/14 to 09/30/14; (B) accumulated infiltration for 2014.

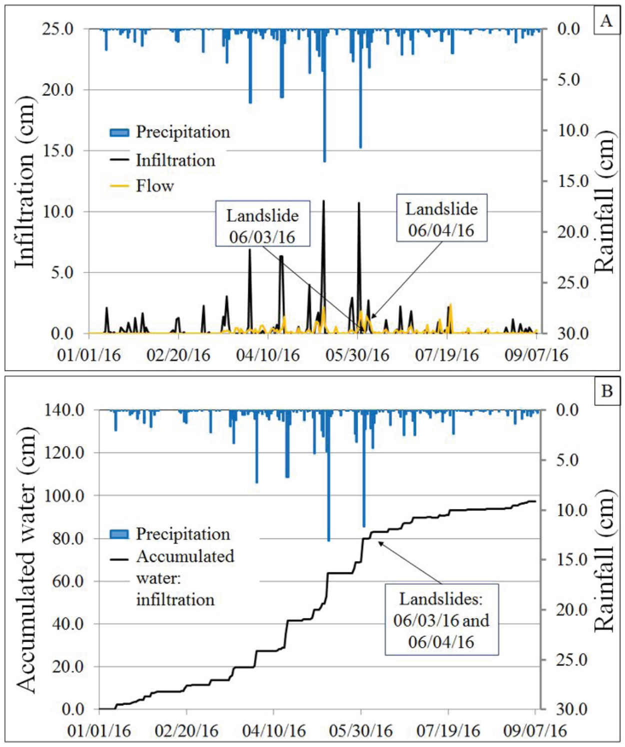

Figure 7. (A) simulated soil water balance for 01/01/16 to 09/30/16. (B) accumulated infiltration for 2016.

According to Table 6, the average infiltration in the soil, until the day of the registered landslides, would be close to 70% of the value of the accumulated precipitation until that day. This data assumes that the soil was subject to the same conditions established for the HYDRUS-1D simulation, but disregarding the influence of the slope, which is a limitation of the model for the open version. In the observed cases, the landslides occurred after the accumulated precipitation, between the first day of the year (see item 3.2.2) until the day of the landslide, was greater than 100 cm of rain. The exposed areas available for infiltration, and subject to urbanization, can be seen in Figure 1.

4.2.2 HYDRUS-1D simulation for Scenario 2 SINMAP for maximum 48h rain

In order to maintain consistency in relation to the analysis in item 3.2.2, it was decided to assess the hydrological balance, using the CPRM/Recife rain station. The year 2016, with a precipitated annual total of 139.40cm of rain, presented an anticipated rainier quarter, between the months of March and May. During the aforementioned months, the precipitated total corresponded to 64% of the annual total, that is, there was a high concentration of precipitation in the period. The rainfall and the infiltrated volume, simulated for scenario 2, is shown in Figure 7. Based on the results of the simulated infiltration, the water that was accumulated in the soil, for the year 2016, is also illustrated in the same figure.

According to Figure 7, a possible landslide that occurred during the critical situation of instability in Scenario 2 would happen after a period of great accumulated infiltration. The accumulation of water in the soil in the days preceding Scenario 2, in addition to the little rain recorded on the day of the event, would be the triggering agents for an eventual landslide. The hydric balance showed that the accumulated precipitation from January 1 to the day of the landslide (June 4, 2016) was 107.2 cm and the infiltration was of 80.1 cm. The simulated infiltrated volume corresponds to 75% of the total precipitated in the year. It is important to note that, unlike HYDRUS-1D, the SINMAP program does not consider the accumulated rain in the period before the landslide, but a punctual rain with a value that can be accumulated, or not. Another difference, which must be considered, is the type of soil involved in the analysis. As previously mentioned, the types of soils used for the two programs are different, but have similarities in their general characteristics.

Considering the simulation for scenario 2, and comparing it with the values presented in real landslide situations for 2014 (Table 6), it is observed that the infiltration values for the referred scenario are similar to those of real landslide cases. In other words, the situation presented to SINMAP, added to the HYDRUS-1D infiltration calculation would result in an approximate representation of a real landslide in the Lagoa Encantada region, in Ibura.

5. Discussion

Using a more accurate DEM in order to improve the analysis by SINMAP of unstable areas, prevented the evaluation of 22.4% of the area provided, as well as of the sliding scars in these areas with "no data". These results are in agreement with Thiebes et al. (2016), who states that the quality of spatial resolution influences the accuracy of the results. However, increasing the quality of the DEM can result in areas with an uncalculated SI ("no data").

The analysis of the SINMAP data obtained showed an increase in susceptible areas from scenario 1 to scenario 2, but the "no data" area remained the same. This is also in accordance with Witt (2005) and Sulaiman et al. (2017), in the following aspects. Witt (2005) showed that SI was not calculated by SINMAP in some regions ("no data"). Sulaiman et al. (2017) tested different DEM resolutions and concluded that the coarser DEM reveals less area which is unstable and, even with 1 meter DEM, it may not be possible to overcome the problems.

According to Figures 2A and 2B, native vegetation is mainly in the steepest areas, which is expected, and did not present identifiable landslides. In Lagoa Encantada, for example, the banana tree is common: it facilitates infiltration and destabilization. According to McGuire et al. (2016), vegetation can increase or decrease stability. The apparent cohesion provided by the roots is a strong factor for stability, in relation to the other factors, which can also exert influence during events of extreme rain. However, according to Guoa et al. (2019), some types of roots can facilitate slipping, increasing infiltration during precipitation.

The HYDRUS results for the real landslide scenarios show the levels of infiltration that probably occurred to cause the landslide situation. The assessment of accumulated rain, with HYDRUS-1D, was based on Gusmão Filho (1990), who studied landslides in Barreiras Formation in Recife and emphasized the importance of evaluating concentrated rain. Chen et al. (2018) used a combined method of landslide susceptibility analysis, which employs soil moisture monitoring through sensors and a numerical simulation model. HYDRUS-2D was used to determine soil parameters and the model data was compared with field measurements. The results show that the combined analysis, using field humidity monitoring with sensors, can reliably predict the potential for future landslides, under heavy rain.

6. Conclusions

The Lagoa Encantada community, located in the area of Barreiras Formation hills, in the city of Recife, is vulnerable and prone to landslides and accidents. That is due to human interventions, the type of soil, high slopes, absence of natural vegetation, and intense rainfall.

This study aimed to contribute to the techniques of assessing susceptibility to landslides, providing a method of combined analysis, which uses exclusively free software and open data, and which can be useful for future risk analyzes and for the creation of warning systems in the studied community. The proposed method uses two analysis: one for landslide susceptibility, and another for hydric balance in the soil. To assess the susceptibility to landslides in the area, the computational model SINMAP was used. The simulation of the hydric balance of the soil in landslide situations was carried out through the HYDRUS-1D program.

As expected, the SINMAP susceptibility map showed an increase in areas susceptible to landslides, due to increased precipitation. The HYDRUS-1D model showed that the landslides occurred in situations of accumulated precipitation greater than 100 cm of rain and infiltration of approximately 70% of this precipitation.

When evaluating the infiltration in the superficial layer in real events, it was observed that landslides occurred when the accumulated infiltration, presented by the program, reached an average value of 82.9 cm, with a variation of more or less 4.3 cm. This information is not yet conclusive, as it was obtained with little data. However, the result is important and promising, as it suggests a practical strategy to better understand the causes of landslides due to infiltration, soil and relief. Thus, more research is necessary to evaluate if the observed or predicted infiltrations, at this level, can potentially work as relevant forecast data for landslides in the region. For instance, it is important to study past landslides in more detail, and see how infiltration may vary.

This work represents an important step in the creation of more accurate models for assessing slip susceptibility, as it allows to consider, in a combined way, important triggering factors for the Barreiras Formation. Future work may try to assess if the method can be used in other susceptible areas (possibly with different soil and relief), the influence of wastewater on the susceptibility to landslides, as well as to evaluate ways of dealing with the presence of uncalculated areas ("no data") in the susceptibility map.

Declaration of interest

The authors declare that there are no conflicting interests.

Authors' contributions

Cristiane Ribeiro de Melo: original draft preparation, investigation, validation, discussion of results, writing – reviewing and approval of the final version of the manuscript. Paulo Abadie Guedes: investigation, discussion of results, writing – reviewing and approval of the final version of the manuscript. Samuel França Amorim: original draft preparation, investigation, validation, discussion of results. Fellipe Henrique Borba Alves: validation, discussion of results and diagram creation. José Almir Cirilo: original draft preparation and discussion of results.

List of symbols

ANA	National Water Agency
APAC	Pernambuco Water and Climate Agency
CL	Low plasticity clay
CODECIR	Coordination of Civil Defense of Recife
CONDEPE/FIDEM	State Planning and Research Agency of Pernambuco
CPRM	Brazilian Geological Survey
DEM	Digital Elevation Model
LIDAR	Light Detection and Raging
PCD	Data Collection Platform
PE	Pernambuco
RMA	Recife Metropolitan Area
SC	Clayey sand
SHALSTAB	Shallow Landsliding Stability Model
SiBCS	Brazilian Soil Classification System
SINMAP	Stability Index Mapping
SM	Silty Sand
SLIP	Shallow Landslides Instability Prediction
TRIGRS	Transient Rainfall Infiltration and Grid-Based Regional Slope-Stability Model
UR2	Residential Unit 2
USCS	Unified Soil Classification System
USDA	United States Department of Agriculture
USGS	United States Geological Survey
C	Dimensionless cohesion
Cr	Root cohesion
Cs	Soil cohesion
g	Acceleration of gravity
h	Depth of the soil
ϕ	Internal friction angle
K	Hydraulic conductivity
R	Recharge
SI	Stability Index
ρ_s	Soil density
T	Transmissivity

References

Agência Estadual de Planejamento e Pesquisas de Pernambuco – CONDEPE/FIDEM. (2019). *Os morros da região metropolitana do Recife. Parte a – morros manual de ocupação. Cap. 01 - características ambientais.* Recife. Retrieved in August 15, 2019, from http://www2.condepefidem.pe.gov.br (in Portuguese).

Agência Nacional de Águas – ANA. (2019). *Hidroweb.* Retrieved in December 15, 2019, from http://hidroweb.ana.gov.br/ (in Portuguese).

Agência Pernambucana de Águas e Clima – APAC. (2017). *Dados meteorológicos.* Retrieved in December 15, 2017, from http://www.apac.pe.gov.br/meteorologia/chuvas-rmr.php (in Portuguese).

Alvioli, M., & Baum, R.L. (2016). Parallelization of the TRIGRS model for rainfall-induced landslides using the message passing interface. *Environmental Modelling & Software*, 81, 122-135. http://dx.doi.org/10.1016/j.envsoft.2016.04.002.

Bandeira, A.P. (2010). *Parâmetros técnicos para gerenciamento de áreas de riscos de escorregamentos de encostas na região metropolitana do Recife* [Doctoral thesis, Federal University of Pernambuco]. Federal University of Pernambuco's repository (in Portuguese). Retrieved in December 15, 2017, from https://repositorio.ufpe.br/handle/123456789/5126

Baum, R., Savage, W.Z., & Godt, J. (2009). *TRIGRS: a Fortran program for transient rainfall infiltration and grid-based regional slope-stability analysis. Version 2.0.* Reston: USGS.

Baum, R.L., & Godt, J.W. (2010). Early warning of rainfall-induced shallow landslides and debris flows in the USA. *Landslides*, 7, 259-272. http://dx.doi.org/10.1007/s10346-009-0177-0.

Baum, R.L., Godt, J.W., & Savage, W.Z. (2010). Estimating the timing and location of shallow rainfall-induced landslides using a model for transient, unsaturated infiltration. *Journal of Geophysical Research*, 115(F3), 1-26. http://dx.doi.org/10.1029/2009JF001321.

Chen, P., Lu, N., Formetta, G., Godt, J.W., & Wayllace, A. (2018). Tropical storm-induced landslide potential using combined field monitoring and numerical modeling. *Journal of Geotechnical and Geoenvironmental Engineering*, 144(11), 1-12. http://dx.doi.org/10.1061/(ASCE)GT.1943-5606.0001969.

Dietrich, W.E., & Montgomery, D.R. (1998). *SHALSTAB: a digital terrain model for mapping shallow landslide potential.* Retrieved in May 15, 2019, from http://calm.geo.berkeley.edu/geomorph/shalstab/index.htm

Dragićević, A.S., Laia, T., & Balramb, S. (2015). GIS-based multicriteria evaluation with multiscale analysis to characterize urban landslide susceptibility in data-scarce environments. *Habitat International*, 45(2), 114-125. http://dx.doi.org/10.1016/j.habitatint.2014.06.031.

Ebel, B.A., Godt, J.W., Lu, N., Coe, J.A., Smith, J.B., & Baum, R.L. (2018). Field and laboratory hydraulic characterization of landslide-prone soils in the Oregon Coast Range and implications for hydrologic simulation.

Vadose Zone Journal, 17(1), 180078. http://dx.doi.org/10.2136/vzj2018.04.0078.

Empresa Brasileira de Pesquisa Agropecuária – EMBRAPA. (2018). *SiBCS - Sistema Brasileiro de Classificação de Solos*. Brasília: Serviço de Produção de Informação. (in Portuguese).

Feltrin, R.M., Paiva, J.B.D., & Paiva, E.M.C.D. (2013). Dinâmica da água no solo simulada pelo modelo HYDRUS-1D e medida a campo para as condições climáticas do Sul do Brasil. In *Anais do 11º Simpósio de Hidráulica e Recursos Hídricos dos Países de Língua Portuguesa* (pp. 1-12), Maputo. Porto Alegre: APRH/ABRH/ACRH. (in Portuguese).

Guoa, W., Chena, Z., Wanga, W., Gaoc, W., Guoa, M., Kanga, H., Lid, P., Wanga, W., & Zhaoa, M. (2019). Telling a different story: the promote role of vegetation in the initiation of shallow landslides during rainfall on the Chinese Loess Plateau. *Geomorphology*, 350(1), 106879. https://doi.org/10.1016/j.geomorph.2019.106879.

Gusmão Filho, J.A. (1990). Ação integrada contra riscos geológicos em morros urbanos. In *Anais do I Simpósio Latino-Americano Sobre Risco Geológico Urbano* (pp. 421-435), São Paulo. São Paulo: ABGE.

Gusmão Filho, J.A., Ferreira, S.R.M., & Amorim, W.M. (1997). Escorregamentos em morros urbanos do Recife: o caso do Boleiro. In *Proceedings of the 2nd Panamerican Symposium on Landslides* (Vol. 1, pp. 985-994), Rio de Janeiro. Rio de Janeiro: ABMS/ABGE/ISSMGE.

McGuire, L.A., Rengers, F.K., Kean, J.W., Coel, J.A., Mirus, B.B., Baum, R.L., & Godt, J.W. (2016). Elucidating the role of vegetation in the initiation of rainfall-induced shallow landslides: Insights from an extreme rainfall event in the Colorado Front Range. *Geophysical Research Letters*, 43(17), 9084-9092. http://dx.doi.org/10.1002/2016GL070741.

Menon-Júnior, W. (2016). *Evolução temporal das áreas de risco à ocorrência de escorregamentos na bacia hidrográfica do córrego do Yung – Juiz de Fora/MG entre 1968 e 2010* [Master's dissertation, Federal University of Juiz de Fora]. Federal University of Juiz de Fora's repository. Retrieved in September 15, 2017, from https://repositorio.ufjf.br/jspui/handle/ufjf/2187

Michel, G.P., Koriyama, M., & Goerl, R.F. (2014). Comparative analysis of SHALSTAB and SINMAP for landslide susceptibility mapping in the Cunha River basin, southern Brazil. Progress in Erosion and Sedimentation in Latin America. *Journal of Soils and Sediments*, 14, 1266-1277. http://dx.doi.org/10.1007/s11368-014-0886-4.

Pack, R.T., Tarboton, D.G., Goodwin, C.N., & Prasad, A. (2005). *A stability index approach to terrain stability hazard mapping - SINMAP 2.* Utah: Utah State University. Retrieved in August 15, 2005, from http://www.engineering.usu.edu/dtarb/sinmap.html

PC-progress. (2019). *Hydrus-1D.* Retrieved in May 15, 2019, from https://www.pc-progress.com/en/Default.aspx?hydrus-1d

PC-progress. (2020). *Hydrus-1D.* Retrieved in October 15, 2020, from http://www.pc-progress.com/en/OnlineHelp/HYDRUS3/Hydrus.html?WaterFlowParameters

Pernambuco. Secretaria de Infraestrutura. (2017). *Programa Pernambuco Tridimensional (PE-3D).* Retrieved in September 15, 2017, from http://www.pe3d.pe.gov.br/

Pernambuco. Programa Pernambuco Tridimensional – PE3D. (2018). *Validação dos produtos aerofotogramétricos e perfilamento a laser. Relatório parcial do bloco 3 - análise de consistência lógica e completude.* Recife: Instituto de Tecnologia de Pernambuco.

Pfaltzgraff, P.A.S. (2007). *Mapa de susceptibilidade ao deslizamento na região metropolitana do Recife* [Doctoral thesis, Federal University of Pernambuco]. Federal University of Pernambuco's repository (in Portuguese). Retrieved in September 15, 2017, from https://attena.ufpe.br/handle/123456789/6331

Pradhan, A.M.S., & Kim, Y.T. (2016). Evaluation of a combined spatial multi-criteria evaluation model and deterministic model for landslide susceptibility mapping. *Catena*, 140, 125-139. http://dx.doi.org/10.1016/j.catena.2016.01.022.

Santana, R.G. (2006). *Análise de soluções de engenharia para estabilização de encostas ocupadas na Região Metropolitana do Recife – PE. Estudo de caso: ruptura ocorrida em encosta com ocupação desordenada na UR2, Ibura* [Degree of master, Federal University of Pernambuco]. Federal University of Pernambuco's repository (in Portuguese). Retrieved in September 15, 2017, from https://repositorio.ufpe.br/handle/123456789/5555

Santos, A.R. (2012). *Enchentes e deslizamentos: causas e soluções: áreas de risco no Brasil*. São Paulo: Pini (in Portuguese).

Sausen, T.M., & Lacruz, M.S.P. (2015). *Sensoriamento remoto para desastres*. São Paulo: Oficina de Textos (in Portuguese).

Schilirò, L., Djueyep, G.P., Esposito, C., & Mugnozza, G.S. (2019). The role of initial soil conditions in shallow landslide triggering: insights from physically based approaches. *Geofluids*, 2019, 2453786. http://dx.doi.org/10.1155/2019/2453786.

Silva, A., & Zuquette, L. (2013). Landslide hazard assessment based on FS_{3D} combined with an infiltration model. In C. Margottini, P. Canuti & K. Sassa (Eds.), *Landslide science and practice* (pp. 21-27). Berlin: Springer. https://doi.org/10.1007/978-3-642-31310-3_4.

Silva, L.A.A., Campos, D.J.S.L., & Aquino, M.R.A. (2010). Vulnerabilidade socioambiental nas cidades: os riscos e perigos de deslizamento de terra nas áreas pobres de Lagoa Encantada e Monte Verde, Recife-PE. In *Anais do XVI Encontro Nacional de Geógrafos*, Porto Alegre. Porto Alegre: ABG.

Šimunek, J., Šejna, M., Saito, H., Sakai, M., & van Genuchten, M.Th. (2013). *The HYDRUS-1D software package for simulating the one-dimensional movement of water, heat, and multiple solutes in variably-saturated media - Version*

4.17. Riverside: Department of Environmental Sciences, University of California Riverside.

Souza, W.M., Azevedo, P.V., & Araújo, L.E. (2012). Classificação da precipitação diária e impactos decorrentes dos desastres associados às chuvas na cidade do Recife-PE. *Revista Brasileira de Geografia Física*, 5(2), 250-268. http://dx.doi.org/10.26848/rbgf.v5i2.232788.

Sulaiman, W.N.A., Rosli, M.H., Samah, M.A.A., & Kamarudin, M.K.A. (2017). Landslide susceptibility mapping: effect of spatial resolution towards the prediction of landslide prone area in a tropical catchment. *Warasan Khana Witthayasat Maha Witthayalai Chiang Mai*, 44(2), 494-507.

Thiebes, B., Bell, R., Glade, T., Wang, J., & Bai, S. (2016). Application of SINMAP and analysis of model sensitivity – case studies from Germany and China. *Romanian Journal of Geography*, 60(1), 3-25.

Utah State University – USU (2017). *SINMAP*. Utah. Retrieved in May 15, 2017, from http://hydrology.usu.edu/sinmap/

van Genuchten, M.T. (1980). A closed-from equation for predicting the conductivity of unsaturated soils. *Soil Science Society of America Journal*, 44(5), 892-898. http://dx.doi.org/10.2136/sssaj1980.03615995004400050002x.

Witt, A.C. (2005). *Using a GIS (Geographic Information System) to model slope instability and debris flow hazards in the French broad river watershed, North Carolina* [Master's thesis, Faculty of North Carolina State University]. North Carolina State University's repository. Retrieved in September 15, 2017, from https://repository.lib.ncsu.edu/handle/1840.16/552

Zhang, X., Yu, G., Li, P., & Li, Z.B. (2017). Landslide zoning analysis in Zhouqu under different rainfall warning levels. *Environmental Earth Sciences*, 76(17), 600. http://dx.doi.org/10.1007/s12665-017-6932-y.

Zizioli, D., Meisina, C., Valentino, R., & Montrasio, L. (2013). Comparison between different approaches to modeling shallow landslide susceptibility: a case history in Oltrepo Pavese, Northern Italy. *Natural Hazards and Earth System Sciences*, 13, 559-573. http://dx.doi.org/10.5194/nhess-13-559-2013.

DISCUSSION

Soils and Rocks
An International Journal of Geotechnical and Geoenvironmental Engineering
www.soilsandrocks.com
ISSN 1980-9743
ISSN-e 2675-5475

Discussion of “Determination of liquid limit by the fall cone method”*

Kátia Vanessa Bicalho[1#], Janaina Silva Hastenreiter Küster[1], Lucas Broseghini Totola[1], Letícia Garcia Crevelin Cristello[1]

Discussion

The readers appreciate the comparative study that the authors have made on the liquid limit (LL) test results obtained by both the Swedish Standard (SS) fall-cone (LL_{FC}) and the Brazilian standard percussion (LL_{cup}) methods presented for soil samples collected from different geological formations in Brazil. The LL obtained by current standard methods are not definitive values but indicators of soil when its conditions reach the limit state (Manafi, 2019). The two LL methods measure different physical quantities (Haigh, 2012). Compared with the percussion (or Casagrande) method, the fall-cone method is less error-prone (Claveau-Mallet et al., 2012).

The most common LL fall-cone devices are the Swedish cone (60°-60g fall-cone) and the British/French cones (30°-80g fall-cone) (Leroueil & Le Bihan, 1996). LL measured by fall-cone test is not standardized in Brazil, and the readers would like to include some additional comments on a comparison of LL_{cup} with LL_{FC} values obtained by the Standard BS 1377 (BSI, 1990) fall-cone method considering different soils having LL_{cup} < 100%. The investigated data come from different operators and laboratories, and it may be expected that some uncontrolled factors during the LL measurements have played a role in the observed differences between the LL_{cup} and LL_{FC} values.

Figure 1 illustrates a comparison of LL data obtained by the SS (Clemente et al., 2020) and BS (Bicalho et al., 2014) fall-cone methods with those obtained by the Brazilian standard percussion method (hard rubber base cup). The solid square symbols are the data reported by the authors (SS fall-cone). The open square symbols are the data from BS fall-cone reported by the Bicalho et al. (2014). The LL for different natural inorganic low plasticity clays from different locations in Brazil were compiled by Bicalho et al. (2014) and included data by Pinto & Castro (1971) and Silveira (2001) with LL_{cup} ranging from 14 to 98% and LL_{FC} from 18 to 98% (BS fall-cone method). The clays are essentially kaolinites and illites. A fitted empirical relationship ($LL_{FC} = LL_{cup} + 2.7$, $R^2 = 0.98$) shows that LL_{cup} values are generally 2.7% lower than LL_{FC} for the data, Figure 1. The linear empirical LL_{FC} - LL_{cup} correlation proposed by Queiroz de Carvalho (1986) for 27 samples of lateritic soils from Brazil (LL_{cup} ranging from 13 to 48%) in which kaolinite is the only clay mineral is also presented in Figure 1. The comparison of data from different sources shows variations in the LL results based on Casagrande and fall-cone methods (Figure 1). It can be observed from Figure 1 that most data fall within $LL_{FC} = 0.8LL_{cup}$ and $LL_{FC} = 1.2LL_{cup}$ lines. The data consistently indicate higher LL being obtained for the fall-cone devices compared to the Casagrande cup for LL_{cup} < 40%, while the difference in LL_{FC} and LL_{cup} is more spread out for LL_{cup} > 40% for the investigated fine-grained soils. Also, the LL_{FC}/LL_{cup} ratio may range to values even greater than 1.2 at low LL_{cup} values (i.e., LL_{cup} < 40%). It is therefore worthwhile to examine the differences in the LL_{cup} and LL_{FC} (SS and BS fall-cone) of fine-grained soils when applying LL values obtained by different standards in soil classification systems and empirical correlations in geotechnical engineering, even for LL_{cup} < 100% where the LL values obtained with the fall-cone and Casagrande methods are often considered approximately equal (Wasti & Bezirci, 1986; Spagnoli, 2012).

#Corresponding author. E-mail address: kvbicalho@gmail.com
[1]Universidade Federal do Espírito Santo, Civil Engineering Department, Vitoria, ES, Brasil.
*Appears in *Soils and Rocks*, 43(4), 661-667.
Submitted on January 29, 2021; Final Acceptance on May 12, 2021.
https://doi.org/10.28927/SR.2021.062721

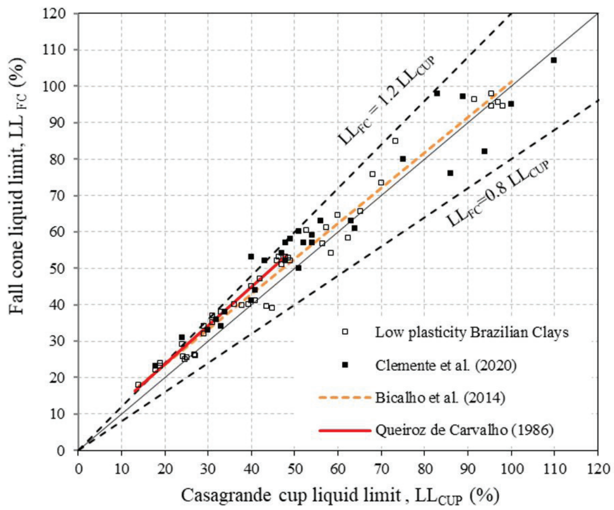

Figure 1. Comparison of LL test results obtained by the SS and BS fall-cone methods with those obtained by the Brazilian standard percussion method for LL data between 14% and 110%.

Declaration of interest

We wish to confirm that there are no known conflicts of interest associated with this publication.

Author’s contributions

Kátia Vanessa Bicalho: conceptualization, supervision, review and approval. Janaina Silva Hastenreiter Küster: discussion, writing – reviewing and editing; Lucas Broseghini Totola: discussion, writing – reviewing and editing. Letícia Garcia Crevelin Cristello: discussion.

List of symbols

LL	Liquid limit
LL_{FC}	Liquid limit obtained by the fall-cone method
LL_{cup}	Liquid limit obtained by the standard percussion method
SS	Swedish Standard
BS	British Standard
R^2	Coefficient of determination in linear regression

References

Bicalho, K.V., Gramelich, J.C., & Santos, C.L.C. (2014). Comparação entre os valores de limite de liquidez obtidos pelo método de Casagrande e cone para solos argilosos brasileiros. *Comunicações Geológicas*, 101(3), 1097-1099. In Portuguese.

British Standards Institution – BSI. (1990). *BS 1377: methods of test for soil for civil engineering purposes. Part 2. Classification tests.* London.

Claveau-Mallet, D., Duhaime, F., & Chapuis, R.P. (2012). Practical considerations when using the Swedish fall cone. *Geotechnical Testing Journal*, 35(4), 618-628. http://dx.doi.org/10.1520/GTJ104178.

Clemente, C.W., Faro, V.P., & Moncada, M.P.H. (2020). Determination of liquid limit by the Fall Cone method. *Soils and Rocks*, 43(4), 661-667.

Haigh, S.K. (2012). Mechanics of the Casagrande liquid limit test. *Canadian Geotechnical Journal*, 49(9), 1015-1023. http://dx.doi.org/10.1139/t2012-066.

Leroueil, S., & Le Bihan, J.P. (1996). Liquid limits and fall cones. *Canadian Geotechnical Journal*, 33(5), 793-798. http://dx.doi.org/10.1139/t96-104-324.

Manafi, M.S.G. (2019). Soil plasticity variability and its effect on soil classification. *Geotechnical Testing Journal*, 42(2), 457-470. http://dx.doi.org/10.1520/GTJ20170273.

Pinto, S., & Castro, P.F. (1971). *Determinação do limite de liquidez pelo método do cone de penetração*. Brasília: Departamento Nacional de Estradas de Rodagem. In Portuguese.

Queiroz de Carvalho, J.B. (1986). The applicability of the cone penetrometer to determine the liquid limit of lateritic soils. *Geotechnique*, 36(1), 109-111. http://dx.doi.org/10.1680/geot.1986.36.1.109.

Silveira, L.C.S. (2001). O cone de penetração como ensaio alternativo na determinação da plasticidade de solos. In *Anais do Congresso Brasileiro de Ensino de Engenharia* (NTM:16-NTM:19), Porto Alegre. Porto Alegre: ABENGE. In Portuguese.

Spagnoli, G. (2012). Comparison between Casagrande and drop-cone methods to calculate liquid limit for pure clay. *Canadian Journal of Soil Science*, 92(6), 859-864. http://dx.doi.org/10.4141/cjss2012-011.

Wasti, Y., & Bezirci, M.H. (1986). Determination of the consistency limits of soils by the fall cone test. *Canadian Geotechnical Journal*, 23(2), 241-246. http://dx.doi.org/10.1139/t86-033.


DF+, YOUR
TRUST FIRST
GEOLOGICAL, GEOTECHNICAL ENGINEERING AND WATER RESOURCES SOLUTIONS FOR THE MINING SECTOR AND OTHERS.
DF+ IS A COMPANY WITH A FOCUS ON THE MINERAL SECTOR AND MORE THAN 15 YEARS OF EXPERIENCE. WE OPERATE IN ALL PHASES OF A PROJECT, FROM FEASIBILITY STUDIES AND PROJECT DEVELOPMENT TO TECHNICAL MONITORING OF CONSTRUCTION AND MINE CLOSURE.
JOIN OUR SOCIAL NETWORKS TO KNOW MORE ABOUT OUR SERVICES.
AVE BARÃO HOMEM DE MELO, 4554 – 5th floor
ESTORIL, BELO HORIZONTE/MG
+55 31 2519-1001
comercial@dfmais.eng.br
DF+GEOTECHNICAL ENGINEERING
AND WATER RESOURCES

PIONEERING
AND INNOVATION
SINCE 1921
LICENCE NO. 24 - PUB
TEIXEIRA DUARTE
ENGENHARIA E CONSTRUÇÕES, S.A.
PORT FACILITY CONSTRUCTION
NACALA - MOZAMBIQUE
Building a better world.
teixeiraduarteconstruction.com

The Best Solution!

***Tecnilab Portugal, S.A.** will provide you with answers to your Geotechnical engineering needs.*

Tecnilab Portugal, S.A. is a professional Geotechnical engineering company and has a lot of experience as a professional group that mainly engages in measurement engineering in dam, subway(Metro), harbor, power plant, soft ground and structure construction.

WE ARE THE DISTRIBUTOR OF PORTUGAL OF ACE INSTRUMENT CO., LTD. IN KOREA.

ACE INSTRUMENT CO., LTD. is a company that obtains worldwide reputation for supplying high precision, high reliability products in all Geotechnical instruments, data logger and in-situ test equipments. Independently developed automatic monitoring system can be used anywhere in the world, including buildings, bridges, ground and any constructions.

Data Acquisition System & Web Monitoring Program

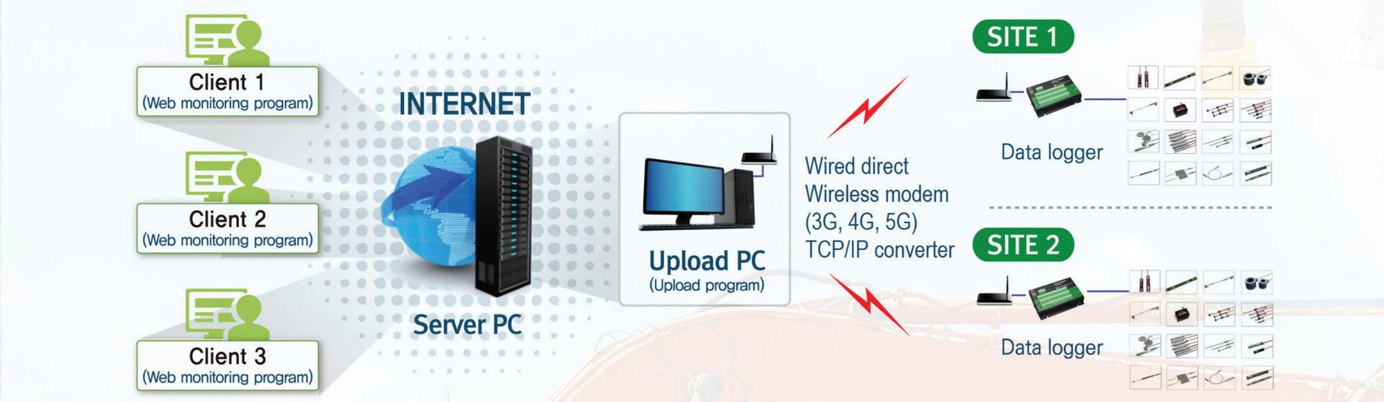


Geotechnical Instruments


Digital Inclinometer Set


Dataloggers, Indicators


Portable Digital Tiltmeter

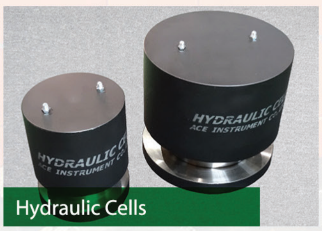
Hydraulic Cells


Inclinometer Casings


In-Situ Test Equipments


Pendulum System

Sales company

Tecnilab Portugal, S.A.
A: Rua Gregorio Lopes, Lote 1512B 1449-041 Lisboa Portugal
T: +351 217 220 870 F: +351 217 264 550
www.tecnilab.pt

Manufacturer

ACE INSTRUMENT CO., LTD.
The first value in Geotechnical & Structural Instrumentation
A: 9, Dangjung-ro 27 beon-gil, Gunpo-si, Gyeonggi-do, Korea
T: +82 31 459 8753-7 F: +82 31 459 8758 E: acens@naver.com
www.aceinstrument.com

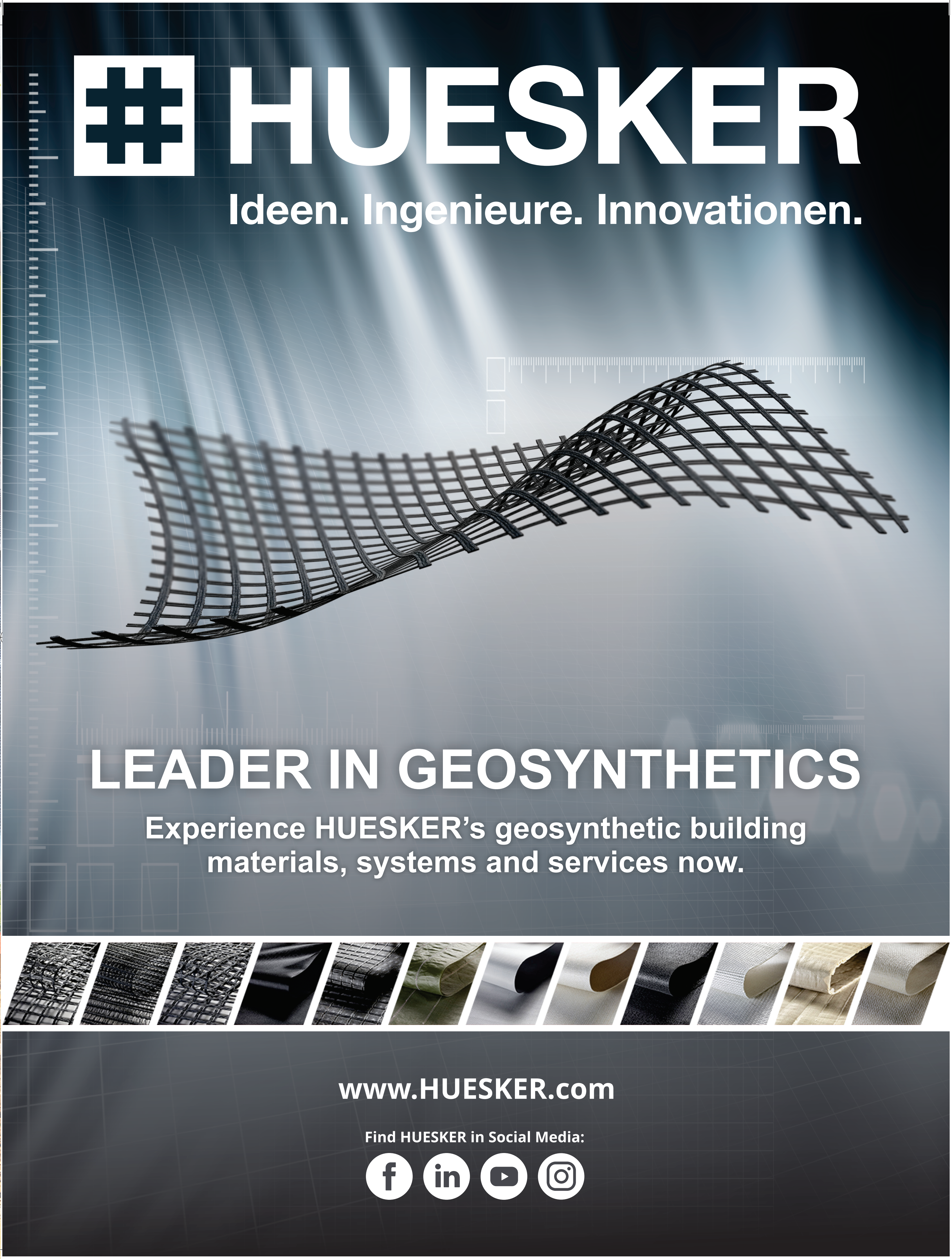
HUESKER
Ideen. Ingenieure. Innovationen.
LEADER IN GEOSYNTHETICS
Experience HUESKER's geosynthetic building materials, systems and services now.
www.HUESKER.com
Find HUESKER in Social Media:

Guide for Authors

Soils and Rocks is an international scientific journal published by the Brazilian Association for Soil Mechanics and Geotechnical Engineering (ABMS) and by the Portuguese Geotechnical Society (SPG). The aim of the journal is to publish original papers on all branches of Geotechnical Engineering. Each manuscript is subjected to a single-blind peer-review process. The journal's policy of screening for plagiarism includes the use of a plagiarism checker on all submitted manuscripts.

Soils and Rocks embraces the international Open Science program and is striving to meet all the recommendations. However, at this moment, the journal is not yet accepting preprints and open data, and has not adopted open peer reviews.

Soils and Rocks provides a manuscript template available at the journal's website.

1. Category of papers

Submissions are classified into one of the following categories:

Article – an extensive and conclusive dissertation about a geotechnical topic, presenting original findings.
Technical Note – presents a study of smaller scope or results of ongoing studies, comprising partial results and/or particular aspects of the investigation.
Case Study – report innovative ways to solve problems associated with design and construction of geotechnical projects. It also presents studies of the performance of existing structures.
Review Article – a summary of the State-of-the-Art or State-of-the-Practice on a particular subject or issue and represents an overview of recent developments.
Discussion – specific discussions about published papers.

Authors are responsible for selecting the correct category when submitting their manuscript. However, the manuscript category may be altered based on the recommendation of the Editorial Board. Authors are also requested to state the category of paper in their Cover Letter.

When submitting a manuscript for review, the authors should indicate the category of the manuscript, and is also understood that they:

a) assume full responsibility for the contents and accuracy of the information in the paper;
b) assure that the paper has not been previously published, and is not being submitted to any other journal for publication.

2. Paper length

Full-length manuscripts (Article, Case Study) should be between 4,000 and 8,000 words. Review articles should have up to 10,000 words. Technical Notes have a word count limit of 3,500 words. Discussions have a word count limit of 1,000 words. These word count limits exclude the title page, notation list (e.g., symbols, abbreviations), captions of tables and figures, acknowledgments and references. Each single column and double column figure or table is considered as equivalent to 150 and 300 words, respectively.

3. Scientific style

The manuscripts should be written in UK or US English, in the third person and all spelling should be checked in accordance with a major English Dictionary. The manuscript should be able to be readily understood by a Civil Engineer and avoid colloquialisms. Unless essential to the comprehension of the manuscript, direct reference to the names of persons, organizations, products or services is not allowed. Flattery or derogatory remarks about any person or organization should not be included.

The author(s) of Discussion Papers should refer to himself (herself/themselves) as the reader(s) and to the author(s) of the paper as the author(s).

The International System (SI) units must be used. The symbols are recommended to be in accordance with Lexicon in 14 Languages, ISSMFE (2013) and the ISRM List of Symbols. Use italics for single letters that denote mathematical constants, variables, and unknown quantities, either in tables or in the text.

4. Submission requirements and contents

A submission implies that the following conditions are met:

- the authors assume full responsibility for the contents and accuracy of the information presented in the paper;
- the manuscript contents have not been published previously, except as a lecture or academic thesis;
- the manuscript is not under consideration for publication elsewhere;
- the manuscript is approved by all authors;
- the manuscript is approved by the necessary authorities, when applicable, such as ethics committees and institutions that may hold intellectual property on contents presented in the manuscript;
- the authors have obtained authorization from the copyright holder for any reproduced material;
- the authors are aware that the manuscript will be subjected to plagiarism check.

The author(s) must upload two digital files of the manuscript to the Soils and Rocks submission system. The size limit for each submission file is 20 MB. The manuscript should be submitted in docx format (Word 2007 or higher) or doc format (for older Word versions). An additional PDF format file of the manuscript is also required upon submission. Currently, the journal is not accepting manuscripts prepared using LaTeX.

The following documents are required as minimum for submission:

- cover letter;
- manuscript with figures and tables embedded in the text (doc or docx format);

manuscript with figures and tables embedded in the text for revision (PDF format);
- permission for re-use of previously published material when applicable, unless the author/owner has made explicit that the image is freely available.

4.1 Cover letter

The cover letter should include: manuscript title, submission type, authorship information, statement of key findings and work novelty, and related previous publications if applicable.

4.2 Title page

The title page is the first page of the manuscript and must include:

- A concise and informative title of the paper. Avoid abbreviations, acronyms or formulae. Discussion Papers should contain the title of the paper under discussion. Only the first letter of the first word should be capitalized.
- Full name(s) of the author(s). The first name(s) should not be abbreviated. The authors are allowed to abbreviate middle name(s).
- The corresponding author should be identified by a pound sign # beside his/her and in a footnote.
- The affiliation(s) of the author(s), should follow the format: Institution, (Department), City, (State), Country.
- Affiliation address and e-mail must appear below each author's name.
- The 16-digit ORCID of the author(s) – mandatory
- Main text word count (excluding abstract and references) and the number of figures and tables

4.3 Permissions

Figures, tables or text passages previously published elsewhere may be reproduced under permission from the copyright owner(s) for both the print and online format. The authors are required to provide evidence that such permission has been granted at the moment of paper submission.

4.4 Declaration of interest

Authors are required to disclose conflicting interests that could inappropriately bias their work. For that end, a section entitled "Declaration of interest" should be included following any acknowledgments and prior to the "Authors' contributions" section. In case of the absence of conflicting interests, the authors should still include a declaration of interest.

4.5 Authors' contributions

Authors are required to include an author statement outlining their individual contributions to the paper according to the CASRAI CRediT roles (as per https://casrai.org/credit). The minimum requirements of contribution to the work for recognition of authorship are: a) Participate actively in the discussion of results; b) Review and approval of the final version of the manuscript. A section entitled "Authors' contributions" should be included after the declaration of interest section, and should be formatted with author's name and CRediT role(s), according to the example:

Samuel Zheng: conceptualization, methodology, validation. Olivia Prakash: data curation, writing - original draft preparation. Fatima Wang: investigation, validation. Kwame Bankole: supervision. Sun Qi: writing - reviewing and editing.

Do not include credit items that do not follow the Taxonomy established by CASRAI CRediT roles.

The authors' contributions section should be omitted in manuscripts that have a single author.

5. Plagiarism checking

Submitted papers are expected to contain at least 50 % new content and the remaining 50 % should not be verbatim to previously published work.

All manuscripts are screened for similarities. Currently, the Editorial Board uses the plagiarism checker Plagius (www.plagius.com) to compare submitted papers to already published works. Manuscripts will be rejected if more than 20 % of content matches previously published work, including self-plagiarism. The decision to reject will be under the Editors' discretion if the percentage is between 10 % and 20 %.

IMPORTANT OBSERVATION: Mendeley software plug-in (suggested in this guide) for MS-Word can be used to include the references in the manuscript. This plug-in uses a field code that sometimes includes automatically both title and abstract of the reference. Unfortunately, the similarity software adopted by the Journal (Plagius) recognizes the title and abstract as an actual written text by the field code of the reference and consequently increases considerably the percentage of similarity. Please do make sure to remove the abstract (if existing) inside Mendeley section where the adopted reference is included. This issue has mistakenly caused biased results in the past. The Editorial Board of the journal is now aware of this tendentious feature.

6. Formatting instructions

The text must be presented in a single column, using ISO A4 page size, left, right, top, and bottom margins of 25 mm, Times New Roman 12 font, and line spacing of 1.5. All lines and pages should be numbered.

The text should avoid unnecessary italic and bold words and letters, as well as too many acronyms. Authors should avoid to capitalize words and whenever possible to use tables with distinct font size and style of the regular text.

Figures, tables and equations should be numbered in the sequence that they are mentioned in the text.

Abstract

Please provide an abstract between 150 and 250 words in length. Abbreviations or acronyms should be avoided. The abstract should state briefly the purpose of the work, the main results and major conclusions or key findings.

Keywords

A minimum of three and a maximum of six keywords must be included after the abstract. The keywords must represent the content of the paper. Keywords offer an opportunity to include synonyms for terms that are frequently referred to in the literature using more than one term. Adequate keywords maximize the visibility of your published paper.

Examples:

Poor keywords – piles; dams; numerical modeling; laboratory testing

Better keywords – friction piles; concrete-faced rockfill dams; material point method; bender element test

List of symbols

A list of symbols and definitions used in the text must be included before the References section. Any mathematical constant, variable or unknown quantity should appear in italics.

6.1 Citations

References to other published sources must be made in the text by the last name(s) of the author(s), followed by the year of publication. Examples:

- Narrative citation: […] while Silva & Pereira (1987) observed that resistance depended on soil density
- Parenthetical citation: It was observed that resistance depended on soil density (Silva & Pereira, 1987).

In the case of three or more authors, the reduced format must be used, e.g.: Silva et al. (1982) or (Silva et al., 1982). Do not italicize “et al.”

Two or more citations belonging to the same author(s) and published in the same year are to be distinguished with small letters, e.g.: (Silva, 1975a, b, c.).

Standards must be cited in the text by the initials of the entity and the year of publication, e.g.: ABNT (1996), ASTM (2003).

6.2 References

A customized style for the Mendeley software is available and may be downloaded from this link.

Full references must be listed alphabetically at the end of the text by the first author’s last name. Several references belonging to the same author must be cited chronologically.

Some formatting examples are presented here:

Journal Article

Bishop, A.W., & Blight, G.E. (1963). Some aspects of effective stress in saturated and partly saturated soils. *Géotechnique*, 13(2), 177-197. https://doi.org/10.1680/geot.1963.13.3.177

Castellanza, R., & Nova, R. (2004). Oedometric tests on artificially weathered carbonatic soft rocks. *Journal of Geotechnical and Geoenvironmental Engineering*, 130(7), 728-739. https://doi.org/10.1061/(ASCE)1090-0241(2004)130:7(728)

Fletcher, G. (1965). Standard penetration test: its uses and abuses. Journal of the Soil Mechanics Foundation Division, 91, 67-75.

Indraratna, B., Kumara, C., Zhu S-P., Sloan, S. (2015). Mathematical modeling and experimental verification of fluid flow through deformable rough rock joints. *International Journal of Geomechanics*, 15(4): 04014065-1-04014065-11. https://doi.org/10.1061/(ASCE)GM.1943-5622.0000413

Garnier, J., Gaudin, C., Springman, S.M., Culligan, P.J., Goodings, D., Konig, D., ... & Thorel, L. (2007). Catalogue of scaling laws and similitude questions in geotechnical centrifuge modelling. *International Journal of Physical Modelling in Geotechnics*, 7(3), 01-23. https://doi.org/10.1680/ijpmg.2007.070301

Bicalho, K.V., Gramelich, J.C., & Santos, C.L.C. (2014). Comparação entre os valores de limite de liquidez obtidos pelo método de Casagrande e cone para solos argilosos brasileiros. *Comunicações Geológicas*, 101(3), 1097-1099 (in Portuguese).

Book

Lambe, T.W., & Whitman, R.V. (1979). *Soil Mechanics, SI version*. John Wiley & Sons.

Das, B.M. (2012). *Fundamentos de Engenharia Geotécnica*. Cengage Learning (in Portuguese).

Head, K.H. (2006). *Manual of Soil Laboratory Testing* - *Volume 1*: Soil Classification and Compaction Tests. Whittles Publishing.

Bhering, S.B., Santos, H.G., Manzatto, C.V., Bognola, I., Fasolo, P.J., Carvalho, A.P., ... & Curcio, G.R. (2007). *Mapa de solos do estado do Paraná*. Embrapa (in Portuguese).

Book Section

Yerro, A., & Rohe, A. (2019). Fundamentals of the Material Point Method. In *The Material Point Method for Geotechnical Engineering* (pp. 23-55). CRC Press. https://doi.org/10.1201/9780429028090

Sharma, H.D., Dukes, M.T., & Olsen, D.M. (1990). Field measurements of dynamic moduli and Poisson´s ratios of refuse and underlying soils at a landfill site. In *Geotechnics of Waste Fills - Theory and Practice* (pp. 57-70). ASTM International. https://doi.org/10.1520/STP1070-EB

Cavalcante, A.L.B., Borges, L.P.F., & Camapum de Carvalho, J. (2015). Tomografias computadorizadas e análises numéricas aplicadas à caracterização da estrutura porosa de solos não saturados. In *Solos Não Saturados no Contexto Geotécnico* (pp. 531-553). ABMS (in Portuguese).

Proceedings

Jamiolkowski, M.; Ladd, C.C.; Germaine, J.T., & Lancellotta, R. (1985). New developments in field and laboratory testing of soils. *Proc. 11th International Conference on Soil Mechanics and Foundation Engineering,* San Francisco, August 1985. Vol. 1, Balkema, 57-153.

Massey, J.B., Irfan, T.Y. & Cipullo, A. (1989). The characterization of granitic saprolitic soils. *Proc. 12th International Conference on Soil Mechanics and Foundation Engineering*, Rio de Janeiro. Vol. 6, Publications Committee of XII ICSMFE, 533-542.

Indraratna, B., Oliveira D.A.F., & Jayanathan, M. (2008b). Revised shear strength model for infilled rock joints considering overconsolidation effect. *Proc. 1st Southern Hemisphere International Rock Mechanics Symposium*, Perth. ACG, 16-19.

Barreto, T.M., Repsold, L.L., & Casagrande, M.D.T. (2018). Melhoramento de solos arenosos com polímeros. *Proc. 19º Congresso Brasileiro de Mecânica dos Solos e Engenharia Geotécnica*, Salvador. Vol. 2, ABMS, CBMR, ISRM & SPG, 1-11 (in Portuguese).

Thesis

Lee, K.L. (1965). *Triaxial compressive strength of saturated sands under seismic loading conditions* [Unpublished doctoral dissertation]. University of California at Berkeley.

Chow, F.C. (1997). *Investigations into the behaviour of displacement pile for offshore foundations* [Doctoral thesis, Imperial College London]. Imperial College London's repository. https://spiral.imperial.ac.uk/handle/10044/1/7894

Araki, M.S. (1997). *Aspectos relativos às propriedades dos solos porosos colapsíveis do Distrito Federal* [Unpublished master's dissertation]. University of Brasília (in Portuguese).

Sotomayor, J.M.G. (2018). *Evaluation of drained and non-drained mechanical behavior of iron and gold mine tailings reinforced with polypropylene fibers* [Doctoral thesis, Pontifical Catholic University of Rio de Janeiro]. Pontifical Catholic University of Rio de Janeiro's repository (in Portuguese). https://doi.org/10.17771/PUCRio.acad.36102*

* *official title in English should be used when available in the document.*

Report

ASTM D7928-17. (2017). Standard Test Method for Particle-Size Distribution (Gradation) of Fine-Grained Soils Using the Sedimentation (Hydrometer) Analysis. *ASTM International, West Conshohocken, PA.* https://doi.org/10.1520/D7928-17

ABNT NBR 10005. (2004). Procedure for obtention leaching extract of solid wastes. *ABNT - Associação Brasileira de Normas Técnicas*, Rio de Janeiro, RJ (in Portuguese).

DNIT. (2010). Pavimentação - Base de solo-cimento - Especificação de serviço DNIT 143. *DNIT -Departamento Nacional de Infraestrutura de Transportes*, Rio de Janeiro, RJ (in Portuguese).

USACE (1970). Engineering and Design: Stability of Earth and Rock-Fill Dams, Engineering Manual 1110-2-1902. Corps of Engineers, Washington, D.C.

Web Page

Soils and Rocks. (2020). *Guide for Authors*. Soils and Rocks. Retrieved in September 16, 2020, from http://www.soilsandrocks.com/

6.3 Artworks and illustrations

Each figure should be submitted as a high-resolution image, according to the following mandatory requirements:

- Figures must be created as a TIFF file format using LZW compression with minimum resolution of 500 dpi.
- Size the figures according to their final intended size. Single-column figures should have a width of up to 82 mm. Double-column figures should have a maximum width of 170 mm.
- Use Times New Roman for figure lettering. Use lettering sized 8-10 pt. for the final figure size.
- Lines should have 0.5 pt. minimum width in drawings.
- Titles or captions should not be included inside the figure itself.

Figures must be embedded in the text near the position where they are first cited. Cite figures in the manuscript in consecutive numerical order. Denote figure parts by lowercase letters (a, b, c, etc.). Please include a reference citation at the end of the figure caption for previously published material. Authorization from the copyright holder must be provided upon submission for any reproduced material.

Figure captions must be placed below the figure and start with the term "Figure" followed by the figure number and a period. Example:

Figure 1. Shear strength envelope.

Do not abbreviate "Figure" when making cross-references to figures.

All figures are published in color for the electronic version of the journal; however, the print version uses grayscale. Please format figures so that they are adequate even when printed in grayscale.

Accessibility: Please make sure that all figures have descriptive captions (text-to-speech software or a text-to-Braille hardware could be used by blind users). Prefer using patterns (e.g., different symbols for dispersion plot) rather than (or in addition to) colors for conveying information (then the visual elements can be distinguished by colorblind users). Any figure lettering should have a contrast ratio of at least 4.5:1

Improving the color accessibility for the printed version and for colorblind readers: Authors are encouraged to use color figures because they will be published in their original form in the online version. However, authors must consider the need to make their color figures accessible for reviewers and readers that are colorblind. As a general rule of thumb, authors should avoid using red and green simultaneously. Red should be replaced by magenta, vermillion, or orange. Green should be replaced by an off-green color, such as blue-green. Authors should prioritize the use of black, gray, and varying tones of blue and yellow.

These rules of thumb serve as general orientations, but authors must consider that there are multiple types of color blindness, affecting the perception of different colors. Ideally, authors should make use of the following resources: 1) for more information on how to prepare color figures, visit https://jfly.uni-koeln.de/; 2) a freeware software available at http://www.vischeck.com/ is offered by Vischeck, to show how your figures would be perceived by the colorblind.

6.4 Tables

Tables should be presented as a MS Word table with data inserted consistently in separate cells. Place tables in the text near the position where they are first cited. Tables should be numbered consecutively using Arabic numerals and have a caption consisting of the table number and a brief title. Tables should always be cited in the text. Any previously published material should be identified by giving the original source as a reference at the end of the table caption. Additional comments can be placed as footnotes, indicated by superscript lower-case letters.

When applicable, the units should come right below the corresponding column heading. Horizontal lines should be used at the top and bottom of the table and to separate the headings row. Vertical lines should not be used.

Table captions must be placed above the table and start with the term "Table" followed by the table number and a period. Example:

Table 1. Soil properties.

Do not abbreviate "Table" when making cross-references to tables. Sample:

Table 1. Soil properties

Parameter	Symbol	Value
Specific gravity of the sand particles	G_s	2.64
Maximum dry density (Mg/m^3)	$\rho_{d(max)}$	1.554
Minimum dry density (Mg/m^3)	$\rho_{d(min)}$	1.186
Average grain-size (mm)	d_{50}	0.17
Coefficient of uniformity	C_u	1.97

6.5 Mathematical equations

Equations must be submitted as editable text, created using MathType or the built-in equation editor in MS Word. All variables must be presented in italics.

Equations must appear isolated in a single line of the text. Numbers identifying equations must be flushed with the right margin. International System (SI) units must be used. The definitions of the symbols used in the equations must appear in the List of Symbols.

Do not abbreviate "Equation" when making cross-references to an equation.